Impact Structures:
How post-impact thermal conditions influence magnetic behavior

Zur Erlangung des akademischen Grades eines

DOKTORS DER NATURWISSENSCHAFTEN (Dr. rer. nat.)

von der KIT-Fakultät für
Bauingenieur-, Geo- und Umweltwissenschaften des

Karlsruher Instituts für Technologie (KIT)

genehmigte

DISSERTATION

von

Bruno Daniel Leite Mendes, M.Sc.

Hauptreferentin: Prof. Dr. Agnes Kontny

Korreferent: Prof. Dr. Stuart Gilder

Mündliche Prüfung: 22/04/2024

Karlsruhe 2024

I dedicate this thesis to my Grandfather, who always wished to see me doctorate. I hope I made you proud.

Abstract

Large scale meteorite impact events are some of the most catastrophic and instantaneous geological processes in nature. These events release high amounts of energy, and generate pressures which will vaporize, melt and metamorphose the target rock. Large impact events create impact structures with very characteristic features, one of which being intense magnetic anomalies. These anomalies are caused by a contrast of the total magnetization in the shocked target, newly formed impactites (that is, rocks formed by, or related to the impact event) and the regional background magnetization. The total magnetization (M_{tot}) is the sum of natural remanent magnetization (NRM) and induced magnetization (κ*B, κ is magnetic susceptibility and B is Earth's magnetic field).

Shock deformation causes a sharp loss of up to 90% of NRM and κ in the magnetite-bearing target. The demagnetization of magnetite is caused by the shock-induced physical deformation, such as brittle grain fracturing and fragmentation, and ductile crystal lattice defects. Physical defects also enhance magnetic domain wall-pinning, which decreases the apparent domain state of magnetite, from originally multi-domain (MD) towards pseudo-single domain (PSD), or even single domain (SD) states. The change in apparent domain state is concomitant with an increase in magnetic coercivity, and further decreases κ. However, a recent study found that post-shock thermal annealing of shocked magnetite causes a "healing" of some of the reversible ductile lattice defects, which reduces domain wall-pinning and allows for the restoration and recovery of some magnetic properties, including an increase of κ.

Natural post-impact magnetic recovery through temperature has not been studied to date, and is particularly relevant for large impact craters such as the Chicxulub (Mexico). In this study we compared the large Chicxulub (diameter ca. 200 km) with the smaller Nördlinger Ries structure (Germany, diameter ca. 25 km). In both impact structures, high temperature impactites (>900°C) and post-impact hydrothermalism may lead to optimal conditions for natural annealing to take place. The effect that this phenomenon has on the characteristic magnetic signature of the craters remains unclear until now.

To address this knowledge gap, magnetite samples from the Chicxulub and Nördlinger Ries craters were investigated through rock-magnetic, petrographic and mineral chemical methods. Two generations of magnetite common to both craters were observed: (1) a pure, stoichiometric shocked magnetite with large (~100 μm) grains in the basement; and (2) a newly formed, generally low-cation substituted (Ti-) magnetite, with smaller (~10-50 μm) grains and no visible shock deformation, in the impactites.

Naturally shocked MD magnetite was found to show an apparent domain state decrease towards PSD, similar to magnetite shocked experimentally in laboratory conditions. Temperatures above 540°C create an irreversible increase in κ, and restore some apparent MD state contributions. The threshold for annealing and magnetic recovery is estimated to be ~540°C. If the magnetite is oxidized and hematite is present in the sample, it transforms back to magnetite if experimentally heated above 560°C in an argon atmosphere. The transformation creates very small magnetite grains with mottled textures and SD to superparamagnetic (SP) domain states, in a process that masks annealing if both occur concomitantly. This is an underappreciated phenomenon, that may lead to NRM remagnetization and overprint in nature, under certain conditions.

In Chicxulub, the shocked magnetite of the uplifted basement shows shock-reduced NRM and κ values, leading to a low total magnetization in the peak-ring. We attribute the negative anomaly in the peak-ring to this lack of magnetization. The hydrothermal system did not significantly overprint the magnetic signal, and its temperatures (~450°C) were not high enough to anneal the magnetite naturally, and thus it did not affect significantly the magnetic anomaly in the peak-ring. Natural annealing takes place in contact with the impact melt, where basement magnetite shows increased κ, and a transformation of pre-impact oxidation-derived hematite into newly formed SD-SP magnetite. The impact melt shows strong NRM and κ values, but in the peak-ring it constitutes only a thin layer, which also does not significantly contribute to the anomaly.

In Nördlinger Ries, the basement magnetite is similarly demagnetized, and natural annealing occurs locally due to the prevalence of melt bearing suevite dykes in the basement, with high emplacement temperatures (>900°C). The hydrothermal system in Nördlinger Ries had shorter duration and lower temperatures than in Chicxulub (max. 300°C), and also does not significantly affect the magnetic anomalies of the crater. The impact melt shows weak magnetization, with κ values comparable to the shocked and demagnetized basement. On the other hand, impact breccia (suevite) in Nördlinger Ries show high κ and strong reverse polarity magnetization, which contributes to the negative magnetic anomalies.

Kurzfassung

Großflächige Meteoriteneinschläge gehören zu den katastrophalsten und am schnellsten ablaufenden geologischen Prozessen in der Natur, bei denen große Energiemengen freigesetzt und hohe Drücke erzeugt werden, die das Zielgestein verdampfen, schmelzen und metamorphisieren können. Große Einschlagsereignisse schaffen Einschlagsstrukturen mit sehr charakteristischen Merkmalen, wie z. B. starke magnetische Anomalien. Diese Anomalien werden durch einen Kontrast zwischen der Gesamtmagnetisierung im geschockten Zielgestein, in neu gebildeten Impaktiten (d. h. Gesteinen, die durch das Einschlagsereignis entstanden sind oder damit in Zusammenhang stehen) und der regionalen Hintergrundmagnetisierung verursacht. Die Gesamtmagnetisierung (M_t) ist die Summe der natürlichen remanenten Magnetisierung (NRM) und der induzierten Magnetisierung (κ*B, κ ist die magnetische Suszeptibilität (MS) und B ist das Erdmagnetfeld).

Schockverformung führt zu einem starken Verlust von bis zu 90 % der NRM und κ im magnetitführenden Zielgestein. Dieser Magnetisierungsverlust wird auf die physikalische Verformung von Magnetit zurückgeführt, wie z. B. Sprödbruch und duktile Kristallgitterdefekte, die ihn entmagnetisieren. Physikalische Defekte führen auch zu einer verstärkten magnetischen "Wandreibung", wodurch der Domänenzustand von ursprünglich Mehrbereichsteilchen (multi-domain, MD) zu Pseudo-Einbereichs-Teilchen (PSD) oder Einbereichssteilchen (SD) abnimmt. Dieser Prozess führt außerdem zu einem Anstieg der magnetischen Koerzitivfeldstärke und einem weiteren Rückgang der κ. In einer kürzlich durchgeführten Studie wurde jedoch festgestellt, dass eine thermische Behandlung von geschocktem Magnetit nach dem Schock einige der reversiblen Gitterdefekte ausglühen lässt, die “Wandreibung” verringert und somit die Wiederherstellung einiger magnetischer Eigenschaften und der κ ermöglicht.

Eine natürliche magnetische Erholung nach einem Meteoriteneinschlag durch Temperatur wurde bisher noch nicht untersucht und ist besonders für große Einschlagskrater wie die Chicxulub-Struktur (Mexiko, Durchmesser ca. 200 km) relevant. In dieser Arbeit wurde die deutlich kleinere Nördlinger-Ries-Struktur (Deutschland, Durchmesser ca. 25 km) zum Vergleich ebenfalls untersucht. In beiden Impaktstrukturen können Hochtemperaturschmelze und Suevite (>900°C) sowie Hydrothermalsysteme nach dem Einschlag zu einer natürlichen Gitterausheilung führen. Es ist bisher unklar, wie sich dies auf die charakteristische magnetische Anomalie in den Kratern auswirkt.

Im Rahmen dieser Arbeit wurden Magnetitproben aus den beiden Einschlagskratern, Chicxulub (Mexiko) und Nördlinger-Ries (Deutschland), mit gesteinsmagnetischen, petrographischen und mineralchemischen Methoden untersucht. In beiden Kratern wurden zwei Generationen von Magnetit beobachtetet: (1) einen reinen, stöchiometrischen geschockten Magnetit mit großen (~100µm) Körnern im Grundgebirge, und (2) einen neu gebildeten, im Allgemeinen kationenarmen (Ti-)Magnetit mit kleineren (~10-50µm) Körnern und ohne sichtbare Schockverformung in der durch den Einschlag erzeugten Schmelze und im Suevit.

Außerdem konnte im Rahmen dieser Arbeit festgestellt werden, dass MD-Magnetit in der Natur eine ähnliche Abnahme des Domänenzustands in Richtung PSD zeigt wie experimentell geschockter Magnetit, unabhängig vom Vorhandensein von Oxidation. Es konnte beobachtet werden, dass eine thermische Behandlung bei über 540 °C zu einem irreversiblen Anstieg der Suszeptibilität und des Domänenzustands von PSD hin zu erhöhten MD-Beiträgen führt. Wenn Hämatit in der Probe vorhanden ist, wandelt er sich in SD-SP-Magnetit um, sobald er über 560 °C erhitzt wird, und zwar in einem Prozess, der das Ausheilen von Defekten im Magnetit verdeckt, wenn beides gleichzeitig geschieht. Dies kann ein neues und unterschätztes Phänomen sein das zu einer Umagnetisierung der NRM führen kann.

In Chicxulub zeigt der geschockte Magnetit des angehobenen Grundgebirges schockreduzierte NRM- und κ-Werte, was zu einer allgemein sehr niedrigen Gesamtmagnetisierung im der zentralen Ringstruktur führt. Das hydrothermale System hat das magnetische Signal nicht wesentlich überlagert, und seine Temperaturen (~450°C) lagen deutlich unter der Glühschwelle (~540°C). Die natürliche Glühung findet im Kontakt mit der Impaktschmelze statt, wo der Magnetit des Grundgebirges erhöhte Suszeptibilitäten, und eine prä-Impakt Umwandlung von Hämatit zu Magnetit aufweist. Die thermische Überprägung nach dem Einschlag in Chicxulub hat die magnetische Anomalie nicht wesentlich beeinflusst, was auf die fehlende Magnetisierung im angehobenen Grundgebirge zurückgeführt werden kann. Die Impaktschmelze weist relativ hohe NRM- und κ-Werte auf, aber es handelt sich um eine dünne Schicht in der zentralen Ringstruktur, die nicht wesentlich zur Anomalie beiträgt.

Im Nördlinger Ries zeigen die Ergebnisse dieser Arbeit, dass der Magnetit aus dem Grundgebirge mit vergleichbarer Intensität entmagnetisiert ist. Hier verursachte der Einschlag ein zweistufiges hydrothermales System mit kürzerer Dauer und niedrigeren Temperaturen (max. 300°C in der ersten, <100°C in der zweiten Stufe). Natürliches Glühen im Grundgebirge wird lokal im Magnetit beobachtet, was auf das Vorhandensein von schmelzhaltigen Suevit-Gängen mit hohen Platznahmetemperaturen (>900°C) zurückzuführen ist. Impaktschmelzen im Nördlinger Ries weisen eine schwache Magnetisierung auf, aber die Suevite zeigen eine starke κ und NRM mit umgekehrten Magnetisierungsrichtungen, was teilweise zu den negativen magnetischen Anomalien beiträgt.

Contents

Acknowledgements

Completing a successful doctorate work requires a healthy amount of passion, devotion, and resilience. I would like to begin this work by thanking those who have lent me their knowledge, insight, and encouragement throughout my journey.

My most sincere thanks to my supervisor, Agnes Kontny, for her guidance, suggestions, patience, and unwavering support during the past years. She initiated and undertook the research that stands at the basis of this work. All the lengthy discussions (including “short” conversations whilst standing at her office’s doorstep) filled me with constant motivation, curiosity, and always gave me new perspectives. I thank her for the opportunity to work in such a fascinating subject and awaken in me a passion for research I hope to take on henceforth.

Stuart Gilder is greatly acknowledged for being the second referee for this work. His expertise and work body provided me great insights during my research.

My sincere acknowledgements to Katarzyna Dudzisz, for her support and discussions, as well as untiring assistance with data collection and interpretation. To Amar Agarwal, I would also like to extend my gratitude, for all our scientific and cultural exchanges, both in the field and remotely. I have learned a lot from our work together.

I would like to express my gratitude towards the whole Structural Geology department at KIT – thank you for making this journey as exciting as it was. Alexander Monsees and Lucas Eskens as particularly acknowledged by the long discussions about a wide range of earth-science subjects, from sedimentology to tectonics and structural geology. Alex, thank you for being my supportive senior during my first months at KIT. Lucas, my fellow UU alumnus, thank you for all the laughs and peeks into the world of seismic modeling. I would like to thank Boris Reznik, who helped me get started with this work, and get familiarized with the intricacies of shock deformation. I want also to thank Christoph Hilgers, for some of the most enthusiastic and passionate geological exchanges of my life. Our discussions in the field in Oman will stay with me and inspire me for the rest of my life.

Martin von Dollen is gratefully acknowledged for the preparation of the best samples and thin sections any geologist could ask for. His innovative planning allowed for accessing critical data which would otherwise be unobtainable. Ulrike Brecht is gratefully acknowledged for the assistance navigating the endless German bureaucracy, and untiring translation of documents. Additional acknowledgements to my colleagues Felix Allgaier and Dennis Quandt, both for the scientific exchange, and being good company for the long hours of driving in the desert. Ruben Winstel is acknowledged as a student worker and B.Sc. student who contributed to the sample acquisition and data gathering. Anna Rothkegel is acknowledged as a student worker who contributed to data gathering and sample preparation.

The German Research Foundation (DFG) is acknowledged for the funding of this project (number 432762445). Chapters 2 and 4 of this work were partially supported by the National Science Centre (NCN), Poland, in the frame of scientific project No. 2019/03/X/ST10/00139. Chapter 3 was partially supported by the Institute for Rock Magnetism (IRM), Minneapolis, USA, through a Visiting Research Fellowship. The IRM is a US National Multi-User Facility supported through the Instrumentation and Facilities program of the National Science Foundation, Earth Sciences Division (NSF EAR-2153786), and by funding from the University of Minnesota.

I thankfully acknowledge Sean Gulick, Joanna Morgan, and Michelle Penkrot in the support for the project and the sampling process for Chapter 2. My thanks to Dietmar Jung, Patrick Müller and Steffen

Stark from the Bohrkern- und Rohstoff-Analytik-Zentrum LfU, as well as Stefan Hölzl and the Rieskrater-Museum staff, for assistance in the sampling process for Chapter 4.

I would like to thank Maxwell Brown, Dario Bilardello, Peter Solheid, and remaining academic staff at the IRM Minneapolis for their assistance, insights, and suggestions. The visiting fellowship was an incredible experience which has inspired me academically and personally, ever since.

Grateful acknowledgements go to the co-authors of the chapters of this thesis Mark Dekkers, Michael Poelchau, Franziska Wilke, Bonny Kuipers and Lennart Fischer, for their cooperation, insights, and discussions, as well as in the process of data gathering. To Mark, I would like to present my sincerest thanks for his continuous assistance, ever since my master's degree work and research. His suggestions helped conceptualize Chapter 3 of this work.

I look back to these past three years, and I cannot help but to be personally thankful for the support of Elgin Achenbach and Geesje Assendorp. They have made my journey exciting and helped me see the sunshine even in the darkest days. To Guilherme Ínsua Pereira, for sharing his doctoral journey with me, and the countless mutual motivational speeches that kept us going in our parallel journeys. To Ida Möckel, for her continuous support and friendship, ever since I first arrived alone in Karlsruhe. And to all my dear friends that are by my side, and the ones lost along the way, thank you for the sweet memories, which in one way or another shaped this work.

Lastly, I would like to thank Carlos and Teresa Mendes, my parents, who have supported and encouraged me in my scientific curiosity since early childhood. Through all the hardships and sacrifices that life threw at them, their unwavering dedication is what allowed me to complete this work. This thesis would have not been possible without them. Thank you.

Declaration of originality

Chapter 2: As first author during his PhD study, Bruno D. L. Mendes performed the majority of the κ-T experiments and thin section analysis, as well as all EPMA, hysteresis and IRM acquisition measurements, with the laboratorial assistance of co-authors Lennart Fischer, Bonny Kuipers, and Katarzyna Dudzisz, respectively. FORC measurements were obtained by Katarzyna Dudzisz, and M-T measurements by co-author Mark Dekkers. Preliminary κ-T, microscope and paleomagnetic data was obtained by co-author Ksenia Gaus. Samples were obtained from co-author Michael Poelchau, and from the IODP repository (Texas, USA). Bruno D. L. Mendes wrote the entire article, with valuable and appreciated inputs from Agnes Kontny, Katarzyna Dudzisz and Mark Dekkers.

Chapter 3: As first author, Bruno D. L. Mendes performed all sample preparation, temperature dependent hysteresis, IRM acquisition, and FORC diagrams, at the Institute for Rock Magnetism (IRM, Minneapolis, USA). The data collection was done with the assistance of Maxwell Brown, Dario Bilardello and Peter Solheid, at the IRM. The article was written with helpful input and discussions with co-author Agnes Kontny.

Chapter 4: As first author, Bruno D. L. Mendes performed the majority of κ-T experiments, thin section analysis, and hysteresis measurements. EPMA data was acquired with the assistance of co-author Franziska Wilke. Preliminary κ-T and thin-section analysis were performed by Ksenia Gaus and Ruben Winstel. Additional EPMA data was collected by Franziska Wilke, and additional hysteresis and IRM acquisition measurements were performed by co-author Katarzyna Dudzisz. Sample acquisition was done at the Bohrkern- und Rohstoff-Analytik-Zentrum LfU, and in cooperation with the Rieskrater-Museum. The article was written with important discussion and input from Agnes Kontny and Katarzyna Dudzisz.

1. Introduction

1.1. Motivation

The magnetic signatures of impact structures on Earth varies widely with target rock composition, impact-derived magnetization, crater fill, and post-impact sedimentation (Pilkington and Grieve, 1992). Despite these factors, large impact structures on Earth consistently denote significant magnetic anomalies related to magnetite (the most prominent magnetic carrier in the Earth's crust), present in both the shocked target and impactites (e.g., Hart et al., 1995; Gattacceca et al., 2007; Quesnel et al., 2013; Gilder et al., 2018). These anomalies are caused by the interplay of the contrasting total magnetization (M_t) in the shocked target, newly formed impactites (that is, rocks formed due to, or related to the impact event), and the regional background magnetization. The total magnetization is the sum of natural remanent magnetization (NRM) and induced magnetization (κ*B, where κ is magnetic susceptibility [occasionally be referred to as "MS" throughout this work] and B is an ambient magnetic field, in this case, Earth's magnetic field). The shockwave created by the impact event causes a sharp loss of NRM and κ in magnetite-bearing target, which has been documented extensively in literature for the past decades.

The loss of NRM in particular has been studied in detail (e.g., Pearce and Karson, 1981; Gilder et al., 2006; Bezaeva et al., 2007; Gattaceca et al., 2010; Tikoo et al., 2015), demonstrating that even under 2 GPa, magnetite may lose up to ~90% of its pre-shock NRM. Shock may also lead to the acquisition of a shock remanent magnetization (SRM), but this is often quite weak, at few percent of original magnetization. Research into κ loss during impact is more recent, and has shown that for shock pressures equal or above 5 GPa, 90% of κ is lost (Reznik et al., 2016).

The impact-related loss of κ and NRM are attributed to physical deformation mechanisms such as permanent brittle fracturing and grain fragmentation, but also plastic deformation-related defects in a slightly distorted crystal lattice. Furthermore, fractures and defects lead to enhanced magnetic domain wall-pinning effects in magnetite (e.g., Lindquist et al., 2015), which lead to a decrease in apparent domain state, from originally multi-domain (MD) towards pseudo-single domain (PSD), or even close to single domain (SD) behaviors. These variations lead to an increase in magnetic coercivity and decrease of κ (Fig. 1.1, black symbols, e.g., Lindquist et al., 2015, Reznik et al., 2016). A follow-up study (Kontny et al., 2018) found that post-shock thermal treatment of magnetite can cause annealing of some of the reversible plastic deformation and lattice defects. Annealing reduces domain wall-pinning, and allows for the recovery and restoration of some magnetic properties, leads to an apparent domain state increase, decrease in coercivities, and increase in κ (Fig. 1.1, red symbols, Kontny et al., 2018).

Post-impact temperature overprint on the magnetic signature of large-scale impact structures has not been studied to date. The experimental observations by Kontny et al. (2018) are particularly relevant for large complex impact craters, such as the Chicxulub (Mexico, ca. 200 km diameter) or Nördlinger Ries (Germany, ca. 25 km diameter) structures, where the formation of high temperature melt and suevites (both of which above 900°C) may lead to conditions favorable for natural annealing. The presence of these high temperature lithologies is also a heat source for hydrothermal systems, which are a common feature of impact events (e.g., Newsom 1980; Ames et al. 1998; Hode et al. 2004; Naumov 2005; Osinski et al., 2013). In Chicxulub, the latent heat from the cooling of the impact melt fueled a long lived (approx. 0.5 to 2.1 Myr) and hot (350°C to 450°C) hydrothermal system (Kring et al., 2020). This system ubiquitously permeated the basement and may have created favorable conditions of magnetic property recovery. In addition, the deposition of new ferrimagnetic phases due to hydrothermal conditions, may further enhance the magnetization of the shocked target.

Lastly, the inhomogeneous effect of chemical alteration in natural samples is not appropriately emulated by laboratorial experiments. This is a major limitation in these studies, as hydrothermalism may cause significant oxidation of magnetite into hematite, even at low temperatures (Horton et al., 2006, 2009a, 2009b). Magnetite to hematite oxidation is widespread in crustal rocks, and can occur pre-, syn- or post-impact, and will influence the properties of the magnetite, including NRM, MS and domain state.

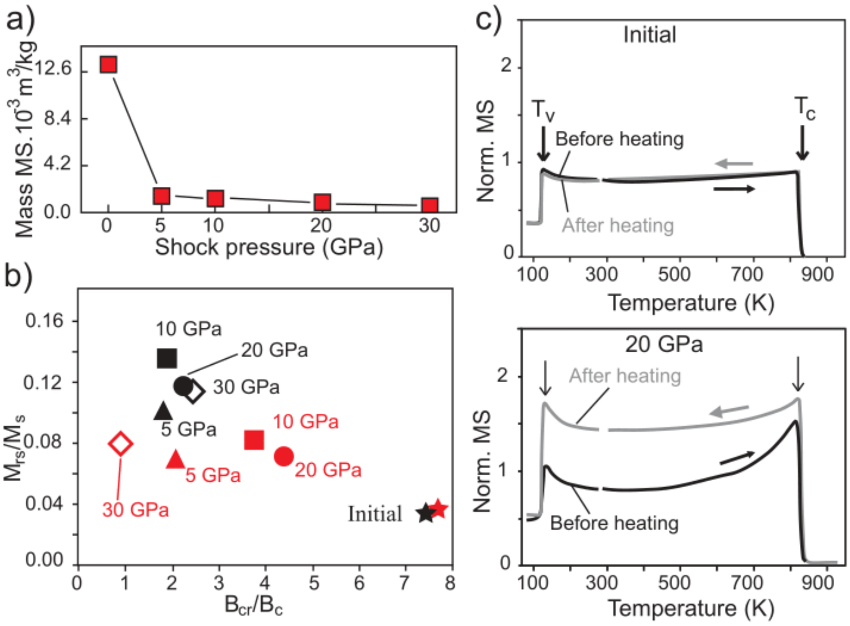

Figure 1.1. Response of magnetic properties of magnetite to shock and post-shock temperature treatment. (a) Mass susceptibility versus shock pressure (after Reznik et al., 2016); (b) Mrs/Ms vs. Bcr/Bc diagram for initial and shocked (black symbols) magnetite (Reznik et al., 2016), and post-shock annealed magnetite (red symbols, Kontny et al., 2018); (c) Temperature-dependent magnetic susceptibility (MS) for initial and shocked magnetite at 20 GPa.

1.2. Aims

The aim of this study is to investigate the effects of post-impact overprint of temperature in two large natural impact structures, in Chicxulub (Mexico) and Nördlinger Ries (Germany). Both craters have associated magnetic anomalies (Fig. 1.2), despite very distinct post-impact evolutions. Chicxulub experienced an extensive, long-lived, and high temperature post-impact hydrothermal system (e.g., Kring et al., 2020), whereas Nördlinger Ries shows lower temperature and localized hydrothermalism (e.g., Osinski et al., 2004, 2005; Sapers et al., 2017). Comparing and contrasting the properties of these two craters provides insight into the controlling factors of natural thermal overprint, and the interaction of shock, temperature, hydrothermalism, and their influence in the magnetic anomaly patterns. To study the interplay between physical (shock) and chemical (e.g., oxidation) processes have on the magnetic properties of shocked magnetite, a detailed investigation on the response of domain states to shock deformation and post-shock temperature treatment was also conducted. My work focuses on five major aspects:

- Characterization of the natural magnetic carriers in the Chicxulub and Nördlinger Ries craters, including composition and stoichiometry, NRM intensity and directions, observed κ versus expected κ from non-shocked analogues, and observed domain state behavior versus expected from grain size.

- The presence or absence of natural thermal overprint from hydrothermalism or impactite heat, and its role in the magnetic properties of the magnetite and resulting anomaly patterns.
- How the high-temperature transformation of secondary hematite to magnetite occurs in nature, its controlling factors, and how the magnetic signal contrasts with the annealing-induced physical response to temperature.
- Magnetic domain state response to shock, chemical alteration, and temperature.
- Comparison with experimentally shocked samples as analogues to nature.

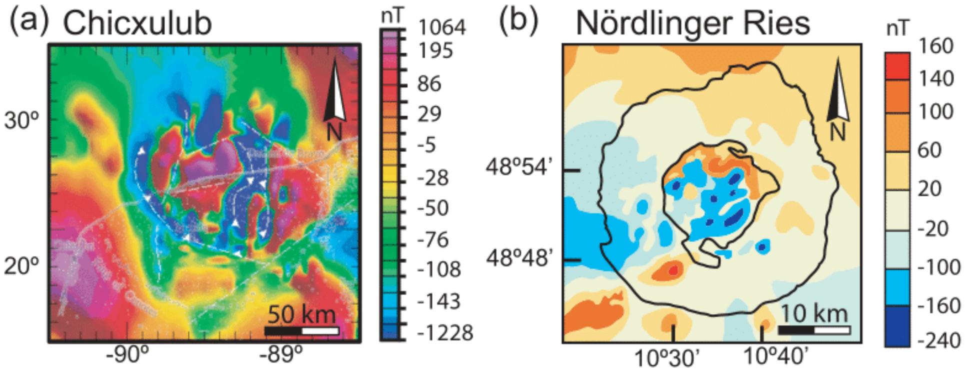

Figure 1.2. Magnetic anomalies in (a) Chicxulub (after Rebolledo-Vieyra et al., 2010); and (b) Nördlinger Ries (after Pohl et al., 2010).

1.3. Overview

1.3.1. Peak-Ring Magnetism (Chapter 2)

Chapter 2 pertains to the Chicxulub impact crater, in the Yucatán peninsula, Mexico. The Chicxulub impact event ~ 66 Ma ago (e.g., Renne, 2013) created the only complex crater on Earth with a preserved peak-ring. The peak-ring was drilled for the first time by the IODP-ICDP Expedition 364, drill core M0077A (Morgan et al., 2017), which revealed that it consists of uplifted and strongly deformed granitoid basement rocks, overlain by 130m of impact melt and suevite (Morgan et al., 2017). Pre- and post-impact hydrothermal systems affected the basement, with post-impact temperatures reaching up to 450ºC (Kring et al., 2020).

The magnetic mineralogy of pre-, syn- and post-impact rocks was characterized through polarized and electron microscopy, mineral chemistry, temperature-dependent magnetic susceptibility (κ-T) and hysteresis properties. The shocked basement granitoid is rich in large, pure and stoichiometric magnetite, but shows unusually low κ (~10^{-4} SI) compared both with theoretical estimates and non-shocked analogue granitoids (~10^{-2} to 10^{-1} SI, Tarling and Hrouda, 1993; Just and Kontny, 2011). These results are in line with experimental shock-related reduction in κ, and decrease in apparent domain state. Cation substituted magnetite in the melt (with varying compositions) carries a higher induced and remanent magnetization, with stable paleomagnetic directions for the time of impact.

In the shocked basement, the magnetite is partially oxidized to hematite before the impact by hydrothermal activity. This transformation is ubiquitous throughout the basement, but is not observed in contact with the impact melt. When exposed to high temperatures during our κ-T experiments in an argon atmosphere, the hematite transforms back to magnetite, with increased bulk-sample coercivity and a decrease of the bulk-sample average domain state. This transformation happens concomitantly with magnetic annealing and both phenomena overlap, making it impossible to distinguish their individual influence in κ-T experiments. Basement samples in contact with the melt show partially recovered magnetic properties and no hematite, which suggests that annealing and/or hematite-to-magnetite transformation also occurs naturally, under high temperatures in non-oxidizing conditions.

The hydrothermal system did not reach temperatures high enough for magnetic annealing, estimated to begin at 540°C, or for hematite to magnetite transformation, estimated to begin between 560°C and 580°C. The demagnetized and reduced κ of the shocked magnetite in the thick uplifted basement section, and the absence of hydrothermal overprint, remain yet unexplored causes of the negative magnetic anomaly in the Chicxulub peak-ring.

1.3.2. Restoration and Transformation (Chapter 3)

Chapter 3 is a follow-up study focusing on the response of the magnetic domain state of both pure and oxidized magnetite to shock, and subsequent thermal treatment and annealing. In chapter 2 it is described how annealing may occur naturally, but can be overprinted by high-temperature hematite-to-magnetite transformation in oxidized samples when heated in non-oxidizing environments.

In this chapter, I isolated these two phenomena, and their effect on domain states of magnetite. The evolution of hysteresis, isothermal remanent magnetization components and first order reversal curve (FORC) diagrams was investigated at different high-temperature steps, starting at the 540°C threshold identified in Chapter 2. The experiments were made in non-shocked and non-oxidized MD magnetite ore; non-shocked but oxidized magnetite from a granitoid of the EPS-1 drill core at Soultz-sous-Forêts, analogue to the Chicxulub granitoid (Just and Kontny, 2011); experimentally shocked but non-oxidized magnetite (shocked at 5-30 GPa, Reznik et al., 2016); and the naturally shocked and oxidized magnetite from Chicxulub explored in Chapter 2.

It was observed that shock clearly changes the apparent domain state of magnetite, from MD towards behavior typical of PSD. With annealing, the apparent domain state increases with increasing temperatures, whilst hematite-to-magnetite transformation creates new SD and SP particles which decrease the bulk-sample average domain state, but strongly increase the magnetization. The two phenomena are observed and distinguished for the first time using FORC diagrams. Where both shock and oxidation occur, hematite-to-magnetite transformation masks annealing. As magnetite oxidation is a ubiquitous process in surface rocks, these results are relevant even outside of impact crater research, and may have broader implications for the paleomagnetic community.

1.3.3. Ries Magnetic Mineralogy (Chapter 4)

Chapter 4 explores the Nördlinger Ries (Ries) impact structure, Germany. Here, the post-impact hydrothermal activity was not as long lasting, nor reached as high temperatures as in Chicxulub. Its magnetic anomaly pattern has been studied in detail before, however the relationship between the magnetic anomaly and the magnetic mineralogy of the target and impactites is not always straightforward.

In the Ries crater, the negative magnetic anomalies are attributed to a reverse polarity NRM in the impact-melt bearing lithologies and suevites. These interpretations contrast with the results from Chapter 2, where the cause of the negative magnetic anomaly in the Chicxulub peak-ring is the demagnetized uplifted basement.

For this chapter, four surface locations were sampled, as well as the NR73 and SUBO-18 drill cores. Chemical, rock- and mineral-magnetic data is presented, from the Ries crater's shocked basement, suevite and melt. Two generations of magnetite carry the magnetization in Ries, with pure, stoichiometric shocked magnetite in the basement, and low cation substituted magnetite in the melts. The shocked basement is strongly demagnetized and presents reduced magnetic susceptibilities ($\sim 10^{-4}$

SI), up to three orders of magnitude lower than its analogues and theoretical estimates (~10^{-2} to 10^{-1} SI; Tarling and Hrouda, 1993; Just and Kontny, 2011, Edel et al., 2013).

The impactites from of SUBO-18, in the inner crater rim, shows weak NRM and intermediate magnetic susceptibilities. A locally different origin for the negative anomalies in the Ries crater is proposed, with both reverse polarity NRM and demagnetized uplifted target controlling the local magnetic anomalies. While NRM and κ of impactites can be locally strong (Pohl et al., 2010), these are local outliers in the suevite and impact melt layers. Thus, the reverse polarity NRM directions seem to be only of minor importance for the magnetic anomaly of the inner ring, with its uplifted crustal basement. This finding is in accordance with our interpretation of data in Chapter 2, where the thickness of a contiguous layer of demagnetized and shocked basement in the uplifted peak-ring created a region of low total magnetization. The comparison of the origin of the anomalies in Nördlinger Ries and Chicxulub indicates that the understanding of magnetic anomalies over impact structures on Earth remains a challenge in impact crater research.

1.4. Published sections

Articles

Mendes, B. D. L., Kontny, A., Poelchau, M., Fischer, L. A., Gaus, K., Dudzisz, K., Kuipers, B. W. M., & Dekkers, M. J. (2023). Peak-ring magnetism: Rock and mineral magnetic properties of the Chicxulub impact crater. *GSA Bulletin*. https://doi.org/10.1130/B36547.1

Mendes, B. D. L., and Kontny, A. (2024). Restoration and Transformation: The Response of Shocked and Oxidized Magnetite to Temperature. *Journal of Geophysical Research: Solid Earth*. https://doi.org/10.1029/2023JB027244

Mendes, B. D. L., Kontny, A., Dudzisz, K., Wilke, F. D. H. (Under Review). Ries Magnetic Mineralogy: Exploring Impact and Post-Impact Evolution of Crater Magnetism. *Meteoritics and Planetary Science.*

Conference and Seminar Contributions

Mendes, B. D. L. (2023). Post-Shock Temperature Effects in Magnetism: The Chicxulub Impact Crater – Natural Case Study. *Visiting Fellow Talk. 1/2/2023, Institute for Rock Magnetism, Minneapolis, USA.*

Mendes, B. D. L. (2022). Rock Magnetism: Basics and applications – Iberian bending and Chicxulub impact. *Wöchentliche Seminar, Wintersemester 2022/2023. 8/12/2022, Karlsruhe Institute of Technology, Karlsruhe.*

Mendes, B. D. L., Kontny, A., Gaus, K., Kuipers, B. W. M., & Dekkers, M. J. (2021). Peak-ring magnetism: Rock and mineral magnetic properties of the Chicxulub impact crater. *GeoKarlsruhe 2021, DGGV Annual Meeting, Karlsruhe.*

Mendes, B. D. L., Kontny, A., Gaus, K., Kuipers, B. W. M., & Dekkers, M. J. (2021). Peak-ring magnetism of the Chicxulub Impact Crater derived from rock and mineral magnetic properties of the IODP-ICDP drill core M0077A. *17th Castle Meeting on Paleo, Rock and Environmental Magnetism, Trakošćan, Croatia.*

Other publications

Phukon, P., Agarwal, A., **Mendes, B. D. L.**, Kontny, A., Joshi., G. (In Press) Changes in thermomagnetic and X-ray diffraction properties of Asby dolerite with distance from the Lockne Impact structure, Sweden. *Physics of the Earth and Planetary Interiors*.

Supplemental files containing the additional information and data files described throughout the chapters of this thesis are available at the **KITopen** repository under **KITopen ID**: 1000167980; **DOI**: https://doi.org/10.35097/1913.

2. Peak-Ring Magnetism: Rock and Mineral Magnetic Properties of the Chicxulub Impact Crater

2.1. Abstract

The Chicxulub impact event ~ 66 Ma ago left in its wake the only complex crater on Earth with a preserved peak-ring, characterized by a well-developed negative magnetic anomaly. To date, little is known about its magnetic properties. The IODP-ICDP Expedition 364 drill core M0077A revealed that the peak-ring consists of uplifted and strongly deformed granitoid basement rocks overlain by a 130 m thick impact melt and suevite layer. Pre- and post-impact hydrothermal systems affected the basement with maximum temperatures up to 450ºC. We used microscopy, mineral chemistry, temperature-dependent magnetic susceptibility, and hysteresis properties, to characterize the magnetic mineralogy of pre-, syn- and post-impact rocks. Compared to its amount of pure and stoichiometric shocked magnetite, the granitoid basement shows conspicuously low magnetic susceptibility, which is in line with earlier experimental studies that suggest shock reduces magnetic susceptibility. Cation substituted magnetite with varying compositions in the melt rocks carries a higher induced and remanent magnetization, compared to the basement. In the granitoid basement, magnetite is partially oxidized to hematite by a pre-impact hydrothermal event, but at lithological contacts with high temperature impact melt rock, this hematite is locally transformed to new magnetite, with mottled textures. Elsewhere in the granitoid basement, the temperature reached in the hydrothermal system was too low for hematite transformation. It was also too low to anneal all the lattice defects in the shocked magnetite, which likely occurs above 540°C. The presence of shocked magnetite in the granitoid basement well explains the negative magnetic anomaly, due to its unusually low induced magnetization and demagnetized NRM.

2.2. Introduction

The Chicxulub impact event marked the end of the Mesozoic era, and is widely regarded as a main contributor to the K-Pg extinction event of the non-avian dinosaurs and to severe global environmental changes (e.g., Hildebrand et al., 1991; Sharpton et al., 1992; Smit, 1999; Schulte et al., 2010). It was the last of the "Big Five" Phanerozoic mass extinctions, and the impact left the 3rd largest impact crater known on Earth (e.g., Witts et al., 2018; Burgess, 2019). The impact took place in the Yucatán peninsula (Fig. 2.1a) at ~66 Ma (e.g., Renne, 2013) by the collision of an asteroid of carbonate chondrite composition ~12 km in diameter, hitting Earth with a steeply inclined trajectory from the NE (Collins et al., 2020).

The size of the impactor caused the formation of a complex impact crater, approximately 200 km in diameter. A so-called peak-ring of ~150 km in diameter formed due to the interaction of the outward collapsing central uplift and inward collapsing transient wall (e.g., Riller et al., 2018), which shows a characteristic negative magnetic anomaly (Fig. 2.1b) and a noteworthy gravity signature (Fig. 2.1c). The Chicxulub structure is the only known complex impact crater on Earth which preserved its peak-ring (e.g., Morgan et al., 2000), largely due to a ~1 km thick Cenozoic sediment cover in the Gulf of Mexico (Fig. 2.1a). Another special feature of the Chicxulub impact crater is the existence of a post-impact, well-developed and long-lived (0.5 up to 2 Myr) hydrothermal system, with fluid temperatures of 350°C to 450°C (Kring et al., 2020).

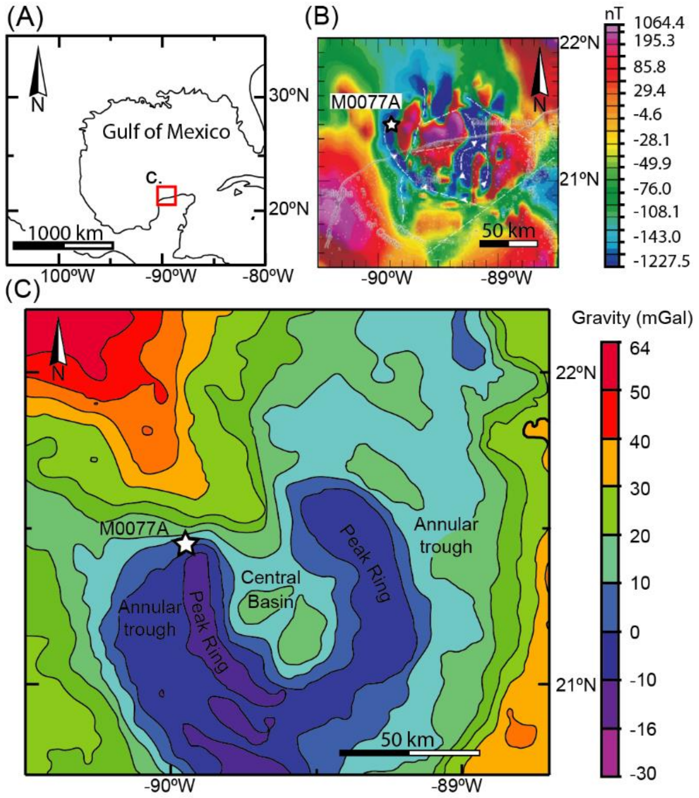

Figure 2.1. (a) Geographic location of the Chicxulub impact crater in the Yucatán Peninsula, (Mexico); (b) Aeromagnetic anomaly map (nT) (after Rebolledo-Vieyra et al., 2010) and (c) Gravity anomaly map (mGal) (modified after Gulick et al., 2013) with location of borehole M0077A indicated with a white star in a magnetic and gravity low corresponding to the peak-ring.

To date, a wide range of scientific and exploration drilling projects were carried out, which makes the Chicxulub structure one of the best investigated impact craters on Earth (e.g., Burgess, 2019). However, only core M0077A from the joined Integrated Oceanic Drilling Program (IODP) and International Continental Scientific Drilling Program (ICDP) Expedition 364 (Morgan et al., 2017) ever drilled and recovered samples from the Carboniferous granitoid basement at the peak ring of the crater (Zhao et al., 2020; Ross et al., 2022). This core drilled through the melt-bearing polymict impact breccia (suevite), Upper Impact Melt layer (UIM), and through the shocked granitoid basement, down to a depth of 1334.69 meters below sea floor (mbsf). The recovery of this wide range of crater lithologies provides a unique opportunity for research into the rock- and paleomagnetic properties which carry the magnetization and are responsible for the characteristic circular high-amplitude aeromagnetic anomalies (Fig. 2.1b).

Previous paleomagnetic research in drill core M0077A focused on the inclination of NRM vectors (e.g., Tikoo et al., 2017; Kring et al., 2020). These works determined reverse polarities in samples from the impact melt unit, with inclinations expected for the impact location during Chron 29r (~-44°). Zones of normal polarity in the upper peak ring suevite unit have been interpreted as chemical remanence from secondary deposited (Ti-)magnetite formed during post-impact hydrothermal activity at sufficiently elevated temperatures (100°C to 250°C; Kring et al., 2020). Other authors argue that a wide variability of inclinations may suggest no post-depositional remagnetization, as temperatures would be too low (Gulick et al., 2019).

The magnetic anomaly above the Chicxulub impact crater was originally discovered in 1981 by Penfield and Camargo (1981) and was crucial for its discovery and exploration (e.g., Hildebrand et al., 1991; Sharpton et al., 1992; Morgan et al., 1997; Gulick et al., 2008; Morgan and Artemieva, 2008). Melt rock, impact breccias, and the central uplift, were argued as major magnetic sources for the composite character of the Chicxulub anomaly field, with large amplitude inverse dipolar anomalies in the central sector (Rebolledo-Vieyra et al., 2010). Pilkington et al. (2004) reported that the predominant magnetic mineral in the drill core Yax-1 from the Chicxulub Scientific Drilling Project is secondary magnetite formed from low temperature (<150°C) hydrothermal alteration. However, exceptionally high magnetic susceptibilities (MS) are related to mafic basement gabbro clasts in the impact breccia (Pilkington et al., 2004). In drill core M0077A rock magnetic measurements indicate high MS in the impact-melt bearing lithologies and dykes, and low MS in granitoid basement rocks (Fig. 2.2; Urrutia-Fucugauchi et al., 2018). Magnetite and titanomagnetite are described as main magnetic carriers (Kring et al., 2020; Urrutia-Fucugauchi et al., 2018), while secondary magnetite and Fe-sulfides are also reported as a high temperature (300-400°C) alteration product (Kring et al., 2017). The basement rocks are highly fractured with a high concentration of planar features and feather features in quartz (Riller et al., 2018) indicating average shock pressures in the range between 10 to 35 GPa, and locally >60 GPa, as suggested by the occurrence of impact melt rock (Morgan et al., 2017; Ferrière et al., 2017). The extreme fracturing explains the very low density and high porosity of the drilled rocks, causing the gravity anomaly (Fig. 2.1c).

Although the principal structural elements of the magnetic anomaly pattern are thought to be largely understood, only direct sampling of one of the magnetized zones within the impact melt layers would provide conclusive information (e.g., Morgan et al., 2000; Pilkington et al., 2004; Rebolledo-Vieyra et al., 2010). Until now, it is not clear how the shocked basement rocks influence the magnetic anomaly pattern, although shock-related reduction of MS is a well-known phenomenon (e.g., Acuña et al., 1999; Plado et al., 1999; Pilkington and Hildebrand, 2000; Ugalde et al., 2005; Reznik et al., 2016; Kontny and Grothaus, 2017). In experimentally shocked multi domain (MD) magnetite the mass-specific bulk susceptibility decreases exponentially by about 90 % for pressures up above 5 GPa (Reznik et al., 2016). Similar results have also been found for experimentally shocked pyrrhotite by Louzada et al. (2010) and Mang et al. (2013). Particularly in the low shock pressure range below 10 GPa this seems to be a general shock-related phenomenon of magnetic material. The main reasons for these changes are apparent magnetic grain size and domain state reduction (Reznik et al., 2016) and alteration of ferrimagnetic phases (e.g., Kontny and Grothaus, 2017). Recent investigations of shocked minerals suggest that a post-shock thermal exposure may lead to a recovery of some of these pre-shock properties through thermal annealing (Kontny et al., 2018).

The M0077A drill core is the first probing into the uplifted shocked basement and provides a unique opportunity to study the multiple lithological contributors to the anomalous magnetic field (Fig. 2.1b). We investigated the rock-magnetic properties and magnetic mineralogy of the impact and shocked basement rocks from the Chicxulub peak-ring in order to better understand impact-related modifications of magnetic properties. To this end, we analyzed 44 samples from drill core M0077A to distinguish pre-, syn- and post-impact magnetite in these lithologies. We also evaluate the shock and post-shock thermal overprint, either due to the remaining heat during cooling of the impact melt rocks, or due to post-impact hydrothermal temperature overprint. This knowledge can be used to better understand the Chicxulub crater magnetic anomaly pattern.

2.3. Geological Setting and Samples

2.3.1. Lithology of core M0077A in the Chicxulub peak ring

The Chicxulub impact structure is located in the northwest of the Yucatán peninsula, Mexico (Fig. 2.1a). Here, the peninsula is comprised of a ~3 km thick lower Cretaceous carbonate platform sequence composed of limestone, dolomite, marl and anhydrite (e.g., Ramos, 1975; Gulick et al., 2008). It overlays the crystalline Maya block, which is mainly composed of Pan-African rocks (e.g., Keppie et al., 2011; Weber et al., 2018). The cored granitoid rock of the Chicxulub peak-ring intruded the Maya block during Carboniferous times in an arc setting with crustal melting related to the closure of the Rheic ocean (Feignon et al., 2021). Rasmussen et al. (2019) and Ross et al. (2022) determined U-Pb zircon ages between 326 – 334 Ma.

A total core length of 1334.69 meter below sea floor (mbsf) was recovered during IODP-ICDP expedition 364 at site M0077A in 2015 (Morgan et al., 2017). The lithologies of the peak-ring can be subdivided into four general units (Morgan et al., 2017; Fig. 2.2). Unit 1 are post-impact Paleogene to Quaternary carbonate rocks, Units 2 and 3 are impactite rocks, syn-genetically formed during the impact event, and Unit 4 represents a Carboniferous basement granitoid rock, which is intruded by impact and pre-impact dykes. As our study investigates the relation between temperature and shock on the magnetic mineralogy in the impact lithologies and basement granitoids, the post-shock carbonate platform sedimentary rocks of Unit 1 are not considered further.

Unit 2 **(**617.33 to 721.61 mbsf) comprises a sequence of melt-bearing suevite layers. Clast sizes decrease from bottom to top (e.g., Gulick et al., 2017b, 2019). This unit is very porous (~15-40%), and shows a generally low magnetic susceptibility (~10-100x10^{-5} SI) (Fig. 2.2). The suevite can be subdivided into three subunits from top to bottom:

Units 2A (617.33 to 664.52 mbsf) and 2B (664.52 to 712.84 mbsf) are resurge sequences of breccia deposited at low temperatures, posterior to crater flooding (Gulick et al., 2019). The distinction between units 2A and 2B is based on the amount of groundmass vs. clasts, grain size, and the presence of sedimentary features: while Unit 2A presents >20 repeated upward-coarsening or upward-fining structures and cross lamination, Unit 2B does not show any sedimentary structures besides a general upward-fining succession (Gulick et al., 2017b). Unit 2A shows a downhole increase of magnetic susceptibility from ~10x10^{-5} to 100x10^{-5} SI. This trend corresponds to a decrease in porosity from around 40% to 30% (Gulick et al., 2017b). In Unit 2B, the porosity varies widely between 20 and 30%, while the magnetic susceptibility remains high, around 100x10^{-5} SI.

Unit 2C (712.84 to 721.61 mbsf) is a suevite sequence with black impact melt clasts in a grey and green matrix, with occasional occurrence of basement granitoid clasts. It is in direct contact with the impact melt of Unit 3. Unit 2C is a coarse-grained, poorly sorted suevite, and the first impact breccia to be deposited after the impact. During deposition, this suevite has probably maintained temperatures above 580°C, the Curie temperature of pure magnetite (de Graaff et al., 2022). This unit was later exposed to explosive melt-water interactions from the tidal resurge that deposited Units 2A and 2B shortly afterwards (Gulick et al., 2019; Osinski et al., 2020). It also shows the highest magnetic susceptibility, increasing progressively from the top of the unit (100x10^{-5} SI) to the basal contact with the melt rock of Unit 3 (1000x10^{-5} SI). This subunit shows the lowest porosity values of the suevites (20-30%), values which are comparable with the melt (unit 3). Units 2C and 3 record a thermal remanent magnetization with inclination around -46°, while Units 2A and 2B show highly scattered (negative and positive) magnetic inclination values (Gulick et al., 2019; Kring et al., 2020).

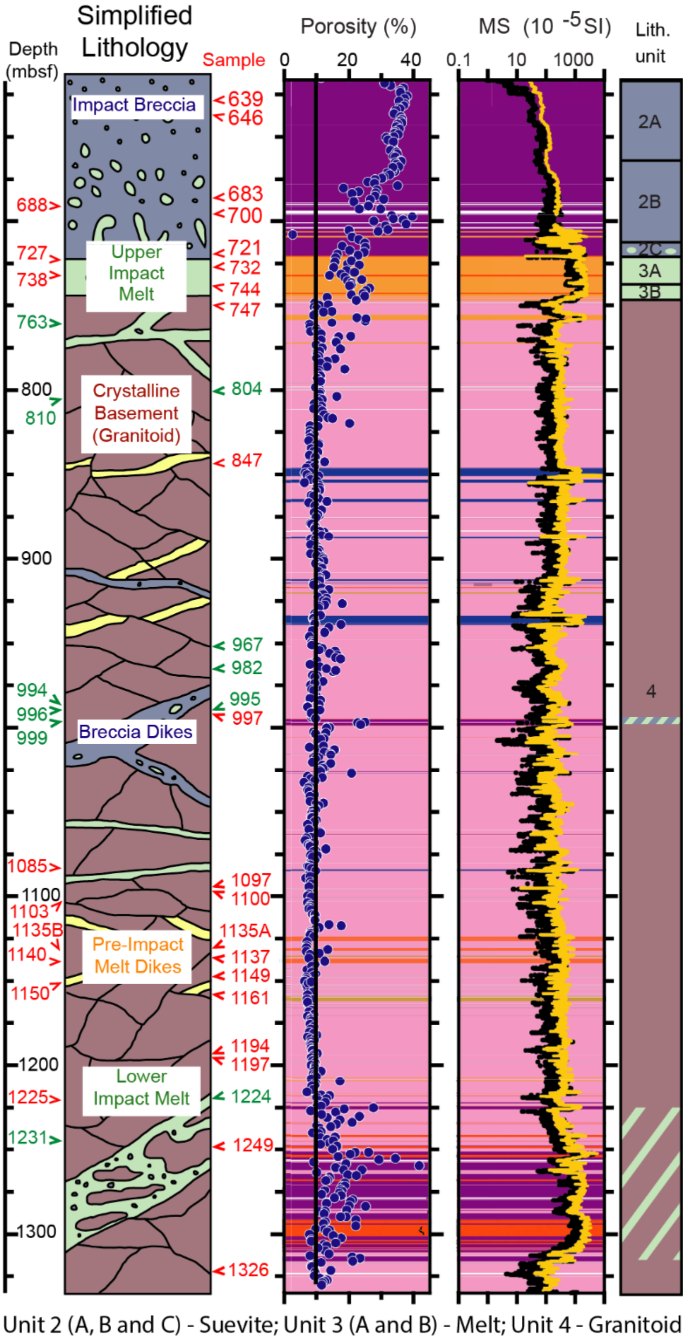

Figure 2.2. Simplified lithological units (Lith. unit) of borehole M0077A, downhole porosity and MS data (modified after Gulick et al., 2017a). Black dots correspond to multisensor core logger (MSCL) measurements, while the grey line represents the downhole log measurements. Sample code corresponds to its approximate depth (mbsf). Samples in black represent samples taken at the onshore science party for Expedition 364 in Bremen (Germany) by M.P., while samples in grey were provided by the Gulf Coast Repository of the International Ocean Discovery Program (IODP), College Station, Texas (USA).

Unit 3 (721.61 to 747.02 mbsf) comprises a ~26 m thick impact melt layer, subdivided into two subunits of different melt compositions: a calcium-rich green schlieren and black impact melt mixture (Unit 3A, 721.61 to 737.56 mbsf) followed downward by a continuous section of silica-rich black melt rock (Unit 3B, 737.56 to 747.02 mbsf). At the transition between Units 3A and 3B the green schlieren disappears, although a similar calcium concentration for both subunits is reported (De Graaff et al., 2022). There are also no differences between subunits concerning porosity (20-30%) or magnetic susceptibility

(~1000x10^{-5} SI); both are similar to Unit 2C. The upper boundary of Unit 3A is a gradual transition from the coarse-grained breccia of Unit 2C, and its lower boundary is characterized by the complete disappearance of the green schlieren. The disappearance of green schlieren occurs gradually, with intense brecciation at the top, via mingling of calcium (similar to carbonatite melts) and silica-rich melts, to a complete mixing of the two melts in Unit 3B (Osinski et al., 2020, De Graaff et al., 2022). Unit 3B is characterized by the black SiO_2-rich melt containing shocked basement clasts (Gulick et al., 2019). Melt temperatures of Unit 3 have been constrained to be potentially between ~650°C and ~750°C (De Graaff et al., 2022). We refer to the whole Unit 3 as Upper Impact Melt (UIM).

Unit 4 (747.02 to 1334.69 mbsf) consists of the shocked felsic granitoid basement. This is a coarse-grained granite, with pre-impact magmatic dykes, as well as pegmatite and aplite dykes. This granite has been shocked at pressures from 10 to 35 GPa and shows – from a granite perspective – a high porosity of around 10% with increased levels in the Lower Impact Melt unit at the bottom. Also, its magnetic susceptibility is generally low: 10-300x10^{-5} SI (Fig. 2.2). It is suggested that the granite was affected by two distinct hydrothermal alteration events (Feignon et al., 2021): (1) a hydrothermal metasomatic event presumably related to the breakup of the supercontinent Pangea, at ~273 ± 21Ma, ~50Myr after the granite emplacement; and (2) a post-impact-related hydrothermal activity (e.g. Kring et al. 2020).

Between 1206.98 and 1334.69 mbsf, a section of prevalent impact melt dykes occurs, including sections with tens-of-meters of continuous impact melt. Henceforth this section is referred to as Lower Impact Melt (LIM) unit. Dykes belonging to this LIM are also exposed at 917.17, 995.24, and 1063.52 mbsf. These dykes occur at different angles and imply heavy deformation of the granite around the contact (Riller et al., 2018).

The LIM unit is broadly characterized as a brecciated impact melt rock, containing both impact melt rock clasts and different basement-derived material (de Graaff et al., 2021). The absence of calcium-rich melt suggests that this unit consists predominantly of crystalline basement melt, with no contribution from the carbonate-rich sedimentary target rocks. These impact melts are interpreted to be injected into the basement during the compression and excavation stage of the cratering process, and are suggested to be delamination surfaces within the crystalline basement which accommodated deformation during peak-ring formation (Riller et al., 2018). The LIM in general also shows a higher concentration of Al_2O_3, MgO and FeO, when compared with the UIM (De Graaff et al., 2021).

After impact, the latent heat from the cooling of the impact melt helped to start and fuel a long lived (approx. 0.5 to 2.1 Myr) and hot (350°C to 450°C) hydrothermal system, which could have extended to depths of 5-6 km below sea floor. All the units described above show ubiquitous hydrothermal alteration including the deposition of secondary sulfide minerals (e.g., pyrite, chalcopyrite) (Kring et al., 2020). These hydrothermal fluids are interpreted as originally pH neutral and undersaturated in Si, as quartz was wholly or partially dissolved in the impact melt rocks. However, they evolved over time towards more alkaline fluids which promote the precipitation of smectite and calcite. It is suggested that secondary (Ti-)magnetite grains precipitated in relation to protracted hydrothermal activity (Kring et al., 2020).

2.4. Methods

2.4.1. Material

A total of 44 half and quarter drill core samples from site M0077A were used for this study (sample codes in black and grey, see Fig. 2.2). All sample names refer to approximate meter below sea floor but we omit the "mbsf" in the following sample names for better readability. Further, we give the sample unit in parenthesis to help the reader contextualize its provenance. From 15 'black' samples, cylindrical specimens with 1.5 cm diameter and 1.2 cm length were stepwise demagnetized. We were able to reorient these cores using a CT scan rotation log (after McCall et al., 2017). See Appendix A.1 and A.2 for a list of samples and CT scan rotation corrections details.

Sample 999 shows a contact between the shocked basement granite and an injection dyke of the Lower Impact Melt (LIM). The contact is a flow-foliated ultra-cataclasite between the granitoid rock and the lower impact melt, likely developed during peak-ring formation, where the melt dykes acted as deformation allocation zones (e.g., Riller et al., 2018; De Graaff et al., 2021). From this sample, we carefully cut six subsamples for temperature dependent susceptibility (κ-T) analysis, two from the basement, two from the melt, and two from the intermediate and contact region, in order to study the spatial temperature overprint of the impact melt injections on the magnetic minerals. From sample 1100 (basement granite) we prepared a polished piece of ~5 mm diameter and subjected it to the same heat treatment as used during temperature-dependent magnetic susceptibility measurement (see section 2.4.3.). This piece was observed under the microscope before and after heat treatment to investigate potential alteration of the magnetic phases due to temperature.

2.4.2. Microscopic and mineral chemical analysis

We performed transmitted and reflected light microscopy with a Leitz polarizing microscope at the Karlsruhe Institute of Technology (KIT). 64 electron probe microanalyses (EPMA) of magnetite and backscattered electron (BSE) images were done on 10 representative carbon-coated samples at the University of Freiburg, Germany, using a Cameca SX100 electron microprobe with five WD spectrometers and an ED detector, with 15nA current and 15kV voltage settings. We used natural and synthetic standards for calibration of Cr, Si, Mg, Fe, Al, Ti, Ni, Mn and Na (Supplemental data files 1 and 2, see Appendix A.6. for details) and calculated the spinel formula assuming a composition of 3 cations and 4 oxygens.

2.4.3.Rock magnetic methods

Rock magnetic investigations include temperature-dependent magnetic susceptibility (*κ-T*), thermomagnetic curves (*M-T*), isothermal remanent magnetization (IRM) component analysis, hysteresis loop analysis, as well as two first order reversal curve (FORC) diagrams for representative sample 1100 before and after heating. κ-T analysis was performed at KIT using an AGICO (Brno, Czech Republic) KLY-4S susceptometer, in a 300 A/m applied magnetic field. The instrument is equipped with CS-L and CS-3 units, respectively for low-temperature analysis ("LT", from -192ºC to 15ºC) and high-temperature analysis ("HT", from room temperature up to 700ºC; then cooled to 40ºC, at an average heating/cooling rate of 12°C/min). Low-temperature curves were obtained by applying liquid nitrogen in the cryostat and cooling the sample down to -192°C and letting it heat up through contact with ambient atmosphere, which causes heating rates to be faster at the beginning of the experiment. Temperatures were measured with a Pt resistance thermometer in contact with the samples. The accuracy of these thermometers is ±1°C up to 150°C, and ±3°C from 150°C up to 700°C (Lattard et al., 2006). High-temperature measurements were performed in a flowing argon atmosphere (110 mL/min, Ar purity of 99.998%) in the furnace to minimize oxidation during analysis. However, it has to be mentioned that argon gas, even in high purity, can contain traces of gases like hydrocarbons (HC) (https://industry.airliquide.us/argon). We also measured some samples in ambient atmosphere, to evaluate the influence of a different measurement environment. κ-T curves are compared with the temperature dependence of magnetization (M-T curves, see below).

Furthermore, we performed stepwise κ-T experiments, where sample 1100 was heated in argon to 450, 500, 520, 540, 560 and 580°C, with intermittent cooling to room temperature. Stepwise κ-T experiments provide insight into the reversibility of the samples, as we expected a shock-pressure overprint in magnetite from the granitoid rocks (see e.g., Reznik et al., 2016), and explored the temperature threshold for annealing of the crystal lattice defects occurs (Kontny et al., 2018).

Lastly, we performed two sets of repeated HT susceptibility experiments from room temperature up to 700°C, to investigate the stability of the magnetic phases after heating, using sample 1100. The first set consists of four consecutive repeated experiments with a standard heating/cooling rate of 12°C/min. The second set consists of two consecutive experiments, with different heating rates: a first "slow" experiment (7°C/min, with 20 min hold at maximum temperature), and a follow-up at the standard heating/cooling rate. Both sets maintain constant flowing argon atmosphere, and the samples were not exposed to air at any point during the process.

Hysteresis loops analyses were performed at the Debye Institute for Nanomaterials Research at Utrecht University (UU), Netherlands, using a EZ Vibrating Sample Magnetometer (VSM), with a sensitivity of ~$5x10^{-10}Am^2$. This method provides insight into the mean coercivity and saturation magnetization behavior of the ferrimagnetic minerals. Sample shards (<20 mg) were glued to a Pyrex 8mm transverse sample holder, and its position is adjusted for each individual measurement. These samples were then exposed to an applied field varying in field direction from 2.2T, to -2.2T and back to 2.2T, in a total of 110 data points. Between (±)2.2T and (±)0.5T, each step is 0.1T, while within the 0.5T to -0.5T interval, each step is 0.01T, for higher resolution. High field slope corrections were applied starting at 0.9T. A second round of hysteresis measurements were done to investigate hysteresis property changes post-heating. We selected 20 samples from UIM (4 samples), LIM (2 samples) and basement granitoid/LIM dykes and contacts (14 samples) and performed HT κ-T measurements in Ar atmosphere, up to 600°C, and repeated the hysteresis measurements. In addition to the hysteresis loops, the FORC diagrams of sample 1100 before and after heating were measured using an alternating gradient magnetometer (MicroMag AGM 2900, Princeton Measurement Corporation, Princeton, NJ, USA). These measurements were done in steps of 2.0 mT, with an averaging time of 150 ms and a saturation field of 0.9 T. In total, 200 curves were measured and then processed, smoothened, and drawn using FORCINEL software (Harrison and Feinberg, 2008; Egli, 2013).

Isothermal remanent magnetization (IRM) was measured stepwise at room temperature by using a Micro-Mag 2900 AGM instrument (Princeton Measurements Corporation, USA) with a maximum magnetic field of 1 T. At least 40 points were measured and further analyzed following the cumulative log-Gaussian functions for statistical analysis according to Kruiver et al. (2001). Three parameters describe the magnetic components obtained from the statistical analysis: SIRM proportional to the mineral content in the sample, the mean coercivity ($B_{1/2}$) at which half of the SIRM is reached, and the dispersion parameter (DP) corresponding to the individual cumulative log-normal distribution. Both, FORC and IRM measurements were done at the Institute of Geophysics, Polish Academy of Sciences in Warsaw, Poland.

Temperature-dependence of magnetization (M-T) measurements were performed at the Fort Hoofddijk Paleomagnetic Laboratory, at Utrecht University. For these measurements we used a modified horizontal translation Curie balance (Mullender et al., 1993). We measured seven representative samples (two suevite samples, two melt rock samples, and three granitoid basement samples), in ambient atmosphere. Heating rate was 6°C/min, cooling rate 10°C/min, peak temperatures of subsequent segments are: 150, 250, 350, 400, 450, 525, 620, 700°C.

2.4.4.Determination of magnetic transition temperatures

We determined the Verwey transition temperature (T_v) of magnetite using low-temperature κ-T curves before and after the heating cycles (T_v1 and T_v2, respectively, Fig. 2.3) applying the first derivate method. In samples where this method was not possible, we used the tangent method as described by Lied et al. (2020). The Verwey transition temperature for pure stoichiometric magnetite is -153ºC (120 K; Verwey, 1939), and it is very sensitive to both lattice defects (i.e., due to shock, Reznik et al., 2016; Biało et al., 2019) and chemical inhomogeneities (i.e., cation substitution, Biało et al., 2019; or vacancy concentration, Aragon et al., 1985). With increasing number of lattice defects, the Verwey transition temperature tends to increase (Reznik et al., 2016), while cation doping and slight oxidation related to a higher number of vacancies cause T_v to decrease, and its expression in κ-T curves becomes less pronounced (Özdemir et al., 1993; Biało et al., 2019). T_v is also stress-sensitive and decreases when measured under pressure (e.g., Carporzen and Gilder, 2010) and increases upon pressure release (e.g., Reznik et al., 2016).

We identified the Curie temperatures from the heating (T_c1) and cooling (T_c2) cycles (Fig. 2.3a) using the first derivate method (Fig. 2.3b; Petrovsky and Kapicka, 2006). This temperature defines the transition of ferro- to paramagnetic behavior in magnetic minerals, and allows to identify the magnetic carriers. For pure magnetite, the Curie temperature is 578°C. Lower values indicate cation substitution (e.g., Engelmann, 2008, Lattard et al., 2006), while oxidation of non-substituted magnetite forms as oxidized end member maghemite (γ-Fe_2O_3) with a T_c up to 640ºC (e.g., Nishitani and Kono 1981; O'Reilly, 1984; Özdemir and Dunlop, 2010).

We normalized both LT and HT κ-T curves to the susceptibility values at room temperature, and the following parameters were used to evaluate them:

- *Verwey peak ratio:* $T_vPR = k_{max}/k_{15}$, where k_{15} is susceptibility value at 15ºC and k_{max} the maximum value around the Verwey transition (Kontny et al., 2018).

- *Hopkinson Peak ratio:* $HPR = k_{max}/K_{40}$, where K_{40} is susceptibility value at 40ºC and k_{max} the maximum value before the Curie temperature (Dunlop, 2014).

According to Dunlop (2014) and Kontny et al. (2018) these ratios describe magnetic domain states and their changes during the heating experiments. In experimentally shocked magnetite, a decrease in peak ratios is associated with annealing of lattice defects and wall unpinning, leading to an increase of magnetic domain size (Kontny et al., 2018).

A third useful parameter is:

- *A40 parameter:* $A40[\%] = 100*((k_{40}-K_{40})/K_{40}) * 100$, where k_{40} and K_{40} are the susceptibility values at 40ºC in the cooling and heating branch, respectively (Hrouda, 2003).

This parameter characterizes the alteration of magnetite during κ-T measurements. A positive A40 indicates an increase of post-heating susceptibility, suggesting the formation of a ferrimagnetic phase, or relaxation of strain in the crystal lattice during the experiment; a negative A40 indicates the decrease of susceptibility during heating due to mineral transformations to a phase with lower magnetic susceptibility (e.g., maghemite to hematite).

A fourth parameter was used to quantify the formation of new magnetite across the Curie temperature:

- *A_{HP} parameter:* A_{HP} [%] = $100*((k_{HP}-K_{HP})/K_{HP}) * 100$, where k_{HP} and K_{HP} are the susceptibility values at the Hopkinson peak, in the cooling and heating branch, respectively (Fig. 2.3).

This parameter is similar to *A40*, as it characterizes the irreversible alteration of magnetite, but here we used it to control the formation of new magnetite during heating in the high-temperature annealing experiments. If this parameter is distinctly positive, it suggests the formation of new magnetite in the sample during heating.

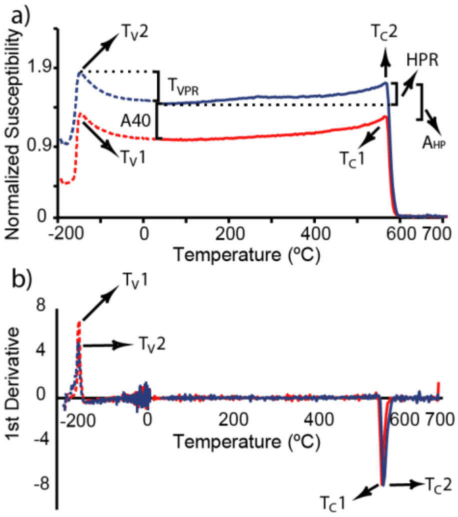

Figure 2.3. Parameters from temperature-dependent magnetic susceptibility that were used in this study. Tv1/Tv2 – Verwey Transition Temperature pre- and post- heating, respectively; Tc1/Tc2 – Curie temperature of heating and cooling cycles, respectively; HPR – Hopkinson Peak Ratio; TvP – Verwey Peak Ratio; A40[%] – Alteration Index at 40ºC; AHP [%] – Alteration Index between Hopkinson Peaks; (b) 1st derivate curve for κ-T example, showing how Tc and Tv were identified (after Petrovsky and Kapicka, 2006).

2.4.5.Paleomagnetic directional analysis

We obtained paleomagnetic directions for 25 specimens with an AGICO JR5A spinner magnetometer, controlled by AGICO's Remasoft 3.0 (Chadima and Hrouda, 2007). Both thermal and alternating field (AF) stepwise demagnetization were performed on duplicate samples from the same core piece. Thermal demagnetization was performed with 40-60ºC steps from room temperature up to 750ºC with a Magnetic Measurement (UK) Thermal Demagnetizer (MMTD1). AF demagnetization was performed using a Magnon International's MI AFD 1.1 demagnetizer, in 12 steps of 2.5-30mT, up to 160mT. All measurements and demagnetization were performed in a low field environment inside an in-house built low-field Faraday cage. We calculated the magnetic component directions from Zijderveld diagrams (Zijderveld, 1967) through principal component analysis (Kirschvink, 1980) and the composite great circle approach described in McFadden and McElhinny (1988). For the UIM and suevite data, a 45° cutoff angle around the average direction was applied, excluding one sample. Interpretation of the data was done using the platform Paleomagnetism.org (Koymans et al., 2016, 2020).

2.5. Results

2.5.1. Texture and composition of magnetic phases

2.5.1.1. Granitoid basement

The main magnetic phase in the shocked granitoid basement is magnetite, which shows grain sizes of ~100 µm up to ~500 µm. These grains are often strongly fractured and show corroded rims (Fig. 2.4a, 2.4b), often with sulfide fillings in cracks. Ubiquitous oxidation to hematite is noticed as well (Fig. 2.4b).

Some of the intra-granular fractures do not extend to the surrounding quartz and feldspar, and often form shear fractures (see blue lines in Fig. 2.4a). Smaller, irregular fractures often cause further fragmentation of magnetite into smaller grains (10-50µm) between the main sets of cracks (Fig. 2.4a, 2.4b). The secondary hematite shows the same fracture patterns as the magnetite, and thus likely pre-dates the impact event. EPMA results indicate that the shocked basement magnetite is generally pure (Table 2.1, samples 747 and 1135 are representative of basement magnetite). These results are consistent throughout the basement, and common to all our granitoid samples.

2.5.1.2. Suevite

In suevite, visible magnetic phases are scarce and mostly occur in basement clasts, with the same characteristics as described in the granitoid. In the matrix, scarce, relatively small (<10 µm) idiomorphic non-fractured grains occur (Fig. 2.4c), with most grains generally too small for EPMA analysis (spot size of 2-3 µm). The grains big enough to be measured show a non-substituted (henceforth referred to as “pure”) magnetite composition (sample 646 and 721 in Table 2.1).

2.5.1.3. Upper Impact Melt

The composition of magnetite in the UIM is not homogeneous throughout the profile. In the green schlieren samples of Unit 3A, scarce clusters of magnetite with skeletal textures occur (clusters reach up to 50µm, with individual grains often <10µm, Fig. 2.4d). These clusters often contain sulfides, pyrite and chalcopyrite, alongside the inverse spinel-group phases. Sulfides are prevalent throughout the impact melt units. Magnetite compositions vary between the uppermost (Table 2.1, sample 727) and lowermost parts (Sample 732) of the UIM, with some of the inverse spinel group minerals ranging from a Ti-, Al- and Mg-substituted magnetite (sample 727 points 2-1 and 2-2) to nearly pure magnetite (sample 732 point 3-11).

A wide variation of Ti-substitution in the oxides is shown by the Ti# (a number that quantifies the ratio between the titanium content with the remaining cations, given by 100x[2Ti/(2Ti+Al+Cr)], see Fig. 2.5). In the titanomagnetite grains, the Ti# varies widely, ranging from 16% in sample 727 ($Fe_{2.69}Mg_{0.19}Al_{0.07}Cr_{0.03}Ti_{0.1}O_4$,) up to 92,7% in sample 732 ($Fe_{2.75}Ti_{0.18}Mg_{0.04}Al_{0.3}Ca_{0.01}O_4$).

We also observe a consistently high Mg# (number quantifying the amount of magnesium for Fe^{2+} substitution in the crystal structure; 100x(Mg/[Mg+Fe^{2+}], see Fig. 2.5) of about 70% in most analyzed grains. Only sample 727 (point 1-6) shows a Cr# (quantifies the ratio between chromium substitution with aluminum; 100x[Cr/(Cr+Al)]) of 30% (Table 2.1), indicating mafic to ultramafic contributions to the impact melt.

Sample 732 shows the widest range of composition. This sample is found at the bottom of Unit 3A, likely in the transition zone between the green schlieren and black melts (Unit 3B).

In the impact melts of Unit 3B, magnetic oxides are more abundant. They occur as small (10-50µm) idiomorphic grains, larger than in Unit 3A, scattered within the melt’s matrix, particularly in the uppermost samples (Fig. 2.4e). The chemical composition of Unit 3B magnetite does not vary as much as in Unit 3A and is generally consistent throughout the subunit (see representative samples 738 and 744, Table 2.1). Within the range of compositions observed in Unit 3A, the grains in Unit 3B show high-end concentrations of Al and Mg (Mg# ~60%) and Ti (up to TiO_2 ~5-7 wt% and Ti# up to 80-85%). Magnetite formulas range from $Fe_{2.65}Ti_{0.19}Mg_{0.08}Al_{0.06}Ca_{0.01}O_4$ to $Fe_{2.67}Ti_{0.14}Mg_{0.10}Al_{0.07}O_4$.

In addition to chemical composition, Table 2.1 shows calculated Curie temperatures for single point analysis in the magnetic minerals, using the empirical formula given in Engelmann (2008) based on synthetic titanomagnetite (K was converted to °C after the calculation) and modified in Lied et al. (2020). The formula considers the cation substitution of Al and Mg, as well as of Cr and Mn in samples that contain these elements. All these elements have a decreasing effect on the Curie temperature compared to magnetite (Fe_3O_4).

- $Tc_{calc\ (Al,Cr,Mg,Mn)} = Tc_{calc} - 539 * [Al+Cr] - 82 * [Mg+Mn]$

We did this in order to compare the Tc_{calc} to the measured T_c for the whole rock sample using the temperature-dependence of magnetic susceptibility (Table 2.2).

2.5.1.4. Lower Impact melt

Sample 999 shows the contact between the granitoid basement with shocked and fractured pure magnetite (Fig. 2.4f and 2.4g) and the LIM (Fig. 2.4h). In this case, magnetite does not show any visible oxidation to hematite. In the LIM, the spinel textures are similar to those in Unit 3B with relatively small, idiomorphic grains (10-50µm) scattered within the melt's matrix, and with occasionally larger (~100µm), non-fractured grains (Fig. 2.4h and 2.4i). In contrast to the UIM, the LIM is characterized by a wider range of compositions even in very close proximity and association, with generally higher concentrations of Ti (Table 2.1). In sample 1224, some of the cation-substituted magnetite appears along veins "injected" into the granite in contact with melt (Fig. 2.4j). In comparison to Unit 3B, magnetite shows varying Ti concentrations (0.24 – 12.6 wt% TiO_2) with no Al and Mg substitution, and formulas ranging from nearly pure magnetite ($Fe_{2.98}Ti_{0.01}O_4$, 1224 III-9) to intermediate titanomagnetite ($Fe_{2.62}Ti_{0.38}O_4$, Ti# 100%, 1224 III-7). These compositions are found in the grains shown in Fig. 2.4j suggesting that there is a poor element homogenization in the melts.

2.5.2.Magnetic Grain Size

Hysteresis data plotted on a Day diagram (Fig. 2.6a) show that the M_{rs}/M_s and B_{cr}/B_c ratios of the different lithologies plot along the multi domain (MD) – single domain (SD) mixing line for magnetite (Day et al., 1977; Dunlop et al., 2002; Lanci et al., 2003). The large, fractured basement magnetite shows predominantly pseudo-single domain (PSD) behavior, and with five samples showing MD magnetite. Magnetite from suevite mostly show PSD behavior. Melt samples from the UIM tend to higher B_{cr}/B_c ratios (>4), with the majority of the magnetite grains showing PSD+MD behavior. Large magnetic grain size variation with some clustering at the PSD-SD boundary (B_{cr}/B_c = ~2; Fig. 2.6a) are typical for magnetite from the LIM.

For 20 samples we measured hysteresis parameters before and after κ-T measurements in order to test if the hypothesis that magnetic domain state changes due to annealing of lattice defects and mineral reactions. Six samples were rejected due to very weak/paramagnetic signals after heating. UIM samples show a significant decrease of B_{cr}/B_c ratios, and increase of M_{rs}/M_s ratios, from PSD+MD towards a more general PSD domain state behavior (Fig. 2.6b, Table 2.2), in line with the formation of new, smaller magnetite grains during heating. The LIM and LIM dykes manifest no change in B_{cr}/B_c, but in general an increase of M_{rs}/M_s. Granitoid basement samples show a small increase of the B_{cr}/B_c ratio, which is however not very significant. Two basement samples in contact with melts show a decrease in B_{cr}/B_c ratios. Samples from the LIM display a general increase of M_{rs}/M_s, and no change in B_{cr}/B_c (Fig. 2.6b). Domain state changes in the cation substituted magnetite after heating suggest a general pattern of grain size reduction on the Day-plot (Fig. 2.6d). Despite this, the interpretation of a Day-diagram in cation-substituted magnetite is not without issues (see e.g., Roberts et al., 2018), and the mechanism through which this grain size reduction occurs remains elusive.

The results of IRM component analysis are presented as normalized gradient acquisition plots (GAPs), in Fig. 2.6c to 2.6f, and Table A.3.1 in Appendix A. For the majority of the samples, a single-component distribution is favored, with mean coercivity ($B_{1/2}$) varying between 30 and 73 mT, which we identify as magnetite. For a few samples we observed a high coercivity component ($B_{1/2}$ >500 mT) with relatively low contribution (<14%), which we identify as hematite (see Fig. 2.6c and 2.6e).

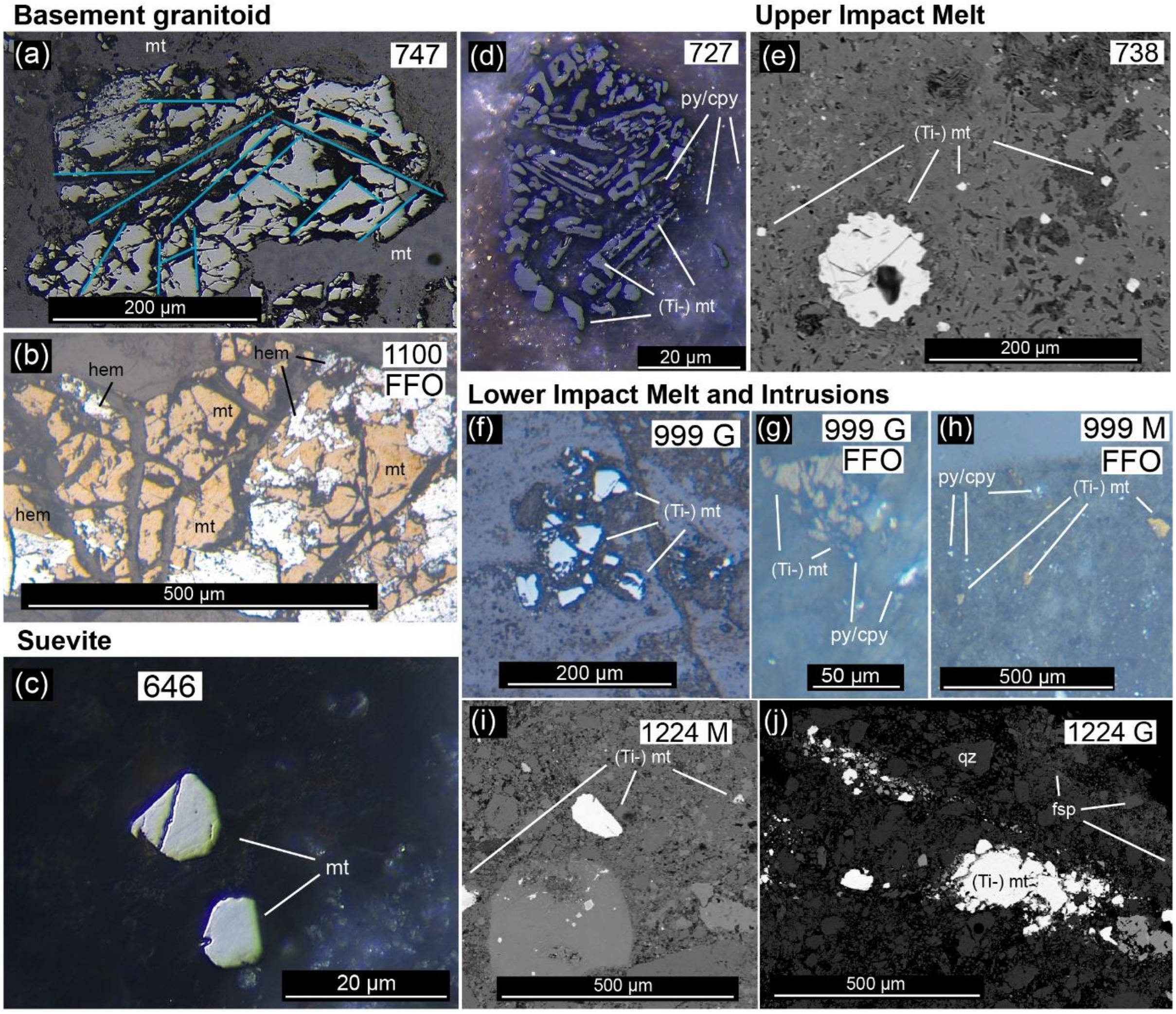

Figure 2.4. Back scattered electron (e, i, j) and reflected light microscopy (a, b, c, d, f, g and h) images of representative grains. mt=magnetite, (Ti-)mt = titanomagnetite, hem = hematite, py = pyrite, cpy = chalcopyrite, qz = quartz, fsp = feldspar, M = melt; G = Granitoid; FFO = Ferrofluid. (a) Large (>200µm) pure, fractured magnetite grain in the basement granitoid. Note shear fractures (blue lines); (b) Very large (~1mm) pure, fractured magnetite grain altered into hematite in the basement granitoid (polished section coated with ferrofluid). Note that shock fractures also occur in hematite, thus both Fe-oxides predate the impact event; (c) Newly formed, small magnetite grains (~10µm) in unit 2A; (d) Small skeletal grains surrounded by dusted sulfides in Unit 3A, and (e) small grains of cation-substituted magnetite in the melt matrix of Unit 3B, together with a larger grain of the same cation-substituted magnetite (in the center); (f) fractured magnetite of sample 999 in contact with melt, note absence of hematite oxidation; (g) fractured magnetite of sample 999 coated with ferrofluid: (h) Newly formed cation-substituted magnetite in 999 LIM intrusion dyke (Unit 4) coated by ferrofluid; (i) Relatively large non-fractured magnetite grains in melt of sample 1224; (j) Melt-injected newly formed cation-substituted magnetite grains close to the contact of granite with melt (see Table 2.1 for mineral chemistry).

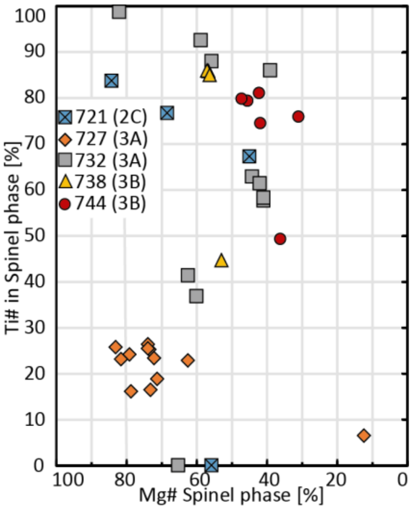

Figure 2.5. Variation of spinel composition in the melt samples of the UIM. For representative analyses, see Table 2.1 (all single analyses are given in Supplemental data file 2, see Appendix A.6 for details). Note the large variability in composition particularly in sample 732 from the transition between the green schlieren zone and black melts of Unit 3B. The grey dots denote an evolution from a more Mg- dominated substitution towards a more Ti-dominated substitution in Unit 3B.

Sample 1100 shows two components before heating, with 95% and 5% contributions of magnetite and hematite, respectively, but only one low coercivity component after heating (Fig. 2.6c, Table A.3.1. in Appendix A). However, it should be noted that some components are skewed and does not fit to the log-normal distribution applied in the excel workbook by Kruiver et al. (2001). As we cannot include skewness in the component analysis, we decided not to use another low-coercivity component that would be artificial to fill the space below the left branch of the fitting line (see e.g., Fig. 2.6f).

Hysteresis measurement data is in Supplemental file 7 (see Appendix A.6. for details), and hysteresis parameters before and after heating experiments are given in Table 2.2. IRM component analysis data is in Appendix A.3., and raw data in Supplemental File 9 (see Appendix A.6. for details).

2.5.3.Magnetic Transition temperatures

2.5.3.1. Granitoid basement

The basement granitoid samples from 747 to 1197 m are characterized by Verwey transitions between -157° and -151°C in the first low temperature measurement (Table 2.3, Fig. 2.7a, Fig. 2.8). In a second low-temperature measurement after a heating cycle, the Verwey transition shows a decrease in temperature up to 3°C (Fig. 2.8). The transition is sharp, and Verwey peak ratios are around ~1.3, with a tendency to decrease to ~1.1-1.15 after the heating cycle (Fig. 2.8, Table 2.3). Curie temperatures of the granitoid samples range mostly from 572° to 585°C (Fig. 2.7; 2.8) and are largely the same in the heating and cooling curves. This observation indicates more or less stoichiometric magnetite, in agreement with the mineral chemical analysis (see Table 2.1). Hopkinson peak ratios are around 1.2 to 1.3, decreasing to 1.1 to 1.2 in the cooling curves (Fig. 2.8).

Most granitoid basement samples show a positive A40 below 50%, with magnetic susceptibility increasing after heating (Fig. 2.7a, sample 1100; Fig. 2.8). This behavior is often observed in rocks containing hematite, when κ-T measurements are done in argon atmosphere (e.g. Just and Kontny, 2011). It implies the presence of a reducing agent in the argon gas (see rock magnetic methods), which enables the transformation of hematite (Fig. 2.4b) to magnetite. A notable exception is sample 747, which shows an essentially reversible behavior (A40 of 3%). This was confirmed by our M-T results, where no sign of hematite was found during heating, and Tc is that of pure stoichiometric magnetite (Fig. 2.7e, sample 747).

Table 2.1. Representative electron microprobe data in wt% of representative magnetite. b.d. – Below detection limit. See text for Mg#, Cr# and Ti# formulas. Curie temperatures are calculated using the formula given in the main text.

Sample (Unit)	**646 (2A)**	**721 (2C)**		**727 (3A)**			**732 (3A)**						**738 (3B)**	**744 (3B)**	**747 (4)**	**1135 (4)**	**1224 (4)**	
Point	**2-3**	**1-1**	**2-6**	**1-6**	**2-1**	**2-2**	**1-1**	**1-2**	**2-8**	**2-9**	**3-10**	**3-11**	**1-3**	**1-2**	**1-4**	**1-2**	**IV-1**	**III-7**
SiO_2	b.d.	b.d.	0.08	b.d.	0.14	b.d.	0.09	b.d.	0.07	0.11	0.09	0.10	0.14	0.19	b.d.	b.d.	b.d.	b.d.
TiO_2	0.11	b.d.	2.18	0.36	1.13	1.16	2.69	2.28	6.06	7.74	0.62	0.43	6.58	5.00	b.d.	b.d.	8.51	12.58
Al_2O_3	b.d.	0.07	0.84	1.59	4.53	4.93	2.02	2.13	0.61	0.67	1.12	0.94	1.36	1.60	b.d.	b.d.	b.d.	b.d.
Cr_2O_3	b.d.	b.d.	b.d.	1.09	b.d.	b.d.	b.d.	b.d.	b.d.	1.38	b.d.	b.d.	b.d.	b.d.	b.d.	b.d.	b.d.	b.d.
Fe_2O_3	68.58	68.41	64.27	67.05	68.28	70.20	60.96	61.73	53.99	48.73	66.11	66.23	52.75	55.95	68.80	68.59	50.26	41.32
FeO	30.95	30.67	30.99	26.09	11.21	5.40	31.64	31.29	34.39	36.45	29.16	29.48	34.12	32.62	30.95	30.86	37.92	41.22
MgO	b.d.	b.d.	1.44	3.43	13.60	17.27	1.27	1.17	0.69	0.34	1.48	1.12	1.43	1.68	b.d.	b.d.	b.d.	b.d.
CaO	b.d.	0.12	0.05	0.19	0.65	0.75	b.d.	b.d.	0.13	0.14	0.05	0.00	0.15	0.10	b.d.	b.d.	b.d.	b.d.
Total	99.64	99.27	99.85	99.80	99.39	99.70	98.58	98.59	95.94	95.56	98.63	98.30	96.52	97.15	99.75	99.44	96.69	95.12
Ti	-	-	0.06	0.01	0.03	0.03	0.08	0.07	0.18	0.23	0.02	0.01	0.19	0.14	-	-	0.25	0.38
Al	-	-	0.04	0.07	0.18	0.19	0.09	0.10	0.03	0.03	0.05	0.04	0.06	0.07	-	-	-	-
Cr	-	-	-	0.03	-	-	-	-	-	0.04	-	-	-	-	-	-	-	-
Fe^{3+}	1.99	2.00	1.83	1.88	1.75	1.75	1.75	1.77	1.61	1.45	1.91	1.92	1.54	1.62	2.00	2.00	1.49	1.24
Fe^{2+}	1.00	1.00	0.98	0.81	0.32	0.15	1.01	1.00	1.14	1.21	0.93	0.95	1.11	1.05	1.00	1.00	1.25	1.38
Mg	-	-	0.08	0.19	0.69	0.85	0.07	0.07	0.04	0.02	0.08	0.06	0.08	0.10	-	-	-	-
Ca	-	-	-	0.01	0.02	0.03	-	-	0.01	0.01	-	-	0.01	-	-	-	-	-
Total	3.00	3.00	3.00	3.00	3.00	3.00	3.00	3.00	3.00	3.00	3.00	3.00	3.00	3.00	3.00	3.00	3.00	3.00
Mg#	-	-	68.44	73.18	79.16	81.59	44.30	41.00	58.86	39.09	62.57	60.11	57.08	57.05	-	-	-	-
Cr#	-	-	-	31.47	-	-	-	-	-	58.01	-	-	-	-	-	-	-	-
Ti#	-	-	76.81	16.44	24.19	23.14	62.95	57.73	92.69	86.09	41.40	36.86	86.06	79.95	-	-	100.00	100.00
Tc Calc	577.3	577.3	517.9	503.2	408.5	389.7	481.4	485.7	456.6	401.7	535.1	543.9	427.4	449.5	579.1	579.1	429.6	345.7

Table 2.2. Hysteresis parameters pre- and post-heating to 600°C.

Sample	Pre-Heating		Post-Heating	
	Mr/Ms	Bcr/Bc	Mr/Ms	Bcr/Bs
727 (2A)	0.088	4.879	0.165	3.723
732 (3A)	0.036	6.665	0.089	2.762
738 (3B)	0.058	4.465	0.091	4.240
744 (3B)	0.051	7.406	0.081	3.325
747 (4)	0.060	4.435	0.063	3.913
804 (4)	0.093	3.327	0.107	3.543
995AG (4)	0.209	1.960	0.242	1.938
995AM (4)	0.172	2.170	0.207	2.000
999C (4)	0.232	2.111	0.258	2.014
1100 (4)	0.263	1.729	0.336	1.629
1100 (4)	0.244	1.763	0.303	1.688
1100 (4)	0.087	2.603	0.089	2.917
1194 (4)	0.051	3.658	0.053	4.249
1224C (4)	0.073	4.052	0.087	3.457
1224DG (4)	0.265	1.810	0.299	1.931

LIM intrusions into the granitoid also show magnetite with Curie temperatures around 570 to 580°C, and are not very different from the granitoid host rocks. However, they show a negative A40 (sample 847 and 1224 in Table 2.3 and Fig. 2.7d), which seems to be characteristic for the impact melts and indicates an instability of the ferrimagnetic phase. A detailed description of a granitoid-LIM contact is given in section 2.5.3.4., below.

2.5.3.2. Suevite

Suevites from Units 2A and 2B (Fig. 2.7b) show Verwey transitions between -165 and -150 °C, and lower T_vPRs after heating (T_vPR2; Table 2.3, Fig. 2.8). Suevites from Unit 2A are characterized by a broad Curie temperature interval between ~500°C to 580°C, and a suppressed, but faintly visible Verwey transition in the first low-temperature measurement (Fig. 2.7b and Fig. 2.8). After heating to 700°C, two better defined Curie temperatures at 441°C and 584°C occur in the cooling curve (Fig. 2.7b). Heating curves of suevites from Unit 2B show a small but sharp transition at 580°C, and in the cooling curve a prominent second transition varying from 440 to 460°C, with large HPRs (Table 2.3, Fig. 2.8). In the M-T curve for sample 646 a decrease of magnetization from 400°C to 460°C and a final Curie temperature at 570-580°C is observed (Fig. 2.7e, Sample 646).

These suevite samples show the highest A40 alteration index (174% to 345%), suggesting mineral transformation to a ferrimagnetic phase during heating (Table 2.3, Fig. 2.8). As the suevite contains high amounts of secondary carbonates (e.g., Kring et al., 2020) it is likely that they transform into Fe and/or Mn-bearing spinel group minerals (Just and Kontny, 2011). One of the ferrimagnetic minerals that is formed by these mineral reactions is stoichiometric magnetite, as evidenced by the Curie temperature close to 580°C in the heating curve and the clear Verwey transition in the second low-temperature measurement.

2.5.3.3. Upper Impact Melt

The uppermost samples of Unit 3A do not show a Verwey transition, neither before or after heating up to 700°C (Fig. 2.7c). Samples between 732 and 744 do show a T_v, but at significantly lower temperatures (below -170°C, see sample 744 in Fig. 2.7c) compared to stoichiometric magnetite (-153°C) (Fig. 2.8). Heating curves show distinctly higher Curie temperatures (512-545°C) compared to those retrieved from the cooling curve (440-530°C; Fig. 2.7 and 2.8, Table 2.3). The lower T_c in the cooling curves is also observed in the M-T curve (Fig. 2.7e, sample 727). Alteration index A40 is mostly negative and suggests a decrease of the ferrimagnetic phase during heating. All data for κ-T measurements are in Supplemental file 3; all M-T measurements are in Supplemental file 4, See Appendix A.6. for details.

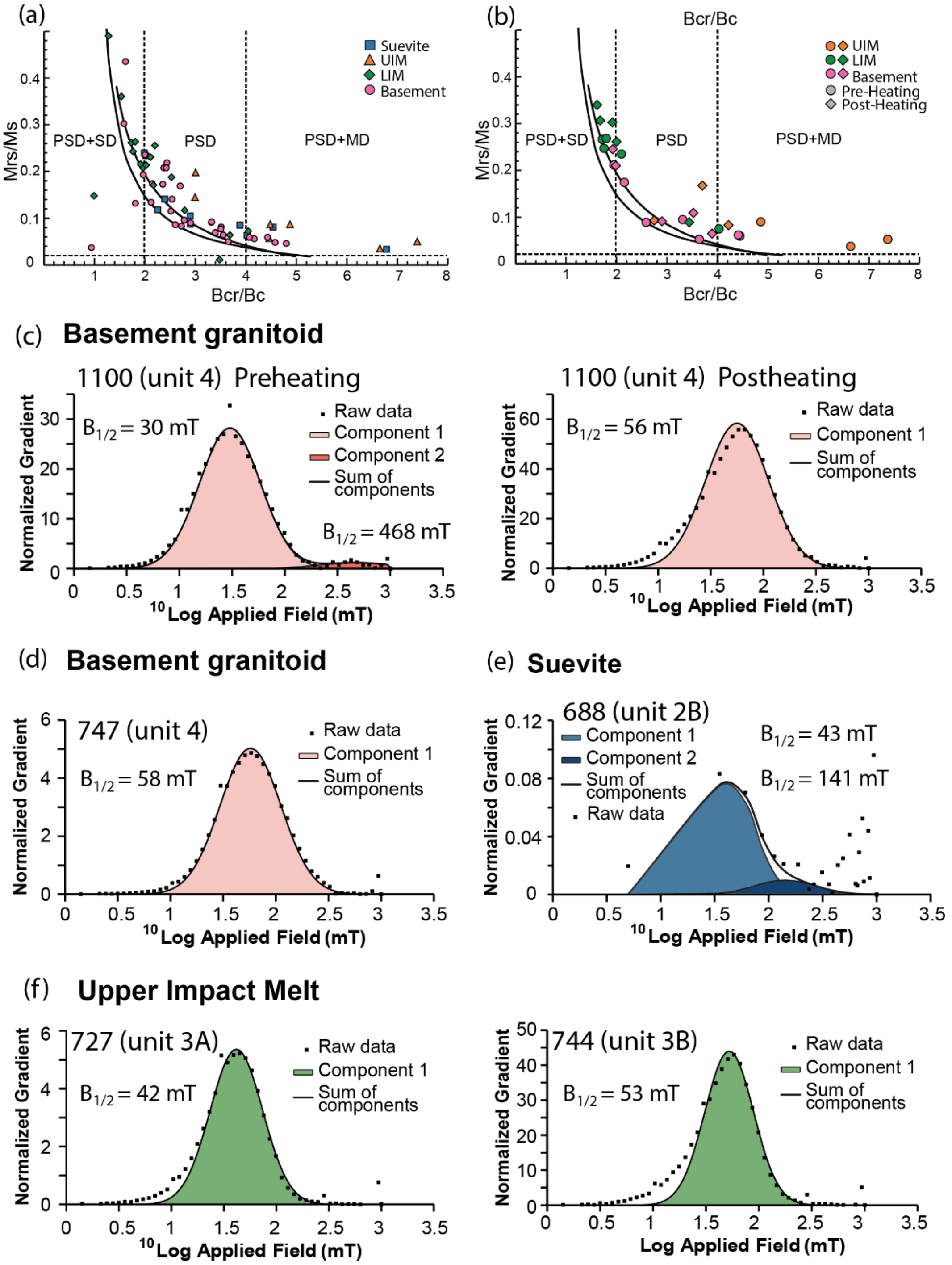

Figure 2.6. (a) Day—Dunlop-plot (Day et al., 1977; Dunlop et al., 2002) for hysteresis data of our samples; (b) Day—Dunlop-plot with pre- and post-heating data of the 14 accepted samples. (c, d, e, f) IRM component analysis GAP for representative samples; (c) basement granitoid sample 1100 before (left) and after (right) heating. Note the disappearance of the second, high coercivity component after heating; (d) Basement granitoid sample 747; (e) Two-component solution for sample 688, which we identify as magnetite and hematite; (f) UIM representative samples from unit 3A (left) and 3B (right). M_{rs}—remanent magnetization; M_s—saturation magnetization; B_c—coercivity; B_{cr}—coercivity of remanence; SD—single domain; MD—multi domain; UIM—upper impact melt; LIM—lower impact melt; $B_{1/2}$—mean coercivity.

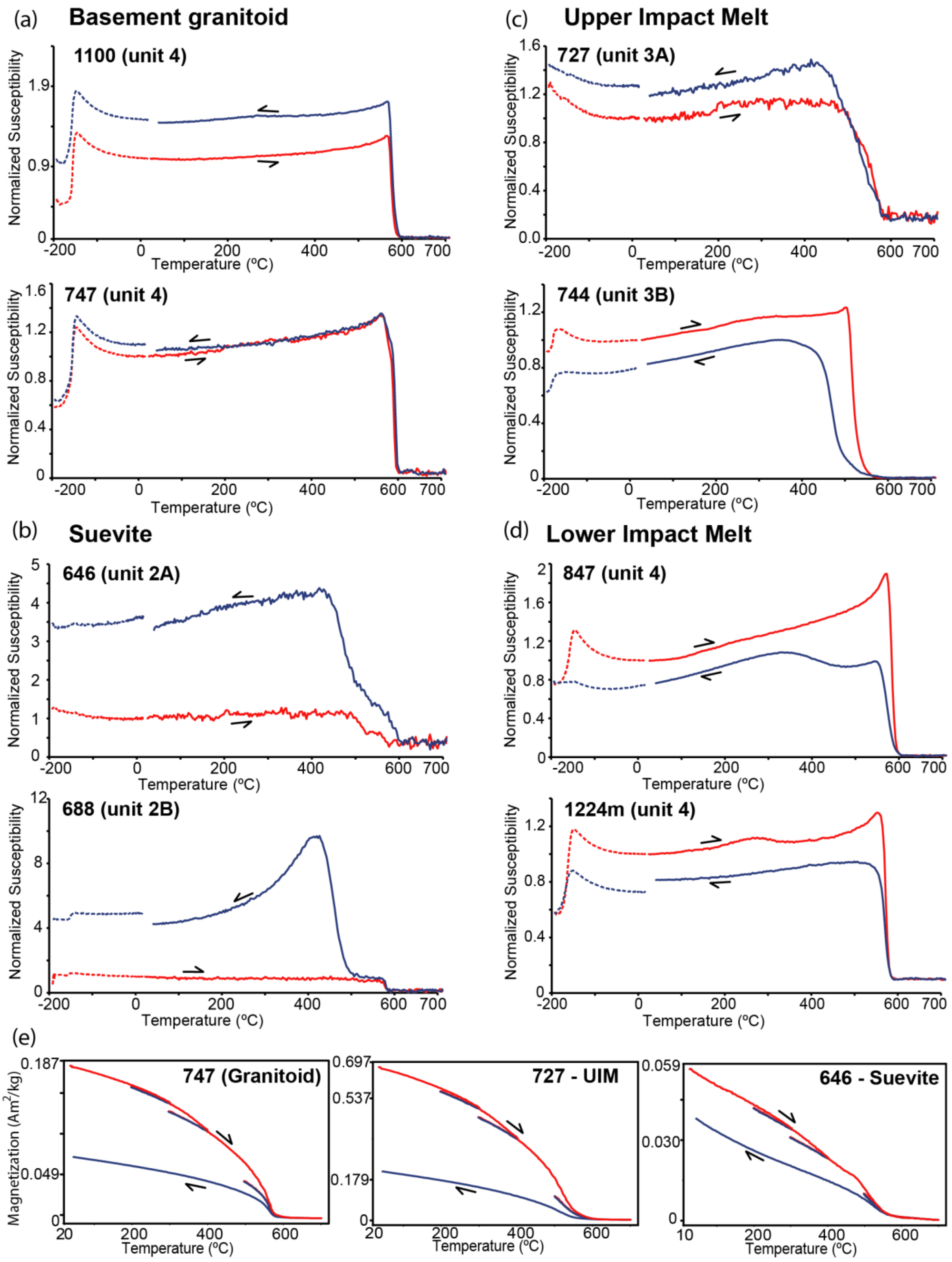

Figure 2.7. Representative k-T curves from different lithological units of drill core M0077A. See Fig. 2.3 for the description of the susceptibility parameters. (a) Granitoid basement; (b) suevite; (c) upper impact melt (UIM); (d) Lower Impact Melt. See main text for formulas. (e) Representative thermomagnetic (M(T)) measurements for units 2, 3 and 4. All M-T curves were done in air atmosphere. Dark line is the heating curve, while lighter is the cooling curve.

Table 2.3. Parameters determined from k-T curves.

Sample (Unit)	Tv1 (°C)	Tv2 (°C)	TcH (°C)	TcC (°C)	TvPR1	TvPR2	HPR1	HPR2	A40[40%]
639 (2A)	-151	-155	573	467	1.27	1.05	1.29	1.29	174.7
646 (2A)	-	-155	491 | 553	441|584	-	0.95	1.28	1.34	207.7
683 (2B)	-150	-	554	579	1.18	-	1.34	2.45	411.4
688 (2B)	-159	-153	574	468 | 581	1.23	1.01	1.02	2.29	345.5
700 (2B)	-	-166	490 | 592	443 | 578	-	1.01	1.34	1.23	-4.4
721 (3A)	-	-	538	481 | 583	-	-	1.32	1.43	-26.2
727 (3A)	-	-	545	529	-	-	1.17	1.25	18.6
732 (3A)	-186	-186	521	481	1.13	1.02	1.01	1.12	-14.0
738 (3B)	-187	-189	513	438	1.08	0.98	1.08	1.22	-20.0
744 (3B)	-180	-184	512	473	1.08	0.97	1.24	1.21	-18.1
747 (4)	-153	-153	589	595	1.24	1.24	1.34	1.29	2.9
763 (4)	-158	-161	572	574	1.28	1.22	1.28	1.19	18.0
804 (4)	-154	-158	583	587	1.31	1.22	1.28	1.18	20.9
810 (4)	-160	-158	572	575	1.31	1.27	1.27	1.21	23.6
847 (4)	-159	-154	582	572	1.31	1.03	1.90	1.42	-23.9
967 (4)	-157	-158	572	578	1.29	1.22	1.23	1.12	15.9
982 (4)	-157	-156	574	579	1.31	1.18	1.17	1.10	37.8
994 (4)	-154	-155	552	577	1.30	1.19	1.17	1.15	26.2
995AM (4)	-157	-157	574	571	1.12	1.16	1.54	1.23	23.3
995AG (4)	-155	-156	576	580	1.24	1.07	1.12	1.21	7.4
995B (4)	-156	-157	572	574	1.32	1.24	1.28	1.17	48.9
996 (4)	-	-	553	567	-	-	1.48	1.19	89.2
997 (4)	-155	-155	574	576	0.97	1.19	1.73	1.26	16.7
999M1 (4)	-151	-163	579	579	1.19	1.09	1.34	1.26	-11.3
999M2 (4)	-156	-158	572	574	1.20	1.10	1.50	1.22	-14.3
999C (4)	-157	-154	571	576	0.98	1.05	1.45	1.82	-40.6
999G3 (4)	-153	-153	311 | 570	581	1.26	1.54	1.31	1.73	-61.2
999G2 (4)	-152	-158	580	577	1.28	1.31	1.11	1.17	9.5
999G1 (4)	-152	-154	582	593	1.57	1.31	1.13	1.12	34.2
1085 (4)	-	-	572	571	-	-	2.25	1.63	197.6
1097 (4)	-153	-154	575	582	1.30	1.20	1.30	1.19	47.8
1100 (4)	-156	-159	573	577	1.33	1.24	1.28	1.19	45.0
1103 (4)	-156	-156	574	581	1.29	1.19	1.25	1.12	45.5
1135A (4)	-158	-160	576	581	1.32	1.23	1.20	1.12	19.3
1135B (4)	-147	-153	585	591	1.19	1.15	1.20	1.15	14.5
1137 (4)	-155	-157	581	577	1.30	1.27	1.28	1.10	166.4
1140 (4)	-159	-157	573	575	1.31	1.25	1.32	1.27	12.3
1149 (4)	-155	-157	574	578	1.28	1.17	1.18	1.26	49.6
1150 (4)	-156	-158	570	573	1.28	1.18	1.21	1.08	19.5
1161 (4)	-153	-159	577	583	1.30	1.26	1.26	1.19	16.9
1194 (4)	-156	-158	574	575	1.29	1.26	1.29	1.22	13.6
1197 (4)	-157	-157	570	576	1.33	1.24	1.12	1.10	14.5
1224A (4)	-157	-161	572	574	1.20	1.20	1.39	1.21	-1.2
1224B (4)	-162	-161	570	577	1.22	1.21	1.36	1.19	-2.2
1224C (4)	-160	-163	576	578	1.19	1.21	1.31	1.08	9.3
1224DG (4)	-160	-163	572	574	1.26	1.21	1.23	1.08	12.7
1224DM (4)	-164	-167	569	573	1.18	1.21	1.30	1.16	-18.7
1225 (4)	-165	-164	582	579	1.05	1.17	1.71	1.37	3.3
1231 (4)	-161	-165	572	577	1.21	1.21	1.23	1.16	8.8
1249 (4)	-167	-175	582	588	1.20	1.24	1.34	1.25	3.5
1326 (4)	-154	-164	580	585	1.17	1.16	1.27	1.15	58.8

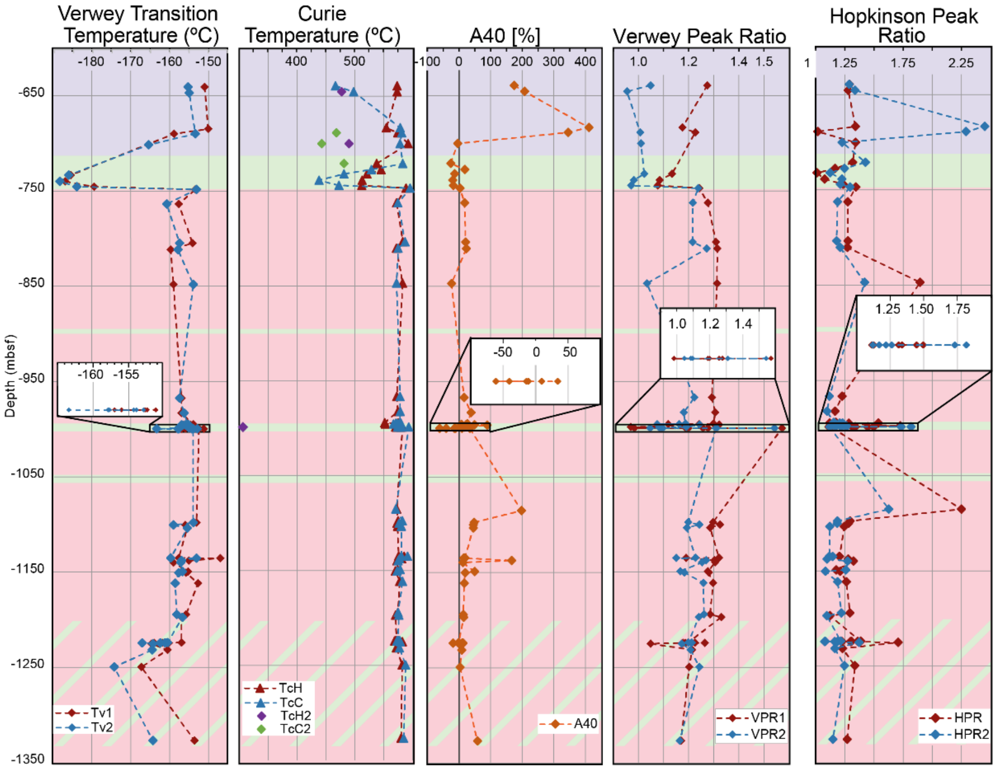

Figure 2.8. Depth variation of susceptibility parameters along core M0077A. Note that Verwey transition temperatures are lower in the UIM and LIM units, while they remain relatively constant between -151ºC and -159ºC in the granitoid unit (Unit 4). Curie temperatures remain constant through Unit 4, and both T_vPR and HPR show a decrease after the heating cycles, suggesting a magnetic domain state increase during the experiment. The background coloring is the same pattern as in Fig. 2.2 (from top to bottom: Suevite, upper impact melt, and basement Granitoid [intercalated with lower impact melt dykes]). T_cH—Curie temperatures (heating); T_cC—Curie temperatures (cooling).

2.5.3.4. High resolution profiles of Lower Impact Melt – Granitoid basement contact

To evaluate the thermal effect of the impact melt on the shocked magnetite from the granitoid basement rocks, we measured six κ-T curves over an eight cm profile across a basement granitoid – LIM contact at 999 mbsf, investigated the magnetic phases microscopically, and performed IRM component analysis (Fig. 2.9). The k-T curves from the granitoid rock show a relatively good reversibility (G1 and G2 in Fig. 2.9). The A40 of G1 and G2 is 34% and 10% respectively, which is lower than the average of the basement (around ~45%). Only at a distance of less than 1 cm from the contact, an alteration effect in form of a hump between 200 and 400°C is observed (G3 in Fig. 2.9). This hump is particularly well exposed in the flow-foliated ultra-cataclasite (C in Fig. 2.9). IRM component analyses show only one low coercivity component with $B_{1/2}$ = 48-51 mT in the granite samples, and 56-62 mT in the melt samples.

The hump also faintly occurs in the impact melt (M1 and M2 in Fig. 2.9). While this hump disappears in the cooling curves of the granitoid rock (G2, G3) and flow-foliated ultra-cataclasite sample (C), it remains visible in the impact melt samples (M1, M2) where it shifts towards slightly higher temperatures. Magnetite grains in the impact melt are too small for a reliable quantitative EMPA determination. However, the Curie temperature near 580°C implies a close to stoichiometric composition of magnetite. The Hopkinson peak at the Curie temperature disappears in the cooling run suggesting that some annealing causes magnetic domain state increase and apparent magnetic grain size growth and/or a mineral reaction forming a non- or less-magnetic phase.

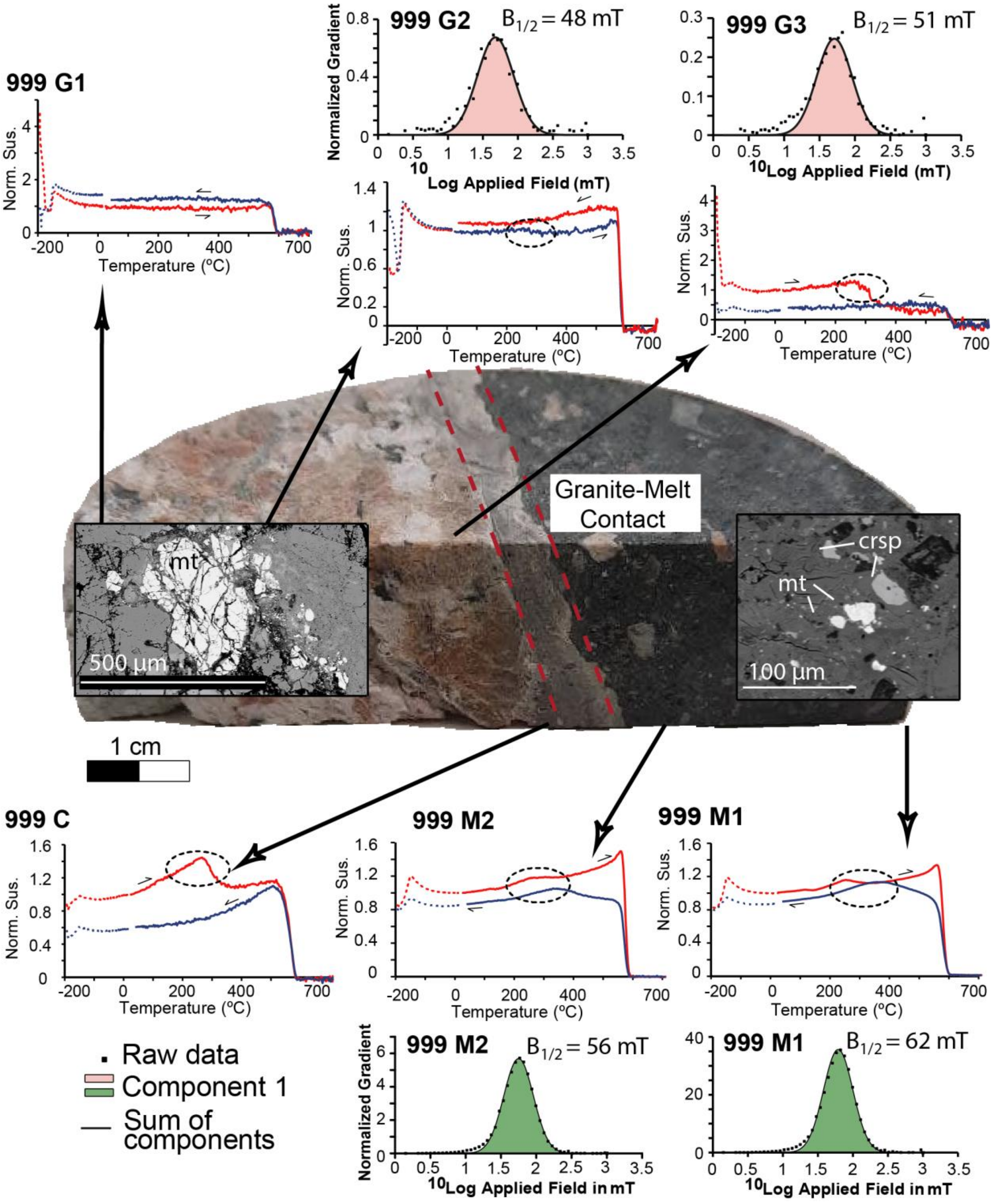

Figure 2.9. High-resolution κ-T curves and IRM analysis at the granitoid rock – ultra-cataclasite – impact melt contact of sample 999. Note the increased prominence of a hump in the heating curve towards the contact and in the melt region. Note also the texture differences between the large, fractured magnetite in the granite (left) and the small grains of newly formed magnetite in the melt (right). Norm. Susc. = Normalized Susceptibility.

2.5.3.5. High temperature annealing experiments

To better understand the role of temperature in the post-impact processes that affect the magnetic mineralogy, we performed a stepwise heating/cooling experiment for sample 1100 from the granitoid basement (for susceptibility parameters see Table 2.3) to investigate the onset of irreversible behavior (Fig. 2.10a). Until 540°C, magnetic susceptibility of heating-cooling runs was reversible (Fig. 2.10a), but at 560°C we observed a significant irreversibility (20% increase in susceptibility) between the heating and cooling curve (Fig. 2.10b) with a decrease of the HPR from 1.38 to 1.24, suggesting a slight domain size increase (Dunlop, 2014; Kontny et al., 2018). The higher susceptibility and lower HPR is maintained in the next heating curve of the subsequent run (to 580°C), and shows once again a decrease in HPR from 1.29 to 1.27, however not as distinct as in the first experiment (Fig. 2.10b). In this curve we observe also a slight increase of MS at the Hopkinson peak. This increase is smaller than the increase in the κ-T curves observed elsewhere in the basement when regularly heated up to 700°C, even in the same sample (sample 1100, see Fig. 2.7a). To quantify this change in magnetic susceptibility, we utilize parameter A_{HP} (see calculation in methods), which is related to the formation of new magnetite during heating. Sample 1100, when heated to 700°C (Fig. 2.7a) shows an A_{HP} value of 33.5%. In our annealing experiments, the curve up to 560°C has an A_{HP} of 0.81%, while the curve up to 580°C has a value of 4.4%. This factor, combined with the positive A40 (14.9%) in the 580°C run, indicates that the formation of new magnetite initiates between 560 and 580°C. We attribute the original ~20% increase in susceptibility between 540°C and 560°C to domain size changes through annealing of the lattice defects.

To further investigate the hematite to magnetite transformation during heating in the shocked magnetite, we performed four repeated heating/cooling cycles from room temperature to a maximum of 700°C until we obtained full reversibility of the heating and cooling curve (Fig. 2.10c). After the first cycle MS increased by around 45% (A40 = 45%), and shows a distinctly positive A_{HP} (26.5%). This irreversibility is related to a transformation of oxidation-derived hematite (as seen in Fig. 2.4b; 10d: pre-heating) to magnetite (Fig. 2.10d: post-heating). This feature also agrees with an interpretation that a positive A40 (<50% in our basement samples) and well-defined magnetite Curie temperatures at ~580°C, are indicators for a hematite to magnetite transformation when measured in an Ar atmosphere, as already suggested by Just and Kontny (2011). In addition, we see a decrease in the HPR from 1.35 to 1.17 indicating annealing of the defects in the shocked magnetite (e.g., Kontny et al., 2018).

The FORC of sample 1100 pre-heating (Fig. 2.10e, left) shows a PSD behavior with some indication of interactions between particles and coercivities up to 50-60 mT. After heating (Fig. 2.10e, right), the sample still shows a well-defined PSD behavior, with a higher coercivity tail up to 150 mT. While still PSD, this may suggest the presence of newly formed SD particles during heating. After heating, we also observe an upward shift of the FORC and more asymmetric contours, which may signal an increase in interactions between magnetic particles (e.g., Roberts et al., 2014).

IRM component analysis shows also a significant increase in coercivity in the measured grains from this sample after heating. Original $B_{1/2}$ values in 1100 range from 30 mT to 63 mT pre-heating, while post heating there is a systematic increase of coercivities in all samples, ranging from 53 to 72 mT. All samples show an increase in coercivity, which may suggest an increased contribution of SD magnetite in the samples after heating. (see Table A.3.1., in Appendix A).

Subsequent 2nd and 3rd cycles show a hump in the heating curve, that can suggest either a transformation between 300 and 400°C into a phase with lower magnetic susceptibility compared to magnetite (likely maghemite or hematite) or a thermal relaxation effect of superparamagnetic (SP) magnetite. As we do not observe oxidation during our measurements in an argon atmosphere (see e.g. Fig. 2.10d post heating), this irreversibility is more likely a grain-size effect of SD-SP magnetite grains (e.g., Zhao and Liu, 2010; Gao et al., 2019), during the transformation from hematite to magnetite. After the 4th heating cycle, heating and cooling curves are reversible, and reached a state where magnetite is the only stable phase (A_{HP} of 1.3%). This behavior is similar to the granitoid sample 747, which occurred close to the basement-UIM- contact (A_{HP} of 0.81%) (Fig. 2.7a). When a slower cooling rate (7°C/min) was used (Fig. 2.10f), the shape of the first curve is the same, while a 2nd cycle (using again the standard heating/cooling rate of 12°C/min) shows a nearly-reversible curve, suggesting the stability of the transformation is not only temperature, but also time-of-exposure dependent.

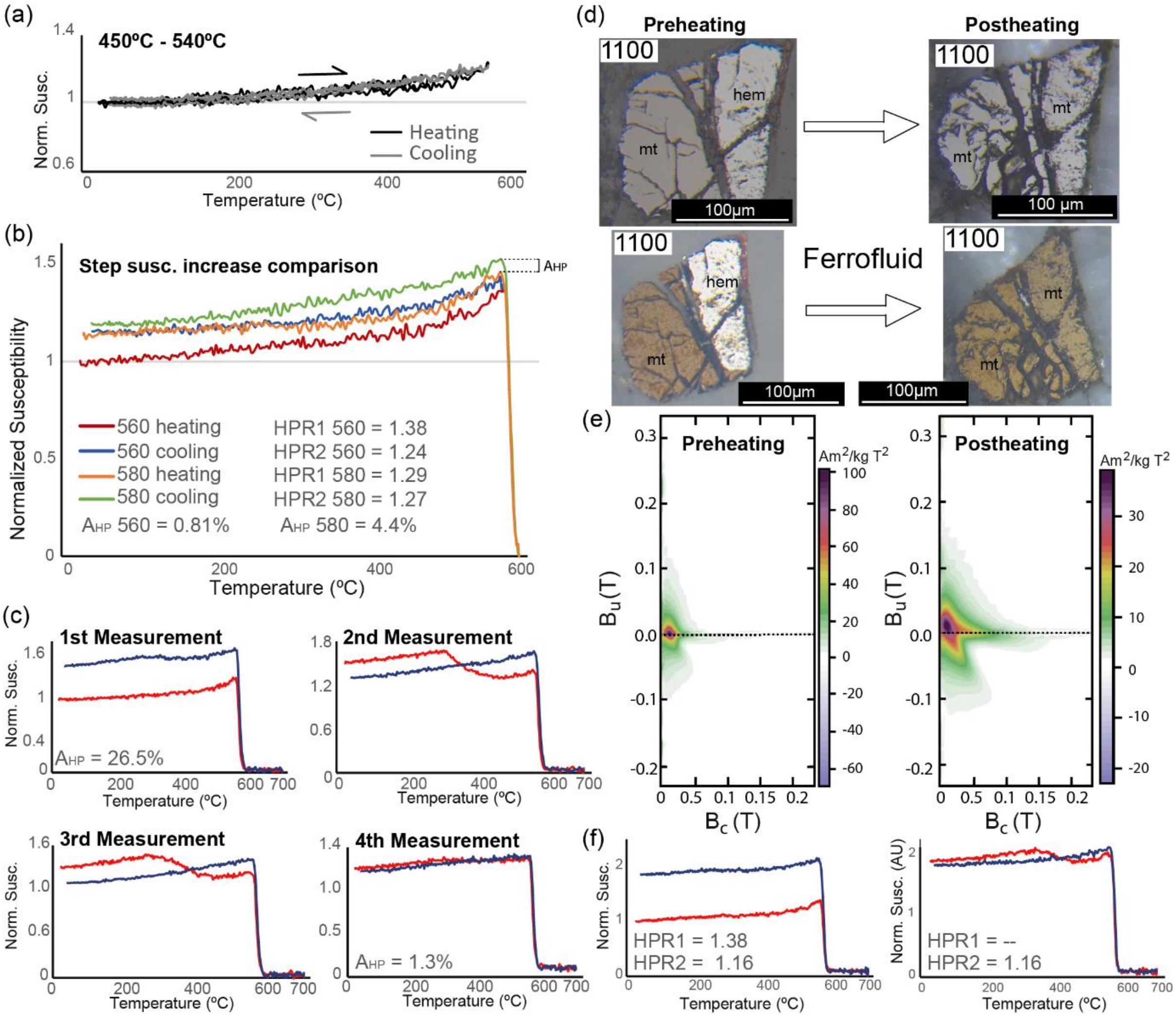

Figure 2.10. Stepwise heating/cooling experiments in Ar atmosphere for sample 1100. (a) Consecutive heating to 450°C, 500°C, 520°C, and 540°C show reversible behavior. (b) At 560°C and 580°C irreversible behavior occurs. HPR1 is determined from the heating and HPR2 from the cooling curve (details in text). Susceptibility is normalized to room temperature value of the 560°C heating curve (red). (c) Four consecutive measurements up to 700°C until reversibility is reached (heating in black, cooling in grey). Susceptibility normalized to the room temperature susceptibility of the first measurement; (d) Magnetite and hematite of sample 1100 before (left) and after (right) 1st heating experiment up to 700°C. Note the incomplete oxidation of the magnetite along the grain boundaries. After the heating experiment, hematite is completely transformed into magnetite. (e) FORC diagrams before (left) and after (right) the same heating treatment as described in (d); (f) Repeated experiments with different heating/cooling rates (slow on the left, fast on the right). See text for details. Norm. Susc. = Normalized Susceptibility.

2.5.4. Rock- and paleomagnetic data

2.5.4.1. Rock magnetic properties

The Koenigsberger ratio (Q-ratio, given by Q = NRM / (*k**B); where B is today's magnetic field, and (*k**B) is induced magnetization) gives the relative importance of remanent (Q>1) or induced magnetization (Q<1) for a given lithology (measurement data are provided in Supplemental file 6, see Appendix A.6. for details). The NRM and susceptibility values of the basement and suevite samples are both quite low, with a dominance of the induced magnetization (Q<1, Fig. 2.11a, 2.11b). The UIM and LIM unit show both higher NRM and susceptibility values (Fig. 2.11a), and a similar contribution of induced and remanent magnetization (Q ≈ 1, Fig. 2.11b). In general, our data show a positive correlation (R = 0.83) between NRM and MS in the impact lithologies suggesting that the amount of magnetite controls the NRM. This is not the case in the basement granitoid with a more scattered distribution (R=0.48).

2.5.4.2. Paleomagnetic directions

Alternating field (7 samples) and thermal (16 samples) demagnetization shows two distinct groups of magnetic directions between the basement and the impactite samples (Fig. 2.11c and 2.11d). After the azimuth corrections based on drill core rotation were applied, we are able to interpret both declination and inclination of our paleomagnetic results. The granitoid basement samples (n = 17) show scattered directions, without a discernible pattern. On the other hand, the impact melt samples (n = 4) show a clear clustering around Dec/Inc: ~180º/-40º (Fig. 2.11c and 2.11d). In the suevite samples of Unit 2A (n = 2) we have fitted and anchored two as great circle interpreted points following the approach described in McFadden and McElhinny (1988) combining great circles and linear best fits. The remaining suevite sample 683 (Unit 2B) is the only direction excluded by a 45° cut off around the average directions. This, together with the anchored great circle fits for Unit 2A demonstrate both, the uncertainty and the variability of paleomagnetic directions in Unit 2. Data files are in Supplemental file 8 (in Paleomagnetism.org 2.0 format; Koymans et al., 2020, see Appendix A.6. for details).

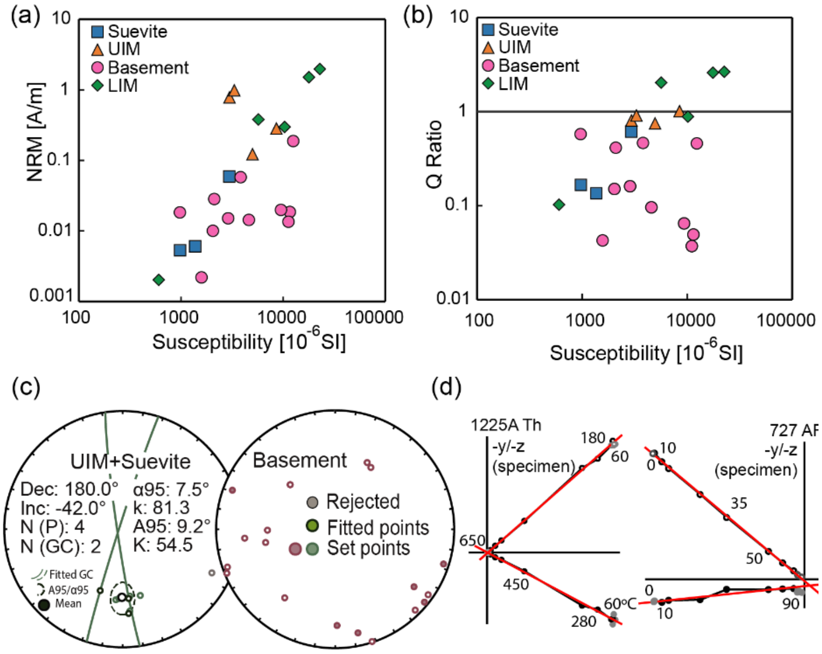

Figure 2.11. (a) NRM vs magnetic susceptibility for selective samples. (b) Q-ratio (NRM/(k*B)) vs magnetic susceptibility. (c) Paleomagnetic results for impactites (suevite and impact melt, left), and granitoid basement (right). (d) representative Zjiderveld diagrams and interpretation of paleomagnetic directions for thermal ("Th", left) and AF demagnetization (right).

2.6. Discussion

2.6.1.Mineral magnetic characteristics

In the lithological units from the Chicxulub peak ring drilled at site M0077A, we distinguished three types of magnetite related to different impact-induced processes: pure, shocked magnetite in the granitoid basement, cation-substituted magnetite crystallized from the impact melt, and pure magnetite formed from hydrothermal fluids, although the latter plays a subordinate role. These magnetite types are essentially the only magnetization carrier in our M0077A samples.

The pure magnetite in the basement granitoid belongs to the pre-impact Carboniferous magmatic mineral assemblage, and is the original carrier of magnetization. This magnetite shows locally pre-impact transformation to hematite (Fig. 2.4b, 2.6c pre-heating), is heavily fractured by the impact, and its hysteresis parameters show a wide variation (Fig. 2.6a), suggesting domain state changes from a likely original MD state. The Curie temperature at ~578°C, and the Verwey transition, usually between -151ºC and -163°C, suggest that this magnetite is close to stoichiometry. The slight shift of the Verwey transition towards lower temperatures (Fig. 2.8) compared to pure magnetite (-153°C; Verwey, 1939) either indicates a certain amount of non-stoichiometry in $Fe_{3(1-\square)}O_4$, or cation substitution (e.g., Özdemir and Dunlop, 1997). Microprobe analysis (Table 2.1) and a sharp Curie temperature at 580°C indicate that magnetite grains from the basement granitoid are rather slightly oxidized than cation-substituted. From the lower T_v values, we estimated that vacancies (δ) in magnetite are very low, approximately $0.001 < \delta < 0.00125$ (Aragon et al., 1985), which is reasonable as slight oxidation is omnipresent in magnetite in all geological settings (e.g., Vahle et al., 2007; Zhang et al., 2020, 2021). In the case of Chicxulub, oxidation is likely concentrated along shock-induced fractures and grain boundaries in magnetite and appears to be a common feature in the shocked crystalline basement rocks (e.g., Mang and Kontny, 2013; Kontny and Grothaus, 2017). For the Chesapeake Bay impact structure (USA), Mang and Kontny (2013) suggest that both fractured basement magnetite and newly formed small magnetite in the suevite, are very sensitive to surface oxidation. Therefore, oxidation of magnetite may preclude its use as a reliable pressure indicator for impact structures, if the Verwey transition is considered (Carporzen and Gilder, 2010; Reznik et al., 2016).

The κ-T curves from the Chicxulub basement show mostly irreversible behavior if measured in an argon atmosphere (see sample 1100 in Fig. 2.7a). This signal is typical for the presence of magnetite and hematite in the sample, where latter is transformed to magnetite above a temperature of about 580°C (Fig. 2.4b; 2.10d). This mineral reaction is probably an artifact of the inert argon gas, as even in high purity it can contain traces of hydrocarbon gases like CH_4. However, this effect helps to identify Fe-bearing minerals due to their typical reactions (e.g., Just and Kontny, 2011). Reversible behavior indicative of magnetite only occurs at the top of Unit 4 near the boundary to the UIM (Fig. 2.4a and 2.7a, sample 747) and in the vicinity of intercalated melt rock layers within the LIM (Fig. 2.8; 2.9 – G2) and is interpreted as high-temperature overprint due to the proximity to the impact melt. IRM analyses confirm the absence of hematite (e.g., Fig. 6d; 2.9, granitoids) in these samples.

Low A40 values indicate a nearly reversible behavior, while distinctly positive values (commonly <50% in the basement granitoids, see Table 2.3, Fig. 2.8) indicate the transformation of hematite into magnetite during heating in argon atmosphere (Table 2.3 and Fig. 2.8; see also Just and Kontny, 2011). If only pure magnetite occurs in the samples, it can be assumed that there was no alteration to hematite before the impact, or that hematite has been transformed back to magnetite in the presence of high enough temperatures (>580°C), either during or after the impact event, as our heating experiment in Fig. 2.10b suggests. Sufficiently elevated temperatures for this reaction were likely reached in the proximity of impact melts for which temperatures between ~650°C and 750°C in the UIM are reported (De Graaff et al., 2021).

In the basement the large range of hysteresis properties across the PSD field (Fig. 2.6a) is noteworthy, as magnetite grains with > 100 µm are expected to be in the MD field. This discrepancy can be attributed to two factors: 1) the fracturing of large grains into smaller individual grains, and 2) the formation of crystal lattice defects inside the larger grains (Reznik et al., 2016). The lattice defects will cause the domain walls to become pinned (e.g., Lindquist et al., 2015) and effectively reduce domain state in an otherwise MD grain. This mechanism is confirmed by the reduction of the Hopkinson peak ratios after heating, which occurs as a result of thermal annealing. Transmission electron microscopy on an experimentally shocked magnetite has shown that shock-induced defects in magnetite can recover after thermal treatment through recrystallization of magnetite and nucleation of new magnetite nano-grains along micro-fractures (Kontny et al., 2018). These mechanisms, combined with thermally-induced relaxation of slightly distorted lattices in the un-fractured sections of the magnetite may cause "unpinning" of the domain walls, and thus apparent domain state increase during the heat treatment (Kontny et al., 2018). However, hysteresis data before and after heating in an argon atmosphere to 600°C revealed only slight changes for magnetite from the granitoid basement (Table 2.2 and Fig. 2.6b, 2.6c) suggesting that fracturing is the more important mechanism, over crystal lattice defects. However, it has to be mentioned that the hysteresis data after heating may mask the annealing of lattice defects, due to the formation of magnetite from hematite, and therefore its contribution might be underestimated.

Cation-substituted (Ti, Mg, and Al) magnetite is present in both impact melt units, and was even injected into the granitoid basement where it occurs as small, skeletal grains (e.g., Fig. 2.4j). These grains are not fractured, show no signs of shock deformation but a large range of compositions (Table 2.1, Fig. 2.5). Both upper and lower impact melt units show similar compositions, denoting a granitoid and dolerite mixed melt source, however different quenching histories are reported (De Graaff et al., 2021). Unit 3A likely cooled at the fastest rates, especially in its upper portions, where water re-entry into the crater would have caused very fast quenching. Here, the newly formed cation-substituted magnetite is enriched in Mg- and Al-, whereas in the lower UIM (Unit 3B) and LIM, Ti-substitution dominates. As for both impact units the whole-rock major elements are similar (De Graaff et al., 2021), the source of the Mg- and Al-substituted magnetite may be different. Ebel and Grossman (2005) reported unaltered grains of magnesioferrite spinel from spherules occurring at the K-T stratigraphic boundary worldwide, and suggested from thermodynamic modelling that this phase has formed due to sequential condensation of solids from the plume of vaporized carbonate and anhydrite target rocks. Therefore, the Mg- and Al-substituted magnetite grains may be a result of some admixing of carbonate melts in the uppermost UIM unit.

The green schlieren in Unit 2C and Unit 3A shows Mg-dominated magnetite compositions ($Fe_{2.69}Mg_{0.19}Al_{0.07}Cr_{0.03}Ti_{0.01}O_4$), with higher Curie temperatures in the heating curve than in the cooling curve, and no Verwey transition (T_v; Fig. 2.7, Table 2.3). The irreversibility of T_c in the heating and cooling curve can be expressed by ΔT_c ($\Delta T_c = T_{c\text{-Heating}} - T_{c\text{-Cooling}}$) and varies between 17°C and 106°C. Such an irreversibility can be either explained by cation ordering processes during the heating and cooling experiments (e.g., Harrison and Putnis, 1998, 1999; Lattard et al., 2006; Bowles et al., 2013), by vacancy-enhanced nanoscale chemical clustering in the octahedral sublattice (Bowles et al., 2019), or by maghemitization (e.g., Bowles et al., 2019; Lied et al., 2020; Zhang et al., 2021). At magmatic temperatures the cation distribution in the inverse spinel structure is highly disordered and the closure temperature defines the temperature at which reordering rates become so slow that a cation ordering state is frozen (Jackson and Bowles, 2014).

Positive ΔT_cs are reported for pyroclastic deposits by Lied et al. (2020), Bowles et al. (2013) and Dudzisz et al., (2022). It occurs in cation substituted magnetite that is quenched very rapidly from magmatic temperatures through the closure temperature. If the temperature after deposition remains constant for a certain time interval, the cation distribution evolves towards equilibrium for this specific temperature, increasing the degree of order and T_c (Jackson and Bowles, 2014). Therefore, T_c in cation-substituted magnetite with an inverse spinel structure depends on the degree of ordering, and is lower for a fully disordered arrangement, compared to a perfectly ordered one (Harrison and Putnis, 1999). The effect of different cation substitutions in natural cation-substituted magnetite is not yet investigated in detail, but studies from Bowles et al. (2013, 2018, 2019) and Lied et al. (2020) point to significant differences in ΔT_c, especially if Mg and Al are involved.

Interestingly, in samples with lower cation substitution but with a higher Mg concentration (compare sample 721 with 738 in Tables 2.1 and 2.3) T_v is suppressed, suggesting that Mg substitution has a stronger suppressing effect on T_v than Ti substitution. Below T_v, the relatively free electron hopping between Fe^{2+} and Fe^{3+} in the octahedral site halts, leading to a sharp increase in resistivity (up to 3 orders of magnitude, e.g., Biało et al., 2019). Since Mg occupies the position of Fe^{2+} in the octahedral sites of the inverse spinel structure (see e.g., Bowles et al., 2019 and references therein), increase in Mg leads to a reduction of the total amount of Fe^{2+}, and increases the Fe^{3+}/Fe^{2+} ratio. An increase of this ratio has been associated to an increase in resistivity at $T > T_v$ (e.g., Mi et al., 2009), leading to a lower resistivity difference below and above T_v, and thus suppressing the intensity of the transition.

The cation-substituted magnetite from the impact melt acquired a TRM with the expected directions for Chron 29r at the time of the impact (Dec/Inc= 180°/-40°, Fig. 2.11c) which agrees with earlier studies (e.g., Gulick et al., 2019). These are the only samples in our study with a Q-ratio close to or above 1, which indicates the magnetization is dominated mostly by the NRM, suggesting these directions are the only reliable paleomagnetic directions in our study.

A third type of magnetite is represented by very small (<5µm) non-shocked and non-fractured grains (Table 2.1, Fig. 2.4e). These grains are found throughout the core in all lithological units, particularly in regions with strong hydrothermal alteration or in basement fractures, and often in assemblage with sulfides such as pyrite or chalcopyrite, as well as hematite. This magnetite does not constitute a main magnetic carrier in any of our samples, with the potential exception of the topmost two samples from Unit 2A suevites, where we measured sections without basement clasts. We consider this magnetite to be secondary and associated with the hydrothermal percolation. Because its abundance is low, it is the least important magnetite type, as its contribution to the samples' magnetic properties is subordinate.

2.6.2.Effect of the post-impact hydrothermal system on shocked magnetite

Despite the fact that hydrothermally formed magnetite may only be of magnetic significance in some sections of the upper suevite layers, post-impact hydrothermal alteration is prevalent throughout the whole peak-ring. Higher temperature (>250°C) secondary minerals tend to form in the shocked crystalline basement, while low-temperature (<250°C) hydrothermal minerals are concentrated in the upper 130 m impactite lithologies (Kring et al., 2020), where vertical alteration channels are interpreted as indicators of post-impact hydrothermal venting. Paleomagnetic data has been interpreted by some authors as to suggest a long-lived hydrothermal system that extends from the reverse Chron 29r to a younger, normal polarity interval (Kring et al., 2020). On the other hand, other authors argue that large scattering of positive and negative inclinations suggest instead these layers retain their primary magnetization post-depositional NRM (i.e., temperatures were not high enough to induce remagnetization, Gulick et al., 2019). These interpretations may be reconciled, as inhomogeneity in the suevite units may lead to some regions having their NRM carried by newly formed hydrothermal magnetite or local chemical remanent magnetization (CRM) acquisition. CRM directions can be imparted at any temperature, and could potentially have Chron 29r or younger directions (see great circle interpretations, Fig. 2.11c). Other sections may be dominated by basement clast magnetite that maintain their primary NRM directions (likely scattered during the cratering process), in the absence of high-enough temperatures to "reset" the NRM vector (see rejected grey dot in Fig. 2.11c, "Suevite+UIM" panel). We are hesitant however in making definitive claims regarding these directions, as we consider our paleomagnetic data obtained from Unit 2 to be unreliable (Q-ratios <<1, Fig. 2.11a). The basement magnetite was also not remagnetized by the hydrothermal system, as remagnetization would have homogenized the NRM directions. This is not the case as we observe scattered "Basement" directions (Fig. 2.11c, "Basement" panel, and Appendix A.5).

After the impact, the cooling of the large impact melt pool in the central basin of the crater created a long-lived hydrothermal system (up to 2 Myr, Kring et al., 2020), with neutral pH conditions and starting temperatures of 350 to 450°C. The fluids are expected to have evolved into a more reducing composition with time, but temperatures would have remained relatively high (Kring et al., 2020). These are the fluids which formed the hydrothermal magnetite previously described.

In close proximity between melt and basement (e.g., samples 995, 999, and 1224D; Fig. 2.8), we observed a hump between 200 and 400°C in κ-T curves that either indicates metastable maghemite (Zhang et al., 2020, 2021) or thermal relaxation due to nm-sized magnetite particles of different diameter (Zhao and Liu, 2010). In natural samples we encounter this hump in regions of higher porosity, such as the ultra-cataclasite at the boundary between the melt and the granitoid, and in the 130 m thick suevite and impact melt layer. These are samples where we would expect hematite to magnetite transformation due to the reducing fluids, and formation of new magnetite with a mottled texture, similar to what we have observed in our transformation experiments (Fig. 2.10b, 2.10c). While bulk-rock hysteresis results are inconclusive regarding thermal annealing (Fig. 2.6b), our IRM component analysis and FORC diagrams show a consistent increase in coercivities after thermal annealing in the granitoid (Fig. 2.6c and 2.10e). We suggest that this increase in coercivity is due to magnetic exchange coupling interaction between newly formed SD-SP magnetite particles formed during the transformation of hematite to magnetite.

In the granitoid basement, post-impact hydrothermal alteration of magnetite is not as severe (A40 ranging from 3 to 90%) as in the impact rock Units 2 and 3. Only locally a stronger alteration of magnetite is indicated by A40 >100% (Table 2.3), or in the proximity of the LIM dykes (see sample 999 G3, Fig. 2.9, Table 2.3). Magnetite transformation into hematite (martitization) is a widespread phenomenon in crustal rocks (e.g., Lagoeiro, 1998), and is a general phenomenon in hydrothermally altered magnetite-bearing granites. The alteration index can be used to detect hydrothermally-induced oxidation of magnetite into hematite as previously mentioned (see section 2.5.3.5, also e.g. Just et al., 2004; Just and Kontny, 2011). Feignon et al. (2021) described a hydrothermal metasomatic event that occurred in the Permian approx. 50 Myr after the Variscan emplacement of the granite in the Maya block, which has likely caused this martitization before the impact.

Ishihara (1979) and Ishihara et al., (2000) have investigated the magnetic susceptibility of Mesozoic and Cenozoic batholiths of Japan and Peru and suggested a value of 3 x 10^{-3} SI (300 x 10^{-5} SI units) units as the boundary dividing magnetite- and ilmenite-series granitoids. In the shocked granitoid basement of the Chicxulub peak ring magnetic susceptibility values are ranging between 50x10^{-5} and 300x10^{-5}SI and therefore rather would belong to the ilmenite instead to the magnetite-series. This is, however, inconsistent with our observations, as the shocked granitoid shows large, albeit fractured, magnetite grains. From petrographic observation one would expect significantly higher MS, as the rock clearly belongs to the magnetite-series granitoids. Therefore, we should compare our results with an analogous magnetite-bearing granite, for which a hydrothermal breakdown from magnetite to hematite was investigated in detail (Just et al., 2004; Just and Kontny, 2011). Two different stages of alteration were described in the Carboniferous Soultz-sous-Forêts ("Soultz") granite in France: Stage I comprises a widespread, syn-emplacement alteration, of which the main effect is a localized formation of hematite. κ-T curves show a clear irreversibility of pure magnetite and positive alteration indexes with the new formation of a ferrimagnetic phase during the measurement in an argon atmosphere. Stage II occurs in fault zones of altered and fresh granite and is characterized by a nearly complete breakdown of magnetite to hematite. This transformation is very prominently seen in MS, which significantly decreases in the fault zones (see Fig. 2.2 in Just and Kontny, 2011). This, is clearly distinct from the granitoid basement of the Chicxulub peak-ring, where magnetite shows a microscopically visible transformation into hematite, but not a complete breakdown (Fig. 2.4b). MS values range between $50x10^{-5}$ and $300x10^{-5}$ SI, which is significantly lower than those of the fresh and stage I granite from Soultz, showing MS values in the order of $1000\text{-}3000x10^{-5}$SI, one order of magnitude higher than in the peak ring granitoid rocks. Our peak ring samples are more in line with the susceptibilities from the stage II Soultz granite ($\sim 50\text{-}150x10^{-5}$SI), however we do not see comparable levels of oxidation in the peak-ring material. Therefore, we have to assume that either the amount of magnetite during original crystallization was significantly lower, or a shock effect must be responsible for the significantly lower MS. Magnetite grains of several hundred μm in size (Fig. 2.4a, 2.4b), even if partially oxidized to hematite, would constitute well above > 0.1 wt% of the basement composition, which would still result in magnetic susceptibility values larger than 300×10^{-5} SI units (see e.g., Fig. 2.1 in Tarling and Hrouda, 1993, where a MS range of $50\text{-}300x10^{-5}$ SI units require magnetite to comprise only 0.01 to 0.1 wt% of the basement). Even relatively low shock pressures (3-5 GPa) can decrease MS by approximately 90% (Reznik et al., 2016; Kontny and Grothaus, 2017). The peak-ring lithologies experienced shock pressures in the order of 10 to 35 GPa (Morgan et al., 2017; Ferrière et al., 2017), and clearly were affected by a reduction of MS. A 90% reduction would imply original values of up to $\sim 1000x10^{-5}$SI (not considering variation due to an inhomogeneous distribution of magnetite in the granite). This is in the range of the fresh Soultz granite in the Upper Rhine Graben, and other ferrimagnetic Carboniferous granites from the Variscides in Europe and elsewhere (e.g., Henry, 1988; Bouchez et al., 1995, 1997; Ishihara et al., 1979, 2000; Henry et al., 2004).

2.6.3. Implications for magnetic sources of the Chicxulub impact structures

Magnetic signatures of complex terrestrial impact craters vary greatly with composition of target rock, impact-related magnetization, and effect of crater fill and post-impact sedimentation (Pilkington and Grieve, 1992). For the Chicxulub impact crater three major magnetic sources were reported for the concentric magnetic anomaly rings (Fig. 2.1b; Rebolledo-Vieyra et al., 2010): (1) melt rock units, (2) suevite-like breccia, and (3) central uplift with highly magnetized breccia sequences and melt sheets. It is also well known that strong positive magnetic anomalies occur when basement rocks are involved (Pilkington and Grieve, 1992). On the other hand, it is well documented that shock causes a reduction of MS and NRM (e.g., Acuña et al., 1999; Plado et al., 1999; Pilkington and Hildebrand, 2000; Ugalde et al., 2005; Bezaeva et al., 2016).

The M0077A core was drilled into a negative magnetic anomaly within the peak-ring of the Chicxulub impact crater. Rebolledo-Vieyra et al. (2010) has related the negative magnetic anomaly pattern to a system of regional vertical faults and the IODP-ICDP Expedition 364 drill core M0077A has revealed that these structures consist of strongly fractured and faulted granitoid rocks (Morgan et al., 2017; Riller et al., 2018). The shock has demagnetized, or at least reduced NRM and likely randomized its directions in the basement granitoid, while NRM is stronger in the non-shocked cation-substituted magnetite formed in the impact melts. The Q-ratios reflect this, but even where the Q-ratios are above 1 (in the LIM melt rock), they are not higher than 3. This observation suggests that the negative magnetic anomalies in the peak ring are dominated by the reduced induced magnetization component of the uplifted and shocked granitoid basement. In the peak-ring, the influence of the impact melts with higher magnetization is negligible, due to their minor thickness (~26 m), when compared to the uplifted basement with a thickness of at least 550 m (Fig. 2.2). The impact melt is likely responsible for the positive magnetic anomaly regions, such as the central basin of the crater (e.g., Rebolledo-Vieyra et al., 2010; Urrutia Fucugauchi et al., 2011), where it likely shows a similar NRM intensity and directions as the peak-ring layer, however no drilling to date has confirmed this assumption.

2.7. Conclusions

The IODP-ICDP Expedition 364 drill core M0077A revealed that the Chicxulub peak ring consists of uplifted granitoid basement rocks overlain by a 130 m thick impact melt and suevite layer. Pre- and post-impact hydrothermal systems affected this basement with maximum temperatures up to 450ºC. We investigated the rock magnetic properties and magnetic mineralogy in order to study magnetic mineral transformation during pre-, syn- and post-impact processes.

The shock from the impact induced lattice defects and fractures in magnetite, which are responsible for demagnetization and a substantial decrease in magnetic susceptibility. Our results suggest that decreased MS and NRM in shocked basement magnetite are responsible for the negative magnetic anomaly in the peak-ring. In the melt rocks, cation substituted magnetite carries the magnetization, with higher MS values and NRM intensities than in the basement. This magnetite acquired a TRM with the expected directions for Chron 29r at the time of the impact (Dec/Inc = 180°/-40°), in agreement with earlier studies (Gulick et al., 2019). The post-impact hydrothermal overprint in the shocked basement magnetite is negligible, from a magnetic properties point of view, and did not significantly influence the magnetic anomaly pattern.

The majority of the basement granitoid shows varying degrees of pre-impact oxidation of magnetite. In the basement, the post-impact hydrothermal activity does not visibly contribute to changes in the chemical properties of magnetite. Locally, we observed a transformation of hematite to magnetite due to the reducing character of the hydrothermal fluids, or due to high temperatures near the impact melt. This transformation creates new, small magnetic grains within the original large grains. The high surface area is expected to be more prone to oxidation due to seawater percolation at any point after the hydrothermal system ceased. However, we found no clear indication for maghemitization.

The temperature onset of a possible hematite to magnetite transformation is found in κ-T curves above 580°C, substantially higher than the upper bound of the hydrothermal system’s temperature (~450ºC). Our experiments further suggest that the hydrothermal system also does not reach high enough temperatures to anneal the magnetite crystal lattice defects, which we suggest to occur between 540ºC and 560ºC. Therefore, high temperature overprints in the peak-ring basement are limited to areas of proximity and in contact with the impact melt rocks.

3. Restoration and Transformation: The Response of Shocked and Oxidized Magnetite to Temperature

3.1. Abstract

Large impact craters on Earth are associated with prominent magnetic anomalies, residing in magnetite of the shocked target rocks and impactites. Shock experiments on magnetite suggest that up to 90% of magnetic susceptibility is lost at pressures >5 GPa, but can be partially restored by post-shock thermal annealing. The magnetic property changes are caused by shock induced grain size reduction, as well as domain wall-pinning at crystal lattice defects. A recent study of granitoids from the Chicxulub crater found that annealing may occur naturally, but can also be overprinted by high-temperature hematite-to-magnetite transformation in non-oxidizing environments. In this study, we isolate the effect annealing and hematite-to-magnetite transformation using the evolution of hysteresis, isothermal remanent magnetization components and first order reversal curve (FORC) diagrams at different high-temperature steps. We used a laboratory-shocked magnetite-quartz ore, a non-shocked naturally oxidized granite, and a naturally shocked and oxidized granite. Our findings suggest that annealing of shock-induced lattice defects partially restores some pre-shock magnetic behavior and causes an apparent average bulk-sample domain state increase. Hematite-to-magnetite transformation creates new fine-grained magnetite that strongly overprints the original signal, and decreases the average bulk-sample domain state. Where annealing and hematite-to-magnetite transformation both occur, the new magnetite masks the annealing-induced property restoration and apparent domain state modification in the shocked magnetite. As magnetite oxidation is a ubiquitous process in surface rocks, these findings are fundamental to understand hematite-to-magnetite transformation as a potential overprint mechanism, and could have broad implications for paleomagnetic interpretations.

3.2. Introduction

Large impact craters on Earth are associated with prominent magnetic anomalies, carried by magnetite in shocked and impact-related rocks (e.g., Hart et al., 1995; Gattacceca et al., 2007; Quesnel et al., 2013; Gilder et al., 2018). In fact, the famous Chicxulub impact crater, associated with the K-Pg boundary and a mass extinction linked to a severe global climate change event (e.g., Hildebrand et al., 1991; Sharpton et al., 1992; Smit, 1999; Schulte et al., 2010), was discovered by Penfield and Camargo (1981) through its aeromagnetic and gravity anomaly. Magnetic anomalies are a result of the displacement of the magnetized rocks in the impact cratering process, decomposition of the existing rock magnetization, and formation of new magnetic phases in impactites (e.g., Pilkington and Grieve, 1992, Hart et al., 1995, Plado et al., 1999). Although magnetic anomalies in impact craters are well documented, the effect of shock on the magnetic behavior of magnetite has only been studied in detail in the last decade (e.g. Carporzen and Gilder, 2010; Louzada et al., 2010; Tikoo et al., 2015; Reznik et al., 2016). The shockwave released by an impact causes a nearly instantaneous compression and decompression of the target, and a loss of up to two-thirds of the magnetic moment (e.g., Gilder et al., 2006) and up to 90% of the magnetic susceptibility (Reznik et al., 2016), if magnetite is responsible for the magnetization. Loss of magnetic susceptibility in particular results from brittle fracturing and fragmentation of large grains, and from plastic deformation such as lattice defects or dislocations, that lead to a deformed and strained crystal lattice (Reznik et al., 2016; Kontny et al., 2018).

The magnetic behavior of magnetite is closely related to its grain size and crystal structure. The smallest magnetite grains (<~30 nm, Dunlop, 1973) are superparamagnetic (SP), and are incapable of carrying a NRM. Larger grains have the ability to record a NRM (given by M_{rs}/M_s, where M_s is the saturation magnetization, and M_{rs} is the saturation remanent magnetization), but this ability is also subordinate to grain size and shape. Small grains (<~80 nm for rounded, and <~300 nm for elongated shapes, Newell and Merrill, 1999; Witt et al., 2005) are generally uniformly magnetized in a single domain (SD) state, and are resistant to changes in magnetization (that is, they have a high coercivity, B_c). With increasing grain size, a single domain becomes unstable and collapses into a circular shape, or "vortex" (V, commonly referred to in literature as pseudo-single domain, PSD; e.g., Roberts et al., 2000, 2017), comprising either a single vortex (SV, see e.g., Pike and Fernandez, 1999) or multiple vortexes (MV), and its coercivity depends on the size, number and shape of the vortexes (Lascu et al., 2018).

For even larger grains, multiple vortexes resolve into multiple discrete domains (MD), separated by narrow so-called domain walls which migrate relatively freely within the grain in response to external magnetic fields. The transition from PSD/V state to MD state has been described to occur in magnetite particles around ~10 µm (Nagy et al., 2019). MD grains have generally low coercivity, due to the relative ease of migration of the domain walls. However, the presence of physical obstacles such as shock-induced fissures and fractures, lattice defects, or dislocation networks, will often "pin" the walls along them, in a process of "domain-wall pinning" (e.g., Moskowitz, 1993; Özdemir and Dunlop, 1997; Lindquist et al., 2015). If a wall becomes pinned it can still migrate, but requires a higher field intensity to do so (manifested as increased coercivity), and will "jump" from one dislocation/defect to the next, in a so called "Barkhausen jump" (Barkhausen, 1919). MD is the most common domain state in natural magnetite, including those from large impact craters, but the associated shock-induced brittle and plastic deformation fundamentally alters these grains, leading to magnetic behaviours more typical of the PSD/V state such as lower magnetic susceptibility, higher coercivity and higher M_{rs}/M_s (Reznik et al., 2016, Kontny et al., 2018).

While brittle fracturing and fragmentation irreversibly reduces grain size, the lattice defects are plastic deformation features that can be annealed through a thermal treatment that reduces wall-pinning (e.g., Pike et al. 2001b). Annealing of shocked magnetite leads to a recovery of magnetic susceptibility and a striking irreversibility of temperature dependent magnetic susceptibility (κ-T curves), as well as a decrease in coercivity and M_{rs}/M_s. These changes in magnetic properties lead to an apparent increase in the domain state after heating, towards a more MD-like behavior (Kontny et al., 2018). A recent study on the effects of natural shock and post-impact high temperature exposure on the magnetic behavior of granitoids from the Chicxulub peak ring, reports that defect annealing can occur naturally (Mendes et al., 2023). However, the effects of annealing are often overprinted by the transformation of secondary hematite into newly formed, fine and mottled textured magnetite (Mendes et al., 2023). The κ-T curves of both phenomena show a similar irreversible behavior (Fig. 3.1) with an onset of annealing and/or chemical transformation at ~540°C (Mendes et al., 2023). Standard magnetic methods such as bulk-sample hysteresis or isothermal remanent magnetization component analysis were not sensitive enough to separate magnetic property changes caused by annealing and hematite-to-magnetite (hem-mt) transformations (Mendes et al., 2023). These effects likely overlap in natural impact craters as oxidized magnetite is not only described from Chicxulub (Mendes et al., 2023), but also in Chesapeake Bay (US) (Mang and Kontny, 2013), Vredefort (S-Africa) (Carporzen et al., 2006), Zhamanshin Astrobleme (Kazakhstan) (Sergienko et al., 2021), Manicouagan (Canada) (Morris et al., 1995), Bosumtwi (Ghana) (Kontny et al., 2007), and the Gusev impact crater on Mars (Morris et al., 2006).

In this study, we used hysteresis, isothermal remanent magnetization components analysis and first order reversal curve (FORC) diagrams at different high-temperature steps to investigate systematically each process and their interactions. Specifically, we aim to (1) isolate physical (shock) and chemical (hem-mt transformation) effects on magnetite, (2) observe and characterize the magnetic properties and (apparent or real) domain state and associated magnetic behavior evolution with temperature in shocked and oxidized samples, (3) define an approximate temperature threshold for annealing and hem-mt transformation, (4) determine the dominant phenomenon in complex natural samples such as the shocked Chicxulub basement and its implications for application of magnetic methods in crustal impact structures, and (5) explore the implications of hem-mt transformation for broader rock-magnetic studies, outside of impact research.

3.3. Samples and methods

3.3.1. Samples

We selected a total of nine samples for this study: seven magnetite ore samples shocked at increasing pressures (from a non-shocked "Initial" sample, to 1, 3, 5, 10, 20 and 30 GPa, as the samples will be referred to as, henceforth), and two natural magnetite samples from the non-shocked Soultz-sous-Forêts granite (France) ("Soultz", or Sample 2533 and 2476), and from the Chicxulub impact crater peak ring granitoid basement (Mexico) ("Chicxulub", or sample 1100).

The magnetite ore used for shock experiments originates from a metamorphosed quartz-magnetite banded iron ore of the Sydvaranger mine (Norway), with alternating polycrystalline quartz layers intergrown with cubic magnetite crystals, and bands of polycrystalline magnetite. This magnetite has a sharp Verwey transition (Tv) at -152°C ± 2°C and a Curie temperature (Tc) at 578°C ± 2°C (Fig. 3.1a). The shocked magnetite ores are from the same shock experiment batches used in the study of Reznik et al. (2016) and Kontny et al. (2018), and none of them contained hematite. The shock experiments were originally commissioned by Reznik et al. (2016) at the Ernst Mach institute (Freiburg, Germany), using a flyer plate that impacts an ARMCO iron container with a disk-shaped target accelerated either by an air gun (1 to 5 GPa) or high explosives (10 to 30 GPa) at a given velocity (see Reznik et al., 2016; and for details on the shock reverberation setup see Müller and Hornemann, 1969, and Fritz et al., 2011). After applying shock pressures of 5 GPa and above, the shocked samples show a mass susceptibility decrease of up to 90% (see Figure 11b in Reznik et al., 2016), and an increase of Tv to -144°C while Tc remains relatively stable. κ-T curves in the shocked magnetite ore are irreversible, and after heating to 700°C the originally strong Hopkinson peak (Hopkinson, 1889) decreased (Fig. 3.1b).

Non-shocked granite samples (2533 and 2476) with magnetite oxidized to hematite (stage I alteration in Just and Kontny, 2012) comes from the EPS-1 drill core of the Soultz-sous-Forêts Variscan granite pluton (France). The Soultz sample comprises large oxidized magnetite grains (Fig. 3.1c, where sample 2540 represents stage I alteration, after Just and Kontny, 2012), has a magnetic susceptibility of ~10-3 SI, shows a Tv of -150 ± 2°C and a Tc of 573 ± 2°C. κ-T curves are irreversible, and after heating to 700°C a much higher magnetic susceptibility indicates the transformation of hematite into magnetite (Fig. 3.1d). Sample 2476, with similar properties, was used in this study for before-after heating experiments, to get an idea of the natural heterogeneity of granite oxidation.

The naturally shocked granite from the peak-ring of the Chicxulub impact crater was obtained from borehole M0077A, drilled during the joint International Ocean Drilling Program and International Continental Scientific Drilling Program Expedition 364 (Morgan et al., 2017). Magnetite experienced pre-impact oxidation to hematite (Fig. 3.1e; Mendes et al., 2023), and was subjected to natural shock pressures in the ~16 to 18 GPa range (as determined by planar deformation features in quartz grains), with slight shock attenuation with increased depth (Feignon et al., 2020). The magnetite is stoichiometric, and the granite displays conspicuously low magnetic susceptibility (~50x10-6 SI), resulting from shock demagnetization (Mendes et al., 2023). Sample 1100, which has been used for this study, shows a Tv of -156 ± 2°C and a Tc of 572 ± 2°C, and the κ-T curve displays a significant increase in magnetic susceptibility and a slight "hump" after heating (Fig. 3.1f).

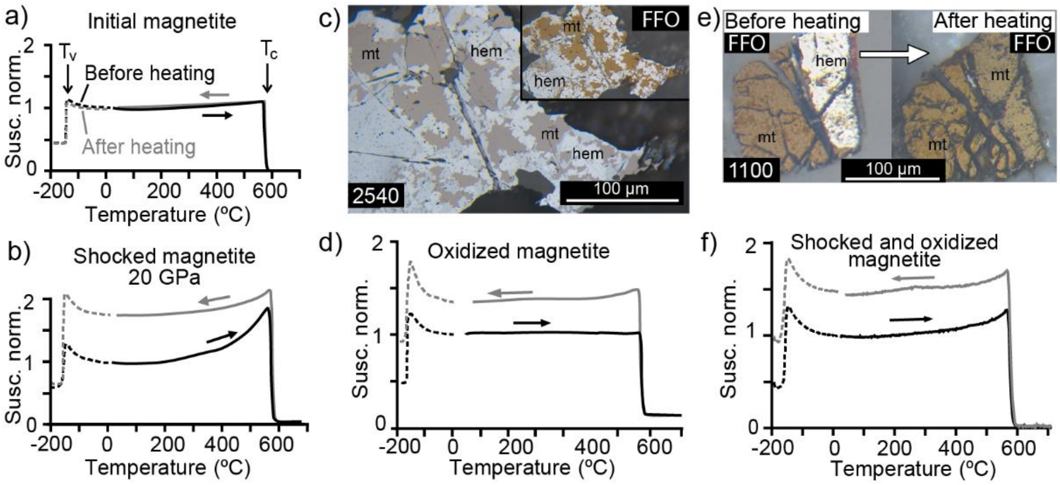

Figure 3.1. Previous literature data on the response of our samples' temperature treatment. a) Temperature-dependent magnetic susceptibility (Susc. norm. versus Temperature) for Initial magnetite ore (after Kontny et al., 2018); b) Temperature-dependent magnetic susceptibility for magnetite ore shocked at 20 GPa, note the peaks at the Verwey transition and Curie temperature (after Kontny et al., 2018); c) Strong transformation of magnetite to hematite in sample representative of the Stage-I alteration of the Soultz-sous-Forêts granite, with and without ferrofluid (FFO) for clear contrast (after Just and Kontny, 2012); d) Normalized temperature dependent susceptibility curve for sample 2533, which is similar oxidized as sample 2540 in c) (Just and Kontny, 2012); e) Hematite-to-magnetite transformation before (left) and after (right) temperature dependent susceptibility measurement to 700°C in sample 1100 from the Chicxulub peak ring, with ferrofluid (FFO) for clear contrast (after Mendes et al., 2023); f) Normalized MS-T curve for the sample represented in a) is taken from Mendes et al. (2023).

Our sample selection for the FORC measurements allows us to isolate the effects of shock and oxidation, if measured stepwise up to high temperatures. The initial magnetite ore is an ideal standard, with a reversible κ-T curve and behavior typical of MD magnetite that remains stable with temperature. The remaining magnetite ore samples have only been exposed to increasing shock and contain no evidence of chemical alteration, which provides insights into domain state evolution with increasing shock and annealing. The natural oxidized magnetite from the Soultz granite (2533) allows us to constrain the effects of the hem-mt transformation with temperature in the absence of shock deformation. Finally, the naturally shocked and oxidized magnetite from the Chicxulub (1100) peak ring granitoid provides sample where both shock-annealing and oxidation-transformation relationships can be investigated.

3.3.2. Sample preparation

We used small magnetite shards from the shocked ore samples Initial, 3 and 5 GPa, and powdered material for the remaining shocked magnetite ore samples (1, 10, 20 and 30 GPa), as they were completely pulverized during the shock experiment. To isolate magnetite in the natural granite samples, we gently crushed the rock and made a magnetic pre-separation using a strong hand-held magnet and a second visual pre-selection of the magnetic grains, to avoid other minerals such as micas. We prepared three additional samples from the granites (1100, 2533 and 2476) for before-after (BA) experiments (see section 2.3), referred to as "[Sample name] BA", henceforth. Sample mass was measured, and from the powdered shocked magnetite ore and magnetite grains from the granites (which are too small to handle) we created sample-pellets using a high-temperature porcelain-like two-part cement concrete from Omega Engineering, to maintain sample integrity throughout the experiments. Although this cement does not contain iron according to the manufacturer information, traces of iron in this batch cannot be ruled out. Cement impurities or potential unexpected mineral reactions were taken into consideration in the interpretation of the results. The shard samples were placed inside size 4 gel caps, and were immobilized with non-reactive fiber flax wool. Whenever these samples broke or needed extra immobilization, an alumina-silica cement (ZIRCAR Ceramics) was used. The sample pellets were prepared according to the holder size and did not require further immobilization.

3.3.3. Methods

All experiments were performed at the Institute for Rock Magnetism (IRM, Minneapolis, USA). We used a LakeShore 8600 Series Vibrating Sample Magnetometer (VSM) instrument with a maximum saturation field of 1 T to measure hysteresis loops, direct current demagnetization (DCD), and FORC acquisition (Pike et al., 1999; Roberts et al., 2000) in sequence for each mass normalized sample, at each temperature step. Samples were heated stepwise using an ASC furnace with a controlled argon (Ar purity of ~99.998%) atmosphere chamber. Each step began with a flooding of the chamber at a constant argon flow for 10 minutes, which was then switched to a slower constant flow (~160 mL/min). For the magnetite ore samples, we used 5 steps, at room temperature (RT), 540, 560, 580 and 700°C, while for the natural samples we added the 600 and 650°C steps ("Full-Run" or "FR" experiments). The threshold value of 540°C was used according to the estimated onset of annealing and/or hem-mt transformation reported by Mendes et al. (2023). In the natural samples we performed additional BA experiments, which consisted of a single temperature step up to 700°C. For FR experiments, the desired temperature was held for 15 minutes, before returning to RT by flowing air around the isolated chamber. For the BA experiments, the maximum temperature was held for one hour, to obtain information about the time-dependence of hem-mt transformation. Sample 1100 BA was exposed to a second 700°C temperature step experiment (held for 15 minutes) to investigate the stability of the newly formed phase.

Bulk-sample hysteresis parameters were determined from hysteresis loops and DCD curves. Saturation magnetization (M_s), saturation remanent magnetization (M_{rs}), and coercivity (B_c) were estimated from hysteresis single-loop measurements, and coercivity of remanence (B_{cr}) was determined from the DCD curves. The DCD curves were also used for IRM component analysis (Robertson and France, 1994), and were processed using the online software MAX UnMix (Maxbauer et al., 2016). IRM component modeling allows us to isolate and track the evolution of the magnetite and hematite components individually with temperature. By isolating the magnetite and hematite contributions in the natural granite samples, it is possible to compare the magnetite properties in the natural and shocked magnetite ore samples. This is not possible to do with bulk-sample parameters, which include also the hematite contribution without distinction. We applied a fixed number of magnetite components (2) to fit each sample, which is required to compensate for a natural skewness and temperature relaxation in natural magnetic particle systems (e.g. Heslop et al., 2004). The component with the highest signal contribution is what we consider our "main" magnetite component. We determined the mean coercivity of remanence of this main magnetite component at each temperature step for all samples (B_h after Maxbauer et al., 2016). We refer to B_h simply as the "coercivity" of the magnetite fraction, and for variations or trends in both bulk (B_c, B_{cr}) or component (B_h) coercivity, we use "coercivity (*s.l.*)" for better readability.

A total of 151 FORCs were collected per heating step, using a saturation field (B_{sat}) of 500 mT. FORC diagrams were processed using the FORCinel software, version 3.08 (Harrison and Feinberg, 2008). The FORC diagrams have a standard range of B_u field from -100 to 80 mT, and a maximum B_c field of 120 mT. Samples 3 and 5 GPa were measured with a lower B_c field (max = 100 mT) in the initial room temperature (RT) measurements. For consistency, we rescaled these diagrams despite there being no data past B_c = 100 mT. Sample 5 GPa broke into two shards after the second step, causing difficulties stabilizing the sample in the holders, so we removed one of the shards and applied a different mass normalization for these steps. We applied a standard smoothing factor of 4 to all diagrams of the magnetite ore, and a smoothing factor of 6 to the natural samples. One exception is the first measurement for sample 1100, which required a smoothing factor of 10.

To help visualize the changes in the FORC signals, we investigated the variations in the irreversible component (ΔM_{irr}, the magnitude of switching events between reversal fields (B_r)) and reversible ridge (the contribution of particles with coercivity = 0 mT, given by the vertical feature density profile along $B_c = 0$, after Pike, 2003), at RT and after heating to 700°C. We also calculated the horizontal FORC feature density distribution (along $B_u = 0$) at each temperature step, to help visualize the evolution in coercivity of the central peak lobe. Furthermore, we quantified domain state changes with temperature using a procedure introduced by Reznik et al. (2016). First, we applied a binarization algorithm incorporated into the ImageJ software (Fig. 3.2, left and center; Rasband, 1997), and determined the ratio [%] of black pixels within the area within a threshold that constrains all positive FORC contributions above the 0.05 significance level (Fig. 3.2, right; Heslop and Roberts, 2012). The defined area is referred to as “SD-MD signal area” (Reznik et al., 2016), and ignores small intensity or coercivity variations while being representative of global FORC signal changes. Further details on the method can be found in the legend of Figure 3.2. A similar outcome can be achieved by tracking the variation of the area within the FORC signal-to-noise envelope at each step, which is readily calculated and displayed by FORCinel, however we decided to use the SD-MD area procedure for a direct comparison with the results presented in Reznik et al. (2016).

In Appendix B.1 the step-by-step procedure for estimating the SD-MD signal area [%] and further IRM parameters are described. See Appendix B.2 for a description of the remaining Supplemental files (2-4; Mendes and Kontny [Dataset], 2023).

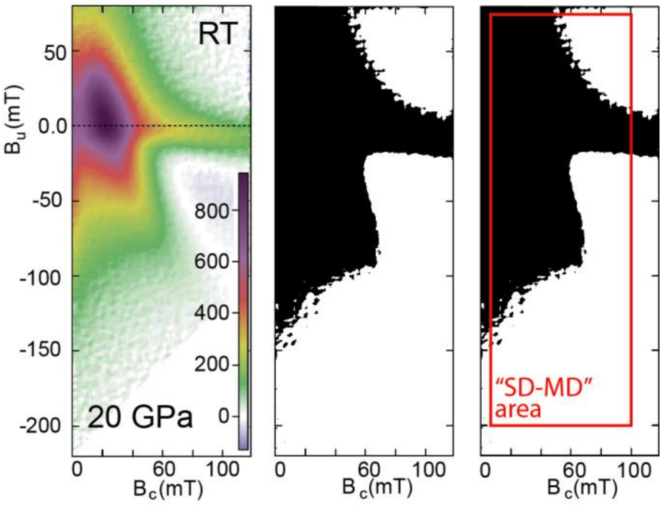

Figure 3.2. “SD-MD” area calculation scheme, as described by Reznik et al. (2016), using the ImageJ software (Rasband, 1997). We start by importing the original diagram (left), and create a binary black-and-white (BW) version of the diagram (center). Once converted to BW, we select the area defined within the thresholds: $-200 < $ Bu (mT) < 65; and $5 <$ Bc(mT) < 100 thresholds (right). This area constrains all positive FORC contributions above the 0.05 significance level (Heslop and Roberts, 2012), and are limited on the bottom and right-hand side to fit the truncated 3 and 5 GPa RT diagrams, as keeping the total diagram area (in pixels) constant, which allows comparisons between samples. The SD-MD area is calculated by the ratio (in percentage) of area covered by the black pixels to the total figure area. Changes in global FORC features with temperature can thus be quantified and compared directly, ignoring subtle intensity or coercivity variations. A detailed step-by-step description is given in Supplemental file 1; all BW and original FORC diagrams are given in Supplemental file 2, together with a calculation sheet for the ratios.

3.4. Results

3.4.1. Room temperature

RT FORC diagrams for the non-shocked Initial magnetite ore (Fig. 3.3a) and Soultz 2533 (Fig. 3.3b) are typical of MD grains, characterized by a low-coercivity vertical elongation of the FORC signal along the B_c (mT) = 0 axis, and a weak high-coercivity horizontal tail along B_u (mT) = 0. According to IRM component analysis, the Initial magnetite ore shows a coercivity of 13.5 mT (Table 3.1, RT; Fig 3.3c). Sample 2533 shows a slightly higher coercivity of 18.2 mT (Table 3.1, RT), as well as an additional high-coercivity component, which accounts ~11% to the total signal contribution, which we attribute to hematite (Table 3.1, green line in Fig. 3.3c). Low shocked (1 and 3 GPa) magnetite ore also retain a MD behavior similar to the non-shocked samples, but with a slightly increased coercivity of 20.1 and 18.2 mT, respectively (Fig. 3.3a, Table 3.1, RT).

For magnetite ore shocked at 5 GPa, the spread in the spectra of coercivity and interaction field increases strongly compared with lower pressures, but the characteristic closed-contour lobed distributions observed for V-state particles (e.g., Pike and Fernandez, 1999; Lascu et al., 2018; Egli, 2021) are not yet well defined. The sample also denotes an increased coercivity of 33.2 mT (Table 3.1, RT), which we attribute to a mixture of MD and coarse MV (behaving) grains (e.g., Roberts et al., 2017, Lascu et al., 2018, Harrison et al., 2018). The high shocked magnetite ore at 10, 20, and 30 GPa displays an asymmetric MV-state FORC signal (see e.g., Lascu et al., 2018), with intense closed-contour peak lobe shape and broad horizontal and vertical dispersion. These samples show even more increased coercivity values, ranging from 42.3 to 50.1 mT (Table 3.1, RT), consistent with an increased contribution of MV (and MV-behaving) grains. The vertically elongated signal at low-coercivity is faintly observable around the origin, which suggests that a small amount of grains may have preserved MD behavior (Fig. 3.3a). The Chicxulub sample 1100 has a similar MV-like lobed distribution signal (Fig. 3.3b), but lower coercivity (34.6 mT) than the high shocked magnetite ore (Table 3.1, RT; Fig. 3.3c). Note that all FORC distributions at RT in samples shocked above 5 GPa are significantly asymmetric, between the positive and negative values of B_u (Fig. 3.3).

3.4.2. Temperature-dependent measurements

3.4.2.1. Shocked magnetite ore

FORC signals for no and low shocked magnetite ore do not show any variations with temperature. Coercivity decreases slightly after heating in the low shocked magnetite ore (-0.3 mT and -5.8 mT for 1 and 3 GPa, respectively; Table 3.1, ΔB_h is the difference between B_h at 700°C and RT). This indicates that MD behavior has not changed with heating (see Supplemental file 2 for all FORC diagrams).

For magnetite ore shocked above 5 GPa, we observe a systematic shift of the FORC lobes towards lower coercivity with increasing temperature, and a noticeable decrease in FORC asymmetry (Fig. 3.4a, Supplemental file 2). This shift is accompanied by a consistent coercivity decrease with each temperature step, causing ΔB_h in the range from -12.0 mT to -17.7 mT (Table 3.1). With temperature, the irreversible component (ΔM_{irr}) decreases (see vertical arrows in Fig. 3.4a, top), and the reversible ridge increases (Fig 4a, bottom, also seen in the FORC density plot in Fig. 3.5a). The FORC central peak lobe denotes a clear (leftward) progression toward lower B_c values with temperature (Fig. 3.5a), which is not observable in the no and low shocked magnetite ore (cf. dashed lines and horizontal arrow in Initial and 20 GPa magnetite ore of Fig. 3.5a). The decrease in FORC asymmetry and shift of its features towards lower coercivity result in a systematic decrease in the SD-MD signal area, with a reduction of 10 to 15% (downward vertical arrows, Fig. 3.5b). Plotting the hysteresis parameters in a M_{rs}/M_s versus B_{cr}/B_c diagram (Fig. 3.6) highlights the evolution of the magnetic behavior: a shock-induced increase of M_{rs}/M_s and decrease of B_{cr}/B_c, from no and low shocked to high shocked (>5 GPa) magnetite ore (cf. stars in Fig. 3.6) is followed by a systematic decrease of M_{rs}/M_s and an increase of B_{cr}/B_c at each temperature step in the high shocked samples (cf. circles and squares in Fig. 3.6).

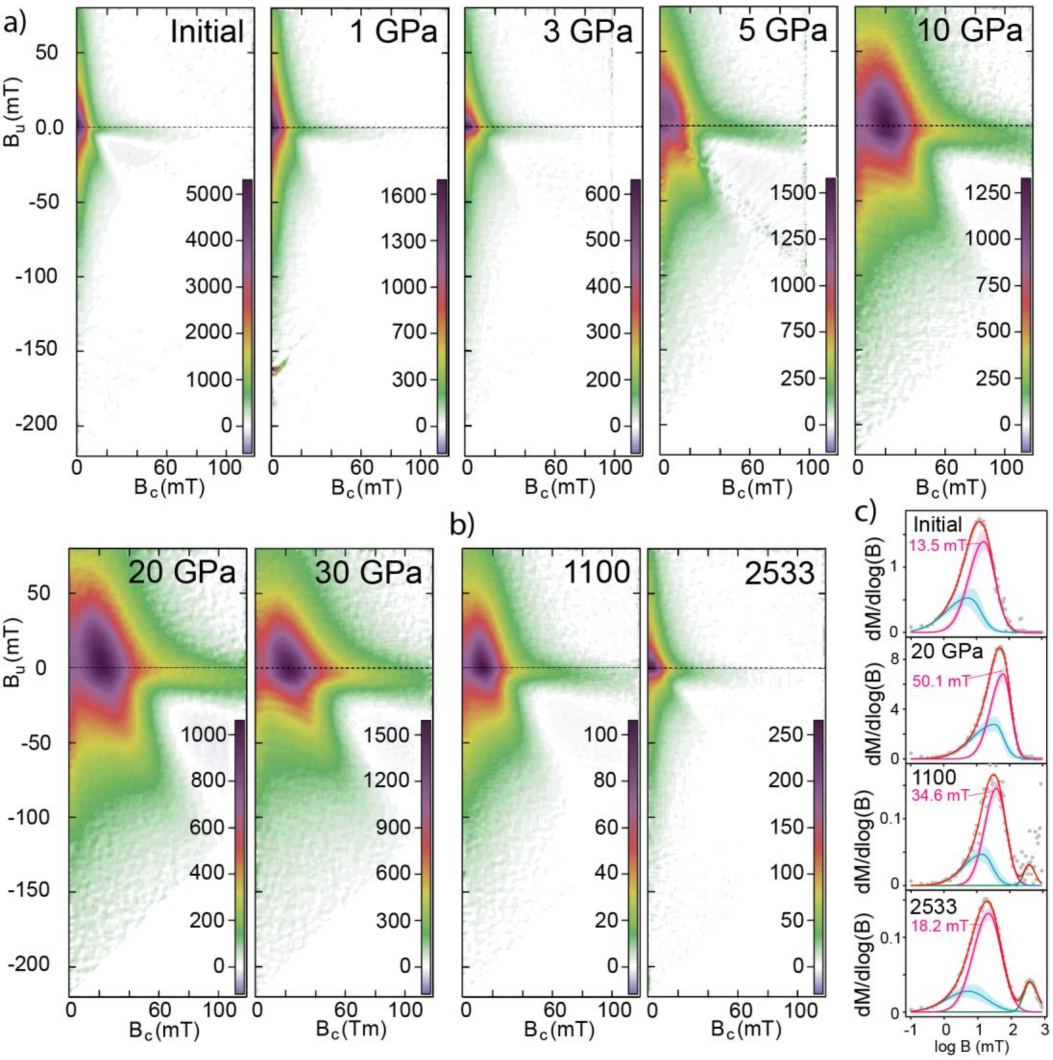

Figure 3.3. a) Room-temperature FORC diagrams of all magnetite ore samples before heating. Note the marked development of the PSD/MV lobes in the FORC diagrams with increasing shock pressures ≥5 GPa; b) Room-temperature FORC diagrams of the natural granite samples, from Chicxulub (1100) and Soultz (2533). We used here sample 1100 BA, due to increased measurement noise on the full run sample); c) Fit of coercivity components to the IRM acquisition curves for representative samples. Note the migration of the components to higher coercivity values between Initial and after 20 GPa shock pressures; note also the presence of a second component (green) in the natural granite samples. Color scale units are in Am^2/kgT^2.

3.4.2.2. Oxidized magnetite from the Soultz granite

The evolution of the oxidized Soultz 2533 granite sample with temperature is divided into two stages: (1) up to 560°C magnetic properties change mildly, while (2) above 560°C changes are much more drastic between each step (Fig. 3.4b).

The first stage up to 560°C, is characterized by a slight strengthening of the horizontal high-coercivity tail (Fig. 3.4b), a reduction of the hematite contribution to the IRM signal from 10.7 to 6.9 %, and an increase in the coercivity of magnetite from 18.2 to 28.9 mT (Table 3.1), suggesting that some hem-mt transformation takes place. At this stage, the central peak lobe does not denote coercivity changes (Fig.

3.5a), the SD-MD signal area remains <5%, similar to the no and low shocked magnetite ore (Fig. 3.5b). Only a slight increase in M_{rs}/M_s values at 560°C (Fig. 3.6) is observed, but MD behavior is broadly preserved.

In the second stage above 560°C, the high-coercivity tail grows in intensity, creating a high-coercivity central-ridge like feature in the FORC diagram and a 45° ridge-like feature in the negative interaction field (Fig. 3.4b). The reversible ridge and irreversible component also increase after 700°C (Fig. 3.4b). The formation of the central ridge is observed to accelerate after 600°C (Fig. 3.5a, vertical arrows in Oxidized (2533)), consistent with a transformation of the hematite component (3.1% after 700°C, Table 3.1), which causes an increase of the total coercivity in the magnetite fraction, to 43.2 mT (ΔB_h = +25.0 mT). Central peak coercivity remains consistent throughout the experiment, meaning that no changes to the original MD magnetite are taking place (cf. dashed lines in Fig. 3.5a). The SD-MD signal area shows an increase to 12% (Fig. 3.5b), and the sample denotes a strong increase of M_{rs}/M_s and decrease of B_{cr}/B_c after 700°C, (Fig. 3.6). As no changes to the MD magnetite fraction are taking place, magnetic property variations are necessarily related to a new magnetite fraction, formed through hem-mt transformation.

3.4.2.3. Shocked and oxidized magnetite from the Chicxulub granite

The RT FORC of the Chicxulub 1100 "FR" granite has a noisy signal (see Fig. 3.4c), however the RT measurement for 1100 BA (used in Fig. 3.3b) allows us to infer an initial asymmetric MV-state FORC diagram, with closed-contour peak lobes similar to the high shocked magnetite ore. The magnetic response to temperature shows now features observed in both the shocked and annealed magnetite ore, and the oxidized and transformed magnetite from the Soultz granite.

Pertaining to the oxidation-related features, Chicxulub 1100 follows the same two-stage evolution described for Soultz 2533, up to and above 560°C. In the first stage up to 560°C, the high-coercivity tail becomes more prominent but no central ridge is formed (Figs. 4c, 5a), around half of the hematite signal contribution disappears (from 7.1% to 3.6%), and magnetite coercivity increases from 34.6 to 41.9 mT (Table 3.1). The SD-MD area largely remains constant, at around 16% (Fig. 3.5b). In the second stage, the central ridge forms (Figs. 4c, vertical arrow in Fig. 3.5a), the hematite contribution disappears entirely, and the coercivity of the magnetite fraction increases to 51.7 mT (ΔB_h = +17.2 mT, Table 3.1). A 45° ridge-like feature in the negative interaction field identical to the one in Soultz 2533 appears, (cf. Figs. 4b and 4c), and an increase of the reversible ridge and irreversible component takes place (vertical arrows in Fig. 3.4c). The changes in the FORC features and formation of the central-ridge causes the SD-MD signal area to increase to around 23% at 700°C (Fig. 3.5b). The evolution in the M_{rs}/M_s, versus B_{cr}/B_c diagram does not follow the same pattern as Soultz 2533, but instead a continuous increase of M_{rs}/M_s and a generally constant B_{cr}/B_c is observed (Fig. 3.6). The shock-related response in this sample is not as distinct as in the high shocked magnetite ore, but is seen in the FORC diagrams as a shift of the central peak toward lower coercivity (cf. lobe shift in Fig. 3.5a, with elongation of color contours towards the origin in Fig. 3.4c). This shift and the decrease in asymmetry are masked by the formation of the central-ridge, but we can still observe a (leftward) progression of the central peak in the horizontal FORC density profile (Fig. 3.5a). Despite the noisy signal at RT, the density of FORC features at low coercivity increases consistently with temperature (Fig. 3.5a, see the region left of the vertical dashed lines), and culminate in the separation of two peaks at 700°C, one at lower and one at higher coercivity compared to the RT peak (horizontal arrows pointing toward red lines in Fig. 3.5a). The low-coercivity peak has identical coercivity as the Initial, 2533, and post-heated 20 GPa peaks (cf. red dashed lines of Fig. 3.5a).

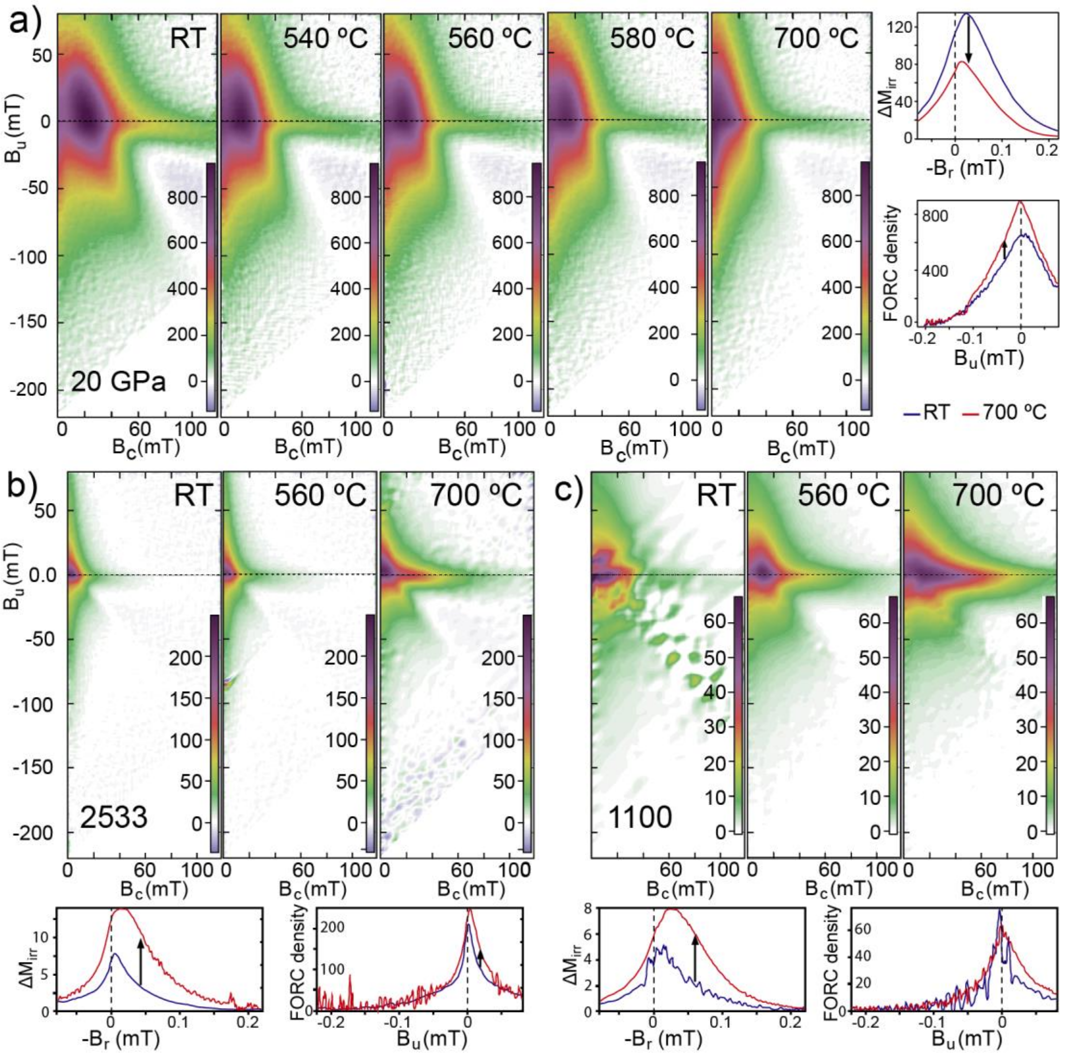

Figure 3.4. FORC diagrams, vertical FORC density profile for B_c=0mT (reversible ridge) and irreversible component (given by ΔM_{irr}), that illustrate sample evolution with temperature. a) Temperature evolution of representative shocked magnetite ore at 20 GPa, which is representative of the high shocked samples; b) evolution of first and second stages of the hem-mt transformation in sample Soutlz 2533; and c) evolution of first and second stages of the Hem-Mt transformation and shock defect annealing in sample Chicxulub 1100. Scale units are in Am^2/kgT^2 for FORC diagrams and ΔM_{irr}. No and low shocked samples have no FORC signal changes. Results for all samples can be found in Supplemental file 2.

3.4.3. Before/After experiments – Time-dependence and phase stability

Before heating, 2533 BA shows a typical MD FORC signal, with a magnetite coercivity of 20.8 mT, and a hematite component with 13.9% signal contribution (Fig 7a, Table 3.2). After heating, we observe a sharp increase in the intensity and the formation of the central ridge, together with a (rightward) shift of the central FORC feature peak to higher coercivity values in the horizontal profile (vertical and horizontal arrows in Fig. 3.7a). The total disappearance of the hematite component is achieved (Table 3.2), as the coercivity of magnetite increases from 20.8 mT to 46.8 mT (Table 3.2). The reversible ridge and irreversible component also increase significantly (vertical arrows in Fig. 3.7a, bottom). In this experiment, the newly formed magnetite doubles the original sample intensity (Fig. 3.7a) and nearly fully overprints the original MD signal. Sample 2476 shows identical results (see Supplemental file 2).

Before heating, sample 1100 BA displays an asymmetric MV-state FORC lobe distribution, a smaller hematite component than its "FR" counterpart (only 1.8%), and a magnetite coercivity of 30.8 mT

(Table 3.2). After heating, the hematite contribution disappears, the coercivity of the magnetite fraction doubles (to 60.9 mT, Table 3.2), and the signal becomes dominated by the newly formed central ridge (Fig. 3.7b). The increase in the reversible and irreversible components is clearer than in the 1100 FR (cf. Fig. 3.7b and 3.4c). In the horizontal profile, two peaks have formed identical to the FR experiment, however both peaks now have lower coercivity than the original (cf. blue and orange horizontal profiles in Fig. 7b). A second heating of sample 1100 BA to 700°C shows only a slight signal intensity increase compared to the first heating (Fig. 3.7b, "After 2").

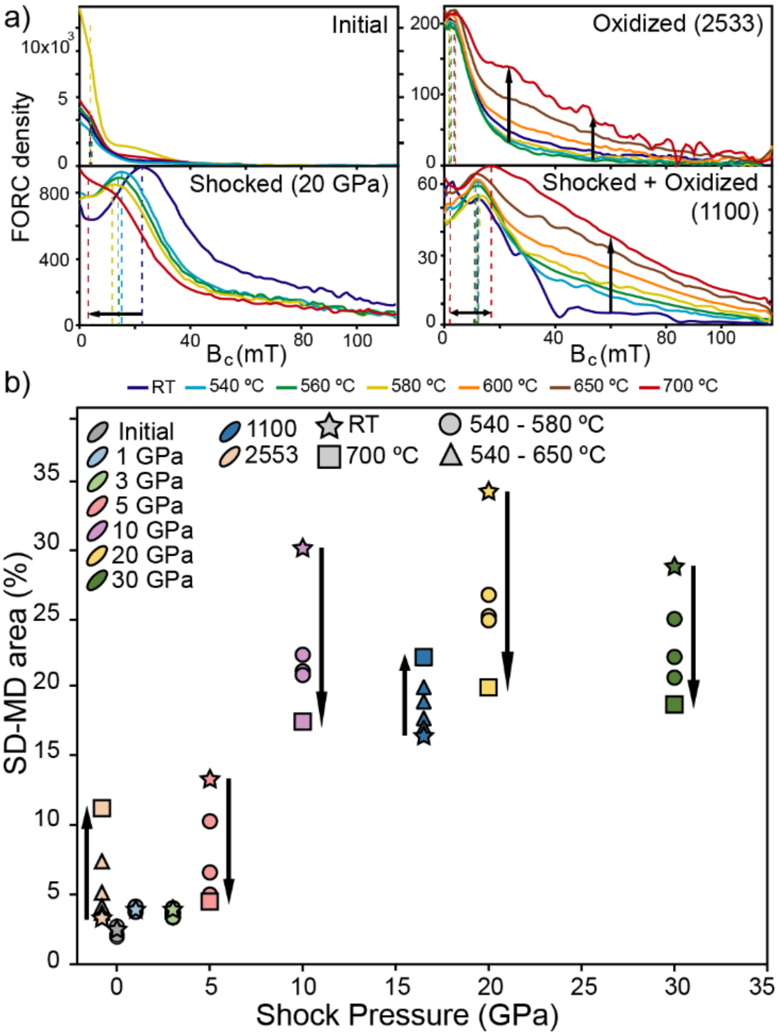

Figure 3.5. Evolution and variation of the FORC signal with temperature. a) Horizontal FORC density profiles along the B_u= 0 mT axis (i.e., horizontal dashed lines in Figures 4.3 and 4.4), at different temperatures, for representative samples of no and low shocked magnetite ore (Initial) and high shocked magnetite ore (20 GPa), as well as both natural granites (2533 from Soultz and 1100 from Chicxulub) b) SD-MD signal area for all investigated samples. Shock pressure of 16.5 GPa for sample 1100 is an approximation (Feignon et al., 2020). Samples that suffered no shock are plotted for clarity at -1 (sample 2533) and 0 (Initial magnetite ore). Description and Data of SD-MD area calculations are provided in Appendix B.1 and Supplemental file 2, respectively.

Table 3.1. (Top) Mean coercivity of remanence (B_h) of the grain population of the main magnetite component 1. (Bottom) Total magnetite (Mt) and hematite (Hem) contribution to the signal with temperature, in the natural granites from Soultz (2533) and Chicxulub (1100). Further IRM modeling parameters can be found in Supplemental file 3.

Sample	Average grain population coercvity [mT]							
	RT	540°C	560°C	580°C	600°C	650°C	700°C	ΔBh [mT]
Ini	13.5	14.3	13.4	8.1	-	-	12.5	-0.9
1 GPa	20.1	18.1	18.3	16.2	-	-	19.9	-0.3
3 GPa	18.2	12.8	13.4	16.1	-	-	12.3	-5.8
5 GPa	33.2	29.8	21.4	19.5	-	-	18.1	-15.2
10 GPa	42.3	32.4	31.1	30.5	-	-	30.3	-12.0
20 GPa	50.1	36.9	36.3	35.7	-	-	32.4	-17.7
30 GPa	47.6	35.1	34.2	31.1	-	-	30.5	-17.1
1100 (Chicx)	34.6	38.2	41.9	43.7	47.6	52.3	51.7	+17.2
2533 (Soultz)	18.2	23.2	28.9	35.1	39.9	43.5	43.2	+25.0

Sample	Contribution to signal [%]						
	RT	540°C	560°C	580°C	600°C	650°C	700°C
1100 mt	92.9	95.9	96.4	96.8	98.1	98.6	100.0
1100 hem	7.1	4.1	3.6	3.2	1.9	1.4	0.0
2533 mt	89.3	92.6	93.1	93.8	94.5	95.3	96.9
2533 hem	10.7	7.4	6.9	6.2	5.5	4.7	3.1

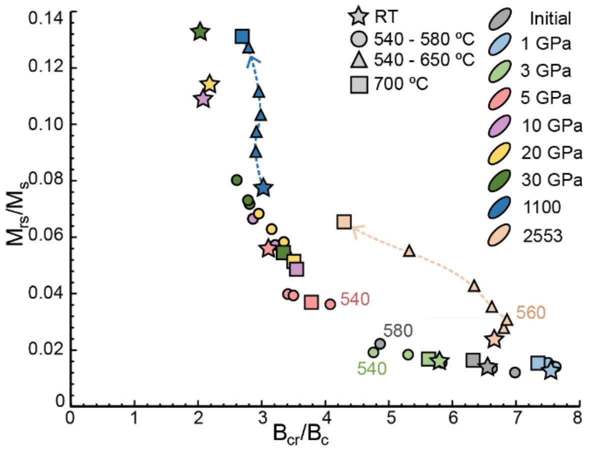

Figure 3.6. M_{rs}/M_s versus B_{cr}/B_c diagram for all samples at room temperature (RT) and with temperature. Note that shocked magnetite ore at RT shows PSD/V domain state behavior, which moves toward a more MD behavior with increasing temperature. Only oxidized (2553) and shocked and oxidized (1100) granite show the contrary trend, with bulk-sample average magnetic domain state decreasing, with increasing temperature (marked by a dashed line and arrows). Numbers mark outliers in samples Initial, 3 and 5 GPa, and the “threshold” of stage 1 and stage 2 of Hem-Mt transformation in sample 2533.

Table 1.2. Mean coercivity of remanence (B_h) of magnetite before and after heating to 700°C for Chicxulub (1100) and Soultz (2476 and 2533) granite, and signal contribution of magnetite and hematite. Further IRM modeling parameters found in Supplemental file 3.

Sample	Before			After			After 2		
	Bh[mT]	mt [%]	hem [%]	Bh[mT]	mt [%]	hem [%]	Bh[mT]	mt [%]	hem [%]
1100 (Chicx)	30.8	98.2	1.8	60.9	100.0	0.0	62.9	100.0	0.0
2533 (Soultz)	20.8	86.1	13.9	46.8	100.0	0.0	-	-	-
2476 (Soultz)	18.9	84.4	15.6	37.7	95.1	4.9	-	-	-

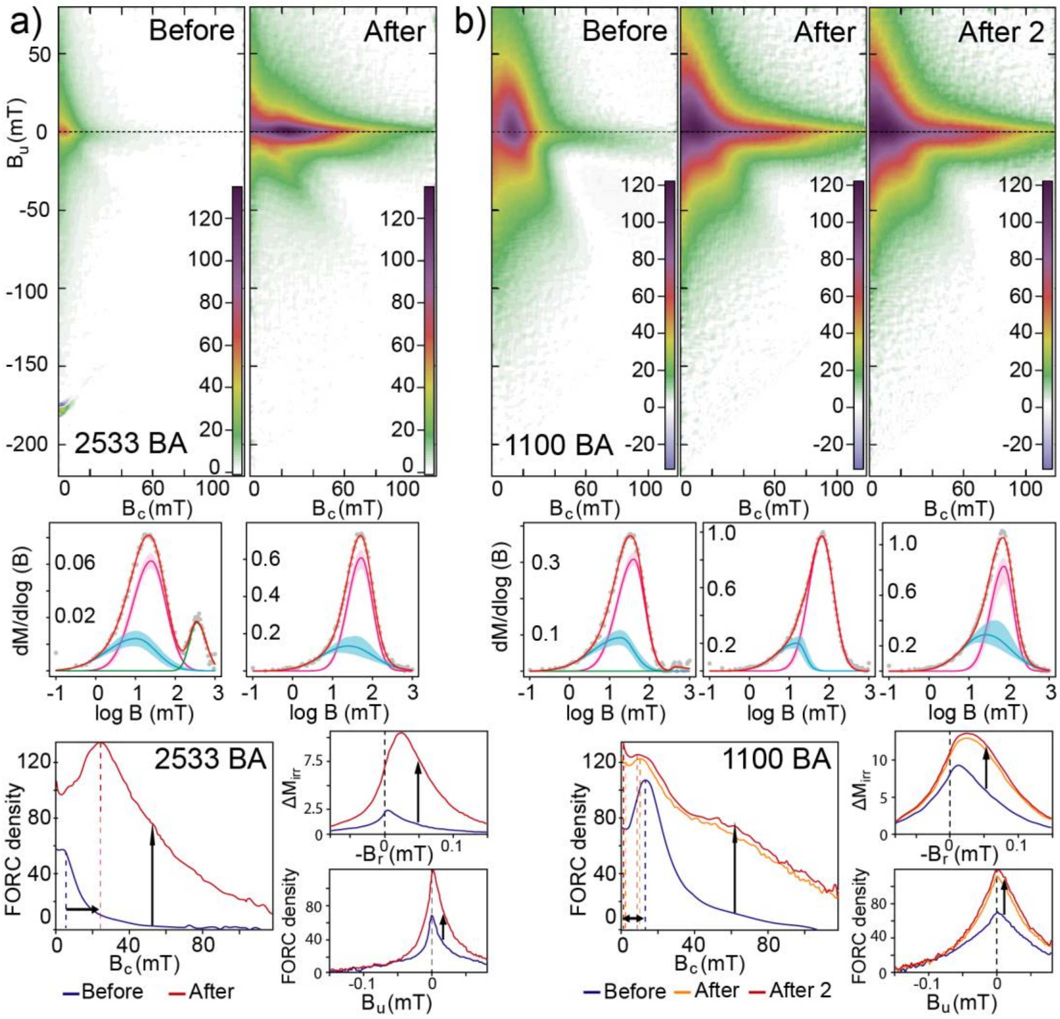

Figure 3.7. FORC diagrams, fit of coercivity components to the IRM acquisition curves, vertical FORC density profile for B_c=0mT (reversible ridge) and irreversible component (given by ΔM_{irr}), for the Before-After (BA) experiments in the natural granites. a) oxidized granite (2533) from Soultz, note more nearly on order of magnitude intensity increase in the central ridge after heating; b) shocked and oxidized granite (1100) from Chicxulub, second measurement "After 2" suggest the newly formed magnetite is stable after repeated heating; see section 3.3 for details.

3.5. Discussion

3.5.1. Shocked magnetite ore

Hysteresis loops, IRM component analysis, and FORC diagrams of the shocked magnetite ore demonstrate that below the Hugoniot elastic limit of magnetite (~5 GPa, Ahrens and Johnson, 1995) shock does not create significant irreversible magnetic domain state changes, and thermal annealing also has no significant effect.

In the low shocked magnetite ore, the magnetic characteristics typical for natural undeformed MD magnetite (e.g. by Pike et al., 2001b) are largely retained after shock and heating. A slight increase in the magnetite coercivity and M_{rs}/M_s ratios from the Initial to the low-shocked 1 and 3 GPa magnetite ore may indicate a limited increase of domain wall-pinning effects in dislocation networks or local micro-cracks in a strained crystal lattice (Lindquist et al., 2015). Previous studies on MD magnetite at this pressure range are limited to hydrostatic compression experiments between 1-4 GPa (see Gilder et al., 2002, 2004, 2006). After decompression, these authors observed a decrease of ~65% in reversible magnetic susceptibility, a slight decrease in the median demagnetization field (field required to demagnetize 50% of the original signal, a proxy for coercivity), and a loss of up to two thirds of magnetic moment. The changes are attributed to a restructuring of domain patterns, increased domain wall nucleation and wall-pinning from an increase in defects. Although a direct comparison of our results with these studies has its limitations (different strain rates between compression-decompression cycles and shock experiments), our results are in agreement with such a model. Gilder et al. (2002, 2004) also noted that magnetic properties only vary slightly below 2 GPa, and become more pronounced between 2 and 3 GPa. The measurements between 2 and 3 GPa were made under pressure thus not directly comparable to ours, however we do observe that annealing at 3GPa causes a decrease of the magnetite coercivity (ΔB_h = -5.8 mT), whilst at 1 GPa temperature has a negligible effect (ΔB_h = -0.6 mT). The behavior changes are not significant, but the onset of defect annealing leads us to consider that the 3GPa ore potentially represents a “transitional” stage in shock-deformation.

For magnetite ore shocked at 5 GPa and above, the RT FORC diagrams (Fig. 3.3; stars in Fig. 3.5b), IRM results (Table 3.1, RT; Fig. 3.3) and hysteresis parameters (stars in Fig. 3.6) demonstrate a trend towards behavior more typical of MV. The lower B_{cr}/B_c and higher M_{rs}/M_s ratios (Fig. 3.6) would also indicate a “PSD” (V) domain state, according to the classical “Day diagram” (Day et al., 1977).

Our FORC results and SD-MD area evolution are similar to observations by Reznik et al. (2016) in different pieces of the same shocked magnetite ore sample material (cf. Figs. 3.3, 3.5b of this work, and Figure 9 in Reznik et al., 2016). These features agree well with a transition from a mainly brittle-elastic mechanical behavior at low-shock conditions, towards irreversible brittle-plastic deformation in the higher shocked magnetite ore. In the 5 and 10 GPa magnetite ore, shear bands and particle fragmentation are reported as the dominant microstructural deformation mechanism (Reznik et al., 2016). At 20 GPa, grain fragmentation becomes more intensive, shear bands grow wider and mosaic-like sub-grains form. At 30 GPa, the shockwave leads to the formation of kink-bands, composed of multiple twinned sub-grains (Reznik et al., 2016). The shear- and kink-bands increase the intra-crystalline strain and anisotropy, which is responsible for the distinctly asymmetric FORC signals. The asymmetry of the FORC diagrams can be explained by different vortices created and destroyed at different fields, depending on their location within the crystal (Lascu et al., 2018). With the formation of shear- and kink-bands, the increased strain leads to a widening of the dispersion of the field distribution of the vortex nucleation and annihilation events (Lascu et al., 2018), and thus increasing the asymmetry. While fracturing and fragmentation causes grain size reduction and reduces the bulk-sample average domain state, plastic deformation features create a denser network of physical barriers to domain wall-migration. As domain walls become increasingly pinned along the dense defect network, the expression of individual domains becomes inhibited, resulting in the high M_{rs}/M_s ratios and coercivity (*s.l.*). This leads to magnetic behaviors typical of MV state, despite the magnetite retaining multiple discrete domains, causing an apparent decrease in domain state.

The effects of plastic deformation are partially recovered with temperature, associated with a systematic decrease in magnetite coercivity, FORC asymmetry and SD-MD area, at each step (Table 3.1, Fig. 3.4a, 3.5b). Hysteresis parameters also change consistently towards lower M_{rs}/M_s and higher Bcr/B_c ratios, along the classic SD-MD mixing line of Day et al. (1977) towards increased MD contributions (see squares in Fig. 3.6). The increased MD behavior is particularly highlighted by the leftward progression of the FORC central peak towards coercivity values identical to the MD no and low shocked samples (Fig. 3.5a). This suggests that our final results are a composite of MD and MV behaviors, from originally dominant MV behaviors before heating. The partial restoration of the original MD state behavior through temperature is caused by a mosaic-like recrystallization of magnetite, in line with a recovery of lattice defects (Kontny et al., 2018). The defect recovery and recrystallization relaxes the elastic crystal strain, and allows the magnetic domain walls to migrate more easily again. Easier migration reduces grain coercivity (*s.l.*) and the occurrence of Barkhausen jumps of domain walls, thus reducing the irreversible component, and consequently increasing the reversible ridge (Fig. 3.4a). It also decreases domain wall-nucleation, which increases the individual domain volume size (Kontny et al., 2018). The MV behavior that is preserved after heating derives from the reduced grain size caused by irreversible brittle fracturing and fragmentation.

3.5.2. Oxidized magnetite from the Soultz granite

The disappearance of hematite with temperature in the natural magnetite-bearing granite is clear and systematic, concomitant with the formation of new magnetite grains from hematite-to-magnetite transformation that causes an increase in coercivity of magnetite (Table 3.1; Fig. 3.4b). The hem-mt transformation process is associated with an increase both in reversible ridge and irreversible components, and the formation of a high coercivity central ridge in the FORC diagrams, which increases the SD-MD signal area (Fig. 3.4b, 3.5a and 3.5b).

The formation of the central ridge is fundamental to understand the properties of the newly formed phase, as central ridges are typical for non-interacting SD (e.g., Harrison et al., 2018; Roberts et al., 2019), or SV (Lascu et al., 2018) grains. SV-dominated FORC diagrams have lobes that are confined to the positive and negative interaction fields (e.g., Zhao et al., 2017) and are as intense as the central ridge. A negative "trough" feature immediately below the central ridge is also characteristic of SV grains (Lascu et al., 2018). On the other hand, SD central ridges are much more intense than the remaining features, and do not show the negative "trough" (Lascu et al., 2018). In our granite samples, the intensity of the ridge and lobes is likely dependent on the extent of the hem-mt transformation. Comparing samples 2533 FR and 2533 BA (cf. Fig. 3.4b and 3.7a), the latter has a ridge that is much stronger than the remaining features (cf. Figs. 7a and 4b). While the real extent of the hem-mt transformation and amount of newly formed magnetite is hard to estimate (a ~11% signal contribution of hematite requires its concentration to be much larger than that of magnetite; see Frank & Nowaczyk, 2008; Liu et al., 2019), we can only assume that the transformation in 2533 BA is more thorough than in 2533 FR (see contributions in Tables 3.1 and 3.2). Therefore, we find it reasonable that given a more complete transformation, the central ridge is significantly stronger than the other contributions (Fig. 3.7a, horizontal profile). Additionally, we do not observe a "trough" feature below the central ridge, which is more in line with a SD state for the newly formed magnetite. The formation of a Hopkinson peak after heating in the κ-T curve for this sample (Fig. 3.1d) supports this interpretation as the Hopkinson peak is a feature associated with the unblocking of SD state just below T_c (Dunlop, 2014). Interaction between the original MD and newly formed SD grains, two fractions of contrasting coercivity, causes the positive area above the 45° ridge in the negative interaction fields. A sharp increase in the irreversible component is well explained by the formation of SD grains, due to an increase in the irreversible rotation of SD magnetization vectors (e.g., Birčáková et al., 2019). As for the reversible ridge, it is unlikely that the increase is caused by changes in domain wall migration, as no fundamental changes to the original MD magnetite take place (Fig. 3.5a). Therefore, the increase must be related to newly formed magnetite, likely a fraction of newly formed SP grains, whose magnetization is entirely reversible (Roberts et al., 2000).

The formation of fine grained SD-SP magnetite causes an increase in bulk-sample coercivity, however the coercivity tail of this newly formed phase extends to at least 120 mT (Fig. 3.5a, 3.7a), a high value even for fine grain sizes. Such high values may be explained by a strained crystal lattice. Jiang et al. (2016) observed that the crystal structure of nanohematite is often preserved in magnetite formed via reduction through heating, which could be a source for such a lattice strain. Alternatively, we also cannot exclude that the high coercivity (*s.l.*) is connected to the formation of some minor maghemite, as the transformation of magnetite to hematite is reported to occur via maghemite as a metastable phase (e.g., Annersten and Hafner, 1973). If present, this maghemite has an insignificant contribution to the magnetic signal, as our IRM modelling results show no signal that can be related to it.

Our results support the hypothesis postulated by Just and Kontny (2012), and Mendes et al. (2023) that hematite, when heated in an inert argon atmosphere, transforms to magnetite (Fig. 3.1e). We assume that the reason for this mineral reaction are traces of hydrocarbons in the argon gas, despite a high Ar purity (~99.998%; https://industry.airliquide.us/argon). From our BA experiments, we suggest that the formation of the new magnetite phase is an instantaneous process, and that this phase is stable and will not decay or alter with further heating. Mendes et al. (2023) observed that the newly formed magnetite has a mottled texture resulting from small grain sizes that are not resolvable by reflected light microscopy, which is consistent with the SD-SP range proposed here. Lastly, we can exclude that the new magnetite grains formed due to impurities in the cement mix, as no new magnetic phase was detected after heating the cemented 1, 10, 20 and 30 GPa magnetite ore. However, we cannot exclude some influence of other minerals such as mica, even in small quantities, in facilitating the hem-mt transformation in the granite.

3.5.3. Shocked and oxidized magnetite from the Chicxulub granite

The Chicxulub granite show features of annealing and hem-mt transformation, both influencing the evolution of the magnetic behavior. These two effects are confirmed by the formation of two FORC feature density peaks (Fig. 3.5a) after temperature treatment.

The shock-induced MV-like behavior is partially reverted through annealing, in the same process described in section 4.1 for the shocked magnetite ore, however the concomitant hem-mt transformation nearly fully masks it. Partial restoration of the pre-shock MD behavior results in the low coercivity peak, at an identical coercivity to the high shocked magnetite ore after annealing (cf. 1100 and 20 GPa in Fig. 3.5a). At the same time, the formation of SD-SP magnetite grains from hem-mt transformation is responsible for the formation of the second, higher coercivity peak (Fig. 3.5a). The new fine SD-SP magnetite causes the sample to present a behavior typical of MV state (Fig. 3.6). Bulk-sample coercivity (*s.l.*) increases, and the positive feature above the 45° diagonal ridge in the negative interaction field highlights the coercivity contrast between the annealed MD-MV and newly formed SD-SP fractions. The κ-T curve for sample 1100 is also in good agreement with SD-SP grain formation (see “hump” below grey arrow in Fig. 3.1f), as such “humps” are suggested to be caused by thermal relaxation of SP particles (Zhao and Liu, 2010, Gao et al., 2019). After heating, the SD-SP grains are dominant and counteract the annealing-induced decrease in coercivity (*s.l.*) and SD-MD area. Whilst the restoration of MD behavior is still observable, the classic bulk-sample hysteresis and IRM modelling methods are not able to distinguish between these two effects. Only FORC diagrams, the most sensitive method to detect small scale domain state changes (e.g. Roberts et al., 2014), can distinguish them.

Our observations are relevant for natural impact crater investigations. Magnetite to hematite oxidation is a ubiquitous product of hydrothermal or meteoric alteration of crustal rocks (e.g., Horton et al., 2006; 2009a; 2009b), so the post-impact high-temperature exposure in impact craters may cause hem-mt transformation naturally, which overprint the original features. This is observed in the Chicxulub crater, where samples in close contact with impact melt have reversible or nearly reversible κ-T curves, with the exception of the same abovementioned “hump” from SD-SP thermal relaxation (Pike et al., 2001a, Mendes et al., 2023). Even at very small percentages, SD-SP grains are able to overprint MD signals, also in non-shocked samples (see e.g., Harrison et al., 2018). Shocked magnetite is already demagnetized, so even the transformation of as low as 1.8% of the signal from hematite will cause a significant overprint (see Fig. 3.7b). Lastly, we believe our results from the natural shocked magnetite validate the models postulated by Reznik et al. (2016) and Kontny et al. (2018), and demonstrate that the laboratory-shock and post-shock annealing experiments are good analogues to the natural system.

3.5.4. Implications

Magnetite is the most dominant ferrimagnetic mineral in the Earth's crust, and consequently also in large impact craters, where prominent negative magnetic anomalies are related to the shock demagnetization and/or extensive alteration and destruction of the magnetite phases (e.g. Pilkington and Grieve, 1992; Scott et al., 1995). Magnetite oxidation is regarded as a near-equilibrium redox phenomenon where magnetite is altered to hematite by oxidation; but the opposite is also possible, where hematite is reduced by hydrogen or organic matter back to magnetite (e.g., Just and Kontny, 2012). Oches and Banerjee (1996) described a hem-mt transformation in oxygen-free environments in loess-paleosol sediments, and Ohmoto (2003) and Otake et al. (2007) even describe non-redox transformations between magnetite and hematite under H_2-rich hydrothermal conditions, a mechanism that is not only restricted to Earth's surface but that can also act at greater depths in the crust. These interpretations have been used to explain irreversibility of κ-T experiments in impact studies (e.g., Mang and Kontny, 2013).

Mendes et al. (2023) postulated that in shocked magnetite from the peak ring of the Chicxulub impact structure, natural hydrothermal temperatures are insufficient to cause annealing or hem-mt transformation. We confirm this interpretation with our results, as the preservation of both the shocked and oxidized state (see RT results from sample 1100 in Fig. 3.3, 3.4c and 3.7b), suggests that even long exposures (from 500 kyr to 2 Myr) to relatively high hydrothermal temperatures of 450°C (Kring et al., 2020) is insufficient to initiate such a process. Because magnetite already shows signs of annealing when heated to 540°C, we place the temperature threshold for the initiation of annealing between 450° and 540°C. The results of the Soultz 2533 sample from this study suggest that most of the hem-mt transformation occurs above 560°C and the bulk of new magnetite formation occurs above 600°C. No transformation is observed below the Curie temperature of magnetite (~580°C) in the κ-T curves of Soultz (Fig. 3.1d), so we estimate that ~580°C is a reasonable threshold for the onset of the hem-mt transformation in most samples.

Several geoscience research subjects report hem-mt transformation at high temperatures: from impact research, loess deposit research, to environmental contamination studies and wildfire related mineral transformations in soils (e.g., Deng et al., 2001; Just and Kontny, 2012; Mang and Kontny, 2013; Jiang et al., 2016; Szczepaniak-Wnuk et al., 2020; Górka-Kostrubiec et al., 2019). Oches and Banerjee (1996) hypothesized about high-temperature hem-mt transformation in κ-T analyses, but to our knowledge no in-depth study of this phenomenon has been published. Despite the pre-impact oxidation being ubiquitous in the Chicxulub peak-ring (Kring et al., 2020), wherever the granite is in proximity to the impact melt hematite is absent and κ-T curves become more reversible or show the "hump" also before heating (Mendes et al., 2023). This suggests that the hem-mt transformation is not exclusively related to an argon atmosphere with traces of hydrocarbons but can also occur in nature under reducing high-temperature conditions, e.g., related to a magmatic pulse (e.g., through orogenic re-burial, dyke emplacement, or sequential plutonic emplacement).

A potential case study for a possible unnoticed overprint of natural hem-mt transformation is the Manteigas granodiorite, in central Portugal (Dias et al., 2022). This is a Lower Ordovician granodiorite (481.1 ± 5.9 ma; Neiva et al., 2009), and was intruded by the adjacent Seia granite in the late Carboniferous (311-306 Ma; Sant'Ovaia et al., 2010). Dias et al. (2022) described the presence of large (>100 μm) magnetite crystals, that are partially oxidized into hematite. IRM modelling for these samples indicate that, where only magnetite is identified, B_h ranges from 25 to 40 mT. However, close to the contact with the younger Seia pluton, some hematite is observed (~15% contribution to the signal), and the magnetite component coercivity is higher (60 - 63 mT). This coercivity difference is similar to the observed increases in our results, attributed to the hem-mt transformation, even when incomplete (see e.g., Sample 2533 in Table 3.1; Table 3.2). If partial hem-mt transformation occurred in the granodiorite due to the emplacement of the Seia granite, this may have led to incorrect conclusions. It would be difficult to identify a hem-mt derived overprint without looking for it. Our results demonstrate that formation of small-scale SD-SP state grains overprint original magnetic signals and increases magnetizations (e.g. Fig. 3.7a). SD grains are more stable and reliable recorders of paleomagnetic directions than MD grains at a geological time-scale (e.g., Heider et al., 1988; Roberts et al., 2017), therefore, even a small fraction of SD grains formed by the hem-mt transformation provides a mechanism for overprinting paleomagnetic recordings. We believe that hem-mt transformation may be an under-appreciated mechanism that deserves more attention in future studies.

3.6. Conclusions

Using FORC measurements to detect subtle magnetic behavior and domain state variations, we have characterized how shock, annealing, oxidation and hematite-to-magnetite transformation produce different magnetic behavior responses with temperature. We demonstrate that shock pressures above the Hugoniot elastic limit for magnetite (~5 GPa) have a tangible effect on the apparent domain state of magnetite, causing MD grains to behave PSD/MV-like, despite maintaining multiple discrete domains. Brittle fracturing and grain fragmentation are irreversible, and cause permanent grain size reduction with a bulk-sample average domain state decrease, creating “real” MV state grains. On the other hand, thermal annealing of strained magnetite recovers some of the lattice defects by grain recrystallization and lattice defect recovery. The reduction of intra-crystalline strain and defect networks reduces domain wall pinning, and partially restores some of the original MD behavior. Together, these mechanisms cause a bulk-sample increased domain state, with a composite MD and (real) MV magnetic behavior, after heating. The temperature threshold for annealing is estimated to be between ca. ~500-520°C.

High temperature hematite-to-magnetite transformation in a non-oxidizing argon atmosphere caused the formation of SD-SP magnetite and a bulk-sample average domain state decrease. Even in small amounts, the newly formed SD magnetite causes a strong magnetic signal overprint of the original signal, and masks any thermal annealing effect, making hem-mt transformation the dominant phenomenon of the two. The new SD-SP phase is stable, even after consecutive heating. We estimate transformation to initiate at ~580°C, becoming most prominent above 600°C. Formation of new SD magnetite as a response to temperature may overprint paleomagnetic directions and other magnetic behaviors in nature, creating the need for an extra layer of scrutiny when interpreting paleomagnetic data. It may also be a new process for producing remagnetizations.

4. Ries Magnetic Mineralogy: Exploring Impact and Post-Impact Evolution of Crater Magnetism

4.1. Abstract

Large scale impact events are some of the most catastrophic and instantaneous geological processes in nature and leave in their wake conspicuous geological structures with characteristic magnetic anomalies. Despite magnetic anomalies in craters being well-documented, their relationship with the magnetic mineral composition of the target and impactites is not always straightforward. Furthermore, the influence of impact shock and post-impact events in the magnetism of natural craters remains elusive. In the Ries crater, Germany, the negative magnetic anomalies are attributed to a reverse polarity remanent magnetization in the impact-melt bearing lithologies. We report new chemical, rock- and mineral-magnetic data from the shocked basement and impactites, from surface samples, NR73 and SUBO-18 boreholes, and explore how temperature and hydrothermalism may influence the magnetic mineralogy in the crater. We identified shocked, pure magnetite in the basement, and low cation substituted magnetite in the impactites as the main magnetic carriers. The shocked basement is demagnetized but remain largely unaltered by post-impact hydrothermalism, while the impactites show weak magnetization and are extensively altered by neutral-to-reducing post-impact hydrothermalism. We suggest that the magnetic mineralogy of the demagnetized uplifted basement may contribute significantly to the magnetic anomaly variation, in line with recent findings from the Chicxulub peak-ring.

4.2. Introduction

Large scale impact events are some of the most catastrophic and instantaneous geological processes in nature. Hypervelocity impacts release high amounts of energy and generate pressures that will vaporize, melt and metamorphose the target rock, and may have large scale environmental implications such as a contribution to extinction events (e.g., Hildebrand et al., 1991; Schulte et al., 2010). These events leave in their wake large conspicuous impact structures with very characteristic features, such as gravity and magnetic anomalies (Pilkington and Grieve, 1992). These physical anomalies have been used to detect these structures even after millions of years of sedimentary burial.

Magnetic anomalies in impact structures are very well documented phenomena (e.g., Hildebrand et al., 1991; Pilkington and Grieve, 1992; Gulick et al., 2008; Ugalde et al., 2005), but their relationship with the magnetic mineralogy of both shocked target rocks and impact-derived rocks is not always straightforward. Shock-related reduction of the total magnetization (M_t), which is the sum of natural remanent magnetization (NRM) and induced magnetization (M_t = NRM + κ*B, where κ is magnetic susceptibility and B is an ambient magnetic field, in this case Earth's magnetic field) is well documented in literature. The loss of NRM in target rocks has been studied in detail over the last decades (e.g., Pearce and Karson, 1981; Jackson, et al., 1993; Kletetschka et al., 2004; Gilder et al., 2006; Louzada et al., 2007, 2011; Bezaeva et al., 2007; 2010; Gattaceca et al., 2010; Tikoo et al., 2015), demonstrating that even at pressures under 2 GPa, multi-domain (MD) magnetite, the most important magnetic mineral in the Earth's crust, may lose up to ~90% of its pre-shock NRM. While shockwave deformation may impart a shock remanent magnetization (SRM, e.g., Fuller, 1977; Srnka, et al., 1979; Gattacceca et al., 2006, 2007; Louzada et al., 2011; Tikoo et al., 2015) this is often a very inefficient process, and creates a weak magnetization (only few percent of the original NRM).

Research into the loss of magnetic susceptibility (κ) in experimentally shocked magnetite is more recent and has shown that even relatively low shock pressures of 5 GPa cause a reduction of up to 90% in pure magnetite (Reznik et al., 2016). The reduction in κ is related to physical processes, such as grain fracturing, fragmentation, and intra-crystalline lattice defects, that lead to an apparent decrease in the domain state of originally MD magnetite. Lattice defects enhance domain wall pinning (e.g., Lindquist et al., 2015), and together with fracturing cause a reduction of the apparent magnetic grain size, increase of magnetite coercivity, and further reduction of κ (Reznik et al., 2016). However, follow-up studies on the same shocked magnetite samples has found that through exposure of shocked magnetite to high temperatures (up to 700°C), thermal annealing of the crystal lattice defects could restore some of the lost magnetic properties and κ, and reduce wall pinning effects, leading to a decrease of coercivity and an apparent increase of domain state (Kontny et al., 2018; Mendes and Kontny, in press). The shock-derived reduction of both remanent and induced (through reduction of κ) magnetization in shocked target rocks, and the potential post-impact restoration of some of these properties, will invariably contribute to the magnetic anomaly pattern in impact structures.

However, the effects of impact shock and temperature-related post-impact restoration of magnetic properties, and the influence that these phenomena have in natural impact craters, remain largely unexplored. A recent study in the ~200 km diameter Chicxulub impact crater (first discovered by Penfield and Camargo, 1981) has found that the prominent negative magnetic anomaly in the peak-ring is controlled by the shock-induced demagnetization (~0.01 A/m) and reduction of κ (~50x10^{-5}SI) in the uplifted shocked granitoid basement (Mendes et al., 2023). Here, large magnetite grains (>500µm) show around ~90% lower κ when compared with intact (not shocked) granite containing similar amounts of magnetite (κ = ~1000x10^{-5}SI, see e.g., Ishihara, 1979; Ishihara et al., 2000, and discussion in Mendes et al., 2023). A post-impact, long lasting (up to 2 Myr) hydrothermal system with temperatures up to 450°C (Kring et al., 2020) was not enough to anneal the internal defects and restore some of κ (Mendes et al., 2023), or significantly imprint a secondary NRM in the basement (Mendes et al., 2023). Furthermore, the suevite (impact breccia) in Chicxulub is magnetically very weak (Mendes et al., 2023), and show very low amounts of magnetite, mostly concentrated in small basement or melt fragments.

These observations in the Chicxulub suevite contrasts with the extensively studied ~26 km diameter Nördlinger Ries impact crater (referred to as “Ries crater” henceforth), in Germany. Here, the magnetization is carried by magnetite, newly formed in the impact melt of the suevite, at the time of deposition at high temperatures (up to 900°C in the suevite and >2000°C for the impact melt, Osinski et al., 2004). It was suggested that a very strong reverse polarity NRM in the suevite is the reason for the intense negative anomalies in the inner basin of the crater (Pohl, 1965; Pohl and Angenheister, 1969; Pohl et al., 1977a; 2010; Iseri et al. 1989; Arp et al., 2019). Despite the extensive amount of research, the magnetic characteristics and contribution of the shocked basement have not yet been constrained. Furthermore, the contiguous layers of impact melt in the Ries crater ubiquitously shows low NRM and κ, the reason for which is also unclear. Post-impact hydrothermalism is also reported in this crater (Osinski et al., 2004; Naumov, 2005; Osinski et al., 2013; Arp et al., 2013; Sapers et al., 2017), although with lower temperatures than in Chicxulub (max. 300° in the inner crater, 130°C in the outer regions, see Osinski, 2005) and with a shorter lifespan (max. 250 kyr, Arp et al., 2013). The influence that hydrothermalism had in the magnetic mineralogy and particularly in their magnetic properties also remains unexplored.

The aim of this study is to fill these knowledge gaps in the magnetic mineralogy of the Ries crater lithologies, with special focus on the magnetic properties of the shocked magnetite in the basement. We also constrained the influence of post-impact exposure to natural high temperatures in the basement due to the impactites and studied the influence of hydrothermal alteration on crater magnetism. We investigated drill cores from FBN73 and SUBO-18 (NR73 and SUBO henceforth) and collected surface samples from the megablock zone at four locations (Polsingen, Aumühle, Altenbürg and Wengenhausen). Through rock-magnetic, microscopical and mineral chemical methods, we discriminated pre-, syn- and post-impact geological processes, to gain insight into the different contributions to the magnetic anomaly. Based on our data and previous literature, we propose a conceptual model of the evolution of the magnetic phases before, during, and after the impact. Lastly, we present a short comparison between the Chicxulub and Ries crater system.

4.3. Geological Setting and Samples

4.3.1. Crater structure and stratigraphy

The ~26 km diameter Ries impact crater is located in southern Germany (Fig. 4.1a). It was formed in a sequence of layered Permian, Mesozoic and Oligocene/Upper Miocene sediments of ~600 m thickness, overlaying crystalline basement composed of Variscan granite, gneiss and amphibolite (Fig. 4.1b and 4.1c; e.g., Graup 1975). The age of the impact is dated to 14.808±0.038 Ma (Schmieder et al., 2018). This crater is classified as a complex impact structure (e.g. Pohl et al., 1977a), and is divided into an inner crater, delimited by the “inner ring” with ~12 km in diameter, and an outer megablock zone (Fig. 4.1b). The inner crater is characterized by shocked Variscan basement overlain by an allochthonous crater-fill deposit, called crater suevite (see e.g., Osinski et al., 2004), later covered by Tertiary crater-fill lake sediments (Fig. 4.1b, 4.1c and 4.2).

The inner ring consists of uplifted shocked basement and separates the inner crater from the megablock zone. The inner ring is also the boundary of the post-impact crater lake fill (Fig. 4.1c). The term “megablock” refers to “displaced fragments of all stratigraphic units of the target rocks, which are larger than 25 m in size and can be geologically mapped” (Pohl et al., 1977a). The megablocks are covered by the Bunte Breccia, an impact breccia derived predominantly from the Mesozoic sedimentary target (e.g., Fraas and Branco, 1901; Hüttner, 1969; Hörz et al., 1983). This is a poorly sorted, glass-free breccia which comprises the most volumetrically abundant proximal ejecta, interpreted as a continuous ejecta blanket (e.g., Oberbeck 1975; Morrison and Oberbeck 1978). Two drill cores were sampled for this study, one in the inner crater (NR73), and one on the inner flank of the inner ring (SUBO) (Fig. 4.1c and 4.2).

The most characteristic rock type of the Ries crater is suevite (Schwabenstein), described here for the first time (Sauer, 1920). Currently, suevite is defined as a polymict breccia with a particulate matrix, containing lithic and mineral clasts at all stages of shock metamorphism, including impact melt particles (e.g., Stöffler and Grieve, 2007). The suevite is described to consistently overlie the Bunte Breccia (Fig. 4.1b and 4.1c), and a distinction is made in literature between “main” and “basal” suevite (Bringemeier, 1994). The main suevite is unsorted and well consolidated, with abundant impact glass clasts, and a preferred horizontal orientation of flat glass clasts. This type is the most abundant, and we sampled it at Altenbürg and Wengenhausen, in the megablock zone (Fig. 4.1b). In contrast, the basal suevite is fine grained and poorly consolidated, moderately to well sorted, and deficient in glass clasts (e.g. Chao et al. 1978), which we sampled at the Aumühle quarry.

Coherent impact melt rock, or “red suevite” is rare in the Ries crater compared with other craters (e.g. Chicxulub). The question of “missing melt” in the Ries crater has been raised before (e.g., Graup, 1999; Grieve, 1999; Osinski, 2003, 2004; Osinski et al., 2004, 2008; Wünnemann et al., 2008; Pohl et al., 2010), however no concrete explanations have been provided so far. It occurs as isolated bodies with lateral extents of up to 50 m (Pohl et al., 1977a), and is found on the surface overlaying the Bunte Breccia, containing variably shocked basement (predominantly granite) and mineral clasts (predominantly quartz) (Engelhard et al., 1969, Pohl et al., 1977a). Alkali feldspar, plagioclase, quartz, and ilmenite comprise the microcrystalline groundmass (Osinski, 2004). This “red suevite” is sampled in Polsingen, and in parts of the borehole SUBO (Fig. 4.2).

4.3.2. Lithology of the drill cores

4.3.2.1. NR73

The scientific drilling project Nördlingen 73 was drilled in 1973 at about 3.5 km from the crater center in a region of negative magnetic anomaly (Fig. 4.1d). The borehole is 1206 m deep, and the core is the only one reaching the shocked crystalline basement at depth. It also comprises the longest continuous core of suevite in the crater (~200 meters, Fig. 4.2). The lithologies of interest are found below 314 m of post-impact sedimentary fill, and can generally be subdivided into three sections (e.g. Meyer et al., 2012):

Graded Suevite (314 – 331 m) is interpreted as subaerial fallback material from the ejecta plume (Jankowski, 1977). This section shows a transition from medium grained gravel at its base to silt at its top and is intercalated by pervasively altered breccias. The melt clasts in this subunit are weathered, but this weathering decreases with depth (Meyer et al., 2012).

Melt-Rich Suevite (331-520 m) refers to a section of suevite with an increased melt-clast content. Between 331 – 390 m the lithic and melt contents remain constant with a slight increase of grain size. From 390 m, large basement blocks intersect the suevite (e.g., Bauberger et al., 1974), and below 436 m the impact melt contents decrease until no melt can be discerned macroscopically in the suevite.

Shocked basement (520 -1206 m) refers to a sequence of Variscan basement (Graup, 1975) which has been shocked during the impact. An irregular sequence of gneiss, amphibolite and granite dominates between 520 m and 820 m, below which metabasites are predominant. We focused our sampling on the gneiss-amphibolite-granite sequence, where primary shocked magnetite grains are expected. We used available, low-resolution downhole magnetic susceptibility and NRM intensity data from literature (Fig. 4.2; after Pohl et al., 1977b) to select sampling intervals, attempting to sample regions at the stronger end of intensities of NRM and κ. The basement rocks are mostly continuous, disrupted locally by intercalations or dykes of melt-poor suevite, where melt particles are not macroscopically detectable. This suevite also shows a decreased grain size with depth. Some of these dikes have been interpreted as lateral intrusions by highly turbulent flow, during the crater forming processes (e.g., Stöffler et al., 1977; Stöffler 1977).

4.3.1.1. SUBO

SUBO was drilled in 2006 in the southern section of the inner ring at Enkingen, into a local negative magnetic anomaly (Pohl et al., 2010, Fig. 4.1d, 4.2). It has a total depth of ~100 m and consists of ~21 m of crater fill sediments (not considered in this study), and of 79 m of suevite and impact melt rock (Fig. 4.2, Pohl et al., 2010). The impact rock is a complex sequence of multiple brecciated suevite-melt lithologies, which we broadly subdivide into “suevite” (21.19 - 40 m), “clast-and-melt rich suevite” (41 - 58 m), and “impact melt” (58 - 99.98 m) units, after the dominant macroscopic characteristics described in Pohl et al. (2010).

Suevite (21.19 – 40 m) is characterized by a sandy-clayey matrix, without a carbonate component (Pohl et al., 2010). Here, the suevite is generally coherent, with varied amounts of melt clasts, and evidence of secondary carbonate impregnation (Pohl et al., 2010). Melt fragments show a preferred sub-horizontal orientation, and lithic clasts are abundant, mostly comprising felsic gneiss and granitoid basement (Pohl et al., 2010). The suevite unit also shows strong hydrothermal alteration, with the groundmass substantially altered to phyllosilicates, mainly illite and smectite as alteration products, and rare chlorite, together with both primary and secondary Fe-sulphides, mainly pyrite (Sapers et al., 2017).

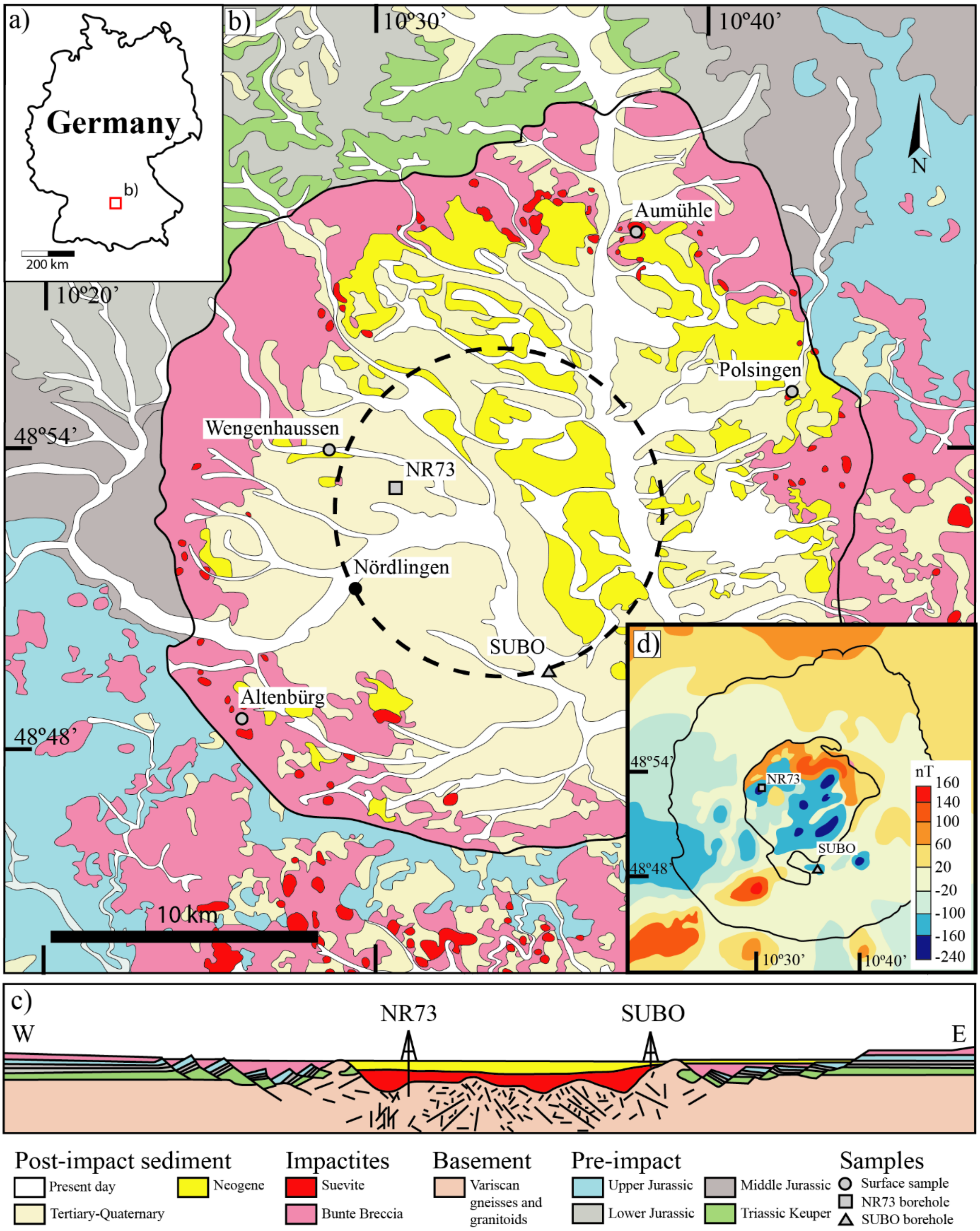

Figure 4.1. a) Geographic location of the Nördlinger Ries impact crater in Germany; b) lithological map of the Ries crater and sampling locations (modified after Zhao et al., 2022); c) Sketch of the crater profile (modified after Zhao et al., 2022); d) Aeromagnetic anomaly map (nT) (after Pohl et al., 2010).

Clast- and melt-rich suevite (41- 71 m) is friable and highly altered, with little core recovery. In this section, we sampled only a 3-meter-long section where the quality was suitable and coherent whitish pink suevite matrix contained increased impact melt and lithic clasts. From 58 – 71 m no cores were recovered.

Melt-rich suevite (71 - 99.98 m) is dominated by melt-clasts. A characteristic dark-red colour in the melt suggests the presence of hematite. Melt clasts form up to 80% of the rock, but individual melt bodies within the previously described white-pink groundmass can be found down to a depth of 86.24 m, locally intersected by suevite. From 86.24 m to 99.98 m, the remaining rock is a coherent and continuous section of impact melt rock.

Pohl et al. (2010) describes a pseudo-single domain (PSD) magnetite as the main ferrimagnetic mineral in SUBO, with sulfidic ferrimagnetic minerals such as pyrrhotite not described. In the crystalline basement clasts magnetite is suggested to be primary but secondary magnetite also occurs, produced by impact-induced thermal decomposition of mafic minerals. Hematite also is found in some samples. Magnetic modelling suggests that the granitic basement of the inner ring is located between 10-20 m below the bottom of the drill core (Pohl et al., 2010).

4.3.3. Hydrothermalism

Post-impact hydrothermal activity is a common feature in impact craters with impact melt-bearing lithologies and an elevated geothermal gradient in central uplifts being the main source of heat (e.g., Newsom 1980; Ames et al. 1998; Hode et al. 2004; Naumov 2005; Osinski et al., 2013). The hydrothermal alteration in the Ries crater is spatially extensive but not laterally continuous (Sapers et al., 2017). Pervasive and high-temperature alteration is restricted to the inner crater, where NR73 and SUBO were drilled. Ejecta in the megablock zone shows locally intense lower temperature hydrothermal alteration (Sapers et al., 2017).

As hydrothermal alteration is localized and concentrated within the suevite, their deposition at temperatures >750-900°C (Osinski et al., 2013) is suggested as dominant heat source. The initial melt temperature of the impact melt was also quite high (>2000°C) with relatively high-water content (>5 wt%) (Osinski et al., 2004), whose latent heat might also have played a role. Hydrothermal activity lasted up to ~250,000 yrs after the impact (Arp et al., 2013). A two-stage cooling is proposed in literature (e.g. Naumov, 2005; Sapers 2017), with a first stage involving rapid convection-driven cooling above boiling temperatures (ca. 200-300°C, Osinski, 2005) through steam generation and degassing, and a second stage with a long-lasting gradual cooling. The fluid sources are described to vary locally, but a combined contribution from both shallow and deep sources is likely, due to fluid-rock interaction with the different target lithologies. In the megablock zone meteoric water dominates, while in the inner crater the fluids derive from the crater lake and the high fracturing and disruption of the groundwater table (Sapers 2017). The heterogeneity of the fracture patterns will further contribute to the different alteration intensities found throughout the crater.

The most pervasive alteration is found in the inner crater, where the crater lake allowed for saturated conditions of the fluids (Osinski, 2005; Sapers 2017). The high temperature early stage is restricted to the crater suevite and is characterized by K-metasomatism throughout the upper sections (Osinski, 2005). Basement alteration is limited to minor albitization and chloritization, which also occurs in this early stage (Osinski, 2005). In the suevite, the main stage of alteration is characterized by a complete replacement of all impact glass and basement clasts, forming saponite, montmorillonite and analcite (Osinski, 2005). Alkali and calcic zeolites are predominant in the altered suevite, indicating weakly alkaline hydrothermal solutions. These alkaline fluids are further responsible for the deposition of goethite throughout the drill core NR73 as minor phase (Osinski, 2005).

To date, the hydrothermal alteration of core SUBO has not been investigated in detail. However, its location in the inner ring, the observation of crater-lake sediments and crater suevite suggest that the hydrothermal system affecting SUBO is comparable to that of NR73. It is unclear at which stage the formation of hematite in impact melt rocks and red suevite of SUBO occurred, as it can represent either a low-temperature hydrothermal phase or vapor deposition, or a combination of the two, like the surface melts in Polsingen (Osinski, 2004, 2005).

Alteration of surface suevite, including the Aumühle quarry (Sapers, 2017), is characterized by the formation of montmorillonite and Ba-phillipsite. The main alteration in this suevite is constrained to be below 100-130°C (Osinski, 2005) and have a slightly more acidic composition in contrast with the inner ring fluids (Muttik et al., 2011; Sapers et al., 2017).

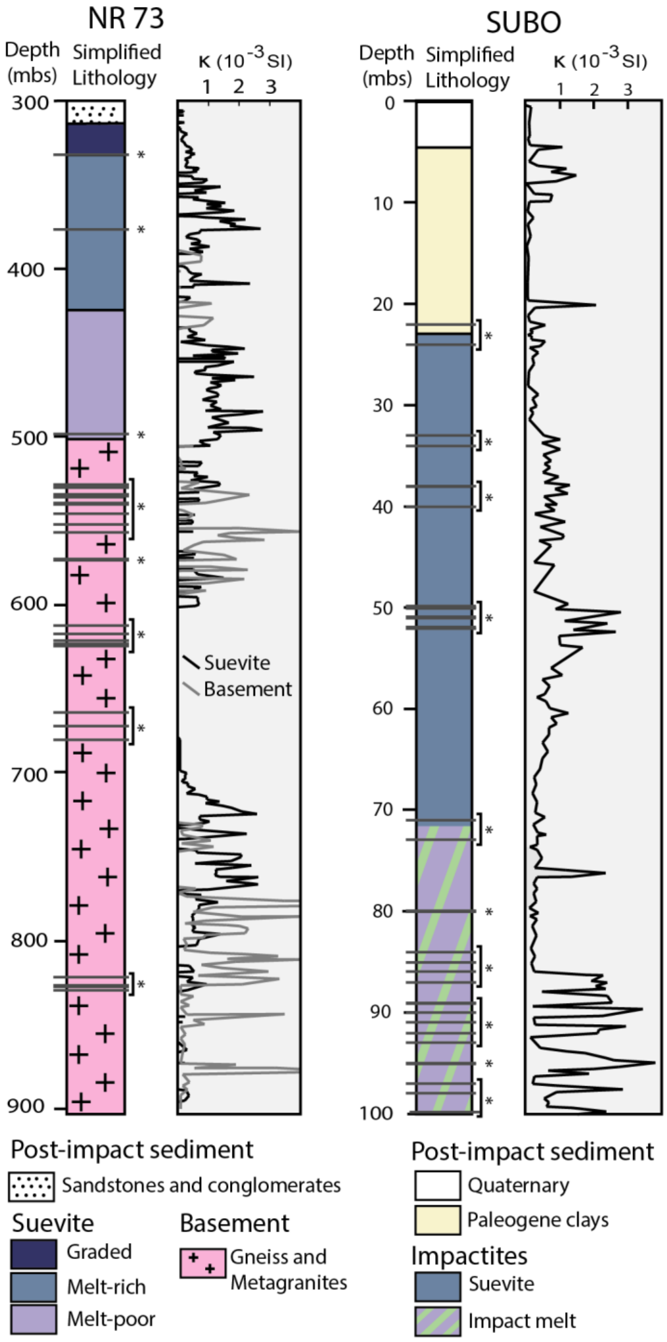

Figure 4.2. Simplified lithological units of boreholes NR73 and SUBO, with highlighted sample locations, and downhole magnetic susceptibility (κ) data. NR73 lithology and κ modified after Pohl et al., 1977b; SUBO lithology and κ modified after Pohl et al., 2010.

4.3.4. Rock magnetism

Previous research has been conducted on the characteristic magnetic anomaly patterns in the crater (Pohl, 1965, Pohl et al., 1977a, 2010). Spots of negative magnetic intensities are mostly concentrated in the inner ring (Fig. 4.1d) and the surface suevite in the western section of the megablock zone. Previous studies (Pohl, 1965; Pohl and Angenheister, 1969; Pohl et al., 1977a; 2010; Arp et al., 2019) have investigated surface samples and drill cores from Otting, Wörnitzostheim, NR73, SUBO and Erbisberg, and related the intense negative magnetic anomalies to a generally reverse polarity of NRM in the high temperature suevites. In surface samples, paleomagnetic directions with Dec/Inc = ~ 194°/-57° (Pohl and Angenheister, 1969) and Dec/Inc = 188.6°/-60.8° (α_{95} = 0.78°; Iseri et al. 1989) are described. These directions are consistent with an acquisition of magnetization at the time of impact. The studies further suggest that titanomagnetite with low Ti concentration is the main carrier of magnetization in the Ries suevite. Maghemite formed during low-temperature oxidation of titanomagnetite is also described, which records the same direction as the titanomagnetite, indicating a hydrothermal alteration shortly after the emplacement of the suevite (Iseri et al. 1989).

4.3.4.1. Surface Samples

Altenbürg shows the highest intensities of NRM (0.4 A/m), followed by Polsingen (0.2 A/m), and being the weakest at Aumühle (<0.1 A/m) (Pohl et al., 2010). The aim for resampling these surface samples was a discrimination between pre- and syn-impact magnetite formation, which may help to better understand the magnetic evolution and anomaly pattern distribution. Samples from the Wengenhausen location have never been studied before. Lastly, the sampling of the Polsingen melt rocks allows us a comparison with the melt sections of SUBO.

4.3.4.2. NR73

Previous data from NR73 have been published by Pohl, 1977a and 1977b (Fig. 4.2). These data show a consistent reverse inclination ~-60° and high average NRM intensity in the suevite (~2.7 A/m), despite a wide variation along the core. High intensity was only found in the suevite, while the shocked basement shows a scatter of positive and negative inclinations, with very low NRM intensities, and decreased magnetic susceptibility in the gneisses and granitoids, and higher values in metabasite sections at greater depths (Fig. 4.2, Pohl et al., 1977b). To our knowledge, no investigations of the magnetic mineralogy and properties of the shocked basement has been done until now, aside from the low-resolution downhole κ and NRM intensity data published by Pohl et al. (1977b) (see Fig. 4.2).

4.3.4.3. SUBO

A detailed magnetic survey including rock magnetic investigations was performed by Pohl et al. (2010) in the SUBO drill cores. This study confirmed again a stable reversed polarity magnetization in suevite, in a local negative magnetic anomaly (Fig. 4.1d). The inclination in the "melt" unit of the SUBO drill core shows the same ~-60° average inclination, but the reported intensity (1.5 A/m) is lower than those described from the NR73 drill cores. Magnetic susceptibility seems to be generally lower in the suevite (~0.5×10^{-3} SI), when compared with the impact melt rock (up to 8×10^{-3} SI), but conversely the melt has lower NRM intensities than the suevite. This leads to very high Koenigsberger (Q-) ratios in the suevite (10 to 40), while in the melt Q-ratios are generally lower (~5), but still showing a clear dominance of remanence over induced magnetization (Q>1).

4.4. Methods

4.4.1. Material

72 samples were used for this study, including four surface samples collected in the megablock zone (Fig. 4.1b), 32 samples from the drill core NR73 (Fig. 4.2, left), and 36 samples from the drill core SUBO (Fig. 4.2, right). All drill core samples were numbered according to their depth (Fig. 4.2).

Samples from NR73 comprise the shocked Variscan basement (25 samples), and suevite (seven samples, three of which are intercalated with basement blocks). Samples from SUBO comprise seven suevite samples, nine basement-melt intercalated samples, and 20 impact melt samples. All four surface samples comprise impact-melt rich suevite.

We provide all data files used for this study in Supplemental Files (SF). SF1 is a text file with a short overview of the contents of the remaining supplemental files. A list with sample names, depths and lithology can be found in Supplemental File SF2. See Appendix C.1. for a description of the contents of the supplemental files.

4.4.2. Microscopic and mineral chemical analysis

We performed transmitted and reflected light microscopy at the Karlsruhe Institute of Technology (KIT) using a Leitz polarizing microscope. For some samples, we applied oil-based ferrofluid coatings (FerroTec EMG 508 and EMG 905) for easier visualization of the ferromagnetic phases. 189 electron probe microanalysis (EPMA) spot-measurements and back-scattered electron (BSE) images were taken of 11 representative carbon-coated samples from suevite surface samples (three samples), NR73 (five samples) and SUBO (three samples) at the Deutsches GeoForschungsZentrum (GFZ) in Potsdam, Germany. We used a JEOL Hyperbole JXA-8530F PLUS microprobe, with five wavelength dispersive spectrometers (WDS) for quantitative analyses and an energy dispersive X-ray (EDX) detector for overview phase identification. For quantitative measurements, we applied 15 kV, 100 nA and a surface probe size of 2 µm. We used natural and synthetic standards for calibration of Cr, Mg, Fe, O, Al, Ti and Mn such as ASTIMEX$^{©}$ magnetite for Fe and O. This routine allowed us to measure individual element weight percentage (wt [%]), with oxygen measured individually, rather than oxide wt [%]. To obtain the spinel formula, we have performed two calculations, one assuming 4 oxygen molecules, and another assuming 3 cations, for stoichiometry control calculation. We present our results in the text assuming 4 oxygens for easier readability. Further, we calculated the average amount of vacancies in the magnetite measurements according to: Vacancies = 3 - [sum of cations], for the formulas normalized to 4 oxygens. Samples were checked randomly for further accessory elements using EDX, but no other elements appeared in quantities larger than the detection limits (≤100 ppm (1s)). Vacancies are therefore likely and well explainable by geochemical processes.

4.4.3. Rock magnetic methods

We performed temperature-dependent magnetic susceptibility measurements (κ-T), bulk-magnetization and bulk magnetic susceptibility measurements, as well as isothermal remanent magnetization (IRM) component and hysteresis loop analysis, to investigate the magnetic properties of our samples.

κ-T curves and bulk κ measurements were performed at the KIT using an AGICO (Brno, Czech Republic) KLY-4S kappabridge, at an applied field of 300 A/m and a frequency of 970 Hz. For κ-T experiments, we used a CS-L and CS-3 unit for the instrument, which allows us to make low-temperature and high-temperature measurements. Low-temperature “LT” measurements were performed by applying liquid nitrogen to the CS-L cryostat and cooling the sample down to ~-192°C and measuring κ throughout warming in contact with ambient atmosphere, which causes warming rates to be faster at the beginning of the experiment. High-temperature “HT” measurements were performed by heating the CS-3 furnace from room temperature (RT) up to 700°C, and cooling it to 40°C, at a constant rate of 12°C/min. High temperature measurements were performed in a flowing argon atmosphere (133 mL/min, Ar purity of 99.998%) to minimize oxidation. During the experiment, temperature is measured with a Pt resistance thermometer in contact with the samples. The accuracy of these thermometers is ±1°C up to 150°C, and ±3°C from 150°C up to 700°C (Lattard et al., 2006). Bulk κ measurements were also performed using the KLY-4S kappabridge, with an applied field of 300 A/m for all samples. Bulk κ is determined by averaging three measurements per sample and applying holder corrections to this average value.

NRM intensities were measured manually using an AGICO JR-5/5A Spinner Magnetometer at KIT. When samples did not have the standard cylindrical shape, cylindrical holders were used to maintain the material stable during measurement. The values were determined by averaging three measurements per sample and applying mass and holder corrections after measuring.

Hysteresis loops were measured to investigate the content of magnetic particles, the mineralogy and magnetic grain size. A Day diagram (Day et al., 1977) with SD-MD mixing lines (Dunlop, 2002) was prepared using the hysteresis parameters obtained from these loops. Our measurements were performed at the Institute of Geophysics of the Polish Academy of Sciences, in Warsaw, Poland, using an alternating gradient magnetometer (MicroMag AGM 2900, Princeton Measurement Corporation, USA) with a maximum operating field of 1T. We determined the hysteresis parameters coercivity (B_c), saturation magnetization (M_s) and remanent magnetization (M_{rs}) after applying paramagnetic contribution (high-field linear trend) correction, background signal correction, and mass normalization. The coercivity of remanence (B_{cr}) was estimated from direct current back-field demagnetization (DCD) of IRM.

DCD curves are also used for IRM modeling and were measured in the same instrument. Cumulative log-Gaussian functions were applied for a statistical analysis of the curves according to Kruiver et al. (2001). Three parameters describe the magnetic components: saturation isothermal remanent magnetization (SIRM), which is proportional to the magnetic mineral content in the sample; mean coercivity of remanence of the grain population that constitutes each component, at which half of the SIRM is reached ($B_{1/2}$), and dispersion parameter (DP), which corresponds to the individual cumulative log-normal distribution. We focus our discussion on the mean coercivity of remanence in the text for easier readability.

4.4.4. Magnetic transition temperatures and susceptibility parameters

We determined the magnetic transition temperatures from the measured κ-T curves applying the first derivate method for data where the transitions are well defined. In samples where this method is unreliable, we have used the tangent method described by Lied et al. (2020).

The Verwey transition temperature (T_v) was determined in samples where magnetite is present, using the LT-curves before (T_v1) and after (T_v2) heating. The Verwey transition for pure stoichiometric magnetite is -153°C (120 K, Verwey, 1939), and is very sensitive to physical (e.g., shock-induced lattice defects or internal crystal stresses, Carporzen and Gilder, 2010; Reznik et al., 2016; Biało et al., 2019) and chemical (e.g., cation substitution or vacancies, Aragón et al., 1985; Biało et al., 2019) alteration of magnetite.

We identified Curie temperatures from the HT-curves during heating (T_c1) and cooling (T_c2). This temperature characterizes the transition from ferro- to paramagnetic behavior in all magnetic minerals, and allows for a quick identification of the magnetic carriers. Pure magnetite has a characteristic sharp drop of κ at a temperature of 578°C, and deviations from this may indicate cation substitution (e.g., Engelmann, 2008; Lattard et al., 2006), or oxidation. Oxidation of non-substituted magnetite forms the oxidized end member maghemite (γ-Fe_2O_3), with a T_c up to 640ºC (e.g., Nishitani and Kono 1981; O'Reilly, 1984; Özdemir and Dunlop, 2010).

Both LT and HT measurements were normalized to the κ values at RT, and were used to determine three other parameters:

Verwey and *Hopkinson* peak ratios (T_vPR and HPR, respectively), which we use as proxy for magnetic domain states and their variation throughout heating. A decrease in these ratios after heating is associated with a change of magnetic behavior, consistent with an increase (real or apparent) in domain state, if chemical reactions can be excluded (Dunlop, 2014; Kontny et al., 2018; Mendes and Kontny, in press). T_vPR = $\kappa_{max}/\ \kappa_{15}$, where κ_{15} is κ value at 15 ºC and κ_{max} the maximum value around the Verwey transition (Kontny et al., 2018); HPR = $\kappa_{max}/\ \kappa_{40}$, where κ_{40} is κ value at 40ºC and k_{max} the maximum value before the Curie temperature (Dunlop, 2014).

The alteration parameter *A40* [%] characterizes the alteration occurring during the κ-T experiment, as a percentage increase or decrease of κ before and after heating to 700°C. A positive A40 value indicates a post-heating increase of κ, which may suggest the formation of a new ferromagnetic phase during heating (e.g., magnetite from hematite, Mendes et al., 2023; Mendes and Kontny, in press), or the relaxation of internal crystal lattice strain through thermal annealing (Kontny et al., 2018). A negative A40 indicates a decrease of κ during experiment, which may indicate syn-heating transformation to a mineral phase with lower κ (e.g., maghemite to hematite or titanomaghemite to ilmenite and magnetite).

Finally, the Koenigsberger (Q-) ratio, calculated as Q = NRM / (κ*B), discriminates the relative importance of remanent (Q>1) or induced magnetization (Q<1) in the total magnetization of a given sample. Total magnetization (M_t) is given by: M_t = NRM + (κ*B), where NRM is the intensity of the natural remanence magnetization, and κ*B is the induced magnetization (B is the present day's Earth magnetic field).

4.5. Results

4.5.1. Rock magnetic data

4.5.1.1. Surface samples

All suevite surface samples (n=4) show Q-ratios above 1 (Fig. 4.3a), ranging from 1.8 to 4.15, despite low NRM intensities (ranging from $2.6\text{x}10^{-4}$ to $37\text{x}10^{-4}$ A/m, Fig. 4.3b), and low κ (from $3.7\text{x}10^{-6}$ to $33.8\text{x}10^{-6}$ SI, Fig. 4.3a, 4.3b). Total magnetizations are quite low, ranging from $3.86\text{x}10^{-4}$ to $47.8\text{x}10^{-4}$ A/m, with the highest values in the Polsingen melt sample (Table 1).

4.5.1.2. NR73

The suevite samples (n=19) show a clear dominance of remanent magnetization (Q>1, Fig. 4.3a) with generally high κ (from $2000\text{x}10^{-6}$ to $12000\text{x}10^{-6}$ SI, Fig. 4.3b) and NRM (0.2 to 3 A/m, Fig. 4.3b). The total magnetization of the suevite is also quite strong, ranging from $2.16\text{x}10^{-2}$ in the suevite dykes in the basement, to 3.2 A/m in the upper suevite section, where it averages 2 A/m (Table 1) in agreement with earlier reports by Pohl et al., (1977b).

In the basement (n=29), the induced magnetization is dominant (Q<1, Fig. 4.3c), although generally low κ (ranging from $4.8\text{x}10^{-6}$ to $3500\text{x}10^{-6}$ SI, Fig. 4.3d) dominate, except for three outlier gneiss samples that locally show higher κ ($23700\text{x}10^{-6}$ up to $39100\text{x}10^{-6}$ SI). NRM intensity in the basement is also lower than in the suevites ($2.9\ \text{x}10^{-4}$ to $520\text{x}10^{-4}$ A/m), with exception of the same three outlier gneiss samples (NRM between 0.5 and 0.9 A/m) (Fig. 4.3d). Despite the lithological differences and the outliers, NRM and κ show a positive correlation (Fig. 4.3d). Total magnetizations are quite low in the basement, ranging from $5.44\text{x}10^{-4}$ to 0.9 A/m, averaging at 0.1 A/m, except for the abovementioned gneiss outliers, which range from 1.3 to 2.2 A/m (Table 1).

4.5.1.3. SUBO

All SUBO samples show a dominance of NRM over induced magnetization (Q>1), with the exception of one melt outlier (Fig. 4.3a, 4.3e). The suevite samples (n=6) show low κ (from $4.2\text{x}10^{-6}$ to $45\text{x}10^{-6}$ SI) and low NRM intensities ($4.5\ \text{x}10^{-4}$ to $70\text{x}10^{-4}$ A/m) (Fig. 4.3b), comparable to the values from the surface samples. One suevite sample is an outlier with higher κ of 208x10^{-6} SI and NRM intensity of 5x10^{-2} A/m. Total magnetizations range from 0.06x10^{-2} to 6.30x10^{-2} A/m, averaging at ~0.014 A/m, two orders of magnitude lower than the suevite in NR73 (Table 1).

In the melt samples (n=28) κ shows a broad range but is generally higher than in the suevite (from 12x10^{-6} to 4900x10^{-6} SI, average of 943x10^{-6} SI, Fig. 4.3e, 4.3f; Table 1). NRM intensity follows the same trend, with a wide range but generally higher values than in the suevite (from 4.4x10^{-3} to 0.5 A/m, average of 0.13 A/m; Fig. 4.3f). Melt sample 80-II was excluded from our analysis, as it showed negative NRM and κ results. Total magnetization ranges between 0.007 and 0.55 A/m, averaging at 0.161 A/m, one order of magnitude higher than the suevites from SUBO, but one order of magnitude lower than the suevites of NR73 (see compare Figs. 3b and 3f; Table 1).

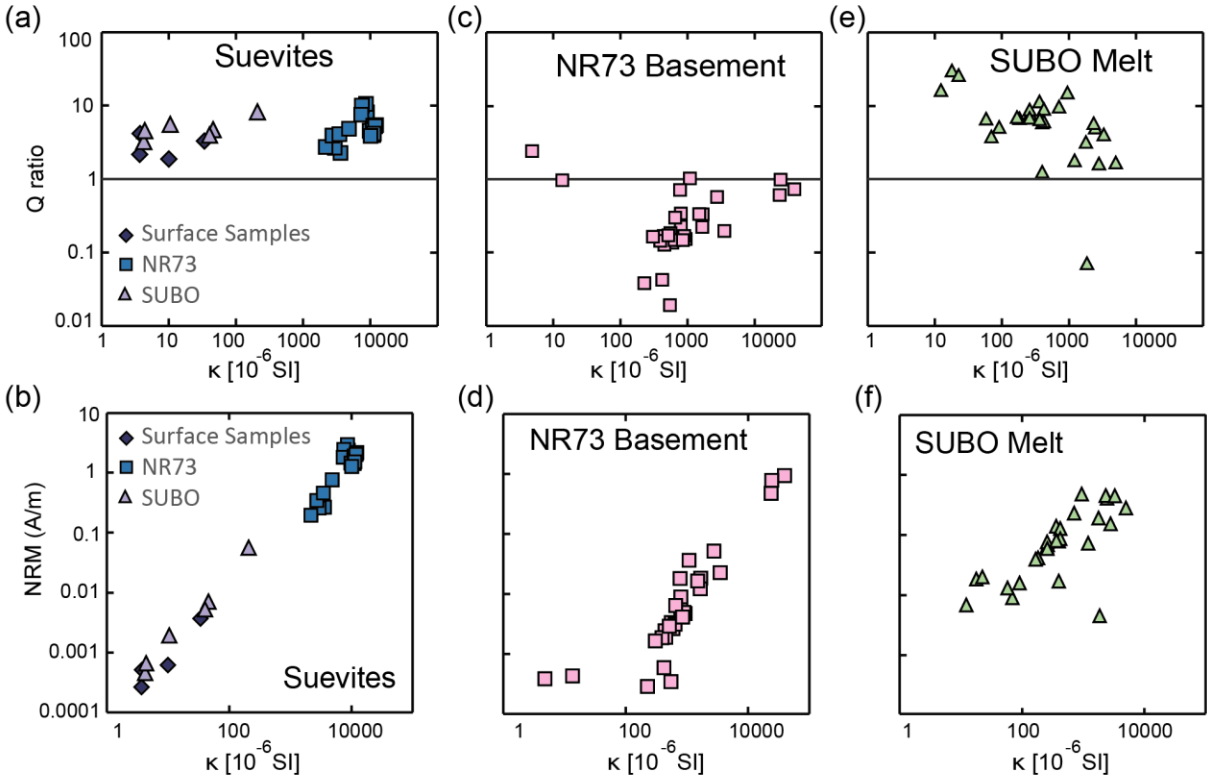

Figure 4.3. Rock magnetic properties: κ = Magnetic susceptibility [SI]; Natural remanent magnetization (NRM) intensity [A/m]; Koenigsberger (Q-) ratios, by sample lithology. a) Suevite samples all demonstrate NRM control of magnetization (Q>1); b) Suevite samples show very strong NRM and κ in the NR73 suevites, and similar values in the suevites in SUBO-18 and surface samples; c) Basement of NR73 demonstrates induced magnetization is the main control of magnetization (Q<1); d) intensity of NRM and κ values are strongly reduced in the basement; e) SUBO-18 melt samples demonstrate NRM control of magnetization; f) SUBO-18 met samples demonstrate generally low NRM intensities, and intermediate κ.

4.5.2. Magnetic grain size and magnetic component analysis

Hysteresis data are plotted in a Day diagram (Day et al., 1977; Fig. 4.4) showing the M_{rs}/M_s and B_{cr}/B_c ratios, which are distributed along the MD-SD (multi-domain and single-domain) mixing lines of magnetite (Dunlop et al., 2002). IRM component analysis are presented as Gradient Acquisition Plots (GAPs), and complimentary Linear Acquisition Plots (LAPs) in Fig. 4.5. Table 2 shows average coercivity of remanence ($B_{1/2}$, shortened to “coercivity” for easier readability) and component contribution to the total magnetization signal [%]. Supplemental file SF3 has all IRM and hysteresis data used in this section, including Supplemental Table (ST) ST3, which contains extra parameters for each sample.

4.5.2.1. Surface samples

The suevite surface samples show pseudo-single domain (PSD) behaviour in the Day diagram (Fig. 4.4), and three out of four samples possess a single component of magnetization with average coercivity between 40 and 52 mT, which is interpreted as PSD magnetite (Fig. 4.5, Table 2). The melt rich Polsingen sample shows a second high coercivity (1778 mT) component with a contribution of 36%, which we interpret as hematite.

Table 4.1. Rock magnetic parameters. κ – magnetic susceptibility; κ*B – Induced magnetization; NRM – Natural Remanent Magnetization; Q – Koeningsberger ratio; Mt = Total Magnetization, given by NRM + κ *B

Sample	κ [SI]	(κ*B)	NRM [A/m]	Q	M total [A/m]
Surface Samples					
Altenburg	9.98E-06	0.0003	0.0006	1.87	0.001
Aumühle	3.70E-06	0.0001	0.0003	2.17	0.000
Polsingen	3.38E-05	0.0011	0.0037	3.30	0.005
Wengehausen	3.75E-06	0.0001	0.0005	4.15	0.001
SUBO					
SUBO-22	4.23E-06	0.0001	0.000	3.23	0.001
SUBO-24	4.39E-06	0.0001	0.001	4.55	0.001
SUBO-33	1.05E-05	0.0003	0.002	5.55	0.002
SUBO-38-I	2.08E-04	0.0068	0.056	8.20	0.063
SUBO-38-II	4.56E-05	0.0015	0.007	4.69	0.009
SUBO-40	4.03E-05	0.0013	0.005	3.95	0.007
SUBO-50-I	2.57E-04	0.0084	0.062	7.38	0.071
SUBO-50-II	6.98E-05	0.0023	0.009	3.83	0.011
SUBO-50-III	3.98E-04	0.0131	0.077	5.91	0.091
SUBO-50-IV	5.80E-05	0.0019	0.013	6.70	0.015
SUBO-50-V	1.80E-05	0.0006	0.018	30.42	0.019
SUBO-51-I	1.83E-04	0.0060	0.041	6.76	0.047
SUBO-51-II	2.63E-04	0.0086	0.068	7.83	0.076
SUBO-52-I	1.67E-04	0.0055	0.039	7.03	0.044
SUBO-52-II	2.58E-04	0.0085	0.076	8.91	0.084
SUBO-71	7.11E-04	0.0234	0.228	9.76	0.252
SUBO-73	2.26E-05	0.0007	0.020	26.32	0.020
SUBO-80-I	9.47E-04	0.0312	0.476	15.26	0.507
SUBO-84	3.63E-04	0.0120	0.138	11.53	0.150
SUBO-85	1.23E-05	0.0004	0.007	16.43	0.007
SUBO-86	1.85E-03	0.0610	0.004	0.07	0.065
SUBO-87	9.11E-05	0.0030	0.015	5.17	0.018
SUBO-89-I	4.00E-04	0.0132	0.017	1.27	0.030
SUBO-89-II	2.46E-03	0.0810	0.409	5.05	0.490
SUBO-90	2.34E-03	0.0770	0.448	5.82	0.525
SUBO-91	4.22E-04	0.0139	0.126	9.10	0.140
SUBO-92-I	4.98E-03	0.1641	0.278	1.69	0.442
SUBO-92-II	2.59E-04	0.0085	0.058	6.86	0.067
SUBO-93	4.21E-04	0.0139	0.085	6.14	0.099
SUBO-95-II	2.79E-03	0.0919	0.151	1.65	0.243
SUBO-95-II	3.29E-03	0.1084	0.444	4.09	0.552
SUBO-97	3.66E-04	0.0120	0.079	6.59	0.091
SUBO-98	1.21E-03	0.0397	0.072	1.81	0.111
SUBO-100	1.79E-03	0.0589	0.189	3.21	0.248

Sample	κ [SI]	(κ*B)	NRM [A/m]	Q	M total [A/m]
NR73					
NR73-332 S	3.6E-03	0.1172	0.268	2.28	0.385
	2.9E-03	0.0968	0.259	2.67	0.355
NR73-376 S	1.1E-02	0.3621	1.437	3.97	1.799
	8.9E-03	0.2913	2.367	8.13	2.658
	8.5E-03	0.2811	2.968	10.56	3.249
	7.4E-03	0.2446	2.455	10.04	2.700
	7.3E-03	0.2396	1.816	7.58	2.056
NR73-475 S	1.1E-02	0.3621	1.899	5.25	2.261
	1.1E-02	0.3588	1.920	5.35	2.279
	1.2E-02	0.3983	2.167	5.44	2.565
NR73-498 SG	9.7E-03	0.3203	1.461	4.56	1.781
	1.1E-02	0.3555	1.662	4.68	2.017
	1.2E-02	0.3884	2.039	5.25	2.427
	1.1E-02	0.3686	1.531	4.15	1.900
	1.0E-02	0.3291	1.279	3.89	1.608
NR73-528 Gn	9.3E-04	0.0308	0.005	0.15	0.035
NR73-529 Gn	5.9E-04	0.0195	0.003	0.14	0.022
NR73-530 Gn	3.9E-02	1.2869	0.943	0.73	2.230
NR73-530 Gn-II	7.9E-04	0.0261	0.006	0.23	0.032
NR73-534 Gn	1.7E-03	0.0553	0.018	0.33	0.074
NR73-535 Gn	1.1E-03	0.0356	0.036	1.02	0.072
NR73-536 Gn	2.8E-03	0.0905	0.052	0.57	0.143
NR73-539 Gn	2.3E-04	0.0075	0.000	0.04	0.008
NR73-540 SG	4.2E-04	0.0139	0.001	0.04	0.014
NR73-546 SG	3.5E-03	0.1155	0.023	0.20	0.138
NR73-552 SG	8.0E-04	0.0262	0.009	0.34	0.035
NR73-557 Gn	5.5E-04	0.0182	0.003	0.18	0.022
NR73-573 Gn	8.9E-04	0.0294	0.005	0.17	0.034
NR73-574 Gn	4.4E-04	0.0145	0.002	0.17	0.017
NR73-612 Gn	1.7E-03	0.0546	0.012	0.22	0.067
NR73-617 A	4.5E-04	0.0148	0.002	0.13	0.017
	3.9E-04	0.0129	0.002	0.15	0.015
NR73-621 Gn	6.4E-04	0.0211	0.003	0.15	0.024
NR73-623 Gn	6.5E-04	0.0215	0.006	0.30	0.028
NR73-624 Gn	1.4E-05	0.0004	0.000	0.97	0.001
NR73-629 Gn	4.8E-06	0.0002	0.000	2.42	0.001
NR73-630 Gn	2.4E-02	0.7801	0.477	0.61	1.257
	2.4E-02	0.7998	0.787	0.98	1.586
NR73-664 Gn	7.7E-04	0.0254	0.018	0.71	0.044
NR73-672 Gn	5.2E-04	0.0170	0.003	0.17	0.020
NR73-680 SG	2.2E-03	0.0711	0.195	2.75	0.266
	2.7E-03	0.0889	0.346	3.90	0.435
	3.4E-03	0.1132	0.461	4.08	0.575
	4.8E-03	0.1573	0.764	4.86	0.922
NR73-820 MB	5.5E-04	0.0180	0.000	0.02	0.018
NR73-826 MB	3.0E-04	0.0100	0.002	0.16	0.012
NR73-827 MB	8.5E-04	0.0280	0.004	0.15	0.032
NR73-829 MB	1.5E-03	0.0492	0.017	0.34	0.066

4.5.2.2. NR73

The basement samples from NR73 show PSD behavior (Fig. 4.4), with generally low M_{rs}/M_s values (< 0.2), and two outlier samples that move further into the MD+PSD area (Fig. 4.4). Suevite samples also show PSD behavior, despite a wider distribution and a trend to higher M_{rs}/M_s values (Fig. 4.4). IRM component analysis does not show a clear distinction from suevite, with 30 out of 35 analyzed samples showing a single component, with coercivity ranging between 23 and 68 mT (average of 40 mT). Five samples show two components, three of which show a 13-25% high-coercivity component contribution (1000-1412 mT), which we interpret as hematite. One suevite sample shows a medium-coercivity component (200 mT) with a contribution of 17%, which we interpret potentially as Ti-maghemite (Table 2).

4.5.2.3. SUBO

Suevite samples from SUBO show similar apparent PSD domain state, but generally with higher M_{rs}/M_s than the NR73 suevites (Fig. 4.4). IRM component analysis suggests a single component of magnetization with coercivity ranging from 55 to 87 mT, averaging at 68 mT. This phase is interpreted as high-coercivity magnetite, suggesting magnetic domain states of fine PSD or SD. All melt samples show a mean component coercivity ranging from 40 to 112 mT (average at 68 mT, like the suevites), which we also interpret as relatively fine PSD or SD magnetite. 22 out of 34 samples show a second component, which we separate into two categories: "medium-coercivity" (200-500 mT), and "high-coercivity" (500-1258 mT). Ten samples show the "medium-coercivity" component, which we interpret as being potentially Ti-maghemite with contributions ranging from 5% to 12%. The "high-coercivity" component is present in 12 samples, which we interpret as hematite, with contributions between 5% and 34%. Melt samples generally show high coercivity PSD state behavior in the Day diagram, with some plotting close to the PSD+SD area, suggesting fine magnetic grain sizes (Fig. 4.4). The results from both suevite and melt in SUBO do not fit within the SD-MD mixing lines from Dunlop et al. (2002) (Fig. 4.4), likely due to the presence of a significant amount of non-magnetite components, which limits the interpretations that can be made from the Day diagram (see Roberts et al., 2018). For this reason, we evaluate the domain state primarily from high-coercivity results of the IRM modelling.

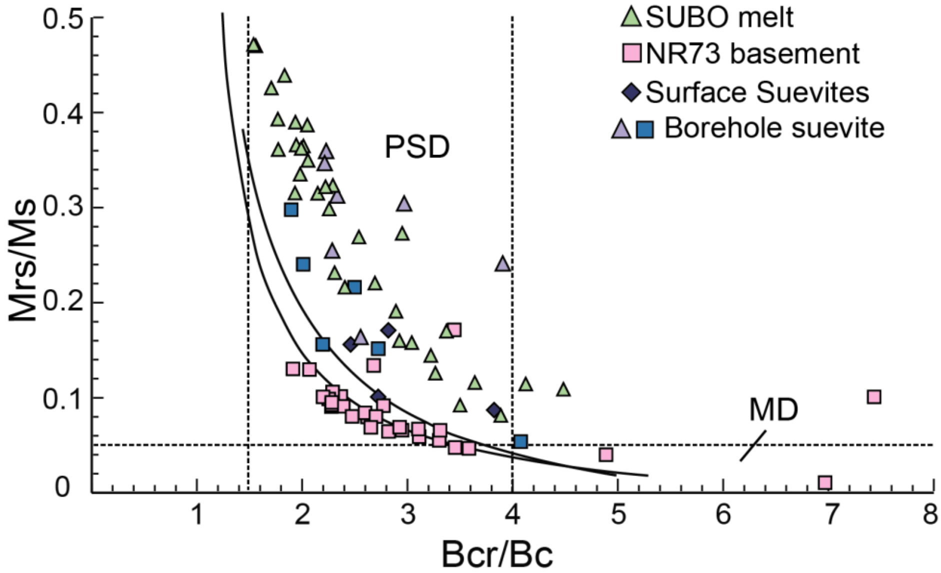

Figure 4.4. Day diagram (Day et al., 1977) with SD-MD mixing lines (Dunlop et al., 2002) for hysteresis data of our samples. SD – Single Domain, PSD – Pseudo Single Domain. Note a preferential close clustering of domain states in basement of NR73 along the SD-MD mixing lines, and a tendency of SUBO melts towards PSD+SD mixed compositions.

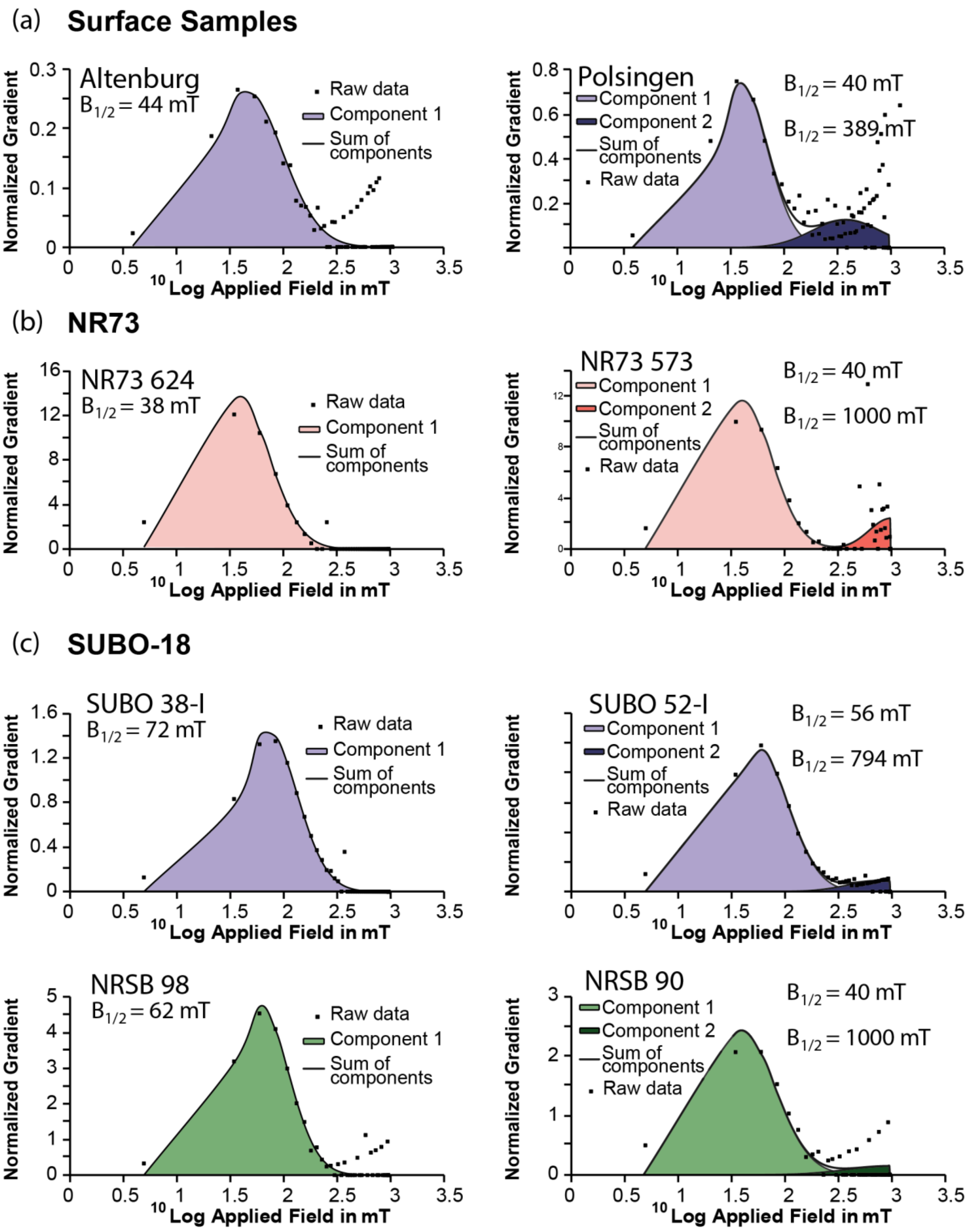

Figure 4.5. IRM component analysis GAP and LAP for representative samples; a) Surface samples with one (left) and two (right) components; b) NR73 shocked magnetite with one (left) and two (right) components; c) SUBO suevite samples with one and two components (top left and right, respectively), and SUBO melt samples with one and two components (bottom left and right, respectively).

Table 4.2. IRM modelling component contribution and average grain population coercivity ($B_{1/2}$) for all our samples, see text for details.

Sample	Component 1		Component 2	
	Cont [%]	B(1/2) [mT]	Cont [%]	B(1/2) [mT]
Surface Samples				
Altenbürg	100	43.7	-	-
Aumühle	100	52.5	-	-
Polsingen	64	41.7	36	1778.3
Wengenhaussen	100	39.8	-	-
NR73				
NR73-332 S	100	67.6	-	-
NR73-376 S	83	44.7	17	199.5
NR73-475 S	100	57.5	-	-
NR73-498 SG	100	57.5	-	-
NR73-528 Gn	100	41.7	-	-
NR73-529 Gn	100	36.3	-	-
NR73-530 Gn	100	38.0	-	-
NR73-530 Gn-II	100	33.1	-	-
NR73-534 Gn	100	43.7	-	-
NR73-535 Gn	100	28.2	-	-
NR73-536 Gn	100	30.2	-	-
NR73-539 Gn	100	42.7	-	-
NR73-540 Gn	100	40.7	-	-
NR73-546 S	100	38.0	-	-
NR73-552 SG	87	39.8	13	1000.0
NR73-557 S	100	35.5	-	-
NR73-557 G	100	35.5	-	-
NR73-573 Gn	100	25.1	-	-
NR73-574 Gn	86	33.9	14	1412.5
NR73-612 Gn	100	28.8	-	-
NR73-617 A	75	63.1	25	1000.0
NR73-621 Gn	100	33.1	-	-
NR73-623 Gn	100	38.0	-	-
NR73-624 Gn	100	39.8	-	-
NR73-629 Gn	50	36.3	50	398.1
NR73-630 Gn	100	40.7	-	-
NR73-664 Gn	100	33.9	-	-
NR73-672 Gn	100	31.6	-	-
NR73-680 SG	100	29.5	-	-
NR73-820 MB	100	60.3	-	-
NR73-826 MB	100	22.9	-	-
NR73-827 MB	100	28.2	-	-
NR73-829 MB	100	30.9	-	-
SUBO				
SUBO-22	100	83.2	-	-
SUBO-24	100	87.1	-	-
SUBO-33	91	57.5	9	223.9
SUBO-38-I	100	72.4	-	-
SUBO-38-II	100	55.0	-	-
SUBO-40g	100	58.9	-	-
SUBO-40m	100	58.9	-	-
SUBO-50-I	100	69.2	-	-
SUBO-50-II	100	66.1	-	-
SUBO-50-III	100	60.3	-	-
SUBO-50-IV	88	44.7	12	398.1
SUBO-50-V Red	88	63.1	12	446.7
SUBO-50-V Wht	100	70.8	-	-
SUBO-51-I	92	56.2	8	251.2
SUBO-51-II	96	60.3	4	794.3
SUBO-52-I	93	56.2	7	794.3
SUBO-52-II g	80	60.3	20	1258.9
SUBO-52-II m	100	66.1	-	-
SUBO-71	95	97.7	5	794.3
SUBO-73	90	89.1	10	1000.0
SUBO-80-I	93	74.1	7	501.2
SUBO-80-II	94	69.2	6	501.2
SUBO-84 Gn	95	100.0	5	501.2
SUBO-84 M	84	79.4	16	489.8
SUBO-85	100	93.3	-	-
SUBO-86	100	75.9	-	-
SUBO-87	88	72.4	12	631.0
SUBO-89-I Gn	100	95.5	-	-
SUBO-89-I M	76	47.9	24	707.9
SUBO-89-II	91	74.1	9	1000.0
SUBO-90	93	39.8	7	1000.0
SUBO-91	100	66.1	-	-
SUBO-92-I	95	44.7	5	251.2
SUBO-92-II	100	70.8	-	-
SUBO-93	95	67.6	5	316.2
SUBO-95-II	90	47.9	10	794.3
SUBO-95-II	66	46.8	34	933.3
SUBO-97	100	63.1	-	-
SUBO-98	100	61.7	-	-
SUBO-100	94	66.1	6	1000.0

4.5.3. Texture and composition of magnetic phases

4.5.3.1. Surface samples

In the Altenbürg suevite the main magnetic phase is magnetite, with small and round void-filling skeletal textures, and grain sizes ranging from ~5 to 10 μm, often grown in multi-grain clusters up to 50 μm in diameter (Fig. 4.6a). In this suevite, some very rare, fractured magnetite grains (~40 μm) were also observed. EPMA analysis indicate that the non-fractured granular grains show compositions near magnetite ($Fe_{2.86}Al_{0.02}Ti_{0.01}Mg_{0.01}O_4$, n=32) with a small number of vacancies (Vacancies = 0.1, see Table 3), indicating some cation deficiency. Vacancies are formed from the oxidation of ferrous Fe due to low-temperature hydrothermal alteration or weathering according to 2 Fe^{2+} = Fe^{3+} + vacancy (Dunlop and Özdemir, 2000). These results suggest some degree of maghemitization of magnetite.

The very melt-rich suevite samples from Polsingen present both magnetite and hematite as the main magnetic phases according to our rock magnetic data. Macroscopically, the samples show a red color, while microscopically hematite shows skeletal (~5μm) growth around and along fractures in quartz crystals. Other oxides contain very high Ti concentrations and are grown as skeletal grains and "clusters" like magnetite in the Altenbürg suevite (Fig. 4.6b). EPMA of suitable grains (n=6) suggests this is a member of the pseudobrookite series ($Fe_{1.89}Ti_{0.67}Mg_{0.16}Al_{0.05}Mn_{0.01}O_5$; SF4, and ST4).

Aumühle suevite does not show any microscopically visible magnetic phase. The Fe-rich phase in this sample consists of cation-substituted and cation-deficient ilmenite ($Ti_{0.89}Fe_{0.67}Mg_{0.03}Mn_{0.01}O_3$, n=36) (Fig. 4.6c; SF4, and ST4).

4.5.3.2. NR73

The main magnetic phase in all lithologies of NR73 is magnetite. In suevite, there is a mix of inherited, shock-fractured magnetite from the basement, and newly formed magnetite. The new magnetite is generally idiomorphic and non-fractured, with grain sizes ranging from ~5 μm up to ~100 μm (Fig. 4.6d). Like in surface suevite, some fractured basement magnetite grains are also found. EPMA analysis (n=14) show low cation substitution in this magnetite ($Fe_{2.99}Ti_{0.01}O_4$) and no vacancies (Table 3). However, one spot measurement indicated that locally some of these non-fractured magnetite grains may show a higher cation-substitution ($Fe_{2.68}Ti_{0.12}Mn_{0.01}Al_{0.01}O_4$), but these grains are very rare (only once observed, see SF4 and ST4).

In the gneiss basement, the magnetite grains are fractured and larger than in the suevite (up to ~200 μm; see Fig. 4.6e and 4.6f). These grains often show ilmenite either filling the fractures in magnetite (see Fig. 4.6e), or intergrown with magnetite (Fig. 4.6f), suggesting that some of the ilmenite is secondary and post-impact. EPMA show that magnetite compositions range from $Fe_{3.02}Cr_{0.01}Al_{0.01}Ti_{0.01}O_4$ to $Fe_{2.93}Ti_{0.01}Al_{0.01}O_4$ (in two samples with n=15 and n=10, see Table 3), with a low vacancy concentration (0 to 0.05). Secondary ilmenite shows a range of compositions from $Ti_{0.76}Fe_{0.73}Mn_{0.24}O_3$ to $Fe_{0.86}Ti_{0.85}Mn_{0.12}O_3$ (SF4 and ST4).

Magnetite from the metabasite basement show a very chromium-rich composition (n=10, $Fe_{2.86}Cr_{0.11}Ti_{0.01}O_4$) and in average a vacancy concentration of 0.13. These magnetite grains occur as dusty grains in silicates (~5-10 μm) and as lightly fractured larger xenomorphic grains (~100 μm) between silicate crystals, fractured during impact (Fig. 4.6g), which we interpret as preserved primary magmatic or metamorphic textures of pre-impact origin. Cation-substituted and cation-deficient ilmenite ($Ti_{0.91}Fe_{0.73}Mn_{0.16}Mg_{0.01}O_3$, n=15) is also present in the metabasite with textures like the magnetite, suggesting a congenic formation of both Fe-oxide phases.

4.5.3.3. SUBO

In the suevite and melt-rich suevite sections (21.19 to 86.24), mostly pyrite and Fe-carbonates occur (see raw and EDX data in SF 3 - EPMA). When Fe-oxides are present, only very small hematite grains are identified. Only in the continuous impact melt rock (86.24 to 99.98), sample 90 shows magnetite grains large enough to be measured by EPMA. Most of the grains is very small (~5-10 μm) with some exceptions where measurement is possible (Fig. 4.6h, 4.6i). These grains are not fractured, show globular shapes that appear to fill pore spaces (Fig. 4.6h and 4.6i), and are often intergrown with other oxides, generally hematite and ilmenite (Fig. 4.6h and 4.6j, see SF4, Table 2). Where magnetite was observed, the compositions are slightly cation-substituted ($Fe_{2.75}Ti_{0.08}Al_{0.05}Mg_{0.01}O_4$) and cation-deficient (vacancies = 0.11).

In addition to chemical composition, Table 3 shows the calculations of expected Curie temperatures for each composition, using the empirical formula described in Engelmann (2008) for comparison with the measured Curie temperature.

4.5.4. Magnetic transition temperatures

4.5.4.1. Classification of κ-T curves

We subdivided four different types according to their main features in the heating κ-T curves. Frequently the κ-T curves are irreversible, with the heating curves reflecting the original magnetic phases. Mineral reactions during heating may mask this phase in the cooling curve, which in turn provides insight into the alteration of the sample.

Type 1 shows paramagnetic behavior in the LT measurement and heating curve. We classify a curve as type 1a if both heating and cooling curves are reversible and paramagnetic (see “AUM1 - Type 1a”, in Fig. 4.7a). Type 1b curves show paramagnetic behavior in the heating curve, but irreversible cooling curves with a strong increase of κ, a large bump between around 200 to 400°C, and generally a A40 >100% (e.g., “WEN1 - Type 1b”, Fig. 4.7a), indicating the formation of a ferrimagnetic phase during the measurement.

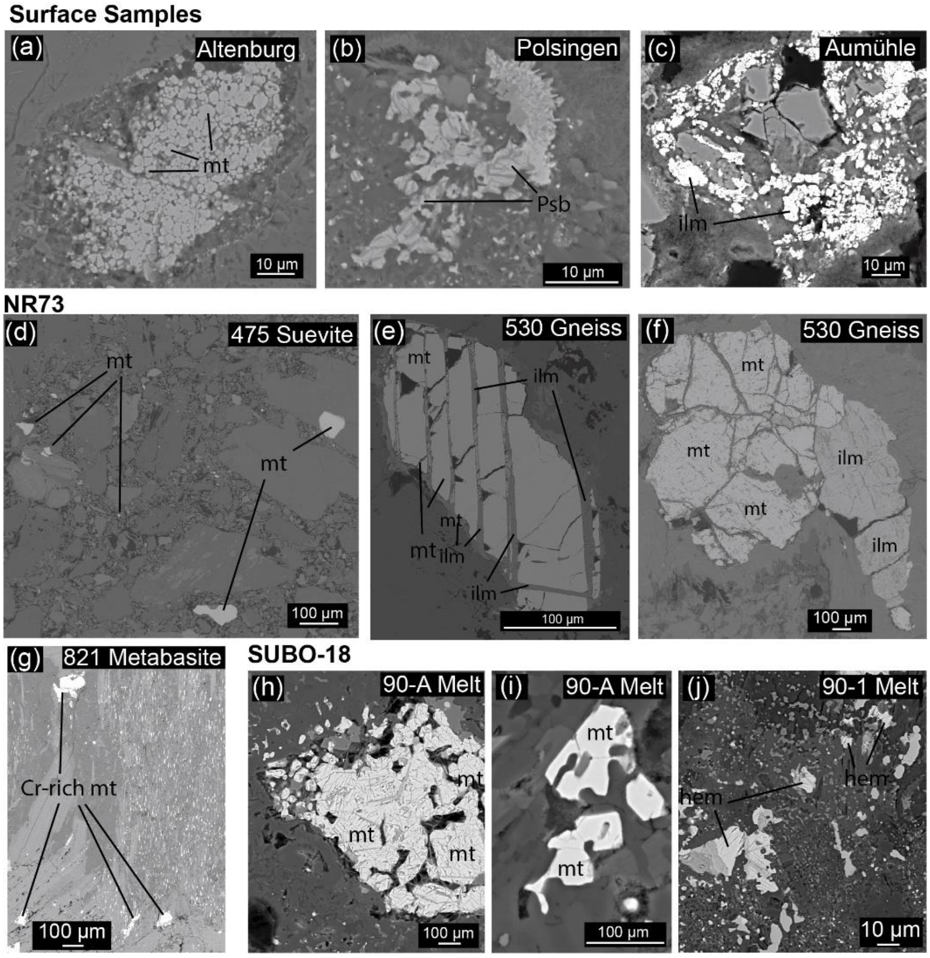

Figure 4.6. Back scattered electron images obtained from electron probe microanalysis (EPMA) of representative grains. mt=magnetite, hem=hematite, ilm=ilmenite, psb=pseudobrookite. a) small and round, void-filling grains, melt-derived, from Altenbürg; b) void-filling textured pseudobrokite-series grain in the Polsingen melt sample; c) secondary ilmenite deposited along cracks of fractured grains in suevite from Aumühle; d) small, newly-formed magnetite grains in the suevite of NR73; e) fractured magnetite grain in the basement of NR73 – note the ilmenite deposited in shock fractures of magnetite; f) shock fractured magnetite and shocked fractured primary ilmenite intergrowth in the basement of NR73; g) Cr-rich skeletal grains in the metabasite sample in NR73; h-j) Examples of suitable, larger-than-usual grains that allowed for EPMA analysis, from the SUBO melt sample 90.

Table 4.3. Averaged Electron Probe Microanalysis data, in wt % and cation contribution per formula unit of surface, NR73, and SUBO-18 samples, refer to text or details. In brackets standard deviations (1s) are given.

	Altenbürg	NR73-475 S	475 Ti-rich	NR73-530 Gn	NR73-530 Gn-II	NR73-821MB	SUBO-90
n	**32**	**14**	**1**	**15**	**10**	**10**	**7**
O	28.09 (1.56)	27.36 (0.56)	28.82	27.21 (0.58)	28.4 (0.49)	27.58 (0.58)	27.91 (1.17)
Cr	0.05 (0.03)	0.07 (0.04)	0.02	0.24 (0.02)	0.03 (0.01)	2.56 (0.51)	0.06 (0.07)
Fe	69.83 (2.00)	71.4 (0.43)	67.46	71.65 (0.35)	67.2 (0.20)	68.87 (0.80)	66.69 (2.29)
Mn	0.07 (0.04)	0.05 (0.04)	0.35	0.02 (0.01)	0.89 (0.02)	0.10 (0.03)	0.11 (0.09)
Al	0.24 (0.19)	0.04 (0.03)	0.11	0.09 (0.04)	0.11 (0.05)	0.023 (0.01)	0.56 (0.48)
Mg	0.13 (0.08)	0.01 (0.01)	n.d.	n.d.	0.01 (0.00)	0.02 (0.00)	0.13 (0.10)
Ti	0.19 (0.29)	0.12 (0.11)	2.54	0.11 (0.04)	2.62 (0.10)	0.13 (0.04)	1.60 (1.00)
Total	98.61 (0.45)	99.06 (0.67)	99.31	99.32 (0.65)	99.27 (0.67)	99.29 (0.81)	97.07 (0.72)
Cr	-	-	-	0.01 (0.00)	-	0.11 (0.02)	-
Fe2+	1.41 (0.00)	1.41 (0.00)	1.41	1.41 (0.00)	1.41 (0.00)	1.41 (0.00)	1.41 (0.00)
Fe3+	1.45 (0.21)	1.58 (0.10)	1.27	1.61 (0.07)	1.52 (0.05)	1.45 (0.06)	1.34 (0.21)
Mn	-	-	0.01	-	-	-	-
Al	0.02 (0.01)	-	0.01	0.01 (0.00)	0.01 (0.00)	-	0.05 (0.04)
Mg	0.01 (0.01)	-	-	-	-	-	0.01 (0.01)
Ti	0.01 (0.01)	0.01 (0.03)	0.12	0.01 (0.00)	0.01 (0.00)	0.01 (0.00)	0.08 (0.05)
O	4.00	4.00	4.00	4.00	4.00	4.00	4.00
# Cations	2.90	3.00	2.82	3.04	2.95	2.87	2.89
Vacancies	0.10	-	0.18	-	0.05	0.13	0.11
Tc Calc (4O)	574	576	513	576	573	576	537
Tc Measured	572	574	574	578	578	556	541

Type 2 and type 3 (3a and 3b) refer to (Ti-)magnetite, usually presenting Verwey transitions between -147° and -175°C; and Curie temperatures between 545° to 604°C, depending on cation substitution and oxidation. Type 2 curves are mostly reversible (Fig. 4.7b), whilst type 3 is irreversible (Fig. 4.7c). Type 3a refers to irreversible (Ti-) magnetite that show stable κ from RT to the Curie temperature (Fig. 4.7d), while type 3b refers to samples with constant κ increase from RT to Hopkinson peak (Fig. 4.7e), generally attributed to very small SD magnetite grains. Type 3a can present two types of irreversibility in NR73, those with a κ decrease after heating (negative A40; Fig. 4.7c), or increase (positive A40, Fig. 4.7d, 7e).

Type 4 shows at least two ferrimagnetic phases, attributed to different (Ti-)magnetite compositions with varying rates of cation-substitution, causing the presence of two different T_c (see two examples in Fig. 4.7d).

We further subdivided the curves into sub-types “O” and “R”, depending on their alteration during the κ-T experiment expressed in the cooling curves.

Subtype “O” is characterized by a “hump” in κ between 200-350°C in the heating curve. Samples with this behavior may show typical (Ti-)magnetite characteristics (e.g., a “3a-O” type), with this “hump” which we associate with transformation of maghemite to magnetite during the experiment (Fig. 4.7d).

Subtype “R” is irreversible and characterized by a very sharp Curie temperature at ~320°C in the cooling curve, which we associate with formation of pyrrhotite from pyrite during the heating experiment in an argon atmosphere (Fig. 4.7e).

These alterations mainly pertain to maghemitization of magnetite, or presence of secondary pyrite in the samples, both of which are diagnostic of hydrothermal alteration. Thus, this subdivision allows us to constrain the hydrothermal conditions (“O” = Oxidizing; “R” = Reducing).

Supplemental file SF5 contains all κ-T curves for the surface samples, NR73 and SUBO.

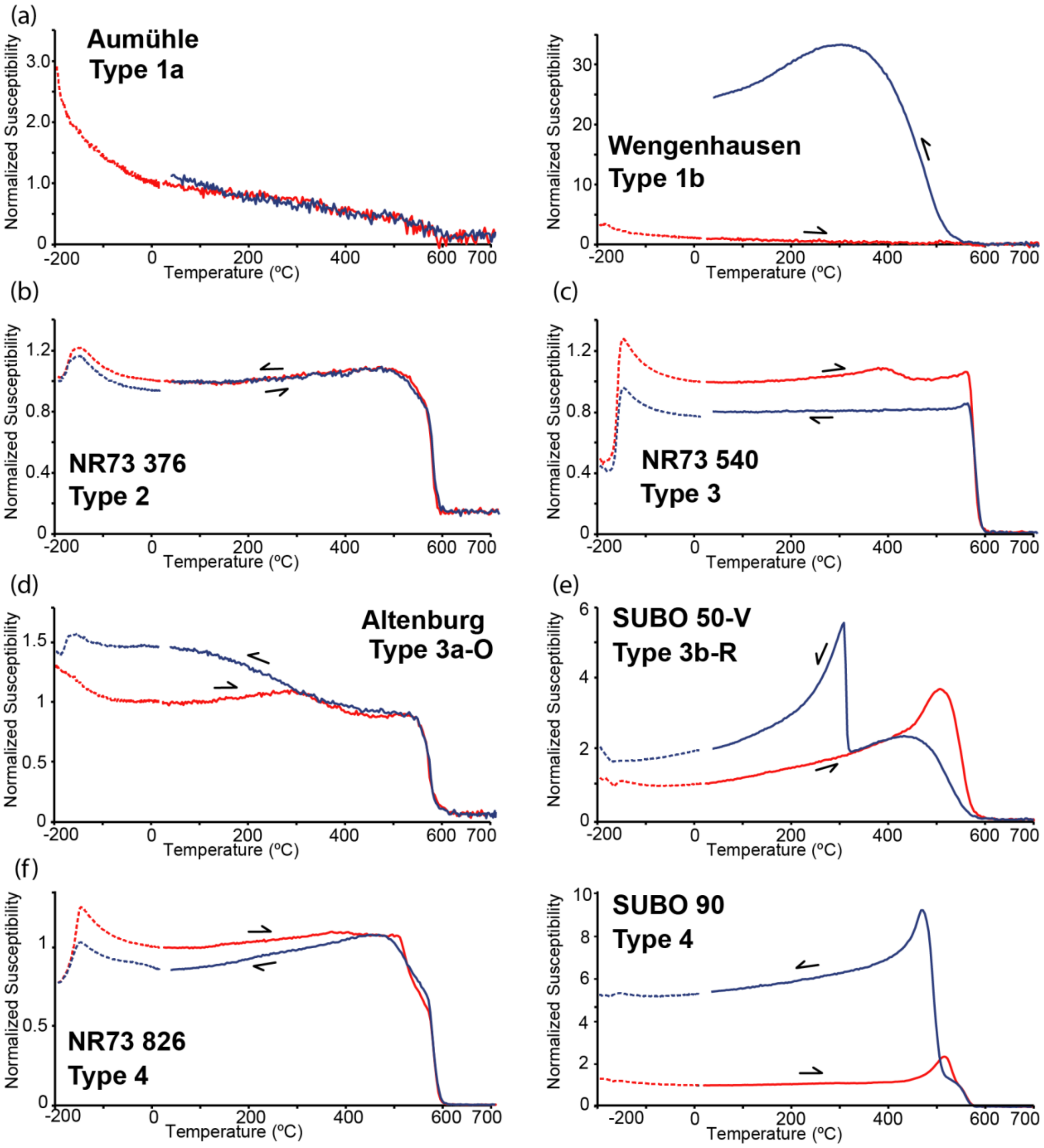

Figure 4.7. Representative κ-T curves from different types found in our samples. a) Type 1 samples, Type 1a (left) shows fully paramagnetic sample, Type 1b (right) shows formation of a new ferrimagnetic phase after an original paramagnetic curve; b) Type 2 shows a reversible κ-T curve denoting (Ti-)magnetite; c) Type 3 shows an irreversible κ-T curve denoting (Ti-)magnetite, 3b denotes a SD (Ti-)magnetite curve; d) Subtype "O" curves are characterized by a "hump" of κ between 200-350°C in the heating curve; e) Subtype "R" curves are characterized by a very sharp Curie temperature at ~320ºC, caused by the syn-experimental formation of pyrrhotite from pyrite; f) Type 4 curves show a multi-component κ-T curve, characterized by two Curie temperatures, at 580ºC, and a second, around 530ºC, regardless of the shape of the curve

4.5.4.2. Surface samples

The Altenbürg suevite (n=2) shows no clear Verwey transition in the first low temperature measurement, but it appears as a broad transition around -175°C (Table 4) in a second low temperature measurement after heating to 700°C. Both measured samples are classified as type 3a-O. The Curie temperature at ~570°C is sharp and reversible, in accordance with the T_c calculated from chemical composition (see Table 3). The cooling curve shows an increase in κ below 400°C, causing an A40 = ~47% (Table 4).

The Polsingen melt and melt-rich suevite both are classified as type 3b-O. A Verwey transition at -165°C can be observed. Curie temperatures of both samples are around 576°C (Table 4), and κ-T curves are reversible in both melt and melt-rich suevite samples, suggesting no difference in the magnetic carriers of melt and suevite.

Both samples in Aumühle and Wengenhausen belong to type 1, with fully paramagnetic behavior. Aumühle is a type 1a sample, whilst Wengenhausen samples show a large positive A40 (Fig. 4.7a, Table 4). A repeated κ-T curve was done for a second Wengenhausen sample (WEN2-1-1 and 2-2; Table 4 and SF5), where the shape of WEN2-1's cooling curve was maintained in WEN2-2, indicating that the newly formed ferrimagnetic phase is stable at RT conditions. We suggest that in Wengenhausen the signal is due to Fe-carbonate alteration into a ferrite of presumably mixed cation (e.g. Fe, Mn, Mg, Ca) composition during the first κ-T experiment.

4.5.4.3. NR73

In the NR73 drill core (n=41), the majority of κ-T curves either belong to type 2 (n=7) or type 3 (n=24), indicating (Ti-)magnetite is the main carrier of magnetization both in the suevite and the basement. Type 1 samples are also common (n=7), and four consist of type 1b. In the lowest sections of the core, type 4 curves can be identified (n=3), with at least two types of cation-substituted magnetite contributing to the magnetization of the sample (see example in Fig. 4.7d; in Table 4 notice the two Curie temperatures in heating and cooling curves from the type 4 metabasite samples).

In the suevites, four out of seven samples show hydrothermal alteration, with three “3b-O” subtype in the lower sections of the unit, and one 3b-R curve at the contact with the basement (Table 4). The observation of type 3b in these samples suggests small SD grain sizes, in agreement with our microscopical observations (Fig. 4.6d). All type 3 curves in the suevites show a positive A40, suggesting the formation of new ferromagnetic material, causing a 16 to 55% increase in κ. Verwey transitions are ~-167°C, and Curie temperatures in the heating curve around ~578°C, in agreement with the calculated from the chemical composition (Table 3).

In the basement, most samples are unaltered, with one 3a-R sample limited to a suevite dyke at 546 m depth (Table 4). Most type 3 show a decrease of κ ranging from 9 to 29%. Only one basement type 3 sample shows a 20% increase in κ. The Verwey transitions are ~-158°C, which is lower than the T_v for pure magnetite (~-153°C, Verwey 1939), only sample 821MB shows an even lower T_v at -180°C. The Curie temperatures average 580°C, with variations related to varying degrees of cation substitution (see calculated T_c in Table 3). Type 4 samples are limited to the lower sections of the core in the metabasite samples, where we attribute the pure magnetite T_c ~580°C to the dusty grains, and the second Curie temperature ranging from 440 to 529°C, to the Cr-rich phases are observed (cf. calculated T_c in Table 3, Table 4; Fig. 4.6g).

4.5.4.4. SUBO

In SUBO (n=35) the most common type is also type 3 (n=22), mainly type 3b, suggesting that SD (Ti-)magnetite is the main magnetic carrier, in line with previous observations (Table 2, 3, Fig. 4.4, 4.5, 4.6). A wider range of cation-substitution is inferred by the wider range of Curie temperatures in the heating curves, ranging from 545°C to 619°C in the main magnetic phase (Table 4). The presence of type 4 samples (n=7) in the melt and suevites demonstrates the range of cation substitution, where a more substituted (Ti-)magnetite creates multiple Curie temperatures, sometimes as low as 484°C (averaging at 530°C, see "T_cH2" in Table 4). After heating, the Curie temperatures are generally irreversible and tend to decrease, which may be attributed to cation order/disorder effects (e.g., Bowles, 2013; Jackson and Bowles, 2014). Verwey transition temperatures are generally lower than in pure magnetite, ranging from ~-149°C to ~-191°C, in agreement with a wide range of generally high cation-substitution rates. The Verwey transition is suppressed in the melt region.

From type 1 (n=6), two samples show "1a" characteristics, one of them shows the formation of pyrrhotite during the experiment (1a-R, Table 4), while the remaining paramagnetic samples are type 1b. In SUBO, hydrothermal alteration is prevalent, with only 11 unaltered samples. The most prevalent alteration is reducing, with subtype "R" samples (n=18) widespread through the core. Subtype "O" (n=2) is only observed in a transitory region with both melt and basement clasts present.

4.6. Discussion

4.6.1. Magnetic mineralogy

We performed a magnetic mineralogy study of basement and impact rocks from the inner ring and megablock zone of the Ries crater using surface and drill core samples. Our study confirms that (Ti-)magnetite is the main ferrimagnetic carrier of the magnetic properties and the paleomagnetic directions as described in Pohl (1965), Pohl and Angenheister (1969), Pohl et al. (1977a; 2010), and Arp et al. (2019). However, it also shows that the magnetic mineralogy is more complex, and magnetization is often carried by multiple co-existing phases, related to shocked and new formed magnetite. In this section, we will discuss the evolution of the magnetic mineralogy in relation to pre-, and syn-impact events.

We will further discuss how post-impact hydrothermalism may have played a role in the observed magnetic characteristics. These details have not been studied before and might be an important aspect to understand the magnetic anomaly pattern.

To this end, we calculated an estimated percentage of magnetic contribution and hydrothermal overprint for each sample location (Fig. 4.8). We used our κ-T data to classify each of our samples into pre- and syn-impact formed magnetite, and divided samples with signs of hydrothermal alteration into those with a more "oxidizing" or "reducing" character. For example, out of 41 κ-T measurements in NR73 (Table 4), seven are paramagnetic. Thus, paramagnetic samples make up 17% of the contribution in NR73. All type 1 samples were excluded from ferrimagnetic contribution calculations.

4.6.1.1. Magnetic contribution

Pre-impact magnetite is only found in the basement of NR73 or in basement clasts in the suevite. These grains are large, originally MD magnetite, which were exposed to a shock pressure of ~25 GPa (Engelhardt and Graup, 1977), causing grain fracturing, fragmentation and crystal lattice defects. All type 2, 3 and 4 basement samples of NR73 show shock features under the microscope and we consider them as pre-impact magnetite (see Fig. 4.6e, 4.6f). Despite the abundance of large magnetite grains, the shocked samples are generally demagnetized (Table 1 and Fig. 4.3) and have lower κ than predicted by empirical calculations (see Tarling and Hrouda, 1993) (Table 1, Fig. 4.3, 4.6e, 4.6f). The magnetite shows intermediate PSD coercivities (~40 mT on average), despite their large grain sizes (>100μm), which would be expected to imply more MD behavior. The finer end of MD state is suggested for grain sizes of ~10 μm (Nagy et al., 2019), but PSD behavior may still occur up to ~100 μm, under certain lattice strain or anisotropy conditions (see Heider et al., 1996). In NR73, 25 out of 41 samples show these characteristics, leading to a 61% pre-impact contribution (17% paramagnetic; Fig. 4.8).

Table 4.4. Parameters obtained from κ-T measurements used in this study. Tv1/Tv2 – Verwey Transition Temperature pre- and post-heating, respectively; TcH/TcC – Curie temperature of heating and cooling cycles, respectively; number after TcH/TcC refers to the highest TcH, TcH1, 2… refers from higher to lowest curie temperature. HPR – Hopkinson Peak Ratio; TvP – Verwey Peak Ratio; A40[%] – Alteration Index at 40ºC, refer to text for details on Type and Classification.

Depth [m]	Lith.	Sample	Tv1	Tv2	TcH 1	TcH 2	TcC 1	TcC 2	TcC 3	TvPR1	TvPR2	HPR1	HPR2	A40[40%]	Type	Class.
Surface Samples																
Surface	Suevite	ALT 1	-	-176	572	579	-	-	-	-	1.08	-	-	46.9	3b-O	Syn + Ox
Surface	Suevite	ALT 2	-	-175	550	542	-	-	-	-	1.07	-	-	47.7	3b-O	Syn + Ox
Surface	Suevite	AUM 1	-	-	-	-	-	-	-	-	-	-	-	17.9	1a	Pm
Surface	Melt	POL-Melt	-	-	575	578	-	-	-	-	-	1.34	1.03	54.8	3b-O	Syn + Ox
Surface	Red Sue.	POL	-166	-	578	575	-	-	-	1.01	-	1.82	1.52	10.1	3b-O	Syn + Ox
Surface	Suevite	WEN 1	-	-	-	478	-	-	-	-	-	-	-	2319.4	1b	Pm + Ox
Surface	Suevite	WEN 2-1	-	-	566	321	-	-	-	-	-	1.10	1.41	3880.4	1b	Pm + Ox
Surface	Suevite	WEN 2-2	-	-	486	493	-	-	-	-	-	-	-	-28.9	-	-
SUBO																
22	Suevite	SUBO-22	-	-177	570	-	567	-	-	-	1.07	-	1.71	2811.8	1b	Pm + Ox
24	Suevite	SUBO-24	-	-153	533	-	569	-	-	-	1.11	6.12	1.42	1206.2	1b	Pm + Ox
33	Suevite	SUBO-33	-	-174	569	-	575	310	-	-	1.57	-	1.34	1524.8	1b-R	Pm+R.O.
38	Suevite	SUBO-38-I	-167	-	546	-	532	323	-	1.01	-	2.76	-	7.3	3b-R	Syn-Red
38	Suevite	SUBO-38-II	-163	-	571	-	578	532	387	0.93	-	1.77	-	112.0	3b-R	Syn-Red
40	Suevite	SUBO-40	-169	-	579	547	529	-	-	1.82	-	3.61	3.08	11.2	4	Syn
50	Suevite	SUBO-50-I	-167	-	573	533	575	521	312	0.85	-	2.54	-	64.0	4-R	Syn-Red
50	Suevite	SUBO-50-II	-167	-	573	536	575	508	312	0.91	-	2.66	-	62.5	4-R	Syn-Red
50	Suevite	SUBO-50-III	-168	-	545	-	536	325	-	1.00	-	2.77	-	4.8	3b-R	Syn-Red
50	Suevite	SUBO-50-IV	-169	-	545	-	550	-	-	1.01	-	2.51	2.11	-1.5	3b	Syn
50	Suevite	SUBO-50-V	-164	-	564	-	533	321	-	1.08	-	3.68	-	93.2	3b-R	Syn-Red
51	B+Melt	SUBO-51-I	-162	-	562	-	576	532	335	0.89	-	2.49	-	157.2	3b-R	Syn-Red
51	B+Melt	SUBO-51-II	-157	-	578	-	622	528	-	0.85		2.56	-	64.4	3b-O	Syn+Ox
52	B+Melt	SUBO-52-I	-157	-	560	-	575	540	423	1.45	-	2.18	-	69.1	3b-O	Syn+Ox
52	B+Melt	SUBO-52-II	-164	-146	572	537	580	529	307	0.94	0.90	2.75	-	29.7	4-R	Syn-Red
71	B+Melt	SUBO-71	-	-	605	-	579	413	-	-	-	2.05	-	38.9	1a	Pm
73	Clast	SUBO-73	-191	-180	586	-	551	326	-	1.24	1.02	5.56	-	286.2	3b-R	Syn-Red
80	Melt	SUBO-80-I	-	-	566	-	321	-	-	-	-	5.37	-	108.4	3b-R	Syn-Red
80	Clast	SUBO-80-II	-	-	561	-	321	-	-	-	-	-	-	428.2	1a+R	Pm + Red
80	Melt	SUBO-84 M	-	-	523	-	414	-	-	-	-	-	-	1726.7	1b	Pm + Ox
84	Clast	SUBO-84 Gn	-173	-191	588	484	540	-	387	1.28	-	-	-	225.5	4	Syn
85	Melt	SUBO-85	-155	-152	576	-	577	535	313	1.28	0.92	5.05	-	617.8	3b-R	Syn-Red
86	Melt	SUBO-86	-	-151	588	-	585	466	321	-	0.98	5.84	-	880.2	3b-R	Syn-Red

Table 4.4. (cont.) Parameters obtained from κ-T measurements used in this study.

Depth [m]	Lith.	Sample	Tv1	Tv2	TcH 1	TcH 2	TcC 1	TcC 2	TcC 3	TvPR1	TvPR2	HPR1	HPR2	A40[40%]	Type	Class.
SUBO																
87	Melt	SUBO-87	-	-	587	-	639	300	-	-	-	-	-	689.3	3a	Syn
89	Melt	SUBO-89-I	-	-	564	545	569	517	-	-	-	2.68	1.71	447.2	4	Syn
89	Melt	SUBO-89-II	-	-	577	-	577	312	-	-	-	-	-	419.9	3a	Syn
90	Melt	SUBO-90	-	-	571	542	572	507	-	1.22	1.00	2.35	1.71	436.6	4	Syn
90	Clast	SUBO-91	-149	-	568	-	549	272	-	1.28	-	1.61	-	63.0	3b-R	Syn-Red
90	Melt	SUBO-92-I	-	-	579	-	586	425	-	-	-	-	-	548.6	3a	Syn
90	Melt	SUBO-92-II	-	-147	571	-	576	310	-	-	-	-	-	795.0	3a-R	Syn-Alt.
90	Melt	SUBO-93	-	-	572	-	575	384	-	-	-	-	-	1596.6	3a-R	Syn-Alt.
90	Melt	SUBO-95-II	-	-	619	-	633	285	-	-	-	-	-	114.8	3a	Syn
90	Melt	SUBO-95-II	-	-	594	-	622	431	316	-	-	-	-	750.7	3a	Syn
90	Melt	SUBO-97	-	-165	576	-	579	319	-	-	-	-	-	791.3	3a-R	Syn-Red
90	Melt	SUBO-98	-	-	534	-	483	-	-	-	-	-	2.25	1854.5	3a	Syn
NR73																
332	Suevite	NR73-332 S	-159	N/a	574	-	582	-	-	1.22	N/A	1.66	1.26	55.2	3b	Syn
376	Suevite	NR73-376 S	-175	N/a	567	-	573	-	-	1.10	N/A	1.21	1.14	-0.4	2	Syn
376	M.Suev.	NR73-376 S II	-173	-175	575	-	575	-	-	1.22	1.24	1.09	1.10	-0.9	2	Syn
475	Suevite	NR73-475 S	-168	N/a	575	-	578	-	-	1.10	N/A	1.63	1.27	17.3	3b-O	Syn + Ox
475	Suevite	NR73-475 S II	-169	-166	574	-	581	-	-	1.10	1.19	1.44	1.23	16.4	3b-O	Syn + Ox
498	S+Gneiss	NR73-498 SG	-174	-	578	-	582	-	-	1.09	-	1.56	1.29	17.7	3b-O	Syn + Ox
498	S+Gneiss	NR73-498 SG II	-152	-170	586	-	551	326	-	1.24	1.02	-	1.88	286.2	3b-R	Syn-Red
528	Gneiss	NR73-528 Gn	-160	-157	590	-	597	-	-	1.35	1.27	1.34	1.21	-24.1	3a	Pre
529	Gneiss	NR73-529 Gn	-157	-165	587	-	592	-	-	1.32	1.37	1.14	1.21	-21.2	3a	Pre
530	Amph.	NR73-530 A	-	N/a	-	-	586	-	-	-	-	-	-	277.8	1b	Pm + Ox
530	Gneiss	NR73-530 Gn	-158	N/a	578	-	579	-	-	1.32	-	1.21	1.19	20.8	3a	Pre
530	Gneiss	NR73-530 Gn-II	-156	-163	587	-	589	-	-	1.58	1.34	1.15	1.24	-12.0	3a	Pre
534	Gneiss	NR73-534 Gn	-158	-149	608	-	600	-	-	1.99	1.26	1.22	1.14	11.1	3a	Pre
535	Gneiss	NR73-535 Gn-Wht	-161	-166	580	-	579	-	-	1.22	1.26	1.09	1.16	-12.0	3a	Pre
535	Gneiss	NR73-535 Gn-Blk	-160	-170	576	-	577	-	-	1.24	1.26	1.10	1.18	-11.7	3a	Pre
536	Gneiss	NR73-536 Gn	-165	-170	578	-	588	-	-	1.30	1.35	1.11	1.25	-16.9	3a	Pre
539	Gneiss	NR73-539 Gn	-155	-157	592	-	599	-	-	1.71	1.18	1.15	1.20	4.7	2	Pre
540	Gneiss	NR73-540 SG	-157	-160	578	-	581	-	-	1.28	1.24	1.07	1.07	-19.4	3a	Pre
540	Suevite	NR73-540 SG	-159	-162	579	-	584	-		1.30	1.31	1.07	1.18	-26.8	3a	Syn

Table 4.4. (cont.) Parameters obtained from κ-T measurements used in this study.

Depth [m]	Lith.	Sample	Tv1	Tv2	TcH 1	TcH 2	TcC 1	TcC 2	TcC 3	TvPR1	TvPR2	HPR1	HPR2	A40[40%]	Type	Class.
NR73																
546	S+Gneiss	NR73-546 SG	-158	-	575	-	580	328	-	1.34	-	1.28	-	172.1	3a-R	Pre + Red
552	S+Gneiss	NR73-552 SG	-147	-153	585	-	591	-	-	1.85	2.97	1.12	1.18	-19.4	3a	Pre
557	Gneiss	NR73-557 Gn	-157	-162	585	-	592	-	-	1.34	1.37	-	1.28	-22.6	3a	Pre
573	Gneiss	NR73-573 Gn	-160	-162	578	-	590	-	-	1.34	1.33	1.18	1.21	-11.5	3a	Pre
574	Gneiss	NR73-574 Gn	-155	-154	583	-	586	-	-	1.48	1.38	1.23	1.66	2.6	2	Pre
612	Gneiss	NR73-612 Gn	-151	-156	590	-	594	-	-	1.42	1.32	-	1.29	-26.9	3a	Pre
617	Amph.	NR73-617 A	-	-	-	-	555	-	-	-	-	-	1.51	665.3	1b	Pm + Ox
621	Gneiss	NR73-621 Gn	-158	-161	580	-	593	-	-	1.38	1.35	1.12	1.15	1.0	2	Pre
623	Gneiss	NR73-623 Gn	-158	-147	582	-	591	-	-	1.49	1.43	1.18	1.16	-1.7	2	Pre
624	Gneiss	NR73-624 Gn	-	-	-	-	-	-	-	-	-	-	-	-	1a	Pm
629	Gneiss	NR73-629 Gn	-	-	-	-	-	-	-	-	-	-	-	-	1a	Pm
630	Gneiss	NR73-630a Gn	-159	-163	579	-	581	-	-	1.34	1.26	1.31	1.24	22.6	3a	Pre
630	Gneiss	NR73-630b Gn	-160	N/a	579	-	583.90	-	-	-	N/A	1.09	1.22	-29.4	3a	Pre
664	Gneiss	NR73-664 Gn	-159	-	584	-	593.50	-	-	1.24	-	1.16	1.16	-9.1	3a	Pre
672	Gneiss	NR73-672 Gn	-156	-157	604	-	593.80	-	-	1.58	1.34	1.26	1.13	-9.7	3a	Pre
680	S+Clast	NR73-680 SG	-	-146	554	456	586	440	-	-	0.97	2.02	1.63	51.6	4	Pre + Syn
680	Suevite	NR73-680 S	-	-	-	-	584	489	-	-	-	-	-	198.7	1b	Pm + Ox
820	Metabas.	NR73-820 MB	-	N/a	-	-	586	349	-	-	-	-	-	390.8	1b	Pm + Ox
821	Metabas.	NR73-821 MB	-180	N/a	556	-	562	-	-	-	-	1.03	1.10	5.9	2	Pre
826	Metabas.	NR73-826 MB	-	-	-	-	-		-	-	-	-	-	-	1a	Pm
827	Metabas.	NR73-827 MB	-165	-161	575	529	571	522	-	1.15	1.21	1.10	1.20	-14.3	4	Pre + Syn
829	Metabas.	NR73-829 MB	-155	-162	579	519	578	526	-	1.25	1.20	1.10	1.26	-14.1	4	Pre + Syn

Syn-impact magnetite formed during or directly related to the impact event from impact melt and occurs in glass-bearing breccia (suevite). These impactite-formed magnetite grains are generally smaller and thus have higher coercivities (~68 mT) than the shocked ones (see e.g., Fig. 4.6d compared with 4.6e and 4.6f), even after shock deformation (~40 mT). κ and NRM are also generally higher in the syn-impact magnetite (Fig. 4.3, Table 1). Syn-impact magnetite comprises type 2 and 3 curves from Altenbürg and Polsingen, as well as in the NR73 suevites (9/41; in total 22%). In SUBO, all samples are classified as syn-impact (83%) except for the paramagnetic type 1 samples (17%) (Fig. 4.8).

4.6.1.2. Hydrothermal conditions

Subtypes O and R can be classified as pre- or syn-impact with hydrothermal overprint of an already existing ferrimagnetic phase. This overprint is either related to oxidation of the original phase (subtype O), or to the presence of hydrothermally deposited pyrite which transforms into pyrrhotite during the heating experiment in an argon atmosphere (subtype R).

Type 1 samples were excluded from the magnetic contribution analysis, however type 1b samples, which indicate the transformation of Fe-carbonate into a ferrimagnetic phase during experiments, require oxidizing conditions for Fe-carbonate deposition. Therefore, we considered samples 1b along with subtype “O”, to characterize the oxidizing hydrothermal overprint. This type of overprint is rare in both NR73 (18%), and SUBO (16%) (Fig. 4.8), however prominent in the surface samples (Wengenhausen, type 1b; Altenbürg and Polsingen, type 3-O).

On the other hand, subtype “R” is characterized by the formation of pyrrhotite during the heating experiment and demonstrate the presence of sulphur-rich minerals like pyrite. The formation of pyrite indicates a reducing nature of the hydrothermal fluids (Osinski et al., 2005). This is the most dominant hydrothermal overprint in SUBO (51%), but rare in NR73 (only 5%).

Samples that do not meet the 1b, “O” or “R” characterization are proposed as hydrothermally unaltered samples, that did not exhibit significant magnetic overprint or a hydrothermal effect in their magnetic properties. This is the vast majority of NR73 (76%) and one third of the samples of SUBO (32%), mostly in the continuous melt section (Table 4).

4.6.2. Magnetic evolution conceptual model

4.6.2.1. Pre-impact

Our results provide the first in-detail characterization of the magnetic mineralogy in the shocked basement of the Ries crater. Before the impact, the regional magnetization was carried mostly by pure magnetite with low rates of oxidation (maximum calculated vacancies around 0.05 for 3 cations, Table 3), and large grain sizes (up to ~200 µm) suggesting an initial MD state (Nagy et al., 2019; Heider et al., 1996). From size and abundance of these grains in thin sections we estimate a concentration of ~1% magnetite in the bulk gneiss samples. At this concentration, we suggest that the original κ in the pre-impact Variscan gneisses range between 10^{-2} and 10^{-1} SI (see Tarling and Hrouda, 1993). This estimate is in line with regional trends. Studies from (not shocked) Variscan granitoid basement rocks, such as the Vosges mountains in France, show κ values ranging from 10^{-3} SI to ~10^{-1} SI (Edel et al., 2013). In fresh, hydrothermally unaltered granite samples from the Soultz-sous-Forêts granitoid, κ values are around 10^{-2} SI (Just and Kontny, 2011), and a borehole of the German Continental Deep Drilling Program (KTB) into the Variscan basement in the Oberpfalz region (Bavaria, Germany) shows κ of (not shocked) gneisses and metabasites in the same range of 10^{-3} to 10^{-1} SI (Berckhemer et al., 1997).

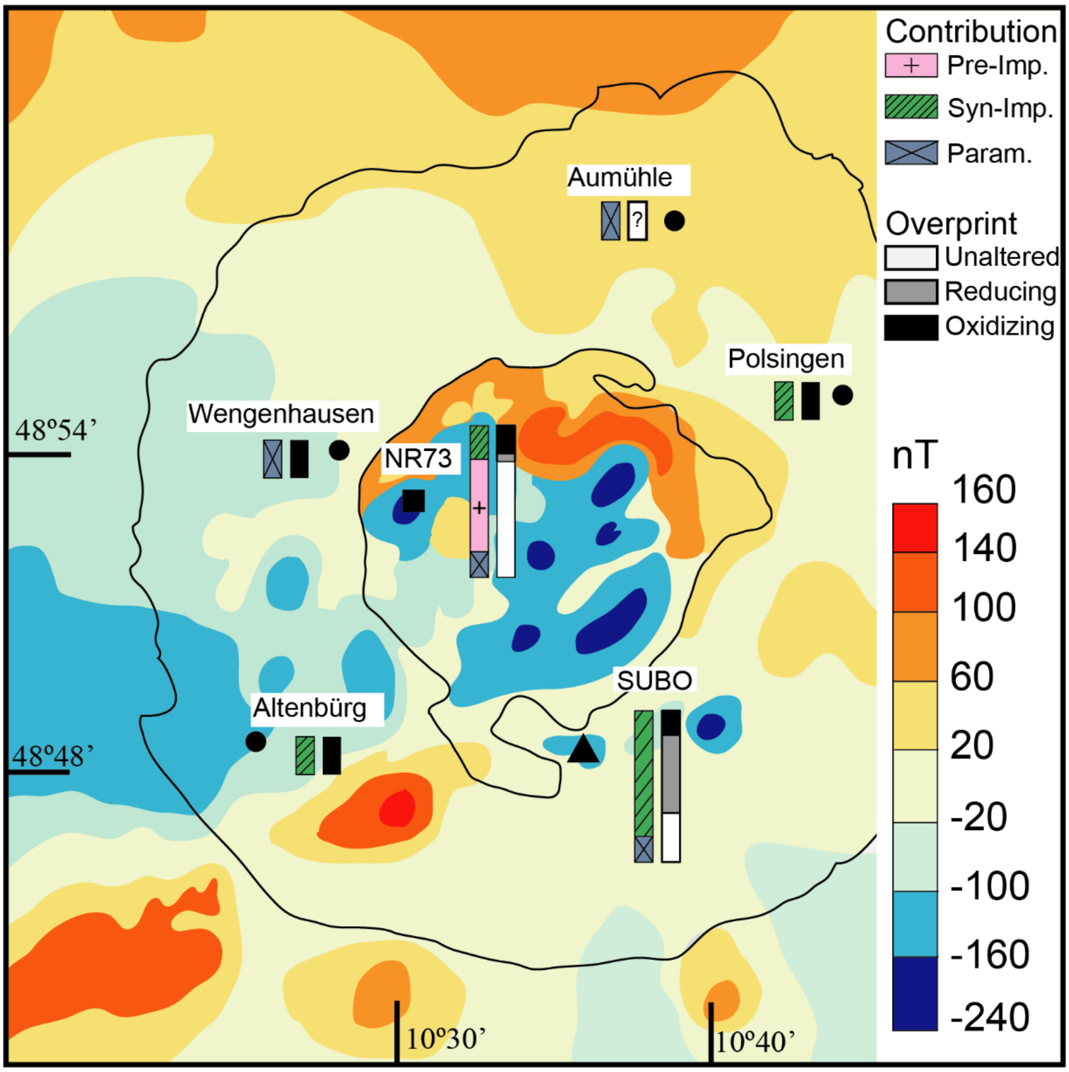

Figure 4.8. Aeromagnetic anomaly map (nT) (after Pohl et al., 2010), with sampling locations. Vertical bars represent the calculated [%] of magnetic contribution (Pre-, Syn- or Paramagnetic) and hydrothermal overprint conditions. Refer to text for details in calculations of percentages.

At impact, the shockwave alters the magnetic properties of magnetite in three distinct and independent ways: κ reduction (e.g., Reznik et al., 2016); demagnetization (e.g., Gilder et al., 2006), and SRM acquisition (e.g., Gattacceca et al., 2006, 2007; Sato et al., 2021). These three effects will irreversibly affect the total magnetization values observed in Table 1, so we must address them individually.

The shock-induced grain fracturing (see Fig. 4.6e and 4.6f), and crystal-lattice defect formation may reduce κ in magnetite by up to 90% after shock pressures of 5 GPa (the Hugoniot Elastic Limit of magnetite, Ahrens and Johnson, 1995; Reznik et al., 2016). Shock deformation causes grain size reduction and associated (apparent or real) domain state decrease, through increased domain wall-pinning (Lindquist et al., 2015; Reznik et al., 2016; Mendes and Kontny, in press). As the basement (expected original κ ~10^{-2} to 10^{-1} SI) was exposed to ~25 GPa, we attribute its reduced κ (observed ~10^{-4} SI, Table 1, Fig. 4.3) and relatively high coercivities (~40 mT, consistent with PSD behavior; Table 2; Fig. 4.4, 4.5) to shock deformation.

NRM intensities in the Ries basement are generally quite low (<0.1 A/m Fig. 4.3, Table 1), compared to the intact Variscan basement (e.g., KTB drill cores show NRM intensities around ~0.1 A/m, locally up to 10 A/m; Berckhemer et al., 1997). At impact, the demagnetization of the target and SRM acquisition occur simultaneously but independently (Gattacceca et al., 2010). It is widely accepted that ferrimagnetic minerals are subject to substantial demagnetization through compression, even at pressures well below 5 GPa (e.g., Louzada et al., 2011). The demagnetization of an existing NRM strongly depends on the coercivity of the target and thus, indirectly, the grain size (e.g., Cisowski and Fuller, 1978). Shock demagnetization is stronger in the low coercivity fraction of the NRM (MD magnetite, Pearce and Karson, 1981; Jackson, et al., 1993; Louzada et al., 2007; Bezaeva et al., 2007, 2010; Gattaceca et al., 2010). In fact, Kletetschka et al. (2004) demonstrated that <2 GPa MD magnetite may lose up to ~90% of its pre-shock NRM, compared to a loss of ~70% in SD magnetite. In (Ti-)magnetite, the demagnetization is also correlated to the Ti content (Bezaeva et al., 2010), however our pre-impact magnetite is mostly pure (Table 3), so this is not a factor to consider in our case. MD magnetite is also particularly susceptible to SRM acquisition (e.g., Tikoo et al., 2015). Compression at low pressures in the presence of an ambient field may allow for SRM acquisition (Fuller, 1977; Gattacceca et al., 2007, 2010; Srnka, et al., 1979; Louzada et al., 2011). Although the acquisition of SRM depends on magnetic mineralogy and grain size (e.g., Sato et al., 2021), it is less efficient and intensities are several times lower than the original NRM acquired through other processes, e.g., TRM (Gattacceca et al., 2006). Therefore, we attribute the decreased NRM intensities of our rocks to shock demagnetization, and rather neglect an SRM contribution to the total magnetization of these rocks. The existing literature for the paleomagnetic directions in the shocked basement of NR73 (Pohl et al., 1977b) suggest scattered inclinations, which implies that no primary pre-impact magnetization was retained, and no stable post-impact remagnetization was acquired. Due to the reduced intensities, dominance of induced magnetization ($Q < 1$), and likely scatter of directions during the modification stage of the crater, the contribution of a potential SRM would be insignificant to the magnetic properties of the basement of the Ries crater.

The shocked Ries basement shows similarities to those observed in the much larger Chicxulub impact crater, Mexico (e.g., Mendes et al., 2023), where shocked magnetite is also the main carrier of magnetization. Magnetite grains with similar sizes (>200 μm), exhibit PSD state with coercivities around ~40 mT, and a strongly reduced κ (Mendes et al., 2023). The κ (~10^{-5} to 10^{-4} SI) and NRM (~0.01 A/m) (Mendes et al., 2023) of the shocked basement in Chicxulub are comparable to the κ and NRM observed here. In Chicxulub, the negative magnetic anomaly along the peak-ring is associated with this shocked magnetite (Mendes et al., 2023). The peak-ring structure in Chicxulub consists of a kilometers-thick section of uplifted basement morphologically like the inner ring in Ries (see Fig. 4.1c), where reduced κ and NRM cause a local drop in total magnetization along the structure, creating the negative magnetic anomaly (Mendes et al., 2023). Due to the preponderance of literature on the systematic reduction of κ and NRM due to shock as described above, we consider the influence of demagnetized basement for negative magnetic anomalies over impact craters to be a universal observation and should be carefully weighed in magnetic anomaly interpretations of these structures.

4.6.2.2. Syn-impact

At the time of impact and the minutes immediately after, the high emplacement temperatures of the suevite and impact melt (up to 900°C in the suevite and >2000°C for the impact melt, Osinski et al., 2004), allowed for the formation of new and thus intact cation-substituted magnetite. The main characteristic of this phase is mostly a low cation substitution, with Curie temperatures ~570°C (Table 3, 4), indicating compositions close to pure magnetite. Some minor cation-substituted magnetite with lower Curie temperatures (~540°C) were also observed in the impact melts of SUBO. All newly formed magnetite phases show Q-ratios >1, indicating that magnetization is mainly controlled by NRM (Fig. 4.3a, 4.3c).

The κ, NRM intensity and domain state of magnetite in suevite (NR73 and Altenbürg) and impact melt (SUBO and Polsingen) varies strongly, and thus we will discuss them separately. The surface suevite from Wengenhausen and Aumühle show a strong hydrothermal overprint, so we will discuss them in detail under the next heading.

In NR73, magnetite in suevite has higher κ and NRM intensity than in shocked basement (Table 2) and the suevite shows a wide range of domain states and coercivities, extending from SD to MD (Fig. 4.4). This range show either that larger shocked magnetite grains inherited from the basement clasts contribute to the total grain population, or that different cooling rates during magnetite crystallization from impact melt caused a range of grain sizes.

In Altenbürg, κ and NRM values are very low, and magnetite shows a low cation substitution (Table 3). The small grains, with skeletal textures in isolated clusters (Fig. 4.6) suggest that the cooling of this surface suevite was faster than in the crater suevite, which may have not allowed for a more prolific magnetite crystallization. Furthermore, the cation deficiency in this sample (vacancies = 0.1; Table 2) and type 3b-O κ-T curves suggest some degree of maghemitization and oxidation. This maghemite seems to be transformed into magnetite during the κ-T experiment, causing a positive A40 of ~47%, and the appearance of the Verwey transition in a second low-temperature run (Table 2). The Verwey transition may have been repressed in the first LT-curve by the maghemitization, since it is sensitive to oxidation (Aragón et al., 1985). We consider the low concentration of magnetite, its small grain sizes, and its oxidation/maghemitization to be the cause of the low magnetization in Altenbürg.

The long exposure to high temperatures after the impact event is also expected to have strong effects on the shocked pre-impact magnetite. Recent studies of experimentally heated shocked magnetite indicate that thermal annealing of shock-induced lattice defects has a significant effect on the recovery of magnetic properties (Kontny et al., 2018; Mendes et al., 2023; Mendes and Kontny, in press). With thermal annealing, domain states appear to increase and some κ is restored (Kontny et al., 2018; Mendes et al., under review). This κ restoration after heating is evident in notoriously irreversible κ-T curves with positive A40[%] values of 20-50% (e.g., see Fig. 4.1 in Kontny et al., 2018). Shocked basement shows irreversible type 3 κ-T curves, however with negative A40[%]. Negative values indicate a transformation of magnetite to a less magnetic phase, such as ilmenite (Hrouda, 2003; Table 4). These negative values do not exclude annealing as a process but may suggest that κ increase through annealing could be masked by a larger κ decrease from mineral transformation. An example for the transformations of hematite to magnetite during heating in argon atmosphere in natural samples of Chicxulub showcase how mineral transformations dominate and overprint the signal of thermal magnetite annealing, although annealing still takes place (Mendes et al., 2023; Mendes and Kontny, in press). Under these circumstances, thermal annealing is only identified through very sensitive methods that identify small domain state variations, such as first order reversal curve (FORC) diagrams (Mendes and Kontny, in press).

The presence of type 2 curves in the shocked basement suggests that not all basement magnetite undergoes mineral transformations, but also do not experience an annealing-induced κ increase during the experiment. Therefore, we propose that these samples may have already been annealed naturally by the emplacement of suevite dykes (>900°C) that intersect the basement. Immediately after emplacement, contact with the suevite could lead to high enough temperatures to anneal the physical defects, without necessarily creating favorable chemical conditions for mineral transformations. In the absence of mineral transformations, magnetite shocked above 5 GPa always shows an increase in κ after heating (Kontny et al., 2018; Mendes and Kontny, in press). The absence of an κ increase necessitates that either: 1) samples already experienced annealing in nature; or 2) the shock pressures in the basement are heterogeneous, and did not reach 5 GPa in NR73, leading to irreversible brittle deformation (fracturing and fragmentation) but no plastic deformation that can be reverted by thermal annealing. We find explanation 2) unlikely for the basement of NR73 however, where shock pressures at the sampled depths (~600 m; Fig. 4.2) are estimated to be around 25 GPa (Engelhardt and Graup, 1977). Some shock attenuation is identified in the basement; however, the shock pressures are described to be still above 5 GPa until around 1200 m depth (Engelhardt and Graup, 1977). Furthermore, the intensity of grain fracturing and fragmentation of the magnetite (Fig. 4.6e, 4.6f), low NRM, κ (Table 1, Fig. 4.3), and the apparently decreased PSD domain state (Table 2, Fig. 4.4), strongly suggests that the magnetite was exposed to shock pressures above the 5 GPa threshold. Thus, we favor the interpretation that an abundance of suevite dyke intercalations within the basement lead to a natural annealing of the magnetite immediately after the impact event. It is possible that the intensity of the irreversible brittle deformation is significantly more extensive over plastic reversible deformation, thus making the restoration of magnetic properties through annealing insignificant at the larger scale.

Impact melts in SUBO and Polsingen have low κ and NRM intensity (Table 1; Fig. 4.3), with general small apparent magnetite grain size, decreased domain state, and associated high coercivity (Table 2; Fig. 4.4, 4.6i and 4.6j). In SUBO, magnetite is slightly more cation-substituted than in the other suevite, with T_c on average at around 570°C in the main phase, and 540°C for minor phases (Table 4). Coercivity values of ~68 mT of the magnetite phase suggest a SD/fine-PSD domain state (Fig. 4.4, 4.5, Table 2), consistent with grain sizes that can be too small for EPMA analysis (with some exceptions, see Fig. 4.6h). Our results are in contrast to previously published data of SUBO (Pohl et al., 2010), that described NRM intensity up to 1.5 A/m, whereas our samples are on average ~0.13 A/m. We attribute the low magnetization to the prevalence of very small SD grains and cation-substituted magnetite in the impact melt, as well as the presence of ilmenohematite which gives these samples their characteristic red color (Osinski et al. 2004; 2005). Low intensities can also be caused by cation-substituted hematite with contribution to the NRM signal ubiquitous in the melt, but rare in in the suevite (Table 2). We attribute the deviation between our results and the results published by Pohl et al. (2010) to natural heterogeneity, with high intensities being outliers to the average. In the Polsingen red suevite, we observed a lower cation-substitution (Tc ~577°C) and mean coercivity of ~40 mT (Table 2; Fig. 4.4, 4.5a), suggesting coarser grains, but also PSD state. PSD state behavior is retained until around ~10 μm (Nagy et al., 2019), but grains of that size are rare in the impact melt (note that Fig. 4.6 depicts the only grain used for EPMA in Fig. 4.6h and 4.6i). As in SUBO, the small (~5 μm) magnetite and (cation-substituted) hematite (Fig. 4.5, Table 2) also explains the low NRM intensities.

4.6.2.3. Post-impact hydrothermal overprint

The post-impact hydrothermal system in the Ries crater was well developed, but generally of low temperature (~130°C to 300°C, Osinski, 2005) and not very laterally extensive (Sapers et al. 2017). The hydrothermal alteration affects each of the magnetic phases, and the main characteristics of the hydrothermal alteration are overall similar in NR73 and SUBO. Surface samples from the megablock zone are limited to a first, high temperature phase (see below).

In pre-impact minerals from the basement and in clasts found in suevite of SUBO, hydrothermal alteration causes minor oxidation of pure magnetite likely along free surfaces of the fractures and grain boundaries (Fig. 4.8). The hydrothermal fluids are also responsible for the deposition of Fe-carbonates responsible for type 1b curves (Table 4, Fig. 4.8). In some pre-impact samples, IRM modeling suggests the presence of some hematite, which we interpret as likely formed from this same hydrothermal phase. The hydrothermal systems described in the Ries impact crater (Newsom et al., 1986; Osinski 2004, 2005; Osinski et al., 2013; Sapers 2017) have generally low temperatures, around ~130 – 300°C in a first, steam dominated phase, and <100°C during a second, long-lasting phase (Osinski et al., 2005).

These temperatures are too low to cause annealing in pre-impact magnetite, with minimum required temperatures ~45 to 540°C (Mendes et al., 2023; Mendes and Kontny, in press). It is worth noting that despite 76% of the ferrimagnetic samples of NR73 being hydrothermally "unaltered", some secondary ilmenite is observed in the cracks of the shocked magnetite (Fig. 4.6e), denoting that hydrothermal alteration happened, but did not overprint or affect strongly the magnetic characteristics in the Ries basement. In NR73, 18% of the samples show oxidizing and only 5% reducing conditions, with most of the alteration is localized in the suevites (Table 4). Thus, despite ubiquitous hydrothermal alteration in NR73, the magnetic phases were generally preserved.

In syn-impact magnetite, the hydrothermal overprint also varies regionally. The paramagnetic type 1a curves from Aumühle were taken from degassing channels, where a large amount of secondary ilmenite is deposited (see EPMA data in SF4, Fig. 4.6c). In Wengenhausen and the upper suevite of SUBO (Table 4), type 1b curves suggest the presence of some Fe-carbonates in the sample, which transform into a ferrimagnetic phase during κ-T experiments, likely (Ti-)maghemite or (Ti-)magnetite. Suevite from NR73 and Altenbürg also show mostly oxidizing hydrothermal alteration and maghemitization (Table 4, Fig. 4.8).

In contrast to NR73, a hydrothermal overprint in SUBO is dominant, with 64% of the samples showing signs of overprint. The majority of the overprint occurring in SUBO is reducing (51% of the samples; Fig. 4.8; Table 4), with a majority of samples showing the formation of pyrrhotite during the heating experiment. Pyrrhotite is formed from paramagnetic pyrite, deposited in a reducing environment. It is worth noting that in SUBO, at least one sample shows the presence of both Fe-carbonates and pyrite (see Table 4 sample SB-33). These results suggest that both alteration conditions affected the samples, possibly requiring continued evolution of the hydrothermal fluids over time.

To our knowledge, this is the first study focusing on the influence of hydrothermalism on magnetic mineralogy. Our results agree well with previously published studies regarding the hydrothermal systems more generally, suggesting that most of the alteration is localized in the suevites (e.g., Osinski et al., 2013). A two-stage cooling model has been proposed in literature (e.g., Naumov, 2005; Sapers 2017) that describes a first, rapid convection-driven cooling above boiling temperatures through steam and degassing, and a second long-lasting gradual cooling stage. The samples from Aumühle which were taken from degassing pipes have been attributed to this first stage (Chao et al., 1978; Newsom et al., 1986; Sapers et al., 2017). We suggest the first stage is responsible for generally reducing conditions, leading to the deposition of the Fe-sulphides in the inner crater suevite. We propose that in the basement, the injection of suevite dykes during the formation of the crater (Stöffler et al., 1977; Stöffler 1977) and partial melting of the gneiss and metabasite, created a very Ti- rich impact melt and fluids at the time of impact. Although vapor convection-driven alteration of the first stage is restricted to the upper suevites, we believe that the high-temperature suevite dykes in the basement have also created conditions that allow for contemporaneous deposition of the secondary ilmenite observed in the fractures of the shocked magnetite throughout the basement.

The second hydrothermal phase (see Sapers et al., 2017) likely lasted for a long time (up to 250 kyr) and was characterized by slow cooling of heated material (e.g., Osinski et al., 2013) and weakly alkaline (pH > 8 – 9) fluids, which are derived from meteoritic water and from the crater lake (Muttik et al., 2011). These alkaline fluids may be responsible for the creation of oxidizing conditions for the formation of the Fe-carbonates, maghemitization, and local oxidation of pyrite to goethite in the surface samples and suevite of NR73 and SUBO. The second stage is stronger in the inner crater, and we suggest that it may locally overprint the first stage through oxidation of the earlier formed pyrite, as subtype "R" is absent in NR73. Alternatively, it is also possible that first-stage pyrite only forms where enough

Fe and S species are available in the fluid. The high carbon content within claystone, such as those from the Mesozoic sedimentary cover (Graup, 1975) could lead to more reducing fluids locally, which enhances the mobility of Fe and S species. While in the inner crater no sedimentary cover is preserved in the crater basement (see Fig. 4.2), it is hypothetically possible that some of the sequence may be preserved closer to the inner ring. Both second-stage oxidation of pyrite or absence of pyrite deposition can reasonably explain the absence of subtype “R” in NR73.

4.6.3. Implications for the magnetic anomaly pattern

Magnetic anomalies in the Ries crater have long been related to the presence of a strong NRM reverse polarity in the crater suevite (Pohl, 1965; Pohl and Angenheister, 1969; Iseri et al., 1989; Pohl et al., 1977a, 2010; Arp et al., 2019). Our results from NR73 corroborate this hypothesis, as the Q-ratios show that the magnetization of the suevite is controlled by the NRM, and a strong total magnetization (~2 A/m). In contrast, the total magnetization of the basement is much weaker (average ~0.1 A/m), and the induced magnetization is dominant over the NRM (Q<1). With κ reduced by up to two orders of magnitude (~10^{-4} from originally estimated ~10^{-2} SI), the magnetization in the basement is very low (~0.1 A/m, Table 1). This allows the thick layer (~200 m) of strongly reverse polarity suevite to dominate the magnetic signal and create the negative magnetic anomalies in the inner crater.

In SUBO this relationship is not so clearly developed. Although the Q-ratio is >1, the total magnetization in the investigated samples is generally one order of magnitude lower than in NR73 (average ~0.14 A/m, Table 1). SUBO, which was drilled into the uplifted inner ring (see Fig. 4.1 and Arp et al., 2019), did not reach the basement, however modeling of the magnetic anomaly performed by Pohl et al. (2010) estimates that the basement is only ~120 m below the surface. This means that the impactite layer of ~100 m, which is only slightly stronger magnetized than the demagnetized basement (Table 3), has only half the thickness of the NR73 impactites. However, the intensity of the negative anomaly is comparable to NR73 (see Fig. 4.1d, and Pohl et al. 2010). The NRM of the suevite is very weak (average ~0.01 A/m), and the melt, albeit stronger (~0.16 A/m), presents only a very thin (at most ~50 m) continuous layer, which is still two orders of magnitude weaker than the impactites layer of NR73. The weakness of the impactites, combined with the thicker and high-uplifted demagnetized basement, lead us to propose that in SUBO the reverse polarity of NRM may not be the dominant reason for the negative anomaly as previously proposed by Pohl et al. (2010), but rather is caused by the overall lack of magnetization instead. While NRM and κ can be locally strong (see Fig. 4.2 and Pohl et al., 2010), these are outliers rather than a lithology wide trend. The absence of magnetization creates a contrast with the background magnetization, which causes the anomaly. This hypothesis can be tested by modeling the anomaly, combining the results presented by Pohl et al. (2010) and in our study, however such modeling is beyond the scope of the present work.

A significant contribution from the uplifted demagnetized basement would agree with observations from the Chicxulub impact structure (Mexico, Mendes et al., 2023), where a layer of shocked, demagnetized basement in the uplifted peak-ring created a region of low total magnetization (κ = ~$1\text{x}10^{-3}$ SI; NRM= ~0.01 A/m). Syn-impact cation-substituted magnetite in the impact melt of the peak-ring shows much stronger NRM (up to 1 A/m), κ (up to $20\text{x}10^{-3}$ SI), Q-ratios >1, and reverse polarity inclinations (Inc. = ~-44°; see Tikoo et al., 2017; Kring et al., 2020; Mendes et al., 2023). Despite the reverse polarity in the peak-ring, the newly formed magnetite from the melt is suggested to cause the positive magnetic anomaly in the adjacent melt pool in the central basin of the crater (e.g., Rebolledo-Vieyra et al., 2010; Urrutia Fucugauchi et al., 2011). However, the relationship between the magnetic mineralogy and the positive anomaly is still under debate, as no drilling has recovered material from this melt pool until now. Nonetheless, the inclination found in the melt layer of the peak-ring agrees with the expected direction for the time of impact at Chron 29r, which lasted for at least 250 ka after the impact (Sprain et al., 2018). This observation raises a question regarding the origin of the magnetic anomaly: if the central basin cooled below 580°C within 250 ka (which is likely) and shows the same reverse inclination as the rest of the melt, why does it present such a strong positive magnetic anomaly? This is different to the observation in the Ries crater made in this paper and in previous studies (Pohl, 1965; Pohl and Angenheister, 1969; Pohl et al., 1977a, 2010; Arp et al., 2019), which considers the direction and intensity of the NRM to be the main controlling factor for the magnetic anomalies. A comparison between Ries and Chicxulub highlights how the understanding of the relationship between magnetic mineralogy, impact processes and magnetic anomalies over craters remains a challenge in impact research. We suggest that the contribution of the demagnetized basement to the magnetic anomaly is generally underestimated, and often overlooked.

4.7. Conclusions

We have investigated the magnetic properties and magnetic mineralogy in suevite, impact melt and shocked basement from the surface (outer ring and megablock zone), and from boreholes NR73 (inner crater) and SUBO (inner ring) in the Nördlinger Ries impact crater, Germany. We discriminated pre-, syn- and post-impact processes to better understand the evolution of crater magnetism, and the contribution for the total magnetization and magnetic anomaly pattern.

The main magnetic mineral in the surface and NR73 suevite is low cation substituted magnetite. This phase is also observed in SUBO, but a second, more cation-substituted magnetite also contributes to the magnetization. Suevites in NR73 have a strong total magnetization (~2 A/m), whilst in SUBO both melt and suevite show much lower magnetizations (~0.14 A/m). We attribute the lower magnetization to the smaller grain sizes and related domain states, higher cation-substitution, and an overall higher concentration of ilmenohematite rather than magnetite, in these rocks.

The shocked basement of NR73 contains pure, shocked, and demagnetized magnetite (~0.1 A/m), with PSD domain state and high coercivity, despite large grain sizes (~200 μm). The shocked magnetite was likely annealed locally, in contact with high temperature suevite and impact melt (900° to 2000°C).

A two-stage hydrothermal system altered but did not significantly overprint the pre-existing magnetic properties of our sampled lithologies. A first, steam driven fluid is responsible for wide-spread formation of Fe-sulphides and ilmenite locally in the shocked basement. This was followed by a weakly alkaline longer lasting system, depositing Fe-carbonates, and oxidizing existing phases.

We propose that the negative magnetic anomalies above NR73 and SUBO have different origins. In NR73 it is caused by a strong reverse polarity NRM, in accordance to previously published literature. However, for the local negative magnetic anomaly at SUBO we suggest that the anomaly is caused by an overall absence of magnetization. A thicker section of contiguous uplifted and demagnetized basement overlain by a magnetically weak melt and suevite layer causes a localized lack of magnetization, that contrasts with the background magnetization, causing the local magnetic anomaly. This mechanism has been observed before and is proposed to explain negative anomalies over other large impact craters, such as the Chicxulub crater (Mexico). However, a holistic understanding of the relationship between magnetic mineralogy and magnetic anomalies in impact craters remains elusive and requires new modeling of the magnetic anomalies, incorporating the here suggested concept.

5. Summary

5.1. Nature versus laboratory

5.1.1. Shock in nature and laboratory

I investigated naturally shocked magnetite in two impact craters, Chicxulub (Mexico) and Ries (Germany). In a first stage, the effects of impact shockwave deformation on the magnetic properties of magnetite were constrained, and then compared to experimentally shocked magnetite. Magnetite in the natural craters loses up to 90% of its magnetic susceptibility (κ), when compared to theoretical estimations and other natural analogues. This is in agreement with shock reverberation experiments and previous studies in shocked magnetite (Reznik et al., 2016). The results presented in this thesis are consistent with brittle fracturing, grain fragmentation, and plastic crystal lattice defect accumulation as the main mechanisms of shock-induced loss in κ. This deformation model postulates a relation between shock pressure, increase in lattice strain, and decrease of apparent domain state through grain fragmentation and domain wall-pinning in fractures and lattice defects. The findings presented in Chapter 3 further show that experimentally shocked magnetite is an adequate analogue for naturally shocked magnetite, particularly with respect to shock-related apparent domain state changes and associated coercivity increase (Fig. 5.1).

The naturally shocked samples also demonstrate a similar response to thermal treatment as the experimentally shocked magnetite, even in the presence of chemical alteration. Thermal annealing is directly observed to occur in the natural samples, and is a phenomenon that conclusively can happen in nature, given high enough temperatures (e.g., contact with high temperature impact melt and suevite).

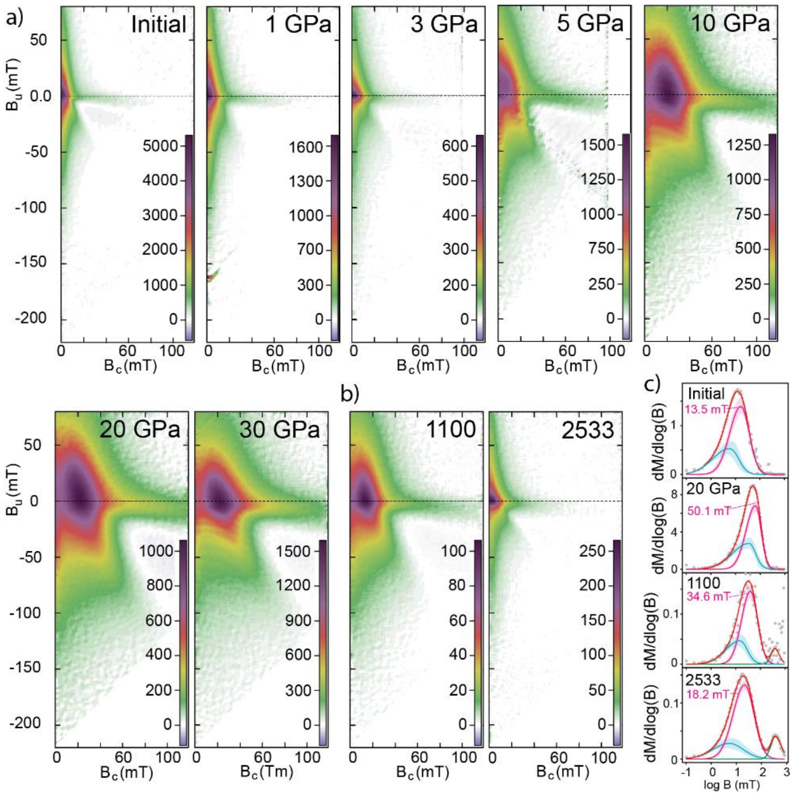

Figure 5.1. a) Room-temperature FORC diagrams of all magnetite ore samples before heating; b) Room-temperature FORC diagrams of the natural granite samples, from Chicxulub (1100) and Soultz (2533). Note that the sample from the Chicxulub crater demonstrates similar domain state behavior as samples experimentally shocked at 10-30GPa; c) Fit of coercivity components to the IRM acquisition curves for representative samples. Color scale units are in Am^2/kgT^2.

5.1.2. Natural temperature and hydrothermal overprint?

The results demonstrate that temperature overprint of magnetic properties also occurs in natural impact craters, but the conditions required are more confined than previously thought. The annealing of lattice defects in magnetite and the recovery of magnetic properties is an instantaneous process, with exposure time having a negligible effect given high enough temperatures. Chapters 2 and 3 establish ~540°C as a minimum temperature threshold for physical annealing, which shows clear irreversible changes in the magnetic domain state of the sample (Fig. 5.2).

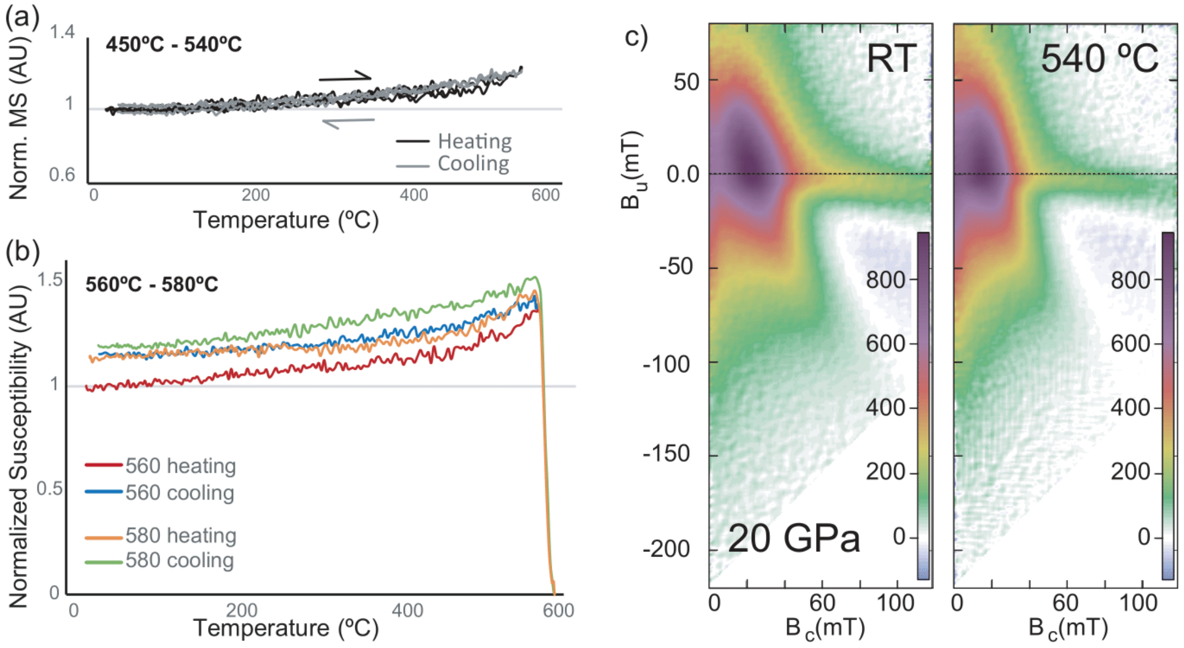

Figure 5.2. Stepwise heating/cooling experiments in Ar atmosphere for sample 1100. (a) Consecutive κ-T heating steps to 450°C, 500°C, 520°C, and 540°C, all showing reversible behavior; (b) At 560°C and 580°C irreversible behavior initiates; (c) experimentally shocked sample at 20 GPa before and after heating to 540°C, denoted a domain state increase towards more MD behavior, and coercivity distribution shift towards lower values.

The maximum temperatures of the natural hydrothermal systems in both Chicxulub and Ries impact structures are significantly lower (~450°C and ~300°C, respectively) than the threshold for magnetic annealing. The results of sample 1100 in Chapter 3 prove that annealing did not occur naturally in the peak-ring of Chicxulub, as its FORC signal is similar to the experimentally shocked samples before annealing (see Fig. 5.1). Even in Chicxulub, where hydrothermal temperatures were highest and exposure time the longest, no natural annealing of magnetite could be observed. This fact, together with only a subordinate signal of hydrothermally deposited ferrimagnetic phases, leads us to believe that post-impact hydrothermalism did not significantly overprint the magnetic properties of the shocked magnetite in Chicxulub and Ries. Despite no magnetic properties being changed, hydrothermal alteration is observed in the form of oxidation or alteration of non-magnetic phases. These phases may later be responsible for the formation of new ferrimagnetic phases with temperature, during the experiments.

5.1.3. Influence of shock and temperature in magnetic anomaly patterns

Natural annealing is observed to occur in contact with high temperature melt or suevite layers or dykes where temperatures are above 700°C. These occurrences are local however, and do not significantly impact the magnetic signature of the shocked basement. As hydrothermalism fails to ubiquitously anneal the magnetite, thermal annealing in natural impact craters does not seem to play a major role in the magnetic anomalies of the studied impact craters.

The investigations carried out in Chapter 2 and 4 suggest that the shocked and magnetically unrecovered target basement systematically show reduced NRM and κ values, which may significantly contribute to the observed negative magnetic anomalies. The role of this demagnetized basement has been underappreciated until now, but it is an important factor to consider as a major contribution to the anomaly patterns over impact structures.

Lastly, the relationship between NRM direction and its influence on magnetic anomalies remains unclear. Observations described in literature for the Ries impact structure describe partially how strong reverse polarity NRM directions controls the magnetic anomalies (e.g., Pohl, 1965; Pohl and Angenheister, 1969; Pohl et al., 1977a; 2010; Arp et al., 2019). However, in Chapter 2 and in some other recent literature (e.g., Tikoo et al., 2017; Kring et al., 2020), the Chicxulub melts demonstrate a similarly strong NRM (~0.1 to 1 A/m), and also reverse polarity directions. This implies that the melt pool in the central basin of Chicxulub would be expected to show an equally strong negative magnetic anomaly, which it does not. The fact the magnetic anomaly in the central basin of Chicxulub is strongly positive despite the likely reverse polarity NRM directions, showcases how the understanding of magnetic anomalies over impact structures on Earth remains a challenge in impact research.

5.2. The hematite question: how does oxidation affect the response to temperature?

5.2.1. Influence in natural craters

The oxidation of magnetite is a ubiquitous process on the Earth's surface, and occurs in multiple impact craters as well. As the most common oxidation process is the alteration of magnetite towards magnetically weaker phases such as hematite, this destruction of the magnetic phases in a crater post-impact inevitably contributes to the magnetic anomaly pattern. This does not apply to the craters studied here, as particularly in Chicxulub the oxidation and formation of hematite occurred before impact, and thus the bulk of the loss of magnetic properties are shock-related rather than oxidation-related.

The work presented in this thesis shows that oxidation-derived hematite will revert back to magnetite if exposed to high enough temperatures, even in near-inert environments such as an Argon atmosphere, potentially due to the presence of trace hydrocarbons. This newly formed phase is much stronger than the existing magnetite, and strongly overprints annealing effects when both happen concomitantly. The fact that this transformation can occur even in near-inert atmospheres suggests it does not require particularly reactive environments, if given high enough temperatures. This transformation also occurs naturally in Chicxulub, in contact with the melt dykes.

Natural hematite to magnetite transformation is not particular to impact craters, and it can take place in a range of geological environments, such as loess deposits, environmental contamination and wildfire related mineral transformations in soils (e.g., Deng et al., 2001; Just and Kontny, 2012; Mang and Kontny, 2013; Jiang et al., 2016; Górka-Kostrubiec et al., 2019; Szczepaniak-Wnuk et al., 2020;). Despite it being wide spread, the magnetic consequences of this phenomenon has until now not been studied in depth.

5.2.2. A new process of remagnetization?

A significant discovery presented in this thesis pertains to the domain state of the magnetite formed from hematite transformation. The transformation is instantaneous and irreversible, and creates new mottled textured magnetite grains, which denote SD-SP domain state due to their fine grain size. The new magnetite substantially overprints the original magnetic signal, even when the transformation is incomplete. The overprint is significant, even in magnetite that has not been exposed to shock or other demagnetization processes, such as the magnetite-series granite occurring at depth near Soultz-sous-Forêts in the Upper Rhine Graben.

We believe that research into the boundary conditions of this phenomenon is an important next step for the paleo- and rock magnetic research community: SD magnetite grains are more stable and reliable recorders of paleomagnetic intensities and directions than MD grains, at the geological time scale. This means that even a small fraction of SD grain forming from hematite transformation could completely remagnetize and overprint the original direction, and we believe that this process has so far been underestimated. However, it remains unclear from our preliminary results if this new phase could maintain a stable NRM direction. Furthermore, the temperature threshold for the transformation estimated here (>560°C) is close to the unblocking and Curie temperatures of natural magnetite, and thus are likely to cause remagnetizations regardless. On the other hand, the chemical conditions associated with such high temperatures in nature are seldom near-inert (like in our 99.998% purity argon atmosphere). If the trace hydrocarbon content in the Argon atmosphere is the cause of transformation, it is reasonable that the transformation would be enhanced in more hydrogen-rich conditions, for example derived from the process of serpentinization (e.g., Osselin et al., 2021). Such environments are known to induce hematite to magnetite transformation at lower temperatures, around ~200°C (Thüns et al., 2019), far from the unblocking and Curie temperatures of magnetite. It also suggests that the temperatures necessary for hematite to magnetite transformation may be inversely related with how reducing the environment where it takes place.

6. Conclusions and outlook

6.1. Conclusions

Magnetic anomaly patterns in the Chicxulub and Ries impact structures are both connected to magnetite as the main magnetic mineral, despite each crater's very different size and post-impact evolution. Both impact structures have two generations of magnetite in common: (1) in the shocked basement, a primary magnetite phase that is pure and stoichiometric, with large shock-deformed and fractured grains (>100 μm), reduced NRM and κ, Q-ratios <1, and decreased domain state from originally MD to PSD/V; and (2) in the impact melts and suevites, a newly formed, non-shocked and generally low-cation substituted (Ti-)magnetite, with smaller (~10-50 μm) grains, generally high NRM and κ, Q-ratios >1, and domain state ranging from SD to PSD.

The Chicxulub impact generated an extensive, high-temperature (up to 450°C) and long-lasting (up to 2 Ma) hydrothermal system that ubiquitously permeated the shocked and porous basement. Hydrothermalism was fueled by the latent heat of the central melt pool, and melt dykes that intrude the peak-ring, particularly in M0077A's lower section. The hydrothermal system did not significantly overprint the magnetic signal in the basement of the Chicxulub peak-ring, as it did not generate a significant new magnetite phase (or destruction of magnetic phases), and the temperatures reached were well below the annealing threshold (~540°C). Regions of contact with the impact melt show that locally magnetic annealing did take place, together with transformation of pre-impact secondary hematite back to magnetite. The post-impact thermal treatment did not affect the magnetic anomaly significantly, and the demagnetized and unrecovered shocked basement is the main contributing factor to the negative magnetic anomaly in the peak-ring. The melt-formed cation-substituted magnetite shows a much stronger magnetization, and the large impact melt pool in the central basin is likely responsible for the positive magnetic anomaly, despite the reverse polarity magnetization.

The Ries impact generated a two-stage hydrothermal system with lower temperatures (max. 300°C in the inner crater, 130°C in the rim and outer crater in the first stage, <100°C in the second stage), and shorter duration (~250 kyr). The high temperature, melt-bearing suevite dykes intruded the basement extensively, leading to high post-impact temperatures which likely naturally annealed part of the basement. While the suevite shows general high NRM intensities, the impact melt in Ries is not as strong as in Chicxulub. This factor suggests that in regions of uplifted basement such as the crater rim, the thickness of the demagnetized basement together with the low-magnetized impactites may be the main contributor to the negative anomaly. The magnetic anomalies in Ries are suggested to have locally two different origins, with some being carried by a strong reverse polarity NRM of the suevites, and others by a weak magnetization of the impactites together with uplifted basement, forming a vertically thick region of demagnetized material.

MD shocked magnetite in nature shows a similar apparent domain state decrease towards PSD as experimentally shocked magnetite, regardless of oxidation. Thermal treatment above 540°C creates an irreversible increase in magnetic susceptibility and restoration of apparent domain state increase towards increased MD contributions. If hematite is present in the sample, it transforms to SD-SP magnetite when heated above 560°C, in a process that masks annealing if both happen concomitantly. Only the most sensitive methods, such as FORC diagrams, can distinguish between the effects of annealing and the effects of hematite to magnetite transformation. This process may be a new, underappreciated, understudied and underestimated remagnetization mechanism relevant for a plethora of geoscience subjects.

6.2. Outlook

The results presented in this thesis are a significant step towards the better understanding of the fundamental mechanisms behind magnetic anomalies in craters, and provide insight into the mechanisms of apparent magnetic domain variation. However, these results also raise two important questions regarding remanent magnetizations, which demand further investigation.

Firstly, the fact that the negative magnetic anomaly of the Ries structure has been studied extensively through the last decades and described as being caused by the reverse polarity of the impactite NRM directions, is in contradiction with the current accepted hypothesis for the positive magnetic anomaly in the Chicxulub central basin's melt pool. The melt samples studied in the peak-ring show a strong reverse polarity (Inc. = ~-44°), in agreement with the expected direction for the time of impact at Chron 29r, which lasted for at least 250 ka after the impact. Q-ratios in the melt are low, but above 1, with NRM dominating the magnetization. If the central basin cooled below 580°C within 250 ka (which is likely), and thus shows the same reverse polarity as the rest of the melt, why does it present such a strong positive magnetic anomaly? For now, this is a question that will remain unanswered, as no drilling into the central basin's melt sheet has taken place to date. As this study was focused on the magnetic effects of post-impact temperature overprint and magnetic recovery, this factor was beyond the scope of the research, but it is important to consider and further research is merited.

The second question concerns the transformation of hematite into magnetite. At the geological timescale, MD magnetite, with its low coercivity, is not considered an ideal paleomagnetic direction recorder. SD magnetite, on the other hand, is a more reliable and stable carrier of magnetization. If the newly formed SD magnetite is capable of holding a stable NRM direction, this could be a significant mechanism of remagnetization or overprint. This is something to keep in mind, not only in the interpretation of primary paleomagnetic directions, but also potentially for thermal demagnetization processes, to avoid the loss of data. We believe further research into this hematite-magnetite transformation is not only relevant but urgent for the paleomagnetic community, as low temperature oxidation of magnetite to hematite is a widespread phenomenon in the Earth's crust.

References

Acuña, M. H., Connerney, J. E. P., Ness, N. F., Lin, R. P., Mitchell, D., Carlson, C. W., McFadden, J., Anderson, K. A., Rème, H., Mazelle, C., Vignes, D., Wasilewski, P., & Cloutier, P. (1999). Global Distribution of Crustal Magnetization Discovered by the Mars Global Surveyor MAG/ER Experiment. *Science*, *284*(5415), 790–793. https://doi.org/10.1126/SCIENCE.284.5415.790

Ahrens, T. J., & Johnson, M. L. (1995). Shock wave data for rocks. *Mineral Physics and Crystallography, A Handbook of Physical Constants*, *3*, 35-44.

Ames, D. E., Watkinson, D. H., & Parrish, R. R. (1998). Dating of a regional hydrothermal system induced by the 1850 Ma Sudbury impact event. *Geology*, *26*(5), 447–450. https://doi.org/10.1130/0091-7613(1998)026<0447:DOARHS>2.3.CO;2

Annersten, H., & Hafner, S. S. (1973). Vacancy distribution in synthetic spinels of the series Fe3O4–y-Fe2O3. Zeitschrift für Kristallographie-Crystalline Materials, 137(1-6), 321-340. https://doi.org/10.1524/zkri.1973.137.16.321

Aragón, R., Buttrey, D. J., Shepherd, J. P., & Honig, J. M. (1985). Influence of nonstoichiometry on the Verwey transition. *Physical Review B*, *31*(1), 430. https://doi.org/10.1103/PhysRevB.31.430

Arp, G., Kolepka, C., Simon, K., Karius, V., Nolte, N., & Hansen, B. T. (2013). New evidence for persistent impact-generated hydrothermal activity in the Miocene Ries impact structure, Germany. *Meteoritics & Planetary Science*, *48*(12), 2491–2516. https://doi.org/10.1111/MAPS.12235

Arp, G., Reimer, A., Simon, K., Sturm, S., Wilk, J., Kruppa, C., Hecht, L., Hansen, B. T., Pohl, J., Reimold, W. U., Kenkmann, T., & Jung, D. (2019). The Erbisberg drilling 2011: Implications for the structure and postimpact evolution of the inner ring of the Ries impact crater. *Meteoritics and Planetary Science*, *54*(10), 2448–2482. https://doi.org/10.1111/maps.13293

Barkhausen, H. (1919). Physik Zeitschrift, 20, 401.

Bauberger, W., and Hubert M. (1974). Petrographiche Profildarstellung Der Forschungsbohrung Nördlingen 1973. *Geologica Bavarica*, *72*, 33-34.

Birčáková, Z., Kollár, P., Jakubčin, M., Füzer, J., Bureš, R., & Fáberová, M. (2019). Reversible and irreversible magnetization processes along DC hysteresis loops of Fe-based composite materials. Journal of Magnetism and Magnetic Materials, 483, 183-190. https://doi.org/10.1016/j.jmmm.2019.03.115

Berckhemer, H., Rauen, A., Winter, H., Kern, H., Kontny, A., Lienert, M., Nover, G., Pohl, J., Popp, T., Schult, A., Zinke, J., & Soffel, H. C. (1997). Petrophysical properties of the 9-km-deep crustal section at KTB. *Journal of Geophysical Research: Solid Earth*, *102*(B8), 18337–18361. https://doi.org/10.1029/96JB03396

Bezaeva, N. S., Gattacceca, J., Rochette, P., Sadykov, R. A., & Trukhin, V. I. (2010). Demagnetization of terrestrial and extraterrestrial rocks under hydrostatic pressure up to 1.2 GPa. *Physics of the Earth and Planetary Interiors*, *179*(1–2), 7–20. https://doi.org/10.1016/J.PEPI.2010.01.004

Bezaeva, N. S., Rochette, P., Gattacceca, J., Sadykov, R. A., & Trukhin, V. I. (2007). Pressure demagnetization of the Martian crust: Ground truth from SNC meteorites. *Geophysical Research Letters*, *34*(23), 23202. https://doi.org/10.1029/2007GL031501

Bezaeva, N. S., Swanson-Hysell, N. L., Tikoo, S. M., Badyukov, D. D., Kars, M., Egli, R., Chareev, D. A., Fairchild, L. M., Khakhalova, E., Strauss, B. E., & Lindquist, A. K. (2016). The effects of 10 to >160 GPa shock on the magnetic properties of basalt and diabase. *Geochemistry, Geophysics, Geosystems*, *17*(11), 4753–4771. https://doi.org/10.1002/2016GC006583

Biało, I., Kozłowski, A., Wack, M., Włodek, A., Gondek, Ł., Kakol, Z., Hochleitner, R., Zywczak, A., Chlan, V., & Gilder, S. A. (2019). The influence of strain on the Verwey transition as a function of dopant concentration:

towards a geobarometer for magnetite-bearing rocks. *Geophysical Journal International*, *219*(1), 148–158. https://doi.org/10.1093/GJI/GGZ274

Bouchez, J. L. (1997). Granite is Never Isotropic: An Introduction to AMS Studies of Granitic Rocks. In *Granite: From Segregation of Melt to Emplaceent Fabrics, 8*, 95–112. https://doi.org/10.1007/978-94-017-1717-5_6

Bouchez, J. L., & Gleizes, G. (1995). Two-stage deformation of the Mont-Louis-Andorra granite pluton (Variscan Pyrenees) inferred from magnetic susceptibility anisotropy. *Journal of the Geological Society*, *152*(4), 669–679. https://doi.org/10.1144/GSJGS.152.4.0669

Bowles, J. A., Gerzich, D. M., & Jackson, M. J. (2018). Assessing New and Old Methods in Paleomagnetic Paleothermometry: A Test Case at Mt. St. Helens, USA. *Geochemistry, Geophysics, Geosystems*, *19*(6), 1714–1730. https://doi.org/10.1029/2018GC007435

Bowles, J. A., Jackson, M. J., Berquó, T. S., Sølheid, P. A., & Gee, J. S. (2013). Inferred time- and temperature-dependent cation ordering in natural titanomagnetites. *Nature Communications*, *4*(1), 1–9. https://doi.org/10.1038/ncomms2938

Bowles, J. A., Lappe, S. C. L. L., Jackson, M. J., Arenholz, E., & van der Laan, G. (2019). Curie Temperature Enhancement and Cation Ordering in Titanomagnetites: Evidence from Magnetic Properties, XMCD, and Mössbauer Spectroscopy. *Geochemistry, Geophysics, Geosystems*, *20*(5), 2272–2289. https://doi.org/10.1029/2019GC008217

Bringemeier, D. (1994). Petrofabric examination of the main suevite of the Otting Quarry, Nördlinger Ries, Germany. *Meteoritics*, *29*(3), 417–422. https://doi.org/10.1111/J.1945-5100.1994.TB00607.X

Burgess, S. (2019). Deciphering mass extinction triggers. *Science*, *363*(6429), 815–816. https://doi.org/10.1126/SCIENCE.AAW0473

Carporzen, L., Gilder, S. A., & Hart, R. J. (2006). Origin and implications of two Verwey transitions in the basement rocks of the Vredefort meteorite crater, South Africa. *Earth and Planetary Science Letters*, 251(3-4), 305-317. https://doi.org/10.1016/j.epsl.2006.09.013

Carporzen, L., & Gilder, S. A. (2010). Strain memory of the Verwey transition. *Journal of Geophysical Research: Solid Earth*, *115*(B5), 5103. https://doi.org/10.1029/2009JB006813

Chadima M, & Hrouda H. (2007). *Remasoft 3.0 Paleomagnetic data browser and analyzer User manual*. www.agico.com

Chao, Edward CT. (1978). Principal exposures of the Ries meteorite crater in southern Germany. *Bayersiches Geologisches Landesamt, 84.*

Cisowski, S. M., & Fuller, M. (1978). The effect of shock on the magnetism of terrestrial rocks. *Journal of Geophysical Research: Solid Earth*, *83*(B7), 3441–3458. https://doi.org/10.1029/JB083IB07P03441

Collins, G. S., Patel, N., Davison, T. M., Rae, A. S. P., Morgan, J. V., Gulick, S. P. S., Christeson, G. L., Chenot, E., Claeys, P., Cockell, C. S., Coolen, M. J. L., Ferrière, L., Gebhardt, C., Goto, K., Jones, H., Kring, D. A., Lofi, J., Lowery, C. M., Ocampo-Torres, R., … Bralower, T. J. (2020). A steeply-inclined trajectory for the Chicxulub impact. *Nature Communications*, *11*(1), 1–10. https://doi.org/10.1038/s41467-020-15269-x

Day, R., Fuller, M., & Schmidt, V. A. (1977). Hysteresis properties of titanomagnetites: Grain-size and compositional dependence. *Physics of the Earth and Planetary Interiors*, *13*(4), 260–267. https://doi.org/10.1016/0031-9201(77)90108-X

de Graaff, S. J., Kaskes, P., Déhais, T., Goderis, S., Debaille, V., Ross, C. H., Gulick, S. P. S., Feignon, J. G., Ferrière, L., Koeberl, C., Smit, J., Mattielli, N., & Claeys, P. (2022). New insights into the formation and emplacement of impact melt rocks within the Chicxulub impact structure, following the 2016 IODP-ICDP Expedition 364. *GSA Bulletin*, *134*(1–2), 293–315. https://doi.org/10.1130/B35795.1

Deng, C., Zhu, R., Jackson, M. J., Verosub, K. L., & Singer, M. J. (2001). Variability of the temperature-dependent susceptibility of the Holocene eolian deposits in the Chinese loess plateau: A pedogenesis indicator. *Physics and Chemistry of the Earth, Part A: Solid Earth and Geodesy*, *26*(11–12), 873–878. https://doi.org/10.1016/S1464-1895(01)00135-1

Dias, J. M., Cruz, C., Sant'ovaia, H., & Noronha, F. (2022). Assessing the Magnetic Mineralogy of the Pre-Variscan Manteigas Granodiorite: An Unexpected Case of a Magnetite-Series Granitoid in Portugal. *Minerals 2022,12*(4), 440. https://doi.org/10.3390/MIN12040440

Dudzisz, K., Kontny, A., & Alva-Valdivia, L. M. (2022). Curie Temperatures and Emplacement Conditions of Pyroclastic Deposits from Popocatépetl Volcano, Mexico. *Geochemistry, Geophysics, Geosystems*, *23*(8). https://doi.org/10.1029/2022gc010340

Dunlop, D. J. (2002). Theory and application of the Day plot (Mrs/Ms versus Hcr/Hc) 1. Theoretical curves and tests using titanomagnetite data. *Journal of Geophysical Research: Solid Earth*, *107*(B3), EPM 4-1. https://doi.org/10.1029/2001JB000486

Dunlop, D. J. (1973). Superparamagnetic and single-domain threshold sizes in magnetite. Journal of geophysical research, 78(11), 1780-1793. https://doi.org/10.1029/JB078i011p01780

Dunlop, D. J. (2014). High-temperature susceptibility of magnetite: a new pseudo-single-domain effect. *Geophysical Journal International*, *199*(2), 707–716. https://doi.org/10.1093/GJI/GGU247

Dunlop, D. J., & Ozdemir, O. (2000). Effect of grain size and domain state on thermal demagnetization tails. *Geophysical Research Letters*, *27*(9), 1311–1314. https://doi.org/10.1029/1999GL008461

Ebel, D. S., & Grossman, L. (2005). Spinel-bearing spherules condensed from the Chicxulub impact-vapor plume. *Geology*, *33*(4), 293–296. https://doi.org/10.1130/G21136.1

Edel, J. B., Schulmann, K., Skrzypek, E., & Cocherie, A. (2013). Tectonic evolution of the European Variscan belt constrained by palaeomagnetic, structural and anisotropy of magnetic susceptibility data from the Northern Vosges magmatic arc (eastern France). *Journal of the Geological Society*, *170*(5), 785–804. https://doi.org/10.1144/JGS2011-138

Egli, R. (2013). VARIFORC: An optimized protocol for calculating non-regular first-order reversal curve (FORC) diagrams. *Global and Planetary Change*, *110*, 302–320. https://doi.org/10.1016/J.GLOPLACHA.2013.08.003

Egli, R. (2021). Magnetic characterization of geologic materials with first-order reversal curves. Magnetic measurement techniques for materials characterization, 455-604.

Engelhardt, W. v., and Graup, G. "Stosswellenmetamorphose im Kristallin der Forschungsbohrung Noerdlingen 1973". *Geologica Bavarica, 75.* 255-271.

Engelhardt, W. v., & Bertsch, W. (1969). Shock induced planar deformation structures in quartz from the Ries crater, Germany. *Contributions to Mineralogy and Petrology*, *20*(3), 203–234. https://doi.org/10.1007/BF00377477

Engelmann, R. (2008). Bestimmung diagnostischer magnetischer Übergangstemperaturen von synthetischen Titanomagnetiten und Ilmenit-Hämatit-Mischkristallen. *PhD dissertation, Ruprecht-Karls-Universität Heidelberg.* https://doi.org/10.11588/HEIDOK.00008392

Feignon, J. G., de Graaff, S. J., Ferrière, L., Kaskes, P., Déhais, T., Goderis, S., Claeys, P., & Koeberl, C. (2021). Chicxulub impact structure, IODP-ICDP Expedition 364 drill core: Geochemistry of the granite basement. *Meteoritics and Planetary Science*, *56*(7), 1243–1273. https://doi.org/10.1111/MAPS.13705

Feignon, J. G., Ferrière, L., Leroux, H., & Koeberl, C. (2020). Characterization of shocked quartz grains from Chicxulub peak ring granites and shock pressure estimates. *Meteoritics and Planetary Science*, *55*(10), 2206–2223. https://doi.org/10.1111/MAPS.13570

Ferrière, L. (2017). Search (and Discovery) of New Impact Craters on Earth. *Elements*, *13*(5), 358–359. https://doi.org/10.2138/GSELEMENTS.13.5.358

Ferrière, L., Rae, A. S. P., Poelchau, M., Koeberl, C., & IODP-ICDP Expedition 364 Science Party. (2017). Macro-and Microscopic Evidence of Impact Metamorphism in Rocks from the Chicxulub Peak Ring IODP-ICDP Expedition 364 Drill Core. In *48th Annual Lunar and Planetary Science Conference, no. 1964*, 1600.

Fraas, E., & Branco, W. (1901). Das vulcanische Ries bei Nördlingen in seiner Bedeutung für Fragen der allgemeinen Geologie. *Verlag der Königl. Akademie der Wissenschaften.*

Frank, U., & Nowaczyk, N. R. (2008). Mineral magnetic properties of artificial samples systematically mixed from haematite and magnetite. *Geophysical Journal International*, *175*(2), 449–461. https://doi.org/10.1111/J.1365-246X.2008.03821.X/3/175-2-449-FIG013.JPEG

Fritz, J., Wünnemann, K., Reimold, W. U., Meyer, C., & Hornemann, U. (2011). Shock experiments on quartz targets pre-cooled to 77 K. *International Journal of Impact Engineering*, *38*(6), 440–445. https://doi.org/10.1016/J.IJIMPENG.2010.10.014

Fuller, M. D. (1977). Review of effects of shock (<60 kbar; <6x109 Pa) on magnetism of lunar samples. *Philosophical Transactions of the Royal Society of London. Series A, Mathematical and Physical Sciences*, *285*(1327), 409–416. https://doi.org/10.1098/RSTA.1977.0082

Gao, X., Hao, Q., Oldfield, F., Bloemendal, J., Deng, C., Wang, L., Song, Y., Ge, J., Wu, H., Xu, B., Li, F., Han, L., Fu, Y., & Guo, Z. (2019). New High-Temperature Dependence of Magnetic Susceptibility-Based Climofunction for Quantifying Paleoprecipitation from Chinese Loess. *Geochemistry, Geophysics, Geosystems*, *20*(8), 4273–4291. https://doi.org/10.1029/2019GC008401

Gattacceca, J., Boustie, M., Lima, E., Weiss, B. P., de Resseguier, T., & Cuq-Lelandais, J. P. (2010). Unraveling the simultaneous shock magnetization and demagnetization of rocks. *Physics of the Earth and Planetary Interiors*, *182*(1–2), 42–49. https://doi.org/10.1016/j.pepi.2010.06.009

Gattacceca, J., Boustie, M., Weiss, B. P., Rochette, P., Lima, E. A., Fong, L. E., & Baudenbacher, F. J. (2006). Investigating impact demagnetization through laser impacts and SQUID microscopy. *Geology*, *34*(5), 333–336. https://doi.org/10.1130/G21898.1

Gattacceca, J., Lamali, A., Rochette, P., Boustie, M., & Berthe, L. (2007). The effects of explosive-driven shocks on the natural remanent magnetization and the magnetic properties of rocks. *Physics of the Earth and Planetary Interiors*, *162*(1–2), 85–98. https://doi.org/10.1016/J.PEPI.2007.03.006

Gilder, S. A., LeGoff, M., Chervin, J. C., & Peyronneau, J. (2004). Magnetic properties of single and multi-domain magnetite under pressures from 0 to 6 GPa. Geophysical Research Letters, 31(10). https://doi.org/10.1029/2004GL019844

Gilder, S. A., LeGoff, M., Peyronneau, J., & Chervin, J. C. (2002). Novel high pressure magnetic measurements with application to magnetite. Geophysical Research Letters, 29(10), 30-1. https://doi.org/10.1029/2001GL014227

Gilder, S. A., Goff, M. Le, & Chervin, J. C. (2006). Static stress demagnetization of single and multidomain magnetite with implications for meteorite impacts. *High Pressure Research*, *26*(4), 539–547. https://doi.org/10.1080/08957950601092085

Gilder, S. A., Pohl, J., & Eitel, M. (2018). Magnetic signatures of terrestrial meteorite impact craters: A summary. *Magnetic fields in the solar system: Planets, moons and solar wind interactions*, 357-382. https://doi.org/10.1007/978-3-319-64292-5_13

Górka-Kostrubiec, B., Werner, T., Dytłow, S., Szczepaniak-Wnuk, I., Jeleńska, M., & Hanc-Kuczkowska, A. (2019). Detection of metallic iron in urban dust by using high-temperature measurements supplemented with microscopic observations and Mössbauer spectra. *Journal of Applied Geophysics*, *166*, 89–102. https://doi.org/10.1016/J.JAPPGEO.2019.04.022

Graup, G. (1975). Das Kristallin im Nördlinger Ries. *PhD dissertation, Tübingen Universität*, 1975.

Graup, G. (1999). Carbonate-silicate liquid immiscibility upon impact melting: Ries Crater, Germany. *Meteoritics & Planetary Science*, *34*(3), 425–438. https://doi.org/10.1111/J.1945-5100.1999.TB01351.X

Grieve, Richard AF. (1999) Some of the missing melt fraction found? *Meteoritics & Planetary Science, 34*, 311-312.

Gulick, S. P. S., Barton, P. J., Christeson, G. L., Morgan, J. V., McDonald, M., Mendoza-Cervantes, K., Pearson, Z. F., Surendra, A., Urrutia-Fucugauchi, J., Vermeesch, P. M., & Warner, M. R. (2008). Importance of pre-impact crustal structure for the asymmetry of the Chicxulub impact crater. *Nature Geoscience*, *1*(2), 131–135. https://doi.org/10.1038/ngeo103

Gulick, S. P. S., Christeson, G. L., Barton, P. J., Grieve, R. A. F., Morgan, J. V., & Urrutia-Fucugauchi, J. (2013). Geophysical characterization of the Chicxulub impact crater. *Reviews of Geophysics*, *51*(1), 31-52. https://doi.org/10.1002/rog.20007

Gulick, S., Morgan, J., Mellett, C. L., Green, S. L., Bralower, T., Chenot, E., Christeson, G., Claeys, P., Cockell, C., Coolen, M. J. L., Ferrière, L., Gebhardt, C., Goto, K., Jones, H., Kring, D., Lofi, J., Lowery, C., Ocampo-Torres, R., Perez-Cruz, L., … Zylberman, W. (2017a). Expedition 364 summary. *Proceedings of the International Ocean Discovert Program*, *364*. https://doi.org/10.14379/IODP.PROC.364.101.201 7

Gulick, S., Morgan, J., Mellett, C. L., Green, S. L., Bralower, T., Chenot, E., Christeson, G., Claeys, P., Cockell, C., Coolen, M. J. L., Ferrière, L., Gebhardt, C., Goto, K., Jones, H., Kring, D., Lofi, J., Lowery, C., Ocampo-Torres, R., Perez-Cruz, L., … Zylberman, W. (2017b). Site M0077A: Upper Peak Ring. *Proceedings of the International Ocean Discovery Program*, *364*. https://doi.org/10.14379/iodp.proc.364.106.2017

Gulick, S. P. S., Bralower, T. J., Ormö, J., Hall, B., Grice, K., Schaefer, B., Lyons, S., Freeman, K. H., Morgan, J. V., Artemieva, N., Kaskes, P., De Graaff, S. J., Whalen, M. T., Collins, G. S., Tikoo, S. M., Verhagen, C., Christeson, G. L., Claeys, P., Coolen, M. J. L., … Wittmann, A. (2019). The first day of the Cenozoic. *Proceedings of the National Academy of Sciences of the United States of America*, *116*(39), 19342–19351. https://doi.org/10.1073/PNAS.1909479116

Harrison, R. J., Feinberg, J. M., Harrison, R. J., & Feinberg, J. M. (2008). FORCinel: An improved algorithm for calculating first-order reversal curve distributions using locally weighted regression smoothing. *Geochemistry, Geophysics, Geosystems*, *9*(5). https://doi.org/10.1029/2008GC001987

Harrison, R. J., Muraszko, J., Heslop, D., Lascu, I., Muxworthy, A. R., & Roberts, A. P. (2018). An Improved Algorithm for Unmixing First-Order Reversal Curve Diagrams Using Principal Component Analysis. *Geochemistry, Geophysics, Geosystems*, *19*(5), 1595–1610. https://doi.org/10.1029/2018GC007511

Harrison, R. J., & Putnis, A. (1998). The Magnetic Properties and Crystal Chemistry of Oxide Spinel Solid Solutions. *Surveys in Geophysics*, *19*(6), 461–520. https://doi.org/10.1023/A:1006535023784

Harrison, R. J., & Putnis, A. (1999). Determination of the mechanism of cation ordering in magnesioferrite (MgFe2O4) from the time- and temperature-dependence of magnetic susceptibility. *Physics and Chemistry of Minerals*, *26*(4), 322–332. https://doi.org/10.1007/S002690050192

Hart, R. J., Hargraves, R. B., Andreoli, M. A. G., Tredoux, M., & Doucouré, C. M. (1995). Magnetic anomaly near the center of the Vredefort structure: Implications for impact-related magnetic signatures. *Geology*, *23*(3), 277–280. https://doi.org/10.1130/0091-7613(1995)023%3C0277:MANTCO%3E2.3.CO;2

Heider, F., Halgedahl, S. L., & Dunlop, D. J. (1988). Temperature dependence of magnetic domains in magnetite crystals. *Geophysical Research Letters*, *15*(5), 499–502. https://doi.org/10.1029/GL015I005P00499

Henry, B. (1988). The magnetic fabrics of the Egletons granite (France): separation and structural implications. *Physics of the Earth and Planetary Interiors*, *51*(4), 253–263. https://doi.org/10.1016/0031-9201(88)90067-2

Henry, B., Djellit, H., Bayou, B., Derder, M. E. M., Ouabadi, A., Merahi, M. K., Baziz, K., Khaldi, A., & Hemmi, A. (2004). Emplacement and fabric-forming conditions of the Alous-En-Tides granite, eastern border of the Tin Seririne/Tin Mersoï basin (Algeria): magnetic and visible fabrics analysis. *Journal of Structural Geology*, *26*(9), 1647–1657. https://doi.org/10.1016/J.JSG.2004.02.003

Heslop, D., McIntosh, G., & Dekkers, M. J. (2004). Using time- and temperature-dependent Preisach models to investigate the limitations of modelling isothermal remanent magnetization acquisition curves with cumulative log Gaussian functions. *Geophysical Journal International*, *157*(1), 55–63. https://doi.org/10.1111/J.1365-246X.2004.02155.x

Heslop, D., & Roberts, A. P. (2012). A method for unmixing magnetic hysteresis loops. Journal of Geophysical Research: Solid Earth, 117(B3). https://doi.org/10.1029/2011JB008859

Hildebrand A, Penfield, G., Kring, D., Mark, P., Camarago, A., Jacobsen, S., & Boynton, W. (1991). Chicxulub Crater: A possible Cretaceous/Tertiary boundary impact crater on the Yucatán Peninsula, Mexico. *Geology*, *19*(9), 867–871. https://doi.org/10.1130/0091-7613(1991)019%3C0867:CCAPCT%3E2.3.CO;2

Hode, T., Von Dalwigk, I., & Broman, C. (2004). A Hydrothermal System Associated with the Siljan Impact Structure, Sweden—Implications for the Search for Fossil Life on Mars. *Atrobiology*, *3*(2), 271–289. https://doi.org/10.1089/153110703769016370

Hopkinson, J. (1889). XIV. Magnetic and other physical properties of iron at a high temperature. Philosophical Transactions of the Royal Society of London. (A.), (180), 443-465. https://doi.org/10.1098/rsta.1889.0014

Horton, J. W., Vanko, D. A., Naeser, C. W., Naeser, N. D., Larsen, D., Jackson, J. C., & Belkin, H. E. (2006). Postimpact Hydrothermal Conditions at the Central Uplift, Chesapeake Bay Impact Structure, Virginia, USA. *LPI*, *956*, 1842. https://ui.adsabs.harvard.edu/abs/2006LPI....37.1842H/abstract

Horton Jr, J. W., Kunk, M. J., Belkin, H. E., Aleinikoff, J. N., Jackson, J. C., & Chou, I. M. (2009a). Evolution of crystalline target rocks and impactites in the Chesapeake Bay impact structure, ICDP-USGS Eyreville B core. *Geol. Soc. Am. Spec. Pap*, *458*, 277-316. https://doi.org/10.1130/2009.2458(14)

Horton Jr, J. W., Gibson, R. L., Reimold, W. U., Wittmann, A., Gohn, G. S., & Edwards, L. E. (2009b). Geologic columns for the ICDP-USGS Eyreville B core, Chesapeake Bay impact structure: Impactites and crystalline rocks, 1766 to 1096 m depth. *Geol. Soc. Am. Spec. Pap*, *458*, 21-49.

Hörz, F., Ostertag, R., & Rainey, D. A. (1983). Bunte Breccia of the Ries: Continuous deposits of large impact craters. *Reviews of Geophysics*, *21*(8), 1667–1725. https://doi.org/10.1029/RG021I008P01667

Hrouda, F. (2003). Indices for Numerical Characterization of the Alteration Processes of Magnetic Minerals Taking Place During Investigation of Temperature Variation of Magnetic Susceptibility. *Studia Geophysica et Geodaetica 2003 47:4*, *47*(4), 847–861. https://doi.org/10.1023/A:1026398920172

Hüttner, R., Schmidt-Kaler, Hermann, & Treibes, W. (1969). Geologische Übersichts-karte des Ries. *Geol. Bavarica*, *61*, 451-454.

Iseri, D. A., J. W. Geissman, H. E. Newsom, and G. Graup. (1989). Paleomagnetic and rock magnetic examination of the natural remanent magnetization of suevite deposits at Ries crater, West Germany. *Meteoritics*, *24*, 280.

Ishihara, S. (1979). Lateral variation of magnetic susceptibility of the Japanese granitoids. *The Journal of the Geological Society of Japan*, *85*(8), 509–523. https://doi.org/10.5575/geosoc.85.509

Ishihara, S., Hashimoto, M., & Machida, M. (2000). Magnetite/Ilmenite–series Classification and Magnetic Susceptibility of the Mesozoic-Cenozoic Batholiths in Peru. *Resource Geology*, *50*(2), 123–129. https://doi.org/10.1111/J.1751-3928.2000.TB00062.X

Jackson, M., Borradaile, G., Hudleston, P., & Banerjee, S. (1993). Experimental deformation of synthetic magnetite-bearing calcite sandstones: Effects on remanence, bulk magnetic properties, and magnetic anisotropy. *Journal of Geophysical Research: Solid Earth*, *98*(B1), 383–401. https://doi.org/10.1029/92JB01028

Jackson, M., & Bowles, J. A. (2014). Curie temperatures of titanomagnetite in ignimbrites: Effects of emplacement temperatures, cooling rates, exsolution, and cation ordering. *Geochemistry, Geophysics, Geosystems*, *15*(11), 4343–4368. https://doi.org/10.1002/2014GC005527

Jankowski, B. (1977). Die gradierte Einheit oberhalb des Suevits der Forschungsbohrung Nördlingen 1973. *Geol. Bavarica*, *75*, 155-162.

Jiang, Z., Liu, Q., Zhao, X., Roberts, A. P., Heslop, D., Barrón, V., & Torrent, J. (2016). Magnetism of Al-substituted magnetite reduced from Al-hematite. *Journal of Geophysical Research: Solid Earth*, *121*(6), 4195–4210. https://doi.org/10.1002/2016JB012863

Just, J., & Kontny, A. (2011). Thermally induced alterations of minerals during measurements of the temperature dependence of magnetic susceptibility: a case study from the hydrothermally altered Soultz-sous-Forêts granite, France. *International Journal of Earth Sciences*, *101*(3), 819–839. https://doi.org/10.1007/S00531-011-0668-9

Just, J., Kontny, A., De Wall, H., Hirt, A. M., & Martín-Hernández, F. (2004). Development of magnetic fabrics during hydrothermal alteration in the Soultz-sous-Forêts granite from the EPS-1 borehole, Upper Rhine Graben. *Geological Society, London, Special Publications*, *238*(1), 509–526. https://doi.org/10.1144/GSL.SP.2004.238.01.26

Keppie, J. D., Dostal, J., Norman, M., Urrutia-Fucugauchi, J., & Grajales-Nishimura, M. (2011). Study of melt and a clast of 546 Ma magmatic arc rocks in the 65 Ma Chicxulub bolide breccia, northern Maya block, Mexico: western limit of Ediacaran arc peripheral to northern Gondwana. *International Geology Review*, *53*(10), 1180–1193. https://doi.org/10.1080/00206810903545527

Kirschvink, J. L. (1980). The least-squares line and plane and the analysis of palaeomagnetic data. *Geophysical Journal International*, *62*(3), 699–718. https://doi.org/10.1111/J.1365-246X.1980.TB02601.X

Kletetschka, G., Connerney, J. E. P., Ness, N. F., & Acuña, M. H. (2004). Pressure effects on martian crustal magnetization near large impact basins. *Meteoritics and Planetary Science*, *39*(11), 1839–1848. https://doi.org/10.1111/j.1945-5100.2004.tb00079.x

Kontny, A., Elbra, T., Just, J., Pesonen, L. J., Schleicher, A. M., & Zolk, J. (2007). Petrography and shock-related remagnetization of pyrrhotite in drill cores from the Bosumtwi Impact Crater Drilling Project, Ghana. *Meteoritics and Planetary Science*, *42*(4–5), 811–827. https://doi.org/10.1111/J.1945-5100.2007.TB01077.X

Kontny, A., & Grothaus, L. (2016). Effects of shock pressure and temperature on titanomagnetite from ICDP cores and target rocks of the El'gygytgyn impact structure, Russia. *Studia Geophysica et Geodaetica*, *61*(1), 162–183. https://doi.org/10.1007/S11200-016-0819-3

Kontny, A., Reznik, B., Boubnov, A., Göttlicher, J., & Steininger, R. (2018). Postshock Thermally Induced Transformations in Experimentally Shocked Magnetite. *Geochemistry, Geophysics, Geosystems*, *19*(3), 921–931. https://doi.org/10.1002/2017GC007331

Koymans, M. R., Langereis, C. G., Pastor-Galán, D., & van Hinsbergen, D. J. J. (2016). Paleomagnetism.org: An online multi-platform open source environment for paleomagnetic data analysis. *Computers & Geosciences*, *93*, 127–137. https://doi.org/10.1016/J.CAGEO.2016.05.007

Koymans, M. R., van Hinsbergen, D. J. J., Pastor-Galán, D., Vaes, B., & Langereis, C. G. (2020). Towards FAIR Paleomagnetic Data Management Through Paleomagnetism.org 2.0. *Geochemistry, Geophysics, Geosystems*, *21*(2). https://doi.org/10.1029/2019GC008838

Kring, D. A., Tikoo, S. M., Schmieder, M., Riller, U., Rebolledo-Vieyra, M., Simpson, S. L., Osinski, G. R., Gattacceca, J., Wittmann, A., Verhagen, C. M., Cockell, C. S., Coolen, M. J. L., Longstaffe, F. J., Gulick, S. P. S., Morgan, J. V., Bralower, T. J., Chenot, E., Christeson, G. L., Claeys, P., … Yamaguchi, K. E. (2020). Probing the hydrothermal system of the chicxulub impact crater. *Science Advances*, *6*(22), 3053–3082. https://doi.org/10.1126/sciadv.aaz3053

Kring, D., Claeys, P., Gulick, S., Morgan, J., & Gareth, C. (2017). Chicxulub and the Exploration of Large Peak-Ring Impact Craters through Scientific Drilling. *GSA Today*, *27*. https://doi.org/10.1130/GSATG352A.1

Kruiver, P. P., Dekkers, M. J., & Heslop, D. (2001). Quantification of magnetic coercivity components by the analysis of acquisition curves of isothermal remanent magnetisation. *Earth and Planetary Science Letters*, *189*(3–4), 269–276. https://doi.org/10.1016/S0012-821X(01)00367-3

Lagoeiro, L. E. (1998). Transformation of magnetite to hematite and its influence on the dissolution of iron oxide minerals. *Journal of Metamorphic Geology*, *16*(3), 415–423. https://doi.org/10.1111/J.1525-1314.1998.00144.X

Lanci, L., & Kent, D. V. (2003). Introduction of thermal activation in forward modeling of hysteresis loops for single-domain magnetic particles and implications for the interpretation of the Day diagram. *Journal of Geophysical Research: Solid Earth*, *108*(B3). https://doi.org/10.1029/2001JB000944

Lascu, I., Einsle, J. F., Ball, M. R., & Harrison, R. J. (2018). The Vortex State in Geologic Materials: A Micromagnetic Perspective. *Journal of Geophysical Research: Solid Earth*, *123*(9), 7285–7304. https://doi.org/10.1029/2018JB015909

Lattard, D., Engelmann, R., Kontny, A., & Sauerzapf, U. (2006). Curie temperatures of synthetic titanomagnetites in the Fe-Ti-O system: Effects of composition, crystal chemistry, and thermomagnetic methods. *J. Geophys. Res*, *111*(12), 12–28. https://doi.org/10.1029/2006JB004591

Lied, P., Kontny, A., Nowaczyk, N., Mrlina, J., & Kämpf, H. (2020). Cooling rates of pyroclastic deposits inferred from mineral magnetic investigations: a case study from the Pleistocene Mýtina Maar (Czech Republic). *International Journal of Earth Sciences*, *109*(5), 1707–1725. https://doi.org/10.1007/S00531-020-01865-1/FIGURES/10

Lindquist, A. K., Feinberg, J. M., Harrison, R. J., Loudon, J. C., & Newell, A. J. (2015). Domain wall pinning and dislocations: Investigating magnetite deformed under conditions analogous to nature using transmission electron microscopy. *Journal of Geophysical Research: Solid Earth*, *120*(3), 1415–1430. https://doi.org/10.1002/2014JB011335

Liu, P., Hirt, A. M., Schüler, D., Uebe, R., Zhu, P., Liu, T., & Zhang, H. (2019). Numerical unmixing of weakly and strongly magnetic minerals: examples with synthetic mixtures of magnetite and hematite. *Geophysical Journal International*, *217*(1), 280–287. https://doi.org/10.1093/GJI/GGZ022

Louzada, Karin L., Sarah T. Stewart, and Benjamin P. Weiss. 2007. “Effect of Shock on the Magnetic Properties of Pyrrhotite, the Martian Crust, and Meteorites.” Geophysical Research Letters 34 (5): 5204. https://doi.org/10.1029/2006GL027685.

Louzada, K. L., Stewart, S. T., Weiss, B. P., Gattacceca, J., & Bezaeva, N. S. (2010). Shock and static pressure demagnetization of pyrrhotite and implications for the Martian crust. *Earth and Planetary Science Letters*, *290*(1–2), 90–101. https://doi.org/10.1016/J.EPSL.2009.12.006

Louzada, K. L., Stewart, S. T., Weiss, B. P., Gattacceca, J., Lillis, R. J., & Halekas, J. S. (2011). Impact demagnetization of the Martian crust: Current knowledge and future directions. *Earth and Planetary Science Letters*, *305*(3–4), 257–269. https://doi.org/10.1016/j.epsl.2011.03.013

Mang, C., & Kontny, A. (2013). Origin of two Verwey transitions in different generations of magnetite from the Chesapeake Bay impact structure, USA. *Journal of Geophysical Research: Solid Earth*, *118*(10), 5195–5207. https://doi.org/10.1002/JGRB.50291

Mang, C., Kontny, A., Fritz, J., Schneider, R., Mang, C., Kontny, A., Fritz, J., & Schneider, R. (2013). Shock experiments up to 30 GPa and their consequences on microstructures and magnetic properties in pyrrhotite. *Geochemistry, Geophysics, Geosystems*, *14*(1), 64–85. https://doi.org/10.1029/2012GC004242

Maxbauer, D. P., Feinberg, J. M., & Fox, D. L. (2016). MAX UnMix: A web application for unmixing magnetic coercivity distributions. *Computers & Geosciences*, *95*, 140–145. https://doi.org/10.1016/J.CAGEO.2016.07.009

Mccall, N., Gulick, S., Hall, B., Riller, U., Poelchau, M., Morgan, J. V, Lofi, J., & 364, E. (2017). Adjustments and Preliminary Analysis of Chicxulub Peak Ring CT scans. *Lunar and Planetary Science, 1964*, 1522.

McFadden, P. L., & McElhinny, M. W. (1988). The combined analysis of remagnetization circles and direct observations in palaeomagnetism. *Earth and Planetary Science Letters*, *87*(1–2), 161–172. https://doi.org/10.1016/0012-821X(88)90072-6

Mendes, B. D. L., Kontny, A., Poelchau, M., Fischer, L. A., Gaus, K., Dudzisz, K., Kuipers, B. W. M., & Dekkers, M. J. (2023). Peak-ring magnetism: Rock and mineral magnetic properties of the Chicxulub impact crater. *GSA Bulletin*. https://doi.org/10.1130/B36547.1

Mendes, B. D. L., and A. Kontny. (2024). "Restoration and Transformation: The Response of Shocked and Oxidized Magnetite to Temperature" *Journal of Geophysical Research: Solid Earth*. https://doi.org/10.1029/2023JB027244

Mendes, B., Kontny, A. (2023). Restoration and transformation: The response of shocked and oxidized magnetite to temperature. [Dataset]. *Mendeley Data, V2*. https://doi.org/ 10.17632/f66zx5bjnp.2

Meyer, Cornelia. (2012). "Sedimentological, structural and geochemical investigations of the suevite of the impact crater Nördlinger Ries, Germany." *PhD dissertation, Freie Universität Berlin*. http://dx.doi.org/10.17169/refubium-13865

Mi, W. B., Jiang, E. Y., & Bai, H. L. (2009). Fe3+/Fe2+ ratio controlled magnetic and electrical transport properties of polycrystalline Fe3(1−δ)O4 films. *Journal of Physics D: Applied Physics*, *42*(10), 105007. https://doi.org/10.1088/0022-3727/42/10/105007

Morgan, J., & Artemieva, N. (2008). Chicxulub Distal Ejecta: Modeling Versus Observations - NASA/ADS. In J. Morgan & N. Artemieva (Eds.), *Large Meteorite Impacts and Planetary Evolution IV, 1423*, 3016

Morgan, J., Gulick, S., Mellett, C. L., & Green, S. L. (2017). Chicxulub: Drilling the K-Pg Impact Crater. *Proceedings of the International Ocean Discovery Program, 364*. https://doi.org/10.14379/IODP.PROC.364.2017

Morgan, J., Warner, M., Brittan, J., Buffler, R., Camargo, A., Christeson, G., Denton, P., Hildebrand, A., Hobbs, R., Macintyre, H., Mackenzie, G., Maguire, P., Marin, L., Nakamura, Y., Pilkington, M., Sharpton, V., Snyder, D., Suarez, G., & Trejo, A. (1997). Size and morphology of the Chicxulub impact crater. *Nature*, *390*(6659), 472–476. https://doi.org/10.1038/37291

Morgan, J. V., Warner, M. R., Collins, G. S., Melosh, H. J., & Christeson, G. L. (2000). Peak-ring formation in large impact craters: geophysical constraints from Chicxulub. *Earth and Planetary Science Letters*, *183*(3–4), 347–354. https://doi.org/10.1016/S0012-821X(00)00307-1

Morris, R. V., Golden, D. C., Bell, J. F., & Lauer, H. V. (1995). Hematite, pyroxene, and phyllosilicates on Mars: Implications from oxidized impact melt rocks from Manicouagan Crater, Quebec, Canada. *Journal of Geophysical Research: Planets*, *100*(E3), 5319–5328. https://doi.org/10.1029/94JE01500

Morris, R. V., Klingelhöfer, G., Schröder, C., Rodionov, D. S., Yen, A., Ming, D. W., de Souza, J. A., Fleischer, I., Wdowiak, T., Gellert, R., Bernhardt, B., Evlanov, E. N., Zubkov, B., Foh, J., Bonnes, U., Kankeleit, E., Gütlich, P., Renz, F., Squyres, S. W., & Arvidson, R. E. (2006). Mössbauer mineralogy of rock, soil, and dust at Gusev crater, Mars: Spirit’s journey through weakly altered olivine basalt on the plains and pervasively altered basalt in the Columbia Hills. *Journal of Geophysical Research: Planets*, *111*(E2). https://doi.org/10.1029/2005JE002584

Morrison, R. H., & Oberbeck, V. R. (1978). A composition and thickness model for lunar impact crater and basin deposits. *Lunar Planetary Science Conference*, 3763–3785.

Moskowitz, B. M. (1993). Micromagnetic study of the influence of crystal defects on coercivity in magnetite. Journal of Geophysical Research: Solid Earth, 98(B10), 18011-18026. https://doi.org/10.1029/93JB01719

Mullender, T. A. T., van Velzen, A. J., & Dekkers, M. J. (1993). Continuous drift correction and separate identification of ferrimagnetic and paramagnetic contributions in thermomagnetic runs. *Geophysical Journal International*, *114*(3), 663–672. https://doi.org/10.1111/J.1365-246X.1993.TB06995.X

Müller, W. F., & Hornemann, U. (1969). Shock-induced planar deformation structures in experimentally shock-loaded olivines and in olivines from chondritic meteorites. *Earth and Planetary Science Letters*, *7*(3), 251–264. https://doi.org/10.1016/0012-821X(69)90062-4

Muttik, N., Kirsimäe, K., Newsom, H. E., & Williams, L. B. (2011). Boron isotope composition of secondary smectite in suevites at the Ries crater, Germany: Boron fractionation in weathering and hydrothermal processes. *Earth and Planetary Science Letters*, *310*(3–4), 244–251. https://doi.org/10.1016/J.EPSL.2011.08.028

Nagy, L., Williams, W., Tauxe, L., & Muxworthy, A. R. (2019). From nano to micro: Evolution of magnetic domain structures in multidomain magnetite. Geochemistry, Geophysics, Geosystems, 20(6), 2907-2918. https://doi.org/10.1029/2019GC008319

Naumov, M. V. (2005). Principal features of impact-generated hydrothermal circulation systems: mineralogical and geochemical evidence. *Geofluids*, *5*(3), 165–184. https://doi.org/10.1111/J.1468-8123.2005.00092.X

Neiva, A. M. R., Williams, I. S., Ramos, J. M. F., Gomes, M. E. P., Silva, M. M. V. G., & Antunes, I. M. H. R. (2009). Geochemical and isotopic constraints on the petrogenesis of Early Ordovician granodiorite and Variscan two-mica granites from the Gouveia area, central Portugal. *Lithos*, *111*(3–4), 186–202. https://doi.org/10.1016/J.LITHOS.2009.01.005

Newsom, H. E. (1980). Hydrothermal alteration of impact melt sheets with implications for Mars. *Icarus*, *44*(1), 207–216. https://doi.org/10.1016/0019-1035(80)90066-4

Newsom, H. E., Graup, G., Sewards, T., & Keil, K. (1986). Fluidization and hydrothermal alteration of the Suevite deposit at the Ries Crater, West Germany, and implications for Mars. *Journal of Geophysical Research: Solid Earth*, *91*(B13), E239–E251. https://doi.org/10.1029/JB091IB13P0E239

Newell, A. J., & Merrill, R. T. (1999). Single-domain critical sizes for coercivity and remanence. Journal of Geophysical Research: Solid Earth, 104(B1), 617-628. https://doi.org/10.1029/1998JB900039

Nishioka, J., Obata, H., & Tsumune, D. (2013). Evidence of an extensive spread of hydrothermal dissolved iron in the Indian Ocean. *Earth and Planetary Science Letters*, *361*, 26–33. https://doi.org/10.1016/J.EPSL.2012.11.040

Nishitani, T., & Kono, M. (1981). Grain size effect on the low-temperature oxidation of titanomagnetite. *Journal of Geophysics*, *50*(1), 137–142. https://journal.geophysicsjournal.com/JofG/article/view/266

Oberbeck, V. R. (1975). The role of ballistic erosion and sedimentation in lunar stratigraphy. *Reviews of Geophysics*, *13*(2), 337–362. https://doi.org/10.1029/RG013I002P00337

Oches, E. A., & Banerjee, S. K. (1996). Rock-magnetic proxies of climate change from loess-paleosol sediments of the Czech Republic. *Studia Geophysica et Geodaetica*, *40*(3), 287–300. https://doi.org/10.1007/BF02300744

Ohmoto, H. (2003). Nonredox Transformations of Magnetite-Hematite in Hydrothermal Systems. *Economic Geology*, *98*(1), 157–161. https://doi.org/10.2113/GSECONGEO.98.1.157

O'Reilly, W. (1984). Magnetic properties of titanomagnetites and titanomaghemites. In *Rock and Mineral Magnetism* (pp. 132–171). Springer US. https://doi.org/10.1007/978-1-4684-8468-7_7

Osinski, G. R. (2003). Impact glasses in fallout suevites from the Ries impact structure, Germany: An analytical SEM study. *Meteoritics & Planetary Science*, *38*(11), 1641–1667. https://doi.org/10.1111/J.1945-5100.2003.TB00006.X

Osinski, G. R. (2004). Impact melt rocks from the Ries structure, Germany: an origin as impact melt flows? *Earth and Planetary Science Letters*, *226*(3–4), 529–543. https://doi.org/10.1016/J.EPSL.2004.08.012

Osinski, G. R. (2005). Hydrothermal activity associated with the Ries impact event, Germany. *Geofluids*, *5*(3), 202–220. https://doi.org/10.1111/j.1468-8123.2005.00119.x

Osinski, G. R., Grieve, R. A. F., Collins, G. S., Marion, C., & Sylvester, P. (2008). The effect of target lithology on the products of impact melting. *Meteoritics & Planetary Science*, *43*(12), 1939–1954. https://doi.org/10.1111/J.1945-5100.2008.TB00654.X

Osinski, Gordon R., Livio L. Tornabene, Neil R. Banerjee, Charles S. Cockell, Roberta Flemming, Matthew R.M. Izawa, Jenine McCutcheon, et al. 2013. "Impact-Generated Hydrothermal Systems on Earth and Mars." Icarus 224 (2): 347–63. https://doi.org/10.1016/j.icarus.2012.08.030.

Osinski, G. R., Grieve, R. A. F., Hill, P. J. A., Simpson, S. L., Cockell, C., Christeson, G. L., Ebert, M., Gulick, S., Melosh, H. J., Riller, U., Tikoo, S. M., & Wittmann, A. (2020). Explosive interaction of impact melt and seawater following the Chicxulub impact event. *Geology*, *48*(2), 108–112. https://doi.org/10.1130/G46783.1

Osinski, G. R., Grieve, R. A. F., & Spray, J. G. (2004). The nature of the groundmass of surficial suevite from the Ries impact structure, Germany, and constraints on its origin. *Meteoritics and Planetary Science*, *39*(10), 1655–1683. https://doi.org/10.1111/j.1945-5100.2004.tb00065.x

Osselin, F., Pichavant, M., Champallier, R., Ulrich, M., & Raimbourg, H. (2022). Reactive transport experiments of coupled carbonation and serpentinization in a natural serpentinite. Implication for hydrogen production and carbon geological storage. Geochimica et Cosmochimica Acta, 318, 165-189. https://doi.org/10.1016/j.gca.2021.11.039

Otake, T., Wesolowski, D. J., Anovitz, L. M., Allard, L. F., & Ohmoto, H. (2007). Experimental evidence for non-redox transformations between magnetite and hematite under H2-rich hydrothermal conditions. *Earth and Planetary Science Letters*, *257*(1–2), 60–70. https://doi.org/10.1016/J.EPSL.2007.02.022

Özdemir, Ö., & Dunlop, D. J. (1997). Effect of crystal defects and internal stress on the domain structure and magnetic properties of magnetite. *Journal of Geophysical Research: Solid Earth*, *102*(B9), 20211–20224. https://doi.org/10.1029/97JB01779

Özdemir, Ö., & Dunlop, D. J. (2010). Hallmarks of maghemitization in low-temperature remanence cycling of partially oxidized magnetite nanoparticles. *Journal of Geophysical Research: Solid Earth*, *115*(B2), 2101. https://doi.org/10.1029/2009JB006756

Özdemir, Ö., Dunlop, D. J., & Moskowitz, B. M. (1993). The effect of oxidation on the Verwey transition in magnetite. *Geophysical Research Letters*, *20*(16), 1671–1674. https://doi.org/10.1029/93GL01483

Pearce, G. W., & Karson, J. A. (1981). On pressure demagnetization. *Geophysical Research Letters*, *8*(7), 725–728. https://doi.org/10.1029/GL008I007P00725

Penfield, G. T., and Camargo, A. (1981). Definition of a major igneous zone in the central Yucatan platform with aeromagnetics and gravity. *Soc. Explor. Geophys. Annu. Meeting, Tech. Progr. Abstracts, 1981*.

Petrovský, E. D., & Kapička, A. (2006). On determination of the Curie point from thermomagnetic curves. *Journal of Geophysical Research: Solid Earth*, *111*(B12), 12–27. https://doi.org/10.1029/2006JB004507

Pike, C., & Fernandez, A. (1999). An investigation of magnetic reversal in submicron-scale Co dots using first order reversal curve diagrams. Journal of applied physics, 85(9), 6668-6676. https://doi.org/10.1063/1.370177

Pike, C. R., Roberts, A. P., & Verosub, K. L. (1999). Characterizing interactions in fine magnetic particle systems using first order reversal curves. Journal of Applied Physics, 85(9), 6660-6667. https://doi.org/10.1063/1.370176

Pike, C. R., Roberts, A. P., & Verosub, K. L. (2001a). First order reversal curve diagrams and thermal relaxation effects in magnetic particles. Geophysical Journal International, 145(3), 721-730. https://doi.org/10.1046/j.0956-540x.2001.01419.x

Pike, C. R., Roberts, A. P., Dekkers, M. J., & Verosub, K. L. (2001b). An investigation of multi-domain hysteresis mechanisms using FORC diagrams. *Physics of the Earth and Planetary Interiors*, *126*(1–2), 11–25. https://doi.org/10.1016/S0031-9201(01)00241-2

Pike, R. (2003). First-order reversal-curve diagrams and reversible magnetization. *Physical Review B*, *68*(10), 104424. https://doi.org/10.1103/PhysRevB.68.104424

Pilkington, M., Ames, D. E., & Hildebrand, A. R. (2004). Magnetic mineralogy of the Yaxcopoil-1 core, Chicxulub. *Meteoritics & Planetary Science*, *39*(6), 831–841. https://doi.org/10.1111/J.1945-5100.2004.TB00933.X

Pilkington, M., & Grieve, R. A. F. (1992). The geophysical signature of terrestrial impact craters. *Reviews of Geophysics*, *30*(2), 161–181. https://doi.org/10.1029/92RG00192

Pilkington, M., & Hildebrand, A. R. (2000). Three-dimensional magnetic imaging of the Chicxulub Crater. *Journal of Geophysical Research: Solid Earth*, *105*(B10), 23479–23491. https://doi.org/10.1029/2000JB900222

Plado, J., Pesonen, L., & Puura, V. (1999). Effect of erosion on gravity and magnetic signatures of complex impact structures: Geophysical modeling and applications. Geological Society of America, Special Paper (339), 229–240. https://doi.org/10.1130/0-8137-2339-6.229

Pohl, J. (1965). Die Magnetisierung der Suevite des Rieses. *Neues Jahrb. Miner. Monatsh (1965)*. 268-276.

Pohl, J., and Gustav A. (1969) "Anomalien des erdmagnetfeldes und magnetisierung der gesteine im Nördlinger Ries." *Geologica Bavarica*, *61*, 327-336.

Pohl, J., Stöffler, D., Gall, H., & Ernstson, K. (1977a). The Ries Impact Crater. In D. J. Roddy, R. O. Pepin, & R. B. Merrill (Eds.), *Impact and Explosion Cratering*. 343–404.

Pohl, J. "Paläomagnetische und gesteinsmagnetische Untersuchungen an den Kernen der Forschungsbohrung Nördlingen 1973." (1977b): Geologica Bavarica 75 (1977): 329-348.

Pohl, J., Poschlod, K., Reimold, W. U., Meyer, C., & Jacob, J. (2010). Ries crater, germany: The Enkingen magnetic anomaly and associated drill core SUBO 18. *Special Paper of the Geological Society of America*, *465*, 141–163. https://doi.org/10.1130/2010.2465(10)

Quesnel, Y., Gattacceca, J. Ô., Osinski, G. R., & Rochette, P. (2013). Origin of the central magnetic anomaly at the Haughton impact structure, Canada. *Earth and Planetary Science Letters*, *367*, 116–122. https://doi.org/10.1016/J.EPSL.2013.02.032

Ramos, E. L. (1975). Geological Summary of the Yucatan Peninsula. In *The Gulf of Mexico and the Caribbean* (pp. 257–282). Springer, Boston, MA. https://doi.org/10.1007/978-1-4684-8535-6_7

Rasband, W. S. (1997). ImageJ. US national institutes of health, Bethesda, MD.

Rasmussen, C., Stockli, D. F., Ross, C. H., Pickersgill, A., Gulick, S. P., Schmieder, M., Christeson, G. L., Wittmann, A., Kring, D. A., & Morgan, J. V. (2019). U-Pb memory behavior in Chicxulub's peak ring — Applying U-Pb depth profiling to shocked zircon. *Chemical Geology*, *525*, 356–367. https://doi.org/10.1016/J.CHEMGEO.2019.07.029

Rebolledo-Vieyra, M., Urrutia-Fucugauchi, J., & López-Loera, H. (2010). Aeromagnetic anomalies and structural model of the Chicxulub multiring impact crater, Yucatan, Mexico. *Revista Mexicana de Ciencias Geológicas*, *27*(1), 185–195.

Renne, P. (2013). Synchrony between the Chicxulub impact and the Cretaceous-Paleogene boundary extinctions: What does it mean? - NASA/ADS. *American Geophysical Union, Spring Meeting*.

Reznik, B., Kontny, A., Fritz, J., & Gerhards, U. (2016). Shock-induced deformation phenomena in magnetite and their consequences on magnetic properties. *Geochemistry, Geophysics, Geosystems*, *17*(6), 2374–2393. https://doi.org/10.1002/2016GC006338

Riller, U., Poelchau, M. H., Rae, A. S. P., Schulte, F. M., Collins, G. S., Melosh, H. J., Grieve, R. A. F., Morgan, J. V., Gulick, S. P. S., Lofi, J., Diaw, A., McCall, N., Kring, D. A., Morgan, J. V., Gulick, S. P. S., Green, S. L., Lofi, J., Chenot, E., Christeson, G. L., … Bralower, T. J. (2018). Rock fluidization during peak-ring formation of large impact structures. *Nature 2018 562:7728*, *562*(7728), 511–518. https://doi.org/10.1038/s41586-018-0607-z

Roberts, A. P., Pike, C. R., & Verosub, K. L. (2000). First-order reversal curve diagrams: A new tool for characterizing the magnetic properties of natural samples. *Journal of Geophysical Research: Solid Earth*, *105*(B12), 28461–28475. https://doi.org/10.1029/2000JB900326

Roberts, A. P., Heslop, D., Zhao, X., & Pike, C. R. (2014). Understanding fine magnetic particle systems through use of first-order reversal curve diagrams. *Reviews of Geophysics*, *52*(4), 557–602. https://doi.org/10.1002/2014RG000462

Roberts, A. P., Almeida, T. P., Church, N. S., Harrison, R. J., Heslop, D., Li, Y., Li, J., Muxworthy, A. R., Williams, W., & Zhao, X. (2017). Resolving the Origin of Pseudo-Single Domain Magnetic Behavior. *Journal of Geophysical Research: Solid Earth*, *122*(12), 9534–9558. https://doi.org/10.1002/2017JB014860

Roberts, A. P., Tauxe, L., Heslop, D., Zhao, X., & Jiang, Z. (2018). A Critical Appraisal of the "Day" Diagram. *Journal of Geophysical Research: Solid Earth*, *123*(4), 2618–2644. https://doi.org/10.1002/2017JB015247

Roberts, A. P., Hu, P., Harrison, R. J., Heslop, D., Muxworthy, A. R., Oda, H., Sato, T., Tauxe, L., & Zhao, X. (2019). Domain State Diagnosis in Rock Magnetism: Evaluation of Potential Alternatives to the Day Diagram. *Journal of Geophysical Research: Solid Earth*, *124*(6), 5286–5314. https://doi.org/10.1029/2018JB017049

Robertson, D. J., & France, D. E. (1994). Discrimination of remanence-carrying minerals in mixtures, using isothermal remanent magnetisation acquisition curves. *Physics of the Earth and Planetary interiors*, *82*(3-4), 223-234. https://doi.org/10.1016/0031-9201(94)90074-4

Ross, C. H., Stockli, D. F., Rasmussen, C., Gulick, S. P. S., Graaff, S. J. de, Claeys, P., Zhao, J., Xiao, L., Pickersgill, A. E., Schmieder, M., Kring, D. A., Wittmann, A., & Morgan, J. V. (2022). Evidence of Carboniferous arc magmatism preserved in the Chicxulub impact structure. *GSA Bulletin*, *134*(1–2), 241–260. https://doi.org/10.1130/B35831.1

Sant'Ovaia, H., Olivier, P., Ferreira, N., Noronha, F., & Leblanc, D. (2010). Magmatic structures and kinematics emplacement of the Variscan granites from Central Portugal (Serra da Estrela and Castro Daire areas). *Journal of Structural Geology*, *32*(10), 1450–1465. https://doi.org/10.1016/J.JSG.2010.09.003

Sapers, H. M., Osinski, G. R., Flemming, R. L., Buitenhuis, E., Banerjee, N. R., Tornabene, L. L., Blain, S., & Hainge, J. (2017). Evidence for a spatially extensive hydrothermal system at the Ries impact structure, Germany. *Meteoritics and Planetary Science*, *52*(2), 351–371. https://doi.org/10.1111/maps.12796

Sato, Masahiko, Kosuke Kurosawa, Shota Kato, Masashi Ushioda, and Sunao Hasegawa. "Shock remanent magnetization intensity and stability distributions of single-domain titanomagnetite-bearing basalt sample under the pressure range of 0.1–10 GPa." Geophysical Research Letters 48, no. 8 (2021): e2021GL092716. https://doi.org/10.1029/2021GL092716

Sauer A. (1920). Erläuterungen zur geologischen. *Karte Württemberg 1:50,000*, *Sheet 20 – Bopfingen*. 15.

Schmieder, M., Kennedy, T., Jourdan, F., Buchner, E., & Reimold, W. U. (2018). A high-precision 40Ar/39Ar age for the Nördlinger Ries impact crater, Germany, and implications for the accurate dating of terrestrial impact events. *Geochimica et Cosmochimica Acta*, *220*, 146–157. https://doi.org/10.1016/J.GCA.2017.09.036

Schulte, P., Alegret, L., Arenillas, I., Arz, J. A., Barton, P. J., Bown, P. R., Bralower, T. J., Christeson, G. L., Claeys, P., Cockell, C. S., Collins, G. S., Deutsch, A., Goldin, T. J., Goto, K., Grajales-Nishimura, J. M., Grieve, R. A. F., Gulick, S. P. S., Johnson, K. R., Kiessling, W., … Willumsen, P. S. (2010). The chicxulub asteroid impact and mass extinction at the cretaceous-paleogene boundary. *Science*, *327*(5970), 1214–1218. https://doi.org/10.1126/SCIENCE.1177265

Scott, R. G., Pilkington, M., Tanczyk, E. I., & Grieve, R. A. F. (1995). Magnetic properties of three impact structures in Canada. *Meteoritics, 30(5),* 576-577.

Sergienko, E. S., Yanson, S. Y., Kosterov, A., Kharitonskii, P. V., & Frolov, A. M. (2021). Suevites and Tagamites of Zhamanshin Astrobleme: Distribution in the Crater and Petrographic Features. *IOP Conference Series: Earth and Environmental Science*, *666*(4), 042080. https://doi.org/10.1088/1755-1315/666/4/042080

Sharpton, V. L., Brent Dalrymple, G., Marín, L. E., Ryder, G., Schuraytz, B. C., & Urrutia-Fucugauchi, J. (1992). New links between the Chicxulub impact structure and the Cretaceous/Tertiary boundary. *Nature*, *359*(6398), 819–821. https://doi.org/10.1038/359819a0

Smit, J. (1999). THE GLOBAL STRATIGRAPHY OF THE CRETACEOUS-TERTIARY BOUNDARY IMPACT EJECTA. *Annual Review of Earth and Planetary Sciences*, *27*, 75–113. https://doi.org/10.1146/ANNUREV.EARTH.27.1.75

Sprain, C. J., Renne, P. R., Clemens, W. A., & Wilson, G. P. (2018). Calibration of chron C29r: New high-precision geochronologic and paleomagnetic constraints from the Hell Creek region, Montana. *GSA Bulletin*, *130*(9–10), 1615–1644. https://doi.org/10.1130/B31890.1

Srnka, L. J., Martelli, G., Newton, G., Cisowski, S. M., Fuller, M. D., & Schaal, R. B. (1979). Magnetic field and shock effects and remanent magnetization in a hypervelocity impact experiment. *Earth and Planetary Science Letters*, *42*(1), 127–137. https://doi.org/10.1016/0012-821X(79)90198-5

Stöffler, D. (1977). Research Drilling Nördlingen 1973: Polymict Breccias, Crater Basement, and Cratering Model of the Ries Impact Structure. *Geologica Bavarica*, *75*. 443-458

Stöffler, D., R. A. F. Grieve, D. Fettes, and J. Desmons. (2007). Impactites. *Metamorphic rocks: A classification and glossary of terms, recommendations of the International Union of Geological Sciences*, 82-92.

Szczepaniak-Wnuk, I., Górka-Kostrubiec, B., Dytłow, S., Szwarczewski, P., Kwapuliński, P., & Karasiński, J. (2020). Assessment of heavy metal pollution in Vistula river (Poland) sediments by using magnetic methods. *Environmental Science and Pollution Research*, *27*, 24129–24144. https://doi.org/10.1007/s11356-020-08608-4

Tarling, D. H. (Donald H., & Hrouda, F. (František). (1993). *The magnetic anisotropy of rocks*. Chapman & Hall.

Thüns, N., Krooss, B. M., Zhang, Q., & Stanjek, H. (2019). The effect of H2 pressure on the reduction kinetics of hematite at low temperatures. International Journal of Hydrogen Energy, 44(50), 27615-27625. https://doi.org/10.1016/j.ijhydene.2019.08.178

Tikoo, S. M., Gattacceca, J., Swanson-Hysell, N. L., Weiss, B. P., Suavet, C., & Cournède, C. (2015). Preservation and detectability of shock-induced magnetization. *Journal of Geophysical Research: Planets*, *120*(9), 1461–1475. https://doi.org/10.1002/2015JE004840

Tikoo, S., Zylberman, W., Quesnel, Y., Gattacceca, J., Rebolledo-Vieyra, M., Fucugauchi, J. U., Expedition 364 Science Party, I. I., Tikoo, S., Zylberman, W., Quesnel, Y., Gattacceca, J., Rebolledo-Vieyra, M., Fucugauchi, J. U., & Expedition 364 Science Party, I. I. (2017). Paleomagnetic insights into impact-related hydrothermal systems and magnetic anomalies at the Chicxulub crater. *AGUFM*, *2017*, P23H-05.

Ugalde, H., Artemieva, N., & Milkeriet, B. (2005). Magnetization on impact structures - Constraints from numerical modeling and petrophysics. In *Large Meteoite Impacts III* (pp. 25–42).

Urrutia-Fucugauchi, J., Camargo-Zanoguera, A., Mexicanos, P., Urrutia-Fucugauchi, J., Camargo-Zanoguera, A., Pérez-Cruz, L., Pérez-Cruz, G., Pérez-Cruz, L., & Pérez-Cruz, G. (2011). The Chicxulub multi-ring impact crater, Yucatan carbonate platform, Gulf of Mexico. *Geofísica Internacional*, *50*(1), 99–127.

Urrutia-Fucugauchi, J., Pérez-Cruz, L. L., Tikoo, S., Riller, U. P., Rebolledo-Vieyra, M., Morgan, J. V., & Gulick, S. P. (2018). Magnetic Fabrics and Properties of Impactites and Basement Beneath the Peak Ring of Chicxulub Crater-IODP-ICDP Expedition 364. *AGUFM*, *2018*, PP51D-1165.

Vahle, C., Kontny, A., Gunnlaugsson, H. P., & Kristjansson, L. (2007). The Stardalur magnetic anomaly revisited—New insights into a complex cooling and alteration history. *Physics of the Earth and Planetary Interiors*, *164*(3–4), 119–141. https://doi.org/10.1016/J.PEPI.2007.06.004

Verwey, E. J. W. (1939). Electronic Conduction of Magnetite (Fe3O4) and its Transition Point at Low Temperatures. *Nature*, *144*(3642), 327–328. https://doi.org/10.1038/144327b0

Weber, B., González-Guzmán, R., Manjarrez-Juárez, R., Cisneros de León, A., Martens, U., Solari, L., Hecht, L., & Valencia, V. (2018). Late Mesoproterozoic to Early Paleozoic history of metamorphic basement from the southeastern Chiapas Massif Complex, Mexico, and implications for the evolution of NW Gondwana. *Lithos*, *300–301*, 177–199. https://doi.org/10.1016/J.LITHOS.2017.12.009

Witt, A., Fabian, K., & Bleil, U. (2005). Three-dimensional micromagnetic calculations for naturally shaped magnetite: Octahedra and magnetosomes. Earth and Planetary Science Letters, 233(3-4), 311-324. https://doi.org/10.1016/j.epsl.2005.01.043

Witts, J. D., Newton, R. J., Mills, B. J. W., Wignall, P. B., Bottrell, S. H., Hall, J. L. O., Francis, J. E., & Alistair Crame, J. (2018). The impact of the Cretaceous–Paleogene (K–Pg) mass extinction event on the global sulfur cycle: Evidence from Seymour Island, Antarctica. *Geochimica et Cosmochimica Acta*, *230*, 17–45. https://doi.org/10.1016/J.GCA.2018.02.037

Wünnemann, K., Collins, G. S., & Osinski, G. R. (2008). Numerical modelling of impact melt production in porous rocks. *Earth and Planetary Science Letters*, *269*(3–4), 530–539. https://doi.org/10.1016/J.EPSL.2008.03.007

Zhang, Q., Appel, E., Basavaiah, N., Hu, S., Zhu, X., & Neumann, U. (2021). Is Alteration of Magnetite During Rock Weathering Climate-Dependent? *Journal of Geophysical Research: Solid Earth*, *126*(10). https://doi.org/10.1029/2021JB022693

Zhang, Q., Appel, E., Stanjek, H., Byrne, J. M., Berthold, C., Sorwat, J., Rösler, W., & Seemann, T. (2020). Humidity related magnetite alteration in an experimental setup. *Geophysical Journal International*, *224*(1), 69–85. https://doi.org/10.1093/GJI/GGAA394

Zhao, X., & Liu, Q. (2010). Effects of the grain size distribution on the temperature-dependent magnetic susceptibility of magnetite nanoparticles. *Science China Earth Sciences*, *53*(7), 1071–1078. https://doi.org/10.1007/s11430-010-4015-y

Zhao, X., Roberts, A. P., Heslop, D., Paterson, G. A., Li, Y., & Li, J. (2017). Magnetic domain state diagnosis using hysteresis reversal curves. Journal of Geophysical Research: Solid Earth, 122(7), 4767-4789. https://doi.org/10.1002/2016JB013683

Zhao, J., Xiao, L., Gulick, S. P. S., Morgan, J. V., Kring, D., Fucugauchi, J. U., Schmieder, M., de Graaff, S. J., Wittmann, A., Ross, C. H., Claeys, P., Pickersgill, A., Kaskes, P., Goderis, S., Rasmussen, C., Vajda, V., Ferrière, L., Feignon, J. G., Chenot, E., … Yamaguchi, K. (2020). Geochemistry, geochronology and petrogenesis of Maya Block granitoids and dykes from the Chicxulub Impact Crater, Gulf of México: Implications for the assembly of Pangea. *Gondwana Research*, *82*, 128–150. https://doi.org/10.1016/J.GR.2019.12.003

Zijderveld, J. D. A. (2013). A. C. Demagnetization of Rocks: Analysis of Results. *Developments in Solid Earth Geophysics*, *3*, 254–286. https://doi.org/10.1016/B978-1-4832-2894-5.50049-5

Appendices

Three folders containing the supplemental files described below are available for download electronically at the **KITopen** repository.

KITopen ID: 1000167980

DOI: https://doi.org/10.35097/1913

Appendix A – Chapter 2

A.1 – Sample list

Table A.1. Sample list from M0077A in the peak ring of the Chixculub impact crater, with lithology, unit and IODP identification code. S=Suevite; SM = Suevite+Melt; M = Melt; G = Granitoid; MGC = Melt-Granitoid Contact.

Sample #	Lithology	Depth	Unit	Core	Sec	Top	Bot	Sample #	Lithology	Depth	Unit	Core	Sec	Top	Bot
639 (S-2A)	Suevite	639	2A	47	2	42	44.5	999 (G3-4)	Granitoid	999	4	192	2	58	60
646 (S-2A)	Suevite	646	2A	49	2	36	38.5	999 (G2-4)	Granitoid	999	4	192	2	58	60
683 (S-2B)	Suevite	683	2B	63	1	13	15.5	999 (G1-4)	Granitoid	999	4	192	2	58	60
688 (S-2B)	Suevite	689	2B	65	1	80	82.5	1085 (G-4)	Granitoid	1085	4	222	1	55	57
700 (S-2B)	Suevite	700	2B	73	2	21	23.5	1097 (G-4)	Granitoid	1098	4	226	1	61	63
721 (SM-3A)	S-M mix	721	3A	87	2	30	31	1100 (G-4)	Granitoid	1100	4	227	1	5	7
727 (M-3A)	I. Melt	727	3A	89	2	56	57	1103 (G-4)	Granitoid	1103	4	228	1	31	33
732 (M-3A)	I. Melt	732	3A	91	1	29	31.5	1135A (G-4)	Granitoid	1135	4	238	1	76	78
738 (M-3B)	I. Melt	739	3B	93	1	78	80.5	1135B (G-4)	Granitoid	1135	4	238	1	98	101
744 (M-3B)	I. Melt	744	3B	95	1	26	28.5	1137 (G-4)	Granitoid	1138	4	239	1	47.5	51.5
747 (G-4)	Granitoid	747	4	96	1	8	10	1140 (G-4)	Granitoid	1140	4	239	2	116	118
763 (G-4)	Granitoid	763	4	111	3	30	32	1149 (G-4)	Granitoid	1149	4	242	3	26	28
804 (G-4)	Granitoid	804	4	115	2	60	62	1150 (G-4)	Granitoid	1150	4	243	2	21	23
810 (G-4)	Granitoid	810	4	118	2	50	52	1161 (G-4)	Granitoid	1161	4	247	2	23	26
847 (G-4)	Gr./Dol.	847	4	134	3	83	86	1194 (G-4)	Granitoid	1194	4	258	1	15	17
967 (G-4)	Granitoid	967	4	182	1	70	72	1197 (G-4)	Granitoid	1197	4	259	1	5	7
982 (G-4)	Granitoid	982	4	187	1	60	62	1224A (G-4)	Granitoid	1224	4	267	2	100	102
994 (GD-4)	Granitoid	994	4	191	1	9	11	1224B (G-4)	Granitoid	1224	4	267	3	9	11
995 (M-4)	Granitoid	995	4	191	1	87	90	1224C (M-4)	I.Melt	1224	4	267	3	24	26
995 (G-4)	Granitoid	995	4	191	1	108	110	1224C (G-4)	Granitoid	1224	4	267	3	24	26
996 (G-4)	Granitoid	996	4	191	3	40	42	1224D (G-4)	Granitoid	1224	4	267	3	32	34
997 (S-4)	S. Dyke	998	4	192	1	65	67	1225 (G-4)	Granitoid	1225	4	268	1	58	60
999 (M1-4)	I. Melt	999	4	192	2	58	60	1231 (G-4)	Granitoid	1231	4	270	1	59	61
999 (M2-4)	I. Melt	999	4	192	2	58	60	1249 (G-4)	Granitoid	1249	4	276	1	15	17
999 (MGC-4)	M-G contact	999	4	192	2	58	60	1326 (G-4)	Granitoid	1327	4	301	2	28	30

A.2 – Core azimuth correction

In order to correctly determine the declination of the paleomagnetic vector, as well as correct geographic directions of the main axes of susceptibility, we have applied an azimuth correction prior to the drilling of our cores.

On a first stage, the cores were marked with an arbitrary "marker line" after drilled, and an acoustic image of the hole walls was done using a slim line tool coupled with a 3-component magnetometer and accelerometer, which provides a magnetic north orientation in these acoustic images. On a second stage, CT scans of the cores were made, and aligned with the acoustic images using recognizable features, such as structures, cracks, and dipping strata. Knowing the direction of "north" in acoustic images of the borehole wall, the angle discrepancy between the "marker line" and north were recorded (+/- angles corresponding to clockwise/counter-clockwise rotations respectively). A ranking of 1-5 was attributed to the correction for each section, depending on the certainty of the correction (5 being certain, 1 being uncertain). For more details, see (McCall et al., 2017). For our sections, the angles and confidence rating are as follows:

Sample	Core	Section	Dp. top	Rot. (°)	Certainty
646	49	2	645.55	-69.7	3
683	63	1	683.47	76.73	1
727	89	2	727.43	52.43	5
744	95	1	744.20	-122.65	5
747	96	1	747.07	-122.65	4
847	134	3	847.01	50.58	4
997	192	1	997.74	-41.36	4
1085	222	1	1085.13	-23.14	5
1135B	238	1	1135.02	66.00	3
1137	239	1	1137.57	126.72	5
1249	268	1	1225.12	97.59	1
1326	276	1	1249.49	-68.33	4

The samples were cut along a plane perpendicular to the "Marker Line", allowing for re-orientation of these pieces accordingly. Lastly, we marked the angle corrections in our samples, prior to drilling the cylindrical specimens for demagnetization and AMS measurements. This guarantees that all our specimens have an orientation of 0/90, allowing for interpretation of the data in specimen coordinates. See diagram below (Fig. A.3.1):

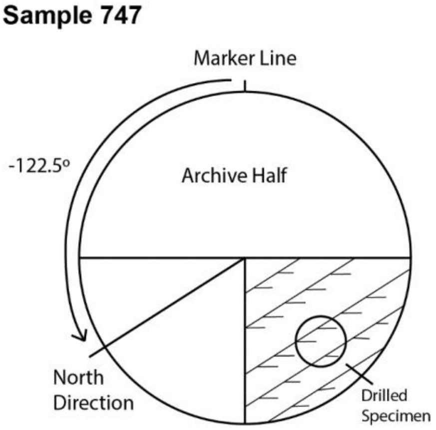

Figure A.2.1. Sketch diagram of orientation procedure, using the data from table 1. Quarter core on the bottom right is our working sample.

A.3 – Isothermal Remanent Magnetization component analysis

Table A.3.1. IRM component analysis results for all samples of M0077A, except 1100.

	Component 1					Component 2				
Sample	Cont. (%)	SIRM (A/m)	log($B_{1/2}$) mT	$B_{1/2}$ (mT)	DP (mT)	Cont. (%)	SIRM (A/m)	log($B_{1/2}$) mT	$B_{1/2}$ (mT)	DP (mT)
639 (2A)	100.0	0.1	1.7	53.7	0.2					
646 (2A)	100.0	0.0	1.7	50.1	0.2					
683 (2B)	100.0	0.1	1.6	43.7	0.2					
688 (2B)	86.8	0.0	1.6	42.7	0.2	13.2	0.0	2.2	141.3	0.3
721 (2C)	100.0	5.8	1.6	38.0	0.3					
727 (3A)	100.0	3.0	1.6	43.7	0.2					
732 (3A)	100.0	3.6	1.6	39.8	0.2					
738 (3B)	100.0	7.1	1.5	34.7	0.3					
744 (3B)	100.0	15.8	1.8	58.9	0.2					
747 (4)	100.0	2.8	1.8	61.7	0.3					
763 (4)	93.8	0.0	1.7	46.8	0.3	6.3	0.0	2.7	446.7	0.3
804 (4)	100.0	0.2	1.5	33.1	0.3					
810 (4)	100.0	0.7	1.7	44.7	0.3					
847 (4)	100.0	72.7	1.9	81.3	0.2					
967 (4)	100.0	1.1	1.7	51.3	0.3					
982 (4)	100.0	0.4	1.6	39.8	0.3					
994 (4)	100.0	1.3	1.7	45.7	0.3					
995b (4)	100.0	5.1	1.7	46.8	0.3					
995G (4)	100.0	0.1	1.7	47.9	0.2					
997 (4)	100.0	1.7	1.9	70.8	0.3					
999 G3 (4)	100.0	0.1	1.7	53.7	0.2					
999 G2 (4)	100.0	0.4	1.7	53.7	0.3					
999 M1 (4)	100.0	18.8	1.8	61.7	0.2					
999 M2 (4)	100.0	29.9	1.8	56.2	0.2					
1085 (4)	100.0	0.2	1.8	67.6	0.2					
1135A (4)	100.0	1.1	1.6	42.7	0.3					
1135B (4)	100.0	2.1	1.7	49.0	0.3					
1137 (4)	100.0	3.8	1.8	56.2	0.3					
1224A (4)	96.4	1.1	1.9	72.4	0.3	3.6	0.0	2.8	575.4	0.4
1224B (4)	100.0	2.7	1.8	63.1	0.3					
1224C (4)	92.2	1.8	1.6	42.7	0.3	7.8	0.2	2.8	616.6	0.3
1224D-g (4)	100.0	0.6	1.7	50.1	0.3					

Table A.3.2. IRM component analysis results for sample 1100 before and after heating. Note the increase of $B_{1/2}$ before and after heating.

	Component 1					Component 2				
Sample	Cont. (%)	SIRM (A/m)	log($B_{1/2}$) mT	$B_{1/2}$ (mT)	DP (mT)	Cont. (%)	SIRM (A/m)	log($B_{1/2}$) mT	$B_{1/2}$ (mT)	DP (mT)
1100 Big	95.4	20.5	1.5	30.2	0.3	4.6	1.0	2.7	467.7	0.3
1100 Big after	100.0	43.9	1.8	56.2	0.3					
1100 n	100.0	0.1	1.7	45.7	0.3					
1100 n After	92.0	0.3	1.9	72.4	0.3	8.0	0.0	2.8	562.3	0.3
1100 white	95.0	0.1	1.7	55.0	0.3	5.0	0.0	2.7	501.2	0.3
1100 white after	100.0	0.6	1.9	72.4	0.3					
1100 pink	100.0	0.1	1.8	63.1	0.3					
1100 pink after	100.0	0.2	1.9	70.8	0.3					

A.4 – Hysteresis parameters with depth

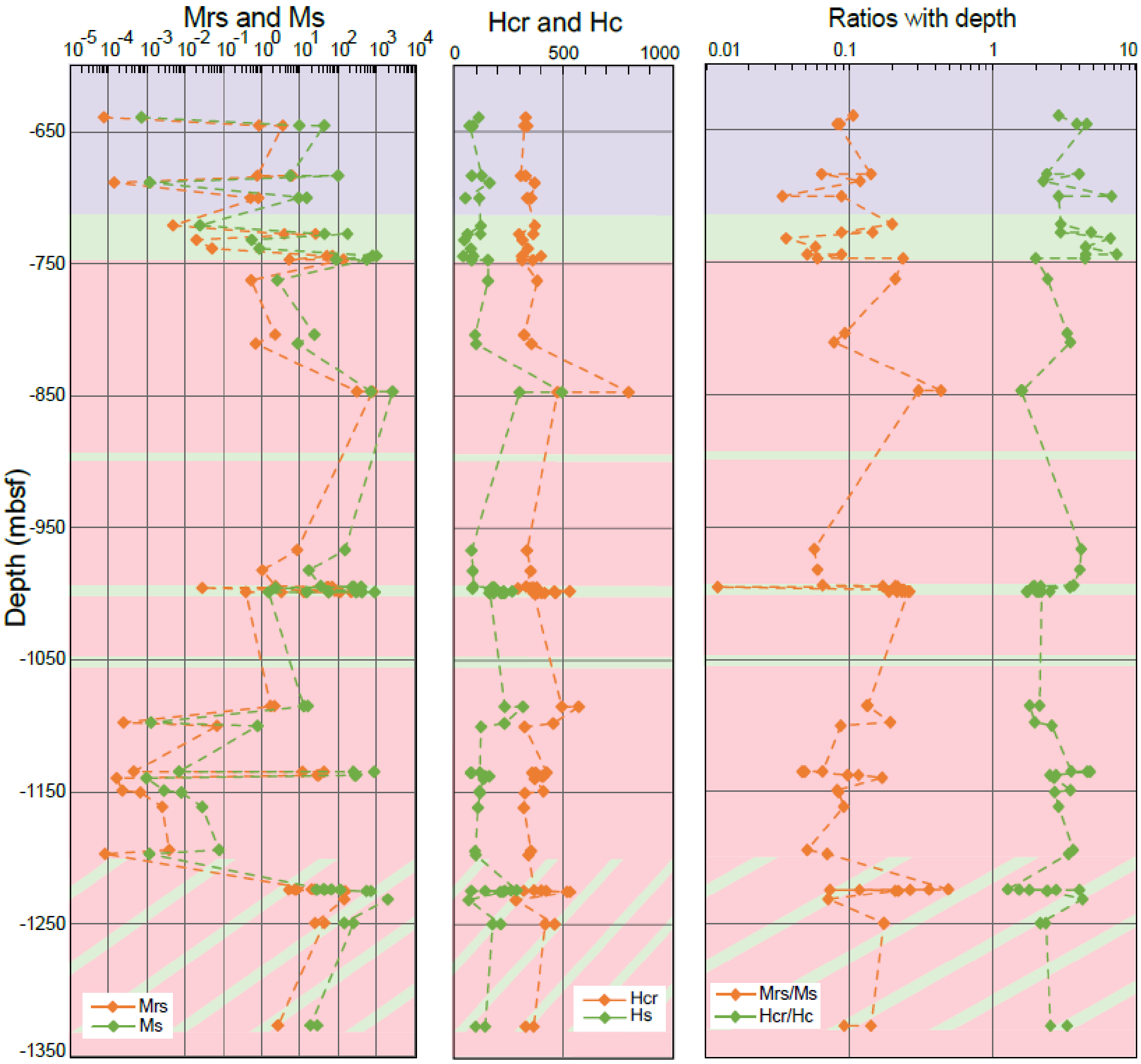

Figure A.4.1. Depth variation of hysteresis parameters along core M0077A.

A.5 – Paleomagnetic directions

Sample	Fr.Code	Dec(°)	Inc(°)	MAD	Steps	Group	Method	Notes
646	005A	199.93	-43.80	12.54	6	NF	Thermal	GC/Anchored
646	005B	174.81	-40.82	11.14	7	NF	AF	GC/Anchored
683	013⍰	115.87	-16.88	10.20	6	NF	Thermal	-
727	026A	173.49	-42.31	1.94	8	NF	AF	-
727	026B	164.95	-41.45	3.74	7	NF	Thermal	-
744	029A	184.96	-39.99	2.56	7	NF	AF	-
744	029B	182.82	-40.79	3.17	7	NF	Thermal	-
747	030B 1	314.78	-46.05	9.82	5	S	Thermal	-
747	030B 2	269.05	-42.97	5.27	4	S	Thermal	-
847	095A	161.68	-0.60	3.83	6	S	AF	Anchored
847	095C	125.04	-4.94	6.42	6	S	Thermal	-
847	095D 1	135.10	-4.86	15.16	6	S	Thermal	-
847	095D 2	178.54	19.94	2.62	5	S	Thermal	-
997	237⍰	167.34	11.53	6.03	7	S	AF	-
1085	262B	107.61	4.51	3.97	5	S	Thermal	-
1135B	262C	126.02	18.94	3.52	5	S	AF	-
1137	263A	250.54	-4.86	5.80	6	S	AF	-
1137	263B	248.00	-2.21	3.66	7	S	Thermal	-
1137	263C	290.79	8.56	9.05	6	S	Thermal	-
1225	313A	30.37	-39.77	1.12	8	S	Thermal	-
1225	313B	25.92	-37.84	2.05	8	S	AF	-
1249	321⍰	216.05	-29.31	5.00	8	S	AF	-
1326	337⍰	264.26	-24.85	5.52	5	s	AF	-

Table A.5.1. Paleomagnetic direction parameters for Chicxulub. Dec/Inc – Declination and inclination (°); MAD – maximum angular deviation; NF – Newly formed; GS – Great Circle.

A.6 – Supplemental Data Files

All data used for Chapter 2 is made available by GSA Buletin (supplement of DOI: 10.1130/B36547.1). This includes all of our Electron Probe Micro-Analysis (EPMA) (Supplemental Data S1), all our temperature dependent magnetic susceptibility data (κ-T, Supplemental Data S2); temperature dependent magnetization (M-T, Supplemental Data S3); Repeated heating experiments κ-T data (Supplemental Data S4); calculations of, and involving Koeningsberger ratios (Q-ratios, Supplemental Data S5); the hysteresis parameters and individual measurements (Supplemental Data S6); and the paleomagnetism data (Supplemental Data S7). Supplemental Data S8 contains all isothermal remanent magnetization (IRM) component analysis data. A supplemental text is also provided, with additional details regarding each data file.

Appendix B – Chapter 3

B.1 – SD-MD area procedure

In order to quantify variations in FORC features with temperature, we took a 4-step approach using the software ImageJ (Rasband, 1997).

1. After importing the original diagram (Fig. B.1.1., left), we create a binary black-and-white (BW) version of the diagram (Fig. B1.1., middle, all available in SF2, read below):
    a. Process -> Binary -> Make Binary.
2. Once converted to BW, we select a rectangle that excludes the X=0 axis, with lower Y threshold of B_u(mT) = -200, and maximum threshold of B_c(mT) = 100 (Fig. B.1.1., right). We selected these dimensions, because RT measurements for the 3 and 5 GPa samples were truncated due to procedural changes after these measurements. Keeping the constant area (in pixels) the same in all diagrams allows for better comparison.
3. We then measured the area of the selected rectangle (see procedure below). This was only done once, because the area for all diagrams is the same. Then, we changed the measurement parameters, to measure only points above the color threshold (in this case, 255 = black).
    a. Analyze → Measure
    b. Analyze → Set Measurement → Limit to threshold [x] (selected). Repeat a) for black area.
4. Finally, we note both the original area and area covered by black pixels in an excel spread sheet (See SF3), and calculate the ratio (in percentage) of black area vs total area.

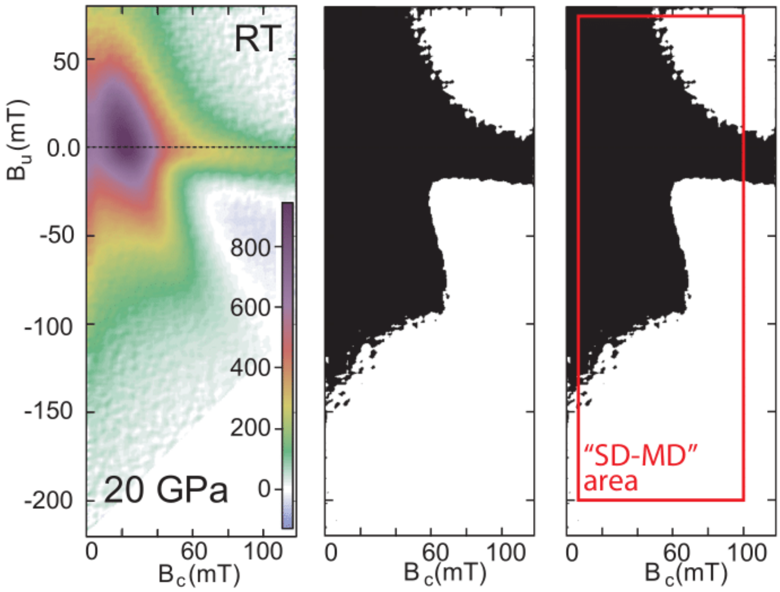

Figure B.1.1. SD-MD area calculation procedure (see text for details); A - original diagram; B – converted binary diagram; C – SD-MD area considered.

B.2 – Supplemental Data Files

All data used in Chapter 3 is available in the Mendeley Data repository, DOI: 10.17632/f66zx5bjnp.2. The dataset is provided in three separate supplemental files (SF) (2-4). This includes all our first order reversal curve (FORC) diagrams (SF 2), all of our isothermal remanent magnetization (IRM) modelling processed files (SF 3); and all data files for hysteresis, backfield, and FORC measurements (SF 4). Additional tables are provided in each of these files, where all data can be accessed. A supplemental text is also provided, with additional details regarding each data file.

Appendix C – Chapter 4

C.1 – Supplemental Data Files

All data used in Chapter 4 is available under supplemental files 2-5. These include a list with all our samples (file 2); all of our hysteresis loop and isothermal remanent magnetization (IRM) modelling processed and raw data files, including a supplemental table with additional model parameters (file 3); all our raw and processed data from electron probe microanalysis (EPMA), and a supplemental table with non-magnetite measurements (file 4); and all our temperature-dependent magnetic susceptibility (κ-T) data (file 5). A supplemental text is also provided, with additional details regarding each data file.